Simulation of the radiative flux at the martian surface between 180 and 1100 nm

Thesis

Simulation of the Radiative Flux at the Martian Surface between 180 and 1100 nm

Stephen Otter

Supervisors:

Professor John Zarnecki

Doctor Manish Patel

September 2009

A thesis submitted to the Open University in the subject of Planetary Sciences for the degree of Doctor of Philosophy

DATE OF SUBMISSION: 30 SEPT 2009

DATE OF AWARD: 4 APR 2010

NO CD

ATTACHED

PLEASE APPLY

TO

UNIVERSITY

Acknowledgments

Thank you to my project supervisors, Professor John Zarnecki and Doctor Manish Patel, for giving me the opportunity to undertake this project in the first place and then for all their subsequent help, advice and motivation that kept me on track. In particular the many hours spent checking, reviewing and commenting on thesis drafts, often at short notice towards the end, was very much appreciated. Thank you too to my examination panel of Professor Ian Wright, Doctor Günter Kargl and Doctor Simon Green for a firm but also fair and constructive session of questioning and discussion during my viva.

I would also like to thank the many other friends and colleagues in PSSRI and in the wider OU, both those who helped dig me out of the many holes my project led me into and also those who, through their friendship and support, contributed to making my time at the OU such a good one. Particularly the other PhD students with who I shared the reports, the deadlines, the conferences, the travelling, the office jokes and debates, the weekend working, ESMO (blame Canada!), the film making, the school visits, the football, the rugby, the darts, the fancy dress balls and, just occasionally, a pint or two. A special thanks also goes to the guys of PSSRI United (the 'Space Balls') for giving me something to kick (usually the ball) when the frustrations of IDL got too much and for allowing me to live out my dreams of football management for a few weeks a year.

Thank you to my family, Mum, Dad and Sally for their ever present support and for throughout eight years of University never once telling me to get a real job! Finally and most importantly, thank you to Lisa for being there for me when I started this and for having the understanding, commitment and saint-like patience to still be there for me when I finished.

To the good people of Lynchburg, Tennessee, particularly those in the employ of Mr Lem Motlow, please keep up the good work.

Abstract

A multi-layer radiative transfer model of the atmosphere of Mars, the UVIS simulation, has been created to simulate the non-ionising radiative flux at the surface of Mars. The simulation operates over the range 180 - 1100 nm and determines the diffuse component of the surface flux using the delta-Eddington approximation. Latitude, *l*, and areocentric longitude, L_s, dependent abundance models of the dust and ice cloud aerosols and of the gaseous species ozone and water vapour are incorporated. Alternative aerosol distributions are also used corresponding to observations made by the Thermal Emission Spectrometer onboard Mars Global Surveyor.

Studies of the variation in surface flux in response to increasing dust optical depth predict reduced surface intensities at UV wavelengths (180 - 400 nm) but at longer wavelengths the surface flux exhibits a local increase relative to the initial incident flux at optical depths < 2.5 for VIS wavelengths (401 - 750 nm) and < 6.0 for NIR wavelengths (751 - 1100 nm). This is explained in terms of the influence of aerosol scattering parameters. Enhancement of the total surface flux by ~20% or greater is shown to occur at latitude and L_s values corresponding to the presence of the aphelion cloud belt and during the annual dust maximum.

The potential of a surface based spectrometer to be utilised as a means of detecting the trace gases, ozone, hydrogen peroxide and methane in the atmosphere is assessed. Ozone proves the only suitable candidate and the spatial and seasonal distribution of ozone is discussed in the context of potential instrument deployment sites. The effects of varying aerosol scattering parameters on the surface flux is characterised and changes in aerosol scattering parameter values of < 5% are shown to be theoretically detectable by a spectrometer of sensitivity 1.0×10^{-2} $Wm^{-2}nm^{-1}$.

Contents

Figures

Acronyms and Abbreviations

ACB	Aphelion Cloud Belt
amu	Atomic mass unit
ASTM	American Society for Testing and Materials
AU	Astronomical Unit
CCD	Charge Couple Device
DNA	Deoxyribonucleic acid
EDL	Entry Descent and Landing
ESA	European Space Agency
GCM	General Circulation Model
GEP	Geophysical and Environmental Package
IMP	Imager for Mars Pathfinder
IRIS	Infrared Interferometer Spectrometer
IRTM	Infrared Thermal Mapper
LIBS	Laser induced break-down spectroscopy
LMD	Laboratoire de Meterologie Dynamique
MCD	Mars Climate Database
MER	Mar Explorations Rover
MOLA	Mars Orbital Laser Altimeter
MPF	Mars Pathfinder
MSL	Mars Science Laboratory
MY	Mars Year
NASA	National Aeronautics and Space Administration
NIR	Near Infrared wavelengths
NPH	North Polar Hood
OMEGA	Observatoire pour la Minéralogie, l'Eau, les Glaces et l'Activité
PFS	Planetary Fourier Spectrometer
RTG	Radioisotope Thermal Generator
sol	A Mars day
SPH	South Polar Hood
SPICAM	Spectroscopy for Investigation of Characteristics of the Atmosphere of Mars
TES	Thermal Emission Spectrometer
UV	Ultraviolet wavelengths
VIS	Visible wavelengths

Terms Used

A	Albedo of planetary surface
e	Orbital eccentricity
F_0	Solar flux at average Sun-Mars distance
F_{inc}	Solar flux incident at top of atmosphere
F_{direct}	Direct component of surface flux
$F_{diffuse}$	Diffuse component of surface flux
F_{total}	Direct + diffuse surface flux
G	Gravitational acceleration
g	Scattering asymmetry parameter
g'	Transformed value of g
g_{eff}	Effective scattering asymmetry parameter
i	Atmospheric layer index
l	Latitude
L_s	Areocentric longitude
M_{mol}	Mean molecular mass of atmosphere
n_0	Atmospheric index of refraction at surface of planet
$n(z)$	Index of refraction at altitude z
$P(z)$	Atmospheric pressure at altitude z
Q_{ext}	Dust extinction parameter
$Q(z)$	Dust mixing parameter at altitude z
R	Average Sun-Mars distance
R_m	Mean radius of planet
r	Current Sun-Mars distance
t	Surface time from local noon
z	Altitude
z_0	Atmospheric scale height
α_0	Constant of polarisability
ε	Rotational obliquity
θ	Solar zenith angle
λ	Wavelength
μ_0	Cosine(θ)
ν	Dust cut-off (Conrath) parameter
ξ	Column abundance
ρ_0	Atmospheric density at planet's surface
$\rho(z)$	Atmospheric density at altitude z
σ_{scat}	Scattering cross-section
σ_{abs}	Absorption cross-section
σ_{tot}	Total cross-section
$\sigma_{Rayleigh}$	Rayleigh scattering cross-section
τ_{scat}	Scattering optical depth
τ_{abs}	Absorption optical depth
τ_{tot}	Total optical depth
τ'	Transformed value of τ
ω_0	Single scattering albedo
ω_0'	Transformed value of ω
$\omega 0_{eff}$	Effective single scattering albedo

Chapter 1 - Introduction

1.1 A brief history of the observation of Mars

The planet Mars has always held a unique fascination for humankind. In ancient history, its distinctive red glow led many civilisations to associate the planet with battle and bloodshed, not least the Romans who gave the planet the name by which it is known today in honour of their god of war. However it was not until the seventeenth century and the invention of the telescope that Mars could be viewed as anything more than simply a red star.

At roughly half the diameter of the Earth, the relatively small size of Mars made it a difficult target to observe with the first primitive telescopes and it was the moons of Jupiter, the rings of Saturn and the phases of Venus that made the first observational headlines (Drake, 1957). As telescope technology improved though, the secrets of Mars slowly began to reveal themselves. Under the gaze of astronomers such as Huygens and Cassini, large scale surface features, such as the polar caps, were observed and records of the progress of these across the face of Mars led to the first calculations of the planet's rotational period (Huygens, 1698, Reeves, 1994).

As technology and technique continued to advance over the next few hundred years, it became possible to draw detailed maps of the martian surface showing how the face of Mars exhibited features which varied over time. Interpretation of these features was made by analogy to the processes known here on Earth and this resulted

in Mars becoming a very Earth-like planet in the eyes of its observers. An ice coated north and south pole, deserts, seas and rivers, and even forests and jungles were all proposed to explain the appearance of the martian disc.

A logical extension of this Earth-like scenario was to assume that, just like Earth, Mars was inhabited. Confirmation of this appeared to come at the end of the nineteenth century when the Italian astronomer Schiaparelli observed a network of unnaturally straight lines criss-crossing the martian surface which he termed 'canali' meaning channels in Italian. Interpretation of these 'canali' by Percival Lowell and others as a series of irrigation canals built by an advanced civilisation captured the public imagination and the place of the 'Martian' was assured in popular culture (Lowell, 1906, 1910).

It is now known of course that the canals, the rivers, the forests and seas were all instrument artefacts, optical illusions or the product of an over zealous imagination. The new era of space telescopes and interplanetary space probes has revealed Mars to be, in fact, a dusty, arid, desert world but one which still remains a source of fascination for humankind. Although expectations may have changed from planet-spanning civilisations to small microbial colonies, the search for life on the Red Planet continues.

1.2 Comparing the Red and Blue planets

It is believed that all the planets formed in the same epoch from the swirling disc of dust and gas left over from the formation of the Sun but from this point on, the evolutionary paths of each of the planets has differed significantly (Cameron, 1983).

Both Earth and Mars would have started out as planetary sized balls of molten rock and as the planets cooled, out-gassing and volcanism combined with volatiles released from impacting meteorites created the first atmospheres which were dominated by carbon dioxide gas (Lange and Ahrens, 1982, Pepin, 1991, Lammer et al., 2008). Further cooling allowed water vapour in the atmospheres to condense and rain down to the surface where it flowed as rivers and collected into lakes, seas and oceans.

Mars' initial carbon dioxide atmosphere may have been of a density comparable to or greater than that of modern day Earth and the resulting greenhouse effect may have produced temperatures suitable for sustaining liquid water on the surface of Mars for time periods on the order of hundreds of thousands of years. However, owing to the smaller size of Mars the continuing cooling process would have occurred more rapidly than for the Earth and this had a number of implications for Mars' evolutionary path. Within the first billion years or so of the planet's evolution Mars lost its internally generated magnetic field. The exact mechanism for this magnetic field loss is not yet known but it may have been caused by the cooling and solidification of the planet's interior halting the field generating dynamo of the planet's core (Curtis and Ness, 1988, Schubert et al., 2000, Connerney et al., 2001). The loss of the planet's inner dynamo would significantly reduce the strength of the magnetic field, leaving only a weak remnant field recorded in the magnetised minerals of the crust. Without the protection of a significant magnetic field the top of the planet's atmosphere is left open to bombardment by the charged particles of the solar wind which can act to strip away the upper atmosphere through a process known as 'sputtering' (Chassefière and Leblanc, 2004, Lundin et al., 2007). Mars'

smaller size also results in a mean gravitational acceleration only approximately a third of that of the Earth. A lower force of gravitational attraction lowers the planet's escape velocity making it easier for the lighter components of the atmosphere to escape into space. This process may have been enhanced in the early solar system by a high rate of comet and meteorite bombardment predicted to have occurred around 4 billion years ago and lasting for a few hundred million years (known as the 'late heavy bombardment'). The shock-front produced by a large body entering the atmosphere at high velocity can impart energy to the atmosphere and provides a potential mechanism to excite the atmospheric components above the required escape velocity (Cameron, 1983, Melosh and Vickery, 1989, Lammer et al., 2008). Combined with the sputtering process, over a time period on the order of a billion years, this has resulted in Mars losing most of its atmosphere with typical surface pressures now being around two orders of magnitude lower than they are on the Earth.

The lack of atmosphere in comparison to the Earth leaves the surface of Mars exposed to a much greater extent to the radiation emitted from the Sun, most notably the high energy ultraviolet photons, i.e. wavelengths shorter than ~300nm (Catling et al., 1999, Cockell et al., 2000, Patel et al., 2003). These are prevented from reaching the Earth's surface by the presence of a protective ozone layer located in the Earth's stratosphere approximately between an altitude of 20 and 40 km (Jacobson, 2006). Here photo-disassociation reactions occur between incoming ultraviolet photons and ozone molecules and the ozone abundance is sufficient that greater than 90% of the incident ultraviolet photons are absorbed before they can reach Earth's surface. Levels of ozone in the martian atmosphere are much lower than those of Earth's

atmosphere and consequently only a small percentage of the high energy ultraviolet photons entering the martian atmosphere are absorbed before reaching the surface.

In some respects however, Mars is very like Earth. The rotational period, i.e. a martian day (known as a 'sol'), is only around 40 minutes longer than that of Earth and a martian year lasts 687 days making each season roughly twice as long as its Earth equivalent. Mars' rotational obliquity currently stands at 25.2°, comparable to Earth's 23.4°. This means Mars' northern and southern hemispheres experience seasons just as those on Earth do, although the enhanced orbital eccentricity of Mars leads to a more pronounced difference between the levels of solar radiation received between summer and winter seasons. This similarity between the rotational obliquities of the two planets may not have always been the case though as the rotational obliquity of Mars is predicted to be subject to chaotic resonances which can result in severe increases in this value; at times effectively tilting the current polar regions of the planet to near equatorial latitudes (Ward and Rudy, 1991, Tourna and Wisdom, 1993). A similar process is likely to affect the angle of the Earth's axis of rotation but the presence of the Moon is believed to have a stabilising effect preventing such dramatic variations in Earth's rotational obliquity (Ward, 1982). Coincidentally the surface area of Mars is very close to that of the dry-land surface of the Earth, with Mars having a surface area on the order of 1.45×10^8 km^2 and Earth's dry-land surface area being on the order of 1.48×10^8 km^2. Despite Earth being larger in size, the surface area of the Earth is of course predominantly (~ 70%) covered by the oceans.

A number of environments within the Solar System have been identified as possible habitats for the development of extraterrestrial life, usually through association with

analogous environments on the Earth. Despite the differences highlighted above, Mars usually features strongly on this list of possible extraterrestrial habitats.

The current environment of Mars, at first glance, clearly appears unable to support life as we know it. The atmosphere is starkly different from that of Earth (see Table 1 for the composition of the martian atmosphere taken from Owen (1992)), the average surface temperature is well below zero degrees centigrade and , without the thermally stabilising effect of a thick atmosphere, subject to large variations over comparatively small timescales; for example, the Viking 1 surface probe recorded diurnal temperature variations on the order of ~ 80 K (Kieffer et al., 1976). With the exception of the ice locked away in Mars' polar caps, both the surface and atmosphere appear almost devoid of water. When combined with the intense ultraviolet radiative flux, which can directly damage cell DNA (the building blocks of all living organisms so far encountered) , and the highly oxidising conditions this creates, the chance of life finding a foothold on the surface seem slim (Patel et al., 2004a).

Species	Abundance
CO_2	95.32%
N_2	2.7%
Ar	1.6%
O_2	0.13%
CO	0.07%
O_3	< 0.04% (variable)
H_2O	< 0.03% (variable)

Table 1 – The gaseous species of Mars' atmosphere relevant to this work (Owen, 1992)

A possible solution to this may be to look a little deeper; in fact when discussing the habitability of Mars, it is usually the sub-surface environment that is under consideration. Studies of data returned by Mars Odyssey's Gamma Ray Spectrometer have inferred significant quantities of water ice may lie within the first few metres below the martian surface (Boynton et al., 2002). At these depths, it is likely that a high degree of shielding would be provided from the surface radiation environment and temperatures would be more stable than at the surface (Rothschild, 1990, Kanavarioti and Mancinelli, 1990, Westall et al., 2000). As the characterisation of microbial life on Earth continues, it constantly astounds just how varied and extreme are the habitats in which life can eke out an existence. From kilometres under ground to near-boiling geothermal springs or the frozen and arid dry valleys of Antarctica, microbial life survives and even thrives in these extreme environments (Rothschild and Mancinelli, 2001). Is it such a logical jump then to consider similar extremophilic organisms populating the martian subsurface?

Although the current surface environment appears openly hostile to life, this may not have always been the case. Studies of mineral composition and distribution and images which appear to show martian surface features of fluvial origin suggest, that in the early history of Mars, the surface may have featured large bodies of open water, perhaps protected from space and kept warm by the blanket of a thick atmosphere replenished from the planet's still warm interior (Jakosky and Phillips, 2001, Squyres and Kasting, 1994, Pieria, 1976, Carr, 1987, Malin and Edgett, 2000, Gulick, 2001, Baker, 2001, Solomon et al., 2005). It was under conditions such as these that life on Earth may well have begun and though the martian surface

conditions may no longer be so favourable, extremophile research here on Earth has shown that once life takes a foothold, it can be hard to dislodge.

1.3 Exploration of Mars

The exploration of Mars has previously been dominated by two nations, the USA and USSR. It may have been overshadowed by the Moon landings but the competition to reach and explore Mars was also an important part of the Cold War Space Race and although the Russians had made attempts to reach the Red Planet starting as early as 1960 it was the American Space Agency NASA who took the honours of the first successful flyby of another planet with Mariner 4 passing close to Mars in 1965 (Leighton et al., 1965). Another two successful flybys by the American probes Mariner 6 and Mariner 7 followed that decade (Leighton et al., 1969) while every one of the eight Russian attempts ended in failure. Mariner 9 in 1971 allowed the Americans to celebrate the first mission to enter Mars orbit successfully (Masursky et al., 1972) but it was the Russians who claimed the first successful landing on the martian surface barely a few months later with the Mars 3 probe (Moroz and Ksanfomaliti, 1972).

Since the mid-1970s, the Americans have been the dominant force in the field of Mars exploration. With the exception of the European Space Agency's (ESA) highly successful Mars Express mission of 2003 (Chicarro et al., 2003), the majority of data gathered from either martian orbit or direct from the surface has come from NASA spacecraft. However, the difficulty of getting a spacecraft off the launch pad and across millions of kilometres of inter-planetary space to rendezvous with the Red

Planet is ably highlighted by that fact that nearly two thirds of the attempted missions so far have failed to achieve this goal.

1.3.1 Missions to the surface of Mars

Although the Russians took the prize for reaching the martian surface first, the Mars 3 probe only functioned for a little less than two minutes before contact was lost. It was not until the arrival of the USA's Viking 1 and 2 landing craft in 1976 that prolonged *in situ* monitoring of Mars' surface was achieved. Viking 1 in particular remained active for over six years but as a static lander was constrained to remain in the same position for this duration (Mutch et al., 1976, Soffen, 1976). The next stage in surface exploration came in the form of a mobile surface rover, something that had been unsuccessfully attempted by the Russians previously but which was achieved by NASA's Mars Pathfinder mission in 1997 (Golombek et al., 1999). The Pathfinder's Sojourner rover had a total range of around five hundred metres from its landing site and a limited battery life which was exhausted after eighty three days. In this time, however, it was able to demonstrate the versatility of a rover mission by allowing scientists to select interesting targets via Sojourner's cameras before guiding the rover towards them for closer investigation by the rover's instrument payload.

The success of Mars Pathfinder paved the way for NASA's Mars Exploration Rovers (MERs) which reached the Red Planet in 2004 and, at the time of writing, are still functional and returning fascinating images and data from the planet's surface. The MER mission is composed of two identical rovers named Spirit and Opportunity which are bigger in scale than the Pathfinder rover and equipped with a more

comprehensive instrument package (Crisp et al., 2003). They were landed at two separate locations on the martian surface deemed of significant scientific interest but also compatible with the rovers' terrain traversing capabilities (Anderson et al., 2003). Originally scheduled for 90 sol missions, both Spirit and Opportunity have undergone numerous mission extensions and have far surpassed their originally predicted life spans (Squyres et al., 2006a, Arvidson et al., 2006b). By January 2009, between them they had travelled over nineteen kilometres across the martian surface.

1.3.2 Mars surface science

The contribution of the surface science missions to the expansion of our knowledge of the Red Planet has been incalculable. Images taken by the rovers have shown how the current martian landscape is constantly being eroded away by aeolian processes generating the ubiquitous martian dust (Golombek et al., 2006, Sullivan et al., 2006). The missions have weathered the dust storms that spring up during the course of a martian year, returning results on the atmospheric dust loading (Lemmon et al., 2004, Wolff et al., 2006) and the optical depths encountered during these massive events and yielding clues about the dust's composition, size distribution and optical properties. There has even been direct imaging of dust devil events swirling across the martian plains (Greeley et al., 2006).

The mobility of the rovers has allowed them to descend into large craters to study the crater walls where the geological history of Mars has been uncovered by the excavating force of the impact. Stratified bedforms consistent with sedimentary rock outcropping have been imaged in a number of locations (Knauth et al., 2005, Grotzinger et al., 2006, Squyres et al., 2006a). Essentially a mobile geologist's

workbench, the MERs were able to conduct quite detailed analyses of the structure and composition of the martian surface (Crumpler et al., 2005, Farrand et al., 2007, Lewis et al., 2008). They have found widespread evidence for minerals that require environments with an aqueous component for their formation, suggesting a prominent role for water in at least one point in Mars' history, and further analysis has led to informed predictions about the probable acidity and salinity (and therefore maybe habitability) of these environments (Arvidson et al., 2006a, Fairén et al., 2009, Hynek, 2004).

The Viking landers conducted the first (and to date only) specific search for life on the martian surface with each lander including four instruments designed to conduct experiments on samples of martian soil to look for tell-tale signatures of possible biological activity (Klein et al., 1976, Soffen, 1976): A Gas Chromatography – Mass Spectrometer (GCMS) was used to analyse the gases given off when a surface soil sample was heated in order to ascertain the presence and abundance of any organic molecules. However, the GCMS results indicated that there were no organic molecules in the collected soil samples (Biemann et al., 1976).

The Gas Exchange (GEX) experiment worked by applying a nutrient solution to a sample of soil held in an inert helium atmosphere, this atmosphere was then periodically sampled in order to detect the presence of any gases evolved from the soil sample. Any changes detected in the abundance of gases such as oxygen, carbon dioxide, methane and nitrogen might have signalled the presence of organisms which were either emitting or consuming these gases but the experiment returned a negative result (Oyama et al., 1977).

The Pyrolytic Release experiment involved exposing a soil sample to a carbon dioxide atmosphere, i.e. similar to Mars' own, and providing the sample with water and light with the idea that any photosynthetic organisms within the soil sample would continue to photosynthesise and absorb the carbon from the atmosphere. After running the experiment for several days the atmosphere was removed, the soil sample baked and any gases given off were sampled. The carbon dioxide atmosphere provided was composed of molecules containing the radioactive carbon-14 isotope and so any of this carbon that had been absorbed by organisms should be released during the baking phase resulting in the detection of a radioactivity signature in the sampled gases. This experiment also returned a negative result (Horowitz et al., 1976).

The Labelled Release experiment comprised adding liquid nutrients to a surface soil sample where the carbon present in the nutrient chemicals was again the radioactive isotope carbon-14. It was proposed that organisms present in the sample may metabolise the nutrients and in doing so release carbon dioxide gas containing the radioactive isotope. Therefore the detection of radioactive gas released from the soil could indicate the presence of active living organisms. This experiment returned a strong positive result when first run but further experimental cycles did not repeat this result and the results of this experiment remain inconclusive and controversial (Levin and Straat, 1976, Klein, 1978). Attempts to simulate the results of this experiment using soil samples containing strongly oxidising agents have yielded similar results and so it is possible that the initial positive result observed from the

Labelled Release experiment could be down to strongly oxidising conditions at the surface of Mars rather than biological processes.

Meteorology packages on all the landers have recorded the changes in the martian atmosphere during its diurnal and annual cycles. Atmospheric surface pressure, composition, wind speeds, temperatures and aspects of the radiation environment have all been characterised in good detail at the location of mission landing sites (Schofield et al., 1997, Spanovich et al., 2006). The data returned by these missions can also provide an excellent means of verifying and complementing the observations of orbital missions as well as improving the accuracy of the input parameters and validating the output data of theoretical global circulation simulations.

1.3.3 Future surface missions

There are currently two major surface missions planned for the near future, the first of which is NASA's Mars Science Laboratory (MSL) (McCleese, 2003, 2006). MSL is a surface exploration rover similar to the MERs that came before it but MSL represents a significant step upwards in terms of the size, exploration range and technological capability on offer. With a mass approaching 1 metric ton MSL is nearly five times more massive than each of the MERs and requires the implementation of a novel and ambitious precision landing technique utilising a 'sky crane' to lower the rover to a soft landing on the martian surface (Lockwood, 2006). MSL will also not have to rely upon solar power but will carry its own power supply with it in the form of radioisotope thermal generators (RTGs) (Misra, 2006). An RTG generates electricity using thermocouples to harness the heat created by the

radioactive decay of an appropriate material and has the advantage over solar power in that it offers a reliable and continuous source of power independent of the diurnal cycle, local weather conditions or solar array efficiencies.

MSL is currently scheduled for a 2011 launch window, to arrive at Mars in 2012 and to have an initial mission length of one Mars year, during which time it is expected to cover a surface distance comparable to that covered by the combined extending MER missions so far. MSL is essentially designed as a mobile geologist's workbench with the large size of the rover allowing it to carry a fairly comprehensive suite of instruments with which to characterise the surface and atmospheric environment. Included amongst these are a number of imaging systems operating at different wavelengths and with capabilities varying from obtaining panoramic pictures of the martian terrain, to microscopic imaging of the rocks and regolith, to terrain mapping for autonomous navigation and hazard avoidance. Other instruments will use techniques such as; laser-induced breakdown spectroscopy (LIBS), mass spectrometry, X-ray spectrometry and diffraction, and gas chromatography, to study the mineralogical and chemical composition of the planet's surface and atmosphere. There will also be a meteorological package with instruments dedicated to monitoring environmental conditions such as surface pressures and temperatures, wind speeds and humidity and also means with which to characterise the radiation environment across various energy ranges.

The second of the two major surface missions is ExoMars (Barnes et al., 2006, Williamson, 2009). ExoMars was originally an ESA mission planned for launch slightly before MSL and was to be one of the flagship missions in ESA's Aurora

programme; an ambitious programme of science and technology demonstration missions culminating with a crewed mission to Mars. However, a recent review of the mission and its budgetary and technological requirements has led to ExoMars being pushed back to a launch date of 2016 or beyond. The mission is now also likely to become a joint venture between ESA and NASA rather than solely an ESA project (Cassi and Giorgio, 2008).

Whereas MSL, like the MERs before it, is primarily intended as a geological mission investigating surface mineralogy and composition, ExoMars is planned as an astrobiology mission, a major scientific objective of which is to search for signs of past and present life on Mars. Other scientific objectives of the mission, as originally envisaged, include; to characterise the water and geochemical distribution as a function of depth in the shallow subsurface of Mars; to study the surface and environment and to identify potential hazards to future human missions; and to investigate the planet's subsurface and deep interior to better understand the evolution and habitability of Mars. It will achieve these objectives by characterising the surface, subsurface and near-surface atmospheric environment using a varied suite of instruments, in particular in terms of the known requirements for life such as indications of the current presence of water and for geochemical signatures of past surface environments recorded in the current surface. This characterisation will also aid in determining the suitability of the surface of Mars for the anticipated missions of the future involving human crews.

The ExoMars mission was originally configured to include a Mars orbiting spacecraft from which would have been deployed a solar powered surface

exploration rover and a complimentary stationary surface lander, both to be delivered simultaneously to the surface of Mars using an ambitious vented airbag system to facilitate a safe landing. The initially proposed mission duration was six months during which time the autonomously navigating rover should have been able to explore the martian surface with a range of around a hundred metres per day. The stationary lander was intended to remain active for a number of Mars years.

The comprehensive suite of instruments planned for ExoMars were divided into two payloads, the larger of which was named Pasteur and was to be located on the rover, while the smaller payload, Humboldt, was to be placed on the stationary lander. The contents of the Pasteur payload could be divided into three distinct classes of instrument: The panoramic instruments were those which operate over larger distance scales or wide angles of view and consisted of a panoramic camera, an infrared spectrometer and a ground penetrating radar system. Between them they would have been able to observe and map the surrounding terrain, identify bulk mineral composition of surface features to highlight targets for more detailed study, probe the sub-surface for deposits of water-ice, and monitor and analyse variable phenomena such as the dust and clouds of the martian atmosphere. The contact instruments were those which require close contact with the martian surface for operation and these included a close-up imager able to study the surface at micrometre to centimetre scales, a Mossbauer spectrometer for the characterisation of iron bearing minerals, and a drill designed to bore down to a depth of two metres or so to retrieve subsurface soil samples. The drill was intended to incorporate an infrared spectrometer for *in situ* analysis of the sub-surface. The final class was the analytical instruments that operate on samples gathered from the martian surface.

Instruments in this class included a Raman-LIBS spectrometer, a microscope operating at visible and infrared wavelengths, an x-ray diffractometer, a mass spectrometer and a device capable of measuring the oxidation state of the surface environment. With analysis from this suite of instruments it was intended to accurately determine mineralogical compositions and elemental abundances on a highly localised scale, to detect trace amounts of organic compounds and even to ascertain the chirality of any organics detected; a key piece of information with regard to whether they are of biogenic origin.

The Humboldt payload was an evolution of an initial proposed Geophysical and Environmental Package (GEP) to be located on the static lander and was intended to have a much longer functional lifespan than the rover. Within the payload were instruments to study the seismological activity of Mars, such as Mars quakes or meteorite impacts, the ionising and non-ionising radiative fluxes at the surface, the size distribution and number density of the atmospheric dust particles, and the temperature, humidity and wind speeds of the near-surface atmosphere. A magnetometer was included to study Mar's weak magnetic field, and a kilometric range ground penetrating radar to probe the planet's interior, while a 'mole' would bore down into the sub-surface to a depth of a few metres in order to monitor the physical properties of the sub-surface regolith.

Unfortunately, one of the outcomes of the ExoMars mission review process included the de-scoping of the mission through the recommended removal of the stationary lander component. This is of particular relevance to this thesis because the studies detailed here were undertaken in support of the development of an optical instrument

planned as part of the ExoMars lander's Humboldt payload. Although the ExoMars mission has been significantly delayed and de-scoped, development of this instrument continues with the aim of inclusion in future mission payloads.

1.4 The UVIS Spectrometer

One of the specific instruments proposed for monitoring the non-ionising radiation environment at the martian surface is UVIS, the UltraViolet and Visible Spectrometer (Patel et al., 2004b). The instrument is based upon commercial technology that has been re-designed to minimise its mass and size and to ensure that it is robust enough to survive the rigours of space flight and prolonged operation on another planet. The primary layout of the spectrometer composes a symmetric Czerny-Turner optical bench housed within a casing of approximate dimensions 16 × 10 × 4 cm. A diffraction grating and two collimating mirrors are used to split the incident radiation into its constituent wavelengths and guide it to a 1024 element CCD detector. The functional wavelength regime of the device is 180 to 650 nm with a resolution of 1 nm. The spectrometer front-end viewing optics consists of a narrow field of view probe (~ 5°) and a wide field of view probe which will measure the full hemispherical flux (this will be the default measurement mode).

The main science objective of UVIS is to characterise the non-ionising radiation environment at the martian surface. It will achieve this by recording the transmission spectrum of the martian atmosphere as viewed at the surface of the planet. In turn, study of these spectra will yield data on the atmospheric composition, the gaseous

species present and their concentrations and the abundance of aerosols, most notably the martian dust and its inherent optical properties.

The chance to study spectra covering such a broad wavelength range using a single instrument is an invaluable step in accurately characterising the martian atmosphere. This will allow a direct comparison of the dust optical properties within the different wavelength regimes of the ultraviolet, visible and infrared, something that has certainly never been achieved *in situ* before.

1.5 The UVIS simulation

This thesis details the development of a computer simulation created to support the development of the UVIS spectrometer. The model, referred to as the UVIS simulation, is capable of simulating the kind of surface spectra that the instrument would be expected to return during operation at the martian surface. This is achieved by modelling the atmosphere of Mars in terms of the gases and aerosol particles present and their abundances and distributions and then approximating the transmission of the solar flux through this model atmosphere to the surface of the planet. The development of the UVIS simulation, its applications and the analysis of the simulation data it has provided form the main elements of this thesis. A detailed account of the UVIS simulation's design and operation are included in Chapter 2 while Chapters 3, 4 and 5 are concerned with the different applications of the UVIS simulation and how they can be applied to assist in the development of the UVIS instrument. It is hoped that in the future it will be possible to use the UVIS simulation data as the starting point for the analysis of actual data returned from the surface of Mars by the UVIS instrument.

Chapter 2 – Development of the UVIS simulation

2.1 Principles behind the simulation

This chapter details the development of a radiative transfer model used to simulate the kind of data expected to be returned by the UVIS instrument during operation at the martian surface. The purpose of this is to provide a platform upon which theoretical tests of the instrument can be carried out, for example, the suitability of UVIS to detect the presence of trace gases via their absorption features, or the inference of dust aerosol optical properties by studying the shape of the returned spectra.

2.1.1 Radiative transfer

The UVIS simulation works by approximating the interaction of the incident solar flux with the constituent components of the martian atmosphere in order to derive the local flux incident at the martian surface. These atmospheric interactions take the form of scattering and absorption events. From the point of view of the UVIS instrument located at the martian surface, absorption events decrease the incident flux of a particular wavelength, as the absorbed radiation will tend to be emitted at wavelengths different to those of the incident photon, while scattering events can both increase and decrease the incident flux, depending on whether the photons are scattered into or out of the path of the incident flux respectively. The total surface flux is composed of two components, one being the direct and the other being the

diffuse component, each of which is calculated separately and then combined. The direct component comprises radiation that has been detected by the instrument without having first undergone any interaction with the planet's atmosphere, while the diffuse component comprises radiation that has undergone scattering interactions, either with the atmospheric constituents or the planet's surface, prior to being detected. These components are illustrated in Figure 2.1 where the cross in the figure represents the location of a surface-based instrument, such as UVIS.

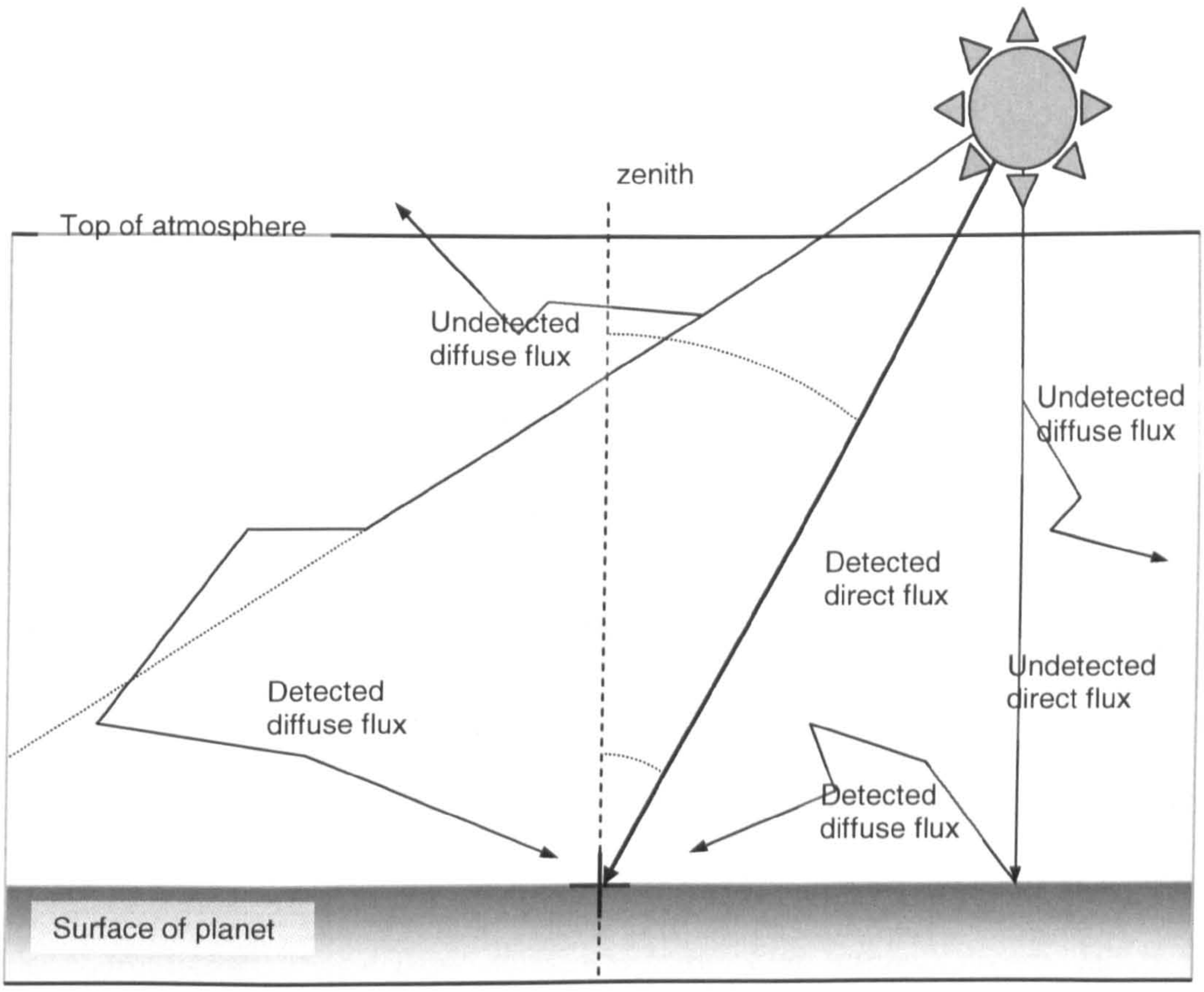

Figure 2.1 – Illustrating how scattering interactions between the incident solar radiation and the planet's atmosphere result in a direct and a scattered diffuse component of surface flux.

2.1.2 Optical depth

The key measure of how transparent or opaque the atmosphere is to the incident radiation is the optical depth value, τ. Optical depth is a dimensionless quantity

which can be defined as the product of a species' cross-section with its column abundance value (equation 2.1). A species' cross-section, σ, is a quantification of the probability of a photon-particle interaction and is represented by assigning a cross-section to each particle equivalent to a physical area that each particle presents to an incident photon; σ therefore has units of area (e.g. cm^2). A species' column abundance, ξ, (sometimes referred to as 'zeta') is the number of particles of that species located vertically above a unit cross-sectional area and therefore it possesses units of number per unit area (e.g. cm^{-2}). Optical depths can be calculated independently for both the scattering, τ_{scat}, and absorption, τ_{abs}, interactions of the incident radiation with each of the atmospheric species. The total optical depth of the atmosphere is then simply the sum of these individual optical depths (equation 2.2).

$$\tau = \sigma \cdot \xi \qquad 2.1$$

$$\tau_{tot} = \tau_{scat} + \tau_{abs} \qquad 2.2$$

2.1.3 Flux scaling owing to geometry

The UVIS simulation uses the ASTM Standard Extraterrestrial Spectrum Reference E-490-00 (ASTM-E490, 2006). This reference spectrum covers a wavelength range of 119 to 1×10^6 nm and is composed of solar spectral irradiance values gathered in Earth orbit, from ground based telescopes, from high altitude aircraft and from sounding rockets and, where required, the values are scaled to an airmass of zero, i.e. equivalent to the spectral irradiance at the top of the Earth atmosphere. The relevant section of this spectrum, between the wavelengths of 180–1100 nm, in units of $Wm^{-2}nm^{-1}$, is shown in Figure 2.2.

The intensity of this spectrum is first scaled to the value required at the average Sun-Mars distance of 1.52 AU, this flux value being referred to as F_0. To account for the elliptical shape of Mars' orbital path, this value is then further scaled using the ratio of the current Sun-Mars distance, r, to the average Sun-Mars distance, R (Lewis et al., 1993). The distance ratio (r/R), equation 2.3, is calculated as a function of the eccentricity of the planet's orbit, e, and the areocentric longitude, L_s, (an angular measure of the position of Mars in its orbit where L_s equal to 0° occurs at the martian northern hemisphere spring equinox, L_s equal to 90° occurs at the northern hemisphere's summer solstice, and so on. The perihelion of Mars' orbit, L_s^{peri}, occurs at L_s equals 250°).

$$\left(\frac{r}{R}\right) = \frac{1 + e \cdot \cos(L_s - L_s^{peri})}{1 - e^2} \qquad \textbf{2.3}$$

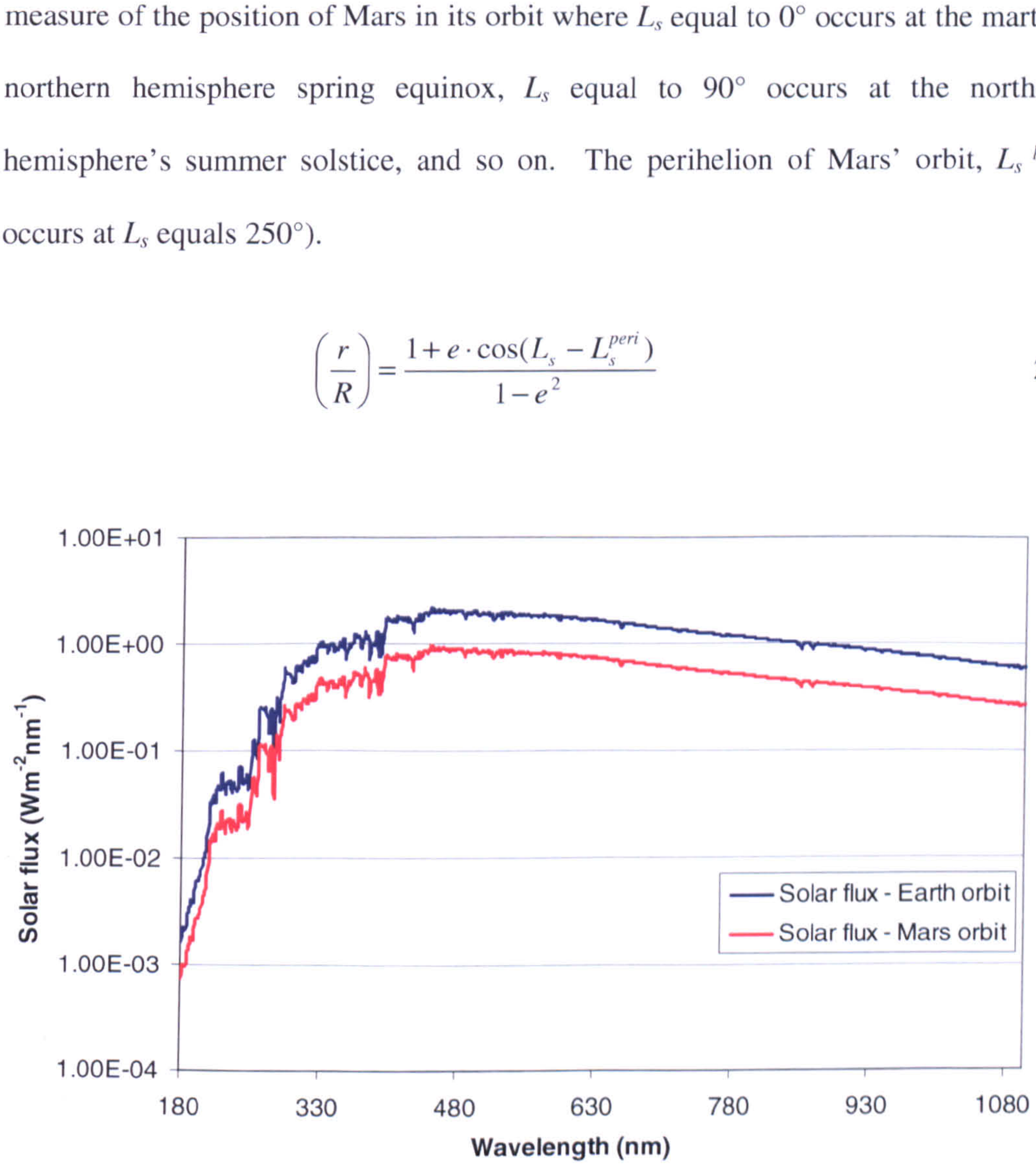

Figure 2.2 – ATSM E-490 solar irradiance spectrum at Earth orbit and scaled to Mars orbit

The effect on the solar spectrum owing to the location of the observer on the planet's surface can be summarised by a scaling factor μ_0 (Lewis et al., 1993). This value is calculated as a function of the planet's current L_s value, obliquity of the planet's rotational axis, ε, the surface latitude, l, and time in seconds from local noon, t, at which the observation is being made (equation 2.4). The bracket containing t in equation 2.4 corresponds to the hour angle where the parameter 88775 represents the length of one martian solar day in seconds. The μ_0 parameter is equivalent to *cosine*(θ) where θ is the solar zenith angle, the angular distance of the Sun from its zenith and therefore at the zenith $\mu_0 = 1$

$$\mu_0 = \sin(l)\cdot(\sin(\varepsilon)\cdot\sin(L_s)) + \cos(\theta)\cdot\cos(\sin^{-1}(\sin(\varepsilon)\cdot\sin(L_s)))\cdot\cos\left(\frac{2\pi\cdot t}{88775}\right) \qquad \textbf{2.4}$$

Finally, the solar flux incident at Mars, F_{inc}, can be calculated using the following equation:

$$F_{inc} = F_0\cdot\mu_0\cdot\left(\frac{r}{R}\right)^2 \qquad \textbf{2.5}$$

2.1.4 Correction for atmospheric curvature

The UVIS simulation uses the assumption of a plane parallel atmosphere but this introduces significant errors when scenarios are run where the Sun lies close to the horizon, i.e. high solar zenith angles, as the curvature of the planetary atmosphere means that a plane parallel assumption will result in an over-estimate of the atmospheric airmass (the thickness of atmosphere) encountered by the incident radiation. The expression used to calculate the airmass as a function of the solar zenith angle, θ, in a plane parallel atmosphere is given in equation 2.6, and returns an

airmass value of 1 when the Sun is at its zenith. Figure 2.3 illustrates how changes in the value of the solar zenith angle can affect the airmass encountered by the incident radiation.

$$airmass(\theta) = \frac{1}{\mu_0} \tag{2.6}$$

Kasten and Young (1989) studied this problem applied to the Earth's atmosphere using the following expression to calculate accurate values for the airmass:

$$airmass(\theta) = \frac{1}{\rho_0 z_0} \int_0^{\infty} \frac{\rho(z)}{\sqrt{1 - \left(\frac{R_m}{R_m + z}\right)^2 \cdot \left(\frac{n_0}{n(z)}\right)^2 \cdot \cos^2(90 - \theta)}} \cdot dz \tag{2.7}$$

Where z is the altitude, z_0 is the scale height of the atmosphere, $\rho(z)$ and ρ_0 are the atmospheric density at an altitude of z and at the planet's surface respectively, R_m is the mean radius of the planet, and $n(z)$ and n_0 are the atmospheric index of refraction at an altitude of z and at the planet's surface respectively. The (90-θ) term comes through the expression assuming the use of the altitude angle, i.e. the solar disc's angular height in degrees measured from the horizon rather than from the zenith. Therefore the altitude angle can be found by subtracting the solar zenith angle value from 90°.

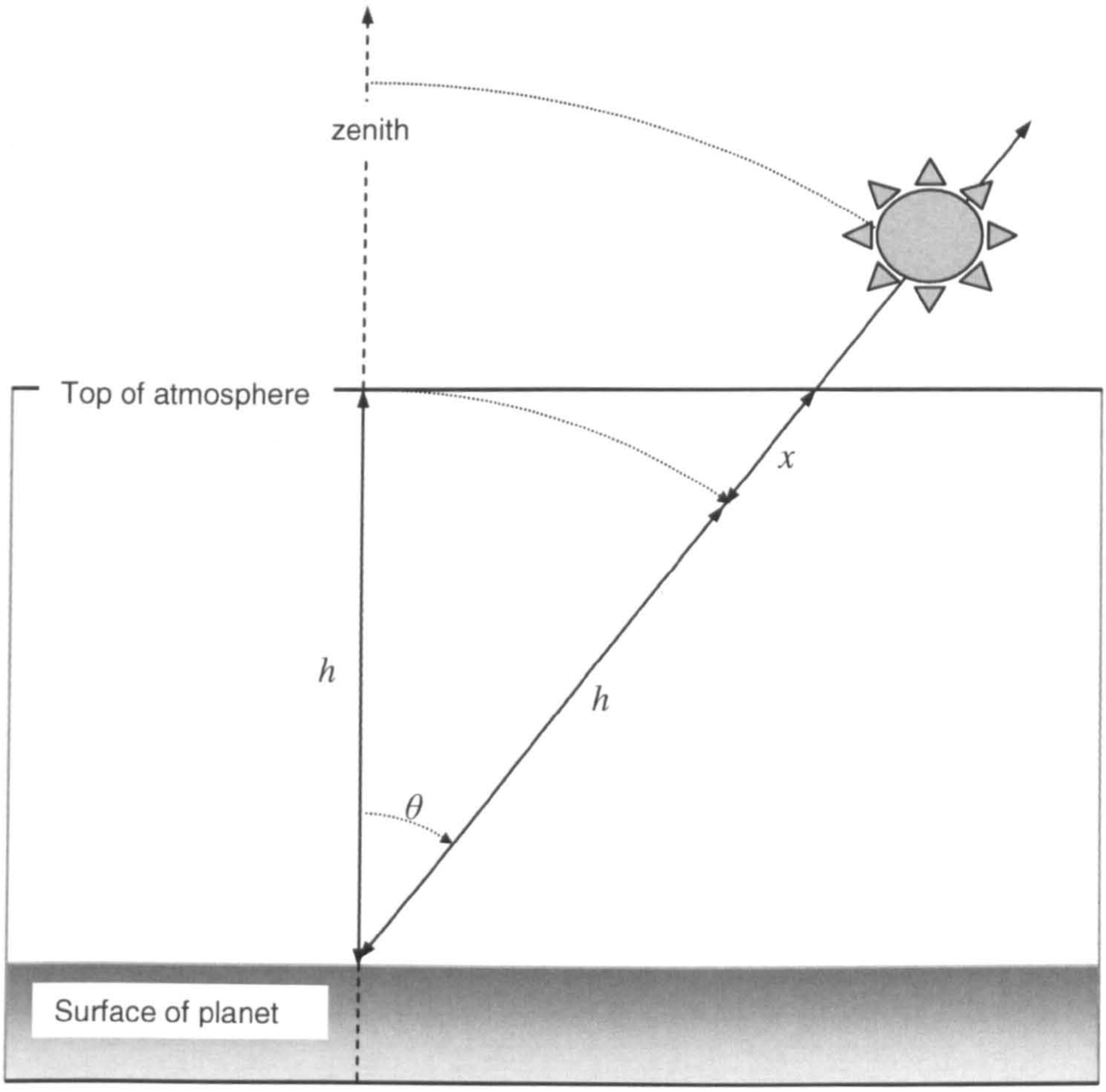

Figure 2.3 – Illustrating how varying the zenith angle varies the thickness of atmosphere encountered by the incident flux. At a zenith angle of zero degrees the thickness of atmosphere encountered is denoted by h, at a zenith angle of θ the thickness of atmosphere encountered is $(h + x)$.

Equation 2.7 has been adapted to the martian atmosphere by setting R_m equal to 3390 km and z_0 equal to 10.8 km. A density versus altitude profile of the martian atmosphere was taken from the Mars Pathfinder mission (MPF) Entry, Descent and Landing (EDL) data (Magalhaes et al., 1999). The ratio $n_0/n(z)$ was set equal to one as the variation of the refractive index of the primarily carbon dioxide martian atmosphere with altitude is sufficiently small as to have little effect on the resulting airmass calculation. Equation 2.7 was then integrated from the surface of Mars to an altitude of 140 km for values of solar zenith angle ranging from 0 to 90° using a

trapezium method numerical integration routine to yield the airmass values for each solar zenith angle value. The trapezium method was deemed appropriate because of the smoothly varying nature of the $\rho(z)$ function meaning that reasonably high accuracy is returned providing that a suitably small integration step size is used.

Having derived the corrected airmass values for the martian atmosphere a function was fitted to these data points allowing the corrected martian airmass to be determined for any value of solar zenith angle. The function is based upon one generated by Kasten and Young (1989) to fit the corrected airmasses produced for the Earth's atmosphere:

$$airmass(\theta) = \frac{1}{\left[\sin(90-\theta)+a((90-\theta)+b)^{-c}\right]} \qquad \textbf{2.8}$$

Where the constants take values of a = 0.15, b = 3.85 and c = 0.84. This approximation deviates from the calculated airmass values by less than 1% for solar zenith angle values in the range 0 to 89.5° with deviations of a few percent higher for the remaining half a degree to the maximum value of solar zenith angle.

Figure 2.4 demonstrates how the plane parallel assumption and the corrected airmass vary. A difference of around 1% becomes evident from approximately 75° onwards and by 85° this has increased to approximately 10%. The plane parallel deviation from the corrected airmass increases rapidly as the plane parallel assumption tends towards infinity as the solar zenith angle value approaches 90°.

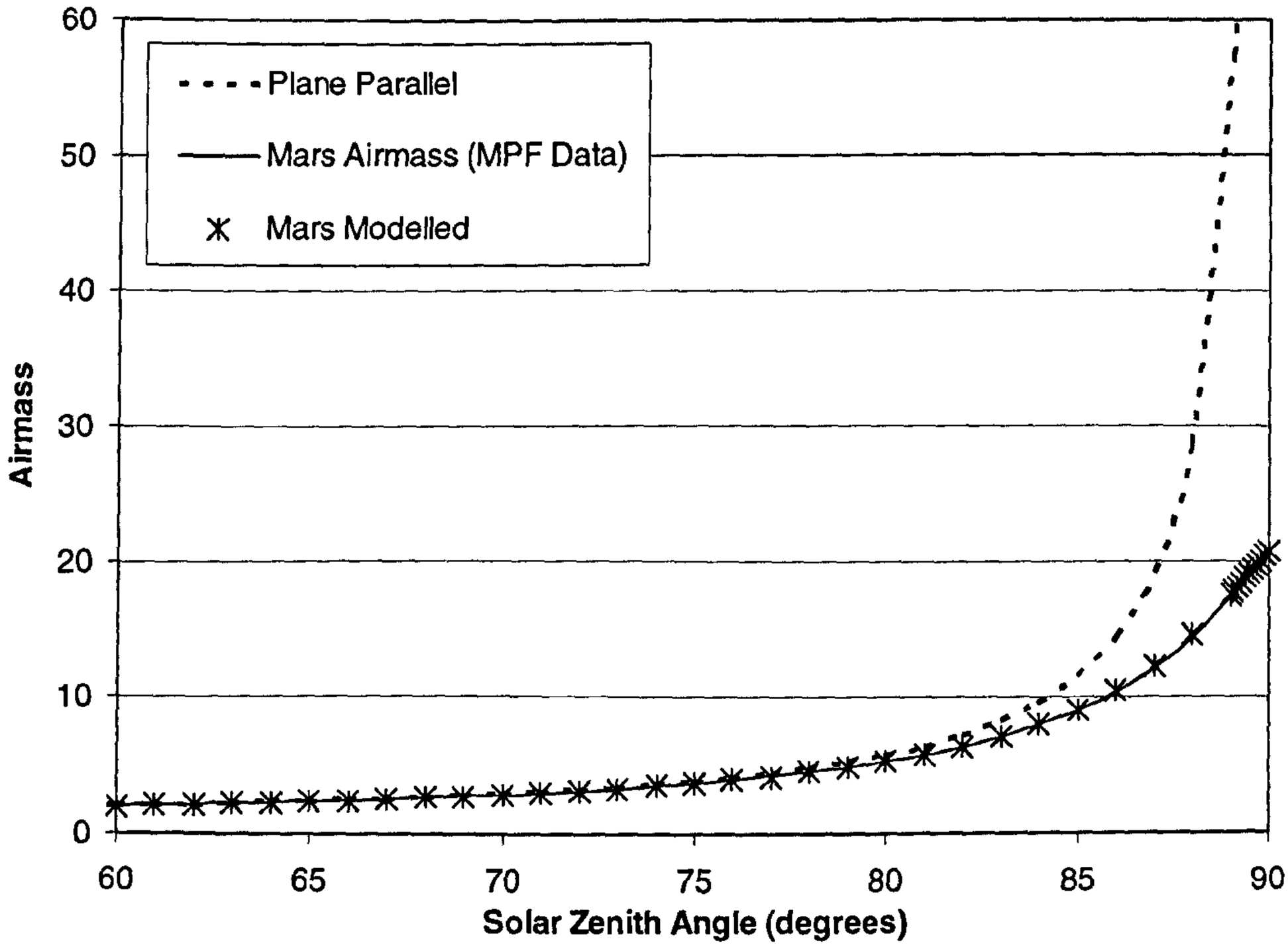

Figure 2.4 – Comparison of plane-parallel and corrected airmass as a function of solar zenith angle

2.1.5 Gaseous component of the atmosphere

The main gaseous component of the martian atmosphere, accounting for over ninety-five percent by volume, is carbon dioxide, with nitrogen and argon accounting for the majority of the rest, see Chapter 1 Table 1. Minor constituents of the atmosphere include water vapour and ozone. The gases are assumed to be uniformly mixed at all altitudes and over all surface coordinates with the exception of ozone and water vapour (Forget et al., 1999, Lewis et al., 1999, Novak et al., 2003). This assumption holds as the atmosphere is predominantly (over 95 %) carbon dioxide with the presence of the other gases only having an influence where significant absorption features occur. The column abundance of each gas species as a function of altitude, z, was inferred using the form of the gas law given in equation 2.9; where $P(z)$ is the

atmospheric pressure at altitude z, G refers to the gravitational acceleration at the surface of Mars and M_{mol} is the average molecular mass of the martian atmosphere (taken to be 43.4 amu).

$$\xi(z) = \frac{P(z)}{G \cdot M_{mol}} \qquad \textbf{2.9}$$

The variation of pressure with altitude was taken from data collected by instruments on the Mars Pathfinder (MPF) Entry, Descent and Landing module (Magalhaes et al., 1999). This dataset begins at an altitude of 140 km and continues at 2 km intervals down to an altitude of 10 km. Pressure readings taken by instruments on the Sojourner rover after its deployment were used as boundary conditions to interpolate the pressure values between 10 km and the surface (Schofield et al., 1997).

Two of the constituent gas species are known to exhibit strong variation in their abundances over the course of a martian year. Ozone, despite being present in only trace amounts, is an important constituent of the atmosphere because of the large absorption cross-sections it exhibits at the wavelengths under study. The abundance of ozone is strongly dependent upon the photochemical reactions occurring in the atmosphere, resulting in a significant seasonal variation (Clancy and Nair, 1996, Novak et al., 2003). This variation has been incorporated into the model using the column abundance distributions created by the three dimensional Laboratoire de Meteorologie Dynamique (LMD) General Circulation Model (GCM) simulations of ozone distribution carried out by Lefevre et al. (2004). Although there are a number of actual observations of ozone column abundance in the martian atmosphere, the coverage of these does not extend to all latitudes and across all L_s values; therefore it was felt that the global and annual coverage provided by the GCM derived data was

the most suitable for application here. To include ozone in the UVIS simulation a look-up table is created using the Lefevre at al data to provide a scaling value, which is referenced as a function of L_s and latitude, with which the manually specified maximum column abundance of this gas is then scaled, to determine the ozone column abundance at the time of year and surface location required. Comparison of the Lefevre et al. data with the ozone column abundances returned by the SPICAM instrument aboard Mars Express, the most complete observational record of ozone abundance taken from Mars orbit, show the two datasets to be in good agreement (Perrier et al., 2006). As shown in Figure 2.5, ozone column abundances tend to be low at equatorial latitudes and high column abundances tend to occur at higher latitudes in each hemisphere's winter time.

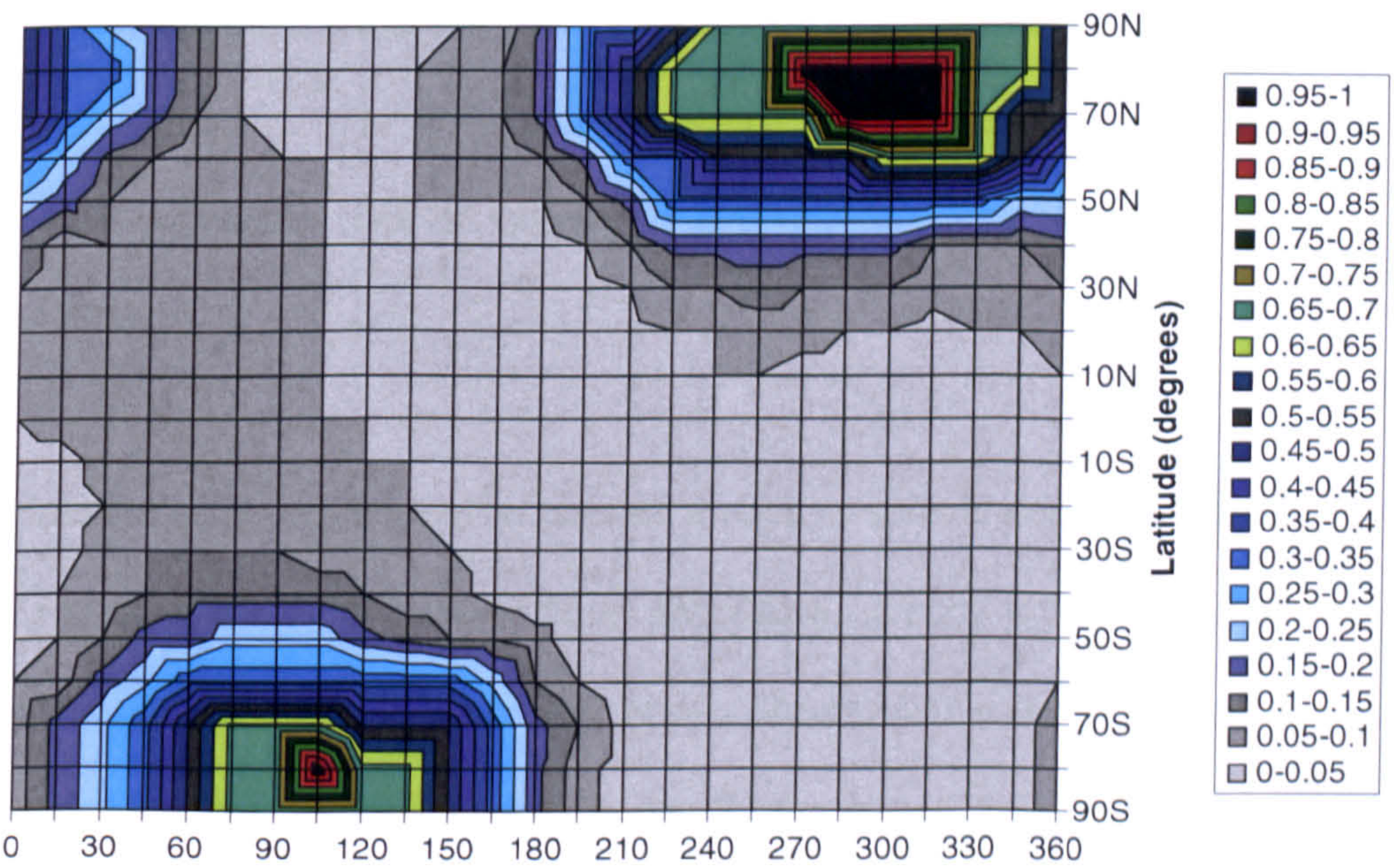

Figure 2.5 – Ozone abundance as a function of areocentric longitude and latitude based on GCM modelling (Lefevre et al., 2004). Key shows ozone abundance as a ratio relative to the annual maximum column abundance.

Ozone also exhibits a strong altitude dependence in its distribution. The chemical reactions that result in the production of ozone tend to occur on the night side of the planet, replenishing the levels of ozone depleted by photolysis reactions during the martian day (Lefevre et al., 2004). The SPICAM instrument aboard ESA's Mars Express spacecraft has also returned excellent data on the vertical distribution of ozone through atmospheric limb observations (Lebonnois et al., 2006). These observations are confined to the night side of Mars and so can be used to determine upper limits for the possible day side abundances (assuming ozone production is confined to the night side). There are currently no *in situ* observations of the day side ozone vertical distribution; however this has also been studied theoretically through the use of GCMs of the martian atmosphere. Altitude dependent ozone distribution profiles were adapted from the work of Lefevre et al. (2004) which looked at the diurnal variations in ozone distribution across the martian seasons and at varying latitudes. The GCM derived altitude profiles are again found to be in quite good agreement with the observational data returned by SPICAM (Lebonnois et al., 2006).

The Lefevre et al data is used to provide a relative altitude dependent profile with which to take the total ozone column abundance, already scaled for season and latitude, and then divide it appropriately over the vertical scale of the atmosphere. Two separate vertical profiles are used, one for the mid latitudes, between $l = 45°N$ and $l = 45°S$, and another for the higher latitudes and both are assumed to apply over the full martian year. Both of these profiles are taken from the same seasonal period covering L_s values 150° to 180°, (northern hemisphere spring), as this represents a mid-point between the extremes of summer and winter. No data were available for

the high latitudes of the southern hemisphere so the vertical profile for the northern hemisphere is assumed to apply at the corresponding southern latitudes too. An interesting feature of the mid-latitude ozone vertical distribution is the clear division into two distinct altitude bands. The first band shows maximum ozone abundance near the planet's surface which then decreases steadily to effectively zero at an altitude of around 20 km. A second band of lower abundance ozone then appears between the altitudes of approximately 30 km and 50 km. A similar trend is observed in the higher latitude vertical distribution where the declining trend in ozone abundance is seen to reverse slightly at an altitude of approximately 20 km before continuing its decline. The ozone column abundance altitude profiles are given in Figure 2.6 below:

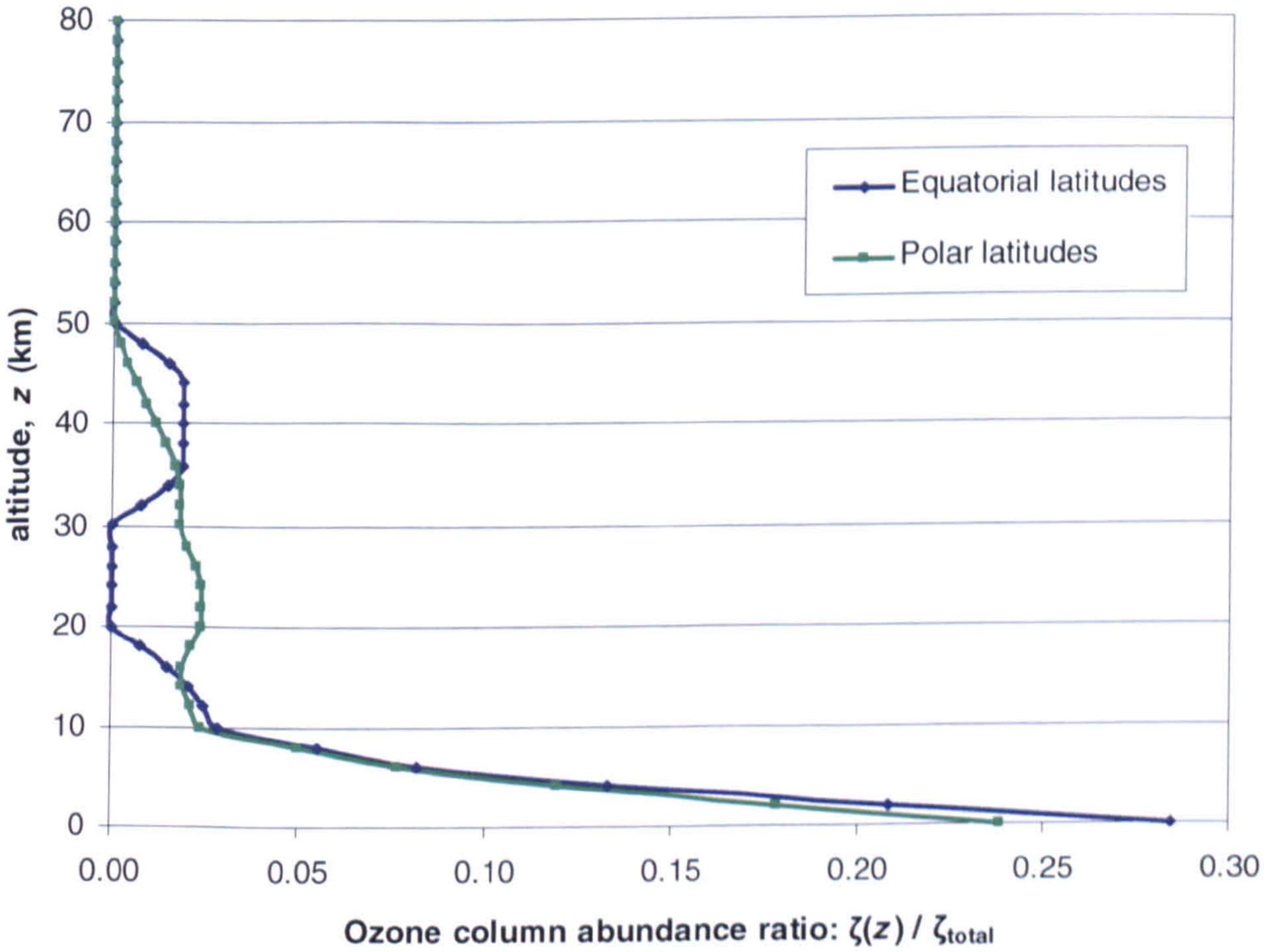

Figure 2.6 – Ozone column abundance vertical distribution scaling ratio as a function of altitude, *z*, based upon GCM data (Lefevre et al., 2004).

The other variable abundance gas component relevant to this model at this stage is water vapour. As is the case with ozone, the variability of water vapour has been studied using the LMD GCM (Montmessin et al., 2004). For the purposes of the simulation, the water vapour is assumed to be uniformly mixed in the atmosphere but its relative abundance is scaled by a look-up table procedure similar to that of the ozone, again using the LMD GCM data. The water vapour column abundance variation with latitude and areocentric longitude is given in Figure 2.7. Comparisons between the GCM dataset and observations conducted by the TES instrument aboard the Mars Global Surveyor orbiter show good agreement (Smith, 2002).

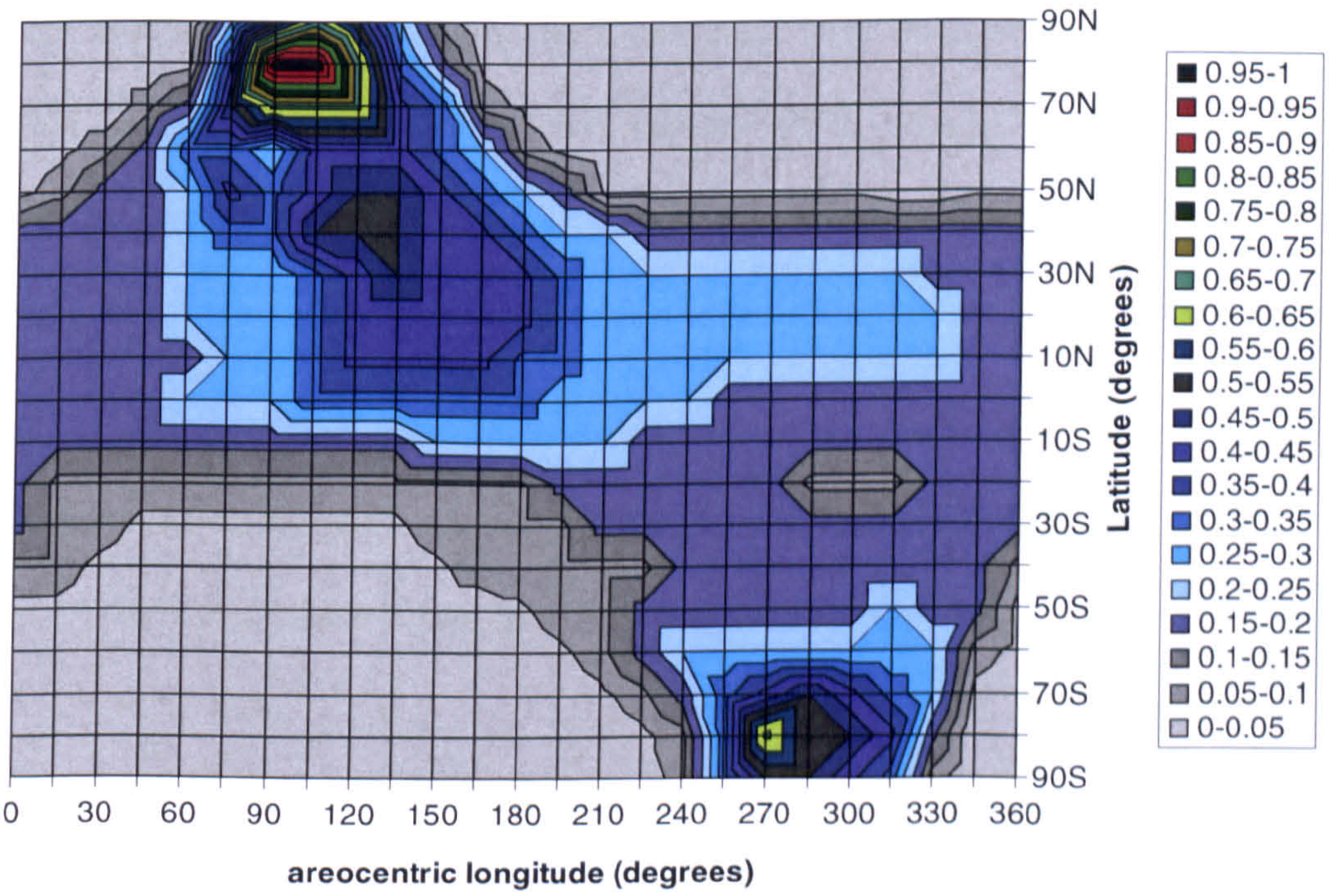

Figure 2.7 – Water vapour abundance as a function of areocentric longitude and latitude based upon GCM modelling (Montmessin et al., 2004). Key shows water vapour abundance as a ratio relative to the annual maximum column abundance.

2.1.6 Dust aerosol component

The aerosol component of the martian atmosphere is dominated by the martian dust. Created by aeons of chemical and physical weathering and transported by aeolian processes, the red dust of Mars can be found across the planet's entire surface. When this surface is warmed by the Sun, swirling 'dust devil' up-draughts can form lofting the dust high into the thin atmosphere where it can remain for extended periods of time (on the order or weeks or months (Conrath, 1975)), giving the martian sky its distinctive pink tint. In extreme cases this dust lofting can occur at such a rapid rate and in sufficient quantity that dust storms can form; large scale events where the dust laden atmosphere can obscure swathes of the planet's surface from orbital view. Sometimes these storm events can begin to overlap and combine into even larger storm systems and occasionally these can grow large enough to cover the entire planet in a dusty shroud (Zurek and Martin, 1993). NASA's MERs have both experienced dust storm conditions first hand, recording increases in the atmospheric optical depth from low levels of around $\tau = 0.1$ to high, dust storm, levels greater than $\tau = 1.0$ (Clancy et al., 2000)). Long term studies by numerous orbiting space craft have shown that dust storm activity tends to increases towards the perihelion of Mars' orbit, i.e. southern hemisphere summer time (Smith, 2004).

The dust's seasonal and latitudinal distribution is another aspect of the martian atmosphere studied by the highly successful TES instrument and the UVIS simulation incorporates this TES data in two forms; one a theoretical model of the averaged TES data over a number of martian years, and the other in the form of a look-up table of observational data for Mars year 25 (MY 25). The designation of Mars Year 25 follows the arbitrary designation introduced by Clancy et al. (2000) to

help identify Mars years for comparison purposes; MY 1 begins on 11th April 1955 and MY 25 covers most of 2001 and 2002.

Taken from the Mars Climate Database GCM, the theoretical model of dust distribution uses the following functions to determine the value of the dust optical depth, τ_{dust} for specified L_s and latitude, l, values (Lewis et al., 1999):

$$\tau_{eq} = 0.2 + 0.3 \cdot \left(\cos\left(0.5 \cdot \left(L_s - L_s^{peri}\right)\right)\right)^{14} \quad \textbf{2.10}$$

If $l > 0°$ then $\tau_{NS} = 0.1$ else

$$\tau_{NS} = 0.1 + 0.4 \cdot \left(\cos\left(0.5 \cdot \left(L_s - L_s^{peri}\right)\right)\right)^{14} \quad \textbf{2.11}$$

$$\tau_{dust} = \tau_{NS} + 0.5 \cdot \left(\tau_{eq} - \tau_{NS}\right) \cdot \left(1.0 + \tanh\left((45 - l) \cdot 10.0\right)\right) \quad \textbf{2.12}$$

The function results in peak values for dust optical depth occurring around an L_s value of 250° and extending southwards from a latitude of 30°N all the way to 90°S. Optical depths decrease either side of this maximum down to values representing approximately 40% of the peak value at mid latitudes and down to 20% of the peak value at higher latitudes. In the simulation, the dust function above is normalised to a manually supplied peak value for dust optical depth and the L_s and latitude values are then used to scale this peak value to the correct season and location. Figure 2.8 shows the dust optical depth distribution over the latitudes of Mars across a martian year with the peak dust optical depth set as $\tau = 0.5$.

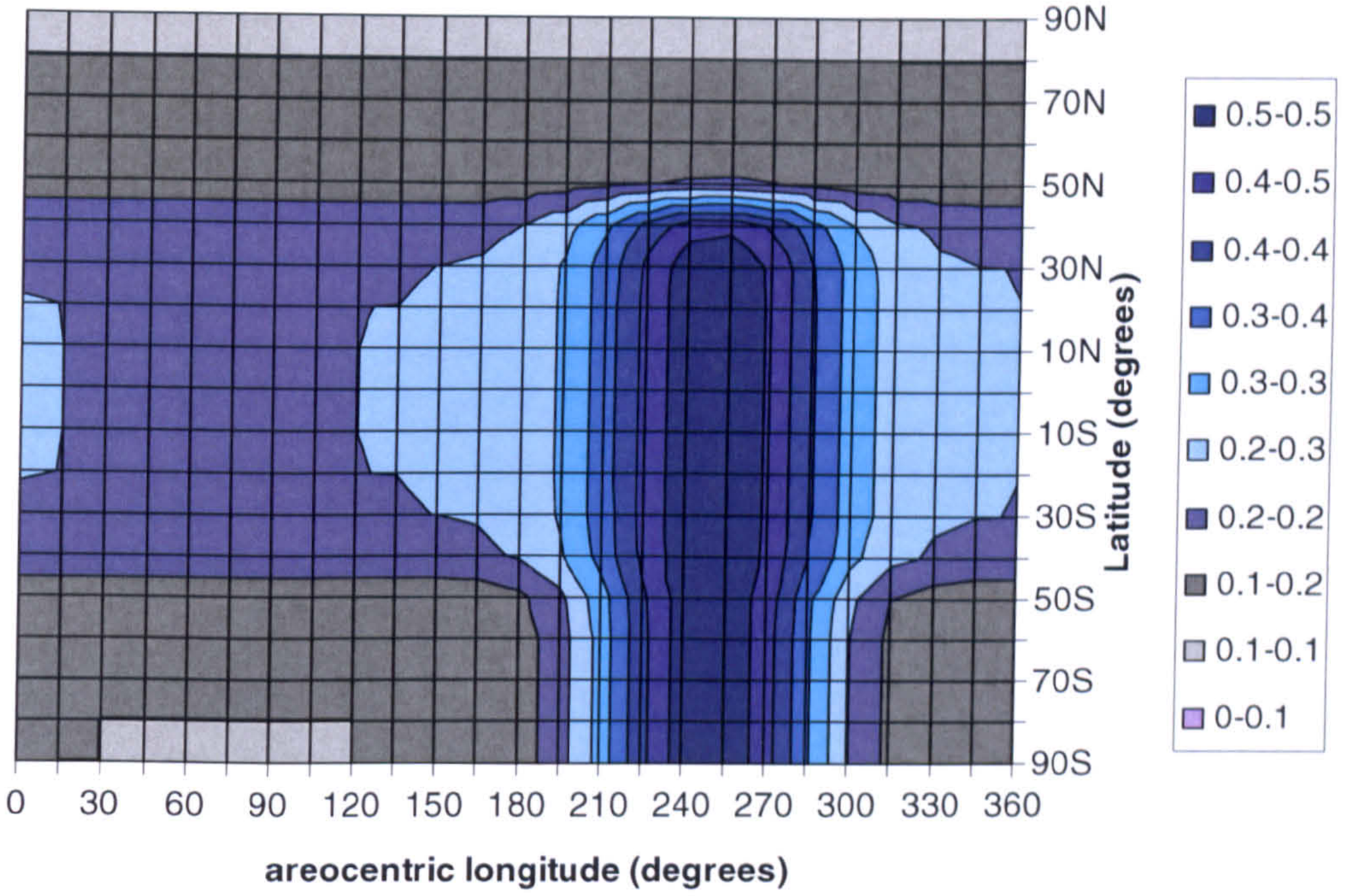

Figure 2.8 – Dust aerosol optical depth over areocentric longitude and latitude using the TES theoretical model (Lewis et al., 1999). Key shows dust optical depth value range from τ = 0-0.5.

An alternative to using the theoretical model of the dust distribution is to use the actual data returned by the TES instrument for MY 25 (Smith, 2004). A look-up table has been created based upon the published dust optical depth distribution and this is again used to scale a manually entered peak dust optical depth value to the appropriate seasonal and latitudinal value, this is shown in Figure 2.9.

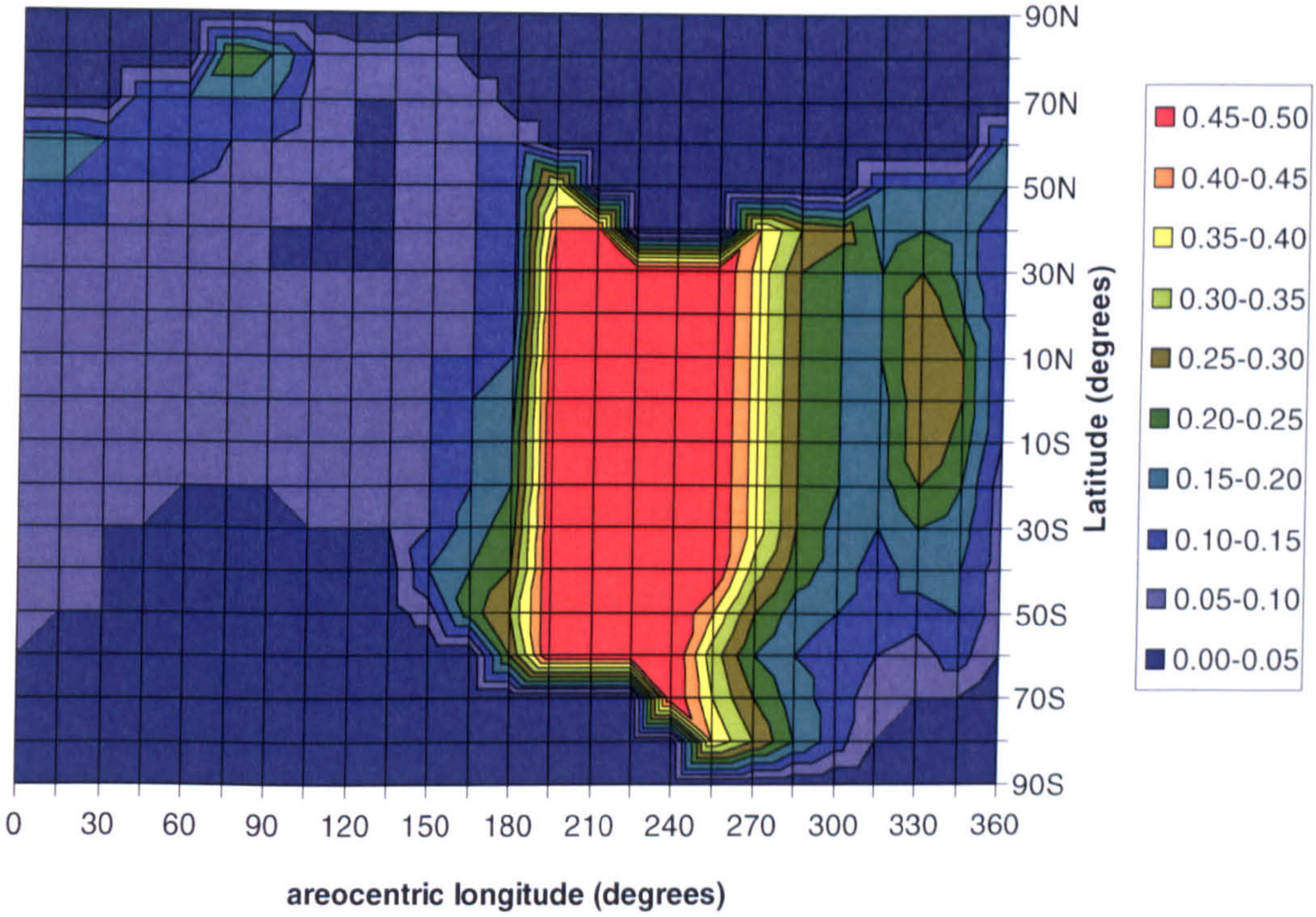

Figure 2.9 – Dust aerosol optical depth over areocentric longitude and latitude using the TES observations of MY25 (Smith, 2004). Key shows optical depth values scaled so that the maximum optical depth is $\tau = 0.5$.

A further distribution profile is also used to model how the dust is distributed as a function of altitude. The altitude distribution is based upon a function used within versions of the Mars Climate Database GCM (Forget et al., 1999) and originally developed by Conrath (1975), which calculates the dust mixing ratio, $Q(z)/Q_0$:

$$\left(\frac{Q(z)}{Q_0}\right) = \exp\left[\nu \cdot \left(1.0 - \left(\frac{P_0}{P(z)}\right)\right)\right] \qquad \textbf{2.13}$$

The values $P(z)$ and P_0 are the pressure at altitude z and the surface pressure respectively. The parameter ν is the dust cut-off parameter which is set to a value of 0.007 (Conrath, 1975). The dust mixing ratio is calculated at a number of altitude steps and gives the dust abundance at each altitude as a ratio with the abundance at

the martian surface, i.e. Q/Q_0 at the surface is always 1.0. This allows the UVIS simulation to use these values to scale the optical depth contribution of the dust with altitude.

2.1.7 Ice cloud aerosol component

There is one further aerosol component of the atmosphere included in the UVIS simulation and this is the water ice particles found in cloud formations. The martian weather system features a well characterised cloud system with regular formations appearing at roughly the same latitudes and the same seasonal intervals year after year (Wolff et al., 1999). These can be classified into three main formations; the Aphelion Cloud Belt (ACB) which occurs close to the equator between L_s = 50°-140°, and the North and South Polar Hoods (NPH and SPH) which are located over their respective poles for approximately two-thirds of each martian year. The NPH reaches its maximum size in the northern hemisphere winter at roughly L_s = 340°-350°, when it can extend down as far as latitudes of 30°N, but it has almost completely disappeared by L_s = 20°. The SPH undergoes similar behaviour in the southern hemisphere winter but does not extend as near to the equator, only reaching as far as about l = 40°S.

As with the dust distribution two separate methods are employed of incorporating the ice aerosol distribution into the UVIS simulation. The first again uses the data from the TES instrument, taken during Mars Year 25, to map the ice aerosol optical depth as a function of L_s and latitude (Smith, 2004). A maximum value for the ice optical depth is input by the user and then a look-up table of the TES map is used to scale this to the location and season. Figure 2.10 shows the water ice aerosol optical depth

distribution from the TES observations of MY 25 as values relative to the manually input maximum optical depth, i.e. $\tau(L_s, l)/\tau_{\text{max ice}}$. The second method uses a simple model of the three major cloud formations devised from data taken from SPICAM observations (Mateshvili et al., 2006), also mapped to an L_s and latitude referenced look-up table. Mateshvili et al. gives an average altitude for the ACB as $z \sim 15$ km while the NPH and SPH occur at a slightly higher average altitude of $z \sim 25$ km. For simplicity, the UVIS simulation sets all ice cloud formations to an intermediate altitude of 20 km with an assumed formation thickness of less than 2 km. Figure 2.11 shows the water ice aerosol optical depth distribution from the modelled SPICAM observations, also as values relative to the manually input maximum optical depth.

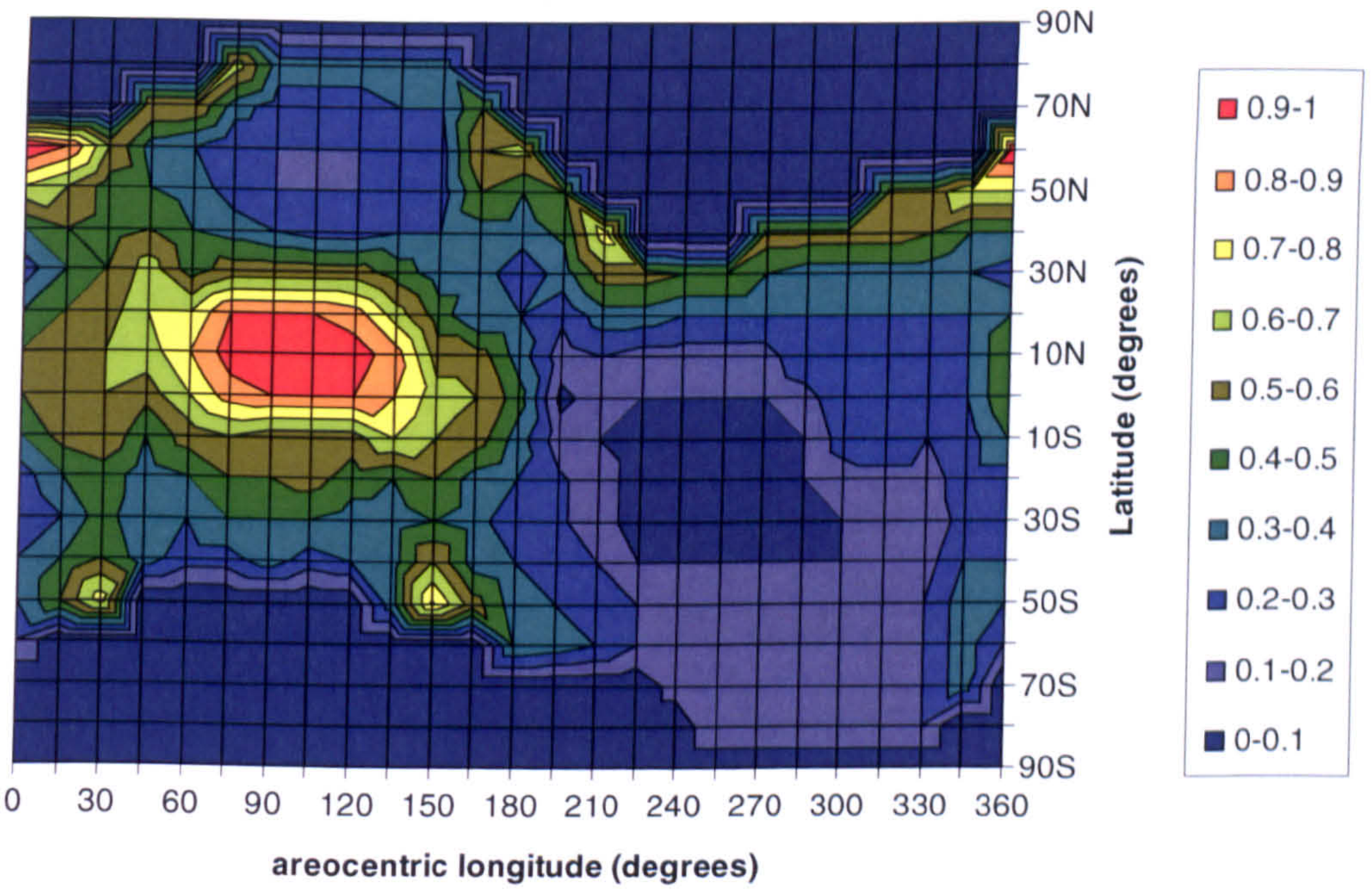

Figure 2.10 – Water ice aerosol optical depth as a function of areocentric longitude and latitude based upon TES observations of MY25 (Smith, 2004). Key shows optical depth as ratio relative to the annual maximum water ice optical depth.

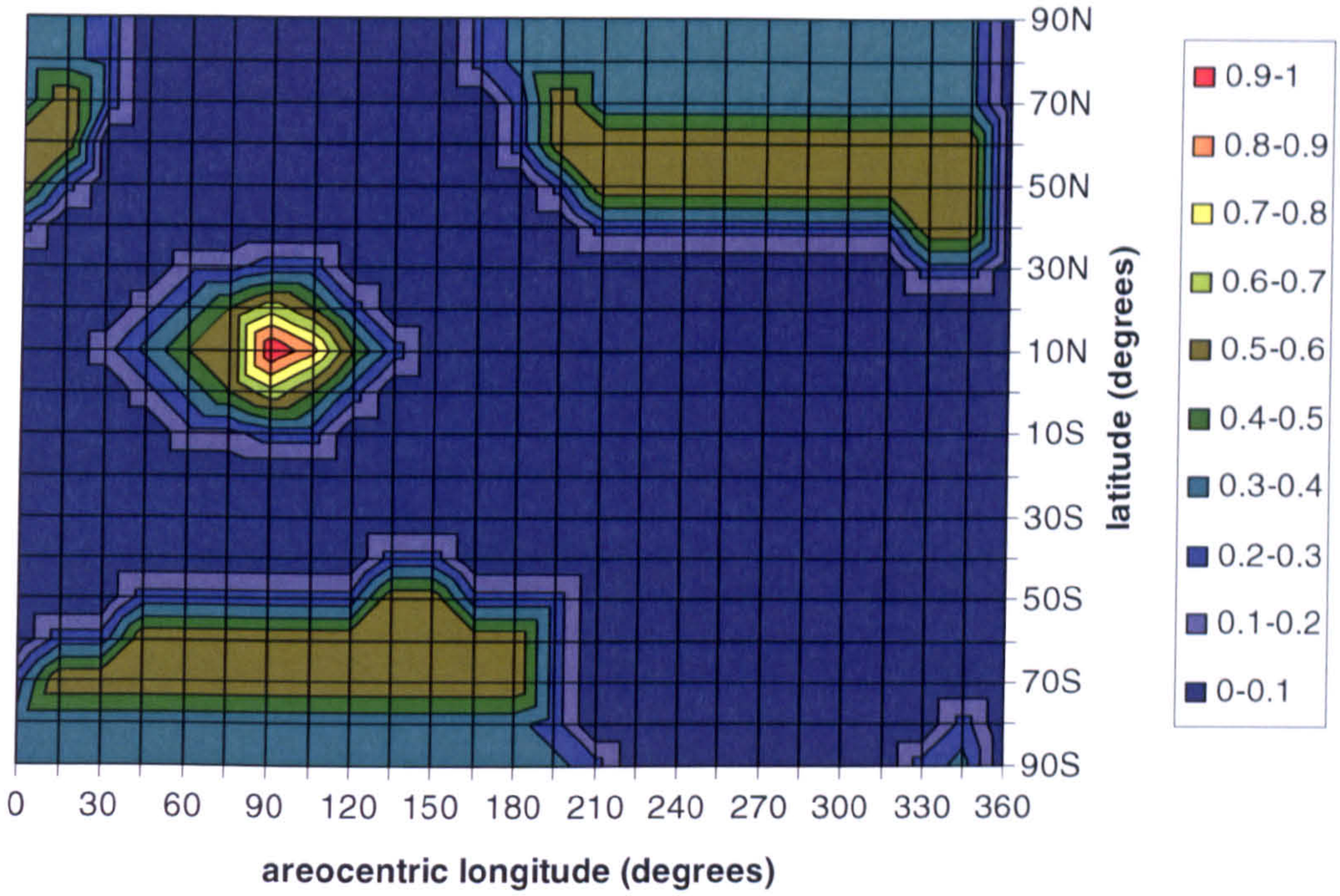

Figure 2.11 – Water ice aerosol optical depth as a function of areocentric longitude and latitude, modelled distribution based upon SPICAM observations (Mateshvili et al., 2006). Key shows optical depth as ratio relative to the annual maximum water ice optical depth.

2.1.8 Calculation of the surface flux

The calculation of the total surface flux is achieved by considering the flux between the top of the atmosphere and the surface as two separate components, the direct and the diffuse flux. The direct flux corresponds to the fraction of the incident flux which has travelled in a direct path from the source to the observer (for example an instrument at the surface of Mars), any photons absorbed or scattered away from this path are considered lost from the direct flux. It can be calculated via the application of Beer's law (equation 2.14), where τ is the total optical depth of the martian atmosphere.

$$F_{direct} = F_{inc} \cdot \exp[-\mu_0 \tau] \qquad \textbf{2.14}$$

The diffuse component of the total surface flux is a more complicated quantity to determine as it comprises the radiation received by the observer from an indirect source, i.e. photons that have been scattered into the observer's line of sight through interactions with the atmosphere. Calculation of the diffuse flux is performed through the application of the delta-Eddington approximation method. This is a method of approximating the scattering and absorption processes occurring in the atmosphere by means of three parameters, one of which is the optical depth, τ, and has been discussed previously in section 2.1.2. The two new parameters are the single scattering albedo, ω_0, and the scattering asymmetry parameter, g. All of the constituent components of the atmosphere are assigned a particular combination of these two parameters and together they describe how that component interacts with incident photons.

The single scattering albedo, ω_0, is an indication of what percentage of the photons interacting with the particle will be scattered, or conversely, absorbed. It can take a value anywhere between $\omega_0 = 0$ and $\omega_0 = 1$, where these extreme values represent 100% absorption and 100% scattering of incident photons respectively. It is defined as the ratio of the scattering cross-section to the total extinction cross-section.

$$\omega_0 = \frac{\sigma_{scat}}{\sigma_{tot}} = \frac{\tau_{scat}}{\tau_{tot}} \qquad \textbf{2.15}$$

The scattering asymmetry parameter, g, indicates how a particle scatters the incident radiation. It can take a value between $g = 1$ and $g = -1$ where a value of $g = 1$ indicates exclusively forwards scattering, i.e. parallel to the path of incidence and propagating in the same direction as the incident photons, and $g = -1$ represents

predominantly backwards scattering, i.e. parallel to the path of incidence but propagating in the opposite direction to the incident photons. The *g* term is used in the calculation of the scattering phase function which describes the angular distribution of the scattered energy around a particle as a function of the angle between incident and scattered photons (the scattering angle). For isotropic energy distributions, such as result from gaseous Rayleigh scattering, the phase function will take a value of 1 for all scattering angles while for particulate scattering, such as that resulting from dust particles, the energy tends to be skewed in a forwards direction, i.e. favouring low scattering angles.

2.1.9 ω_0 and *g* for gas component

For the gaseous component of the atmosphere the main scattering mechanism is Rayleigh scattering which is highly wavelength dependent. Rayleigh scattering is the dominant scattering process when the scattering particles (gas molecules in this case) have dimensions significantly smaller than the wavelength of the scattered radiation. The Rayleigh scattering cross-section of each gaseous species can be calculated from the following formula (equation 2.16) (Heddle, 1962).

$$\sigma_{Rayleigh} = \frac{128\pi^5 \cdot {\alpha_0}^2}{3\lambda^4} \qquad \textbf{2.16}$$

Where λ is the wavelength of the incident radiation and α_0 is the polarisability constant of the molecule. Miller (1991) gives the α_0 values of CO_2, N_2, Ar, O_2, CO and O_3 as α_0 = 2.911, 1.74, 1.641, 1.581, 1.95 and 3.21 (units are $\times 10^{-30}$ m^3) respectively. Rukes and Dooley (2001) gives the α_0 value for H_2O as $\alpha_0 = 1.494 \times 10^{-30}$ m^3.

Rayleigh scattering is highly isotropic in terms of the energy distribution of the scattered radiation. The photons tend to be scattered into either a forwards or backwards lobe (relative to the incident photons) in approximately equal proportions. The Rayleigh scattering gases are also assumed to be 100% scattering and therefore they are assigned ω_0 and g values of 1 and 0 respectively.

Some of the gaseous species, for example ozone, exhibit absorption features within the wavelength range under study. A graph showing the wavelength dependent absorption cross-sections for the relevant gas species can be seen in Figure 2.12. The absorption cross-sections for carbon dioxide are taken from Parkinson et al. (2003), those for oxygen and ozone are taken from Bogumil et al (2003) at wavelengths above 235 nm and Amoruso et al. (1996) and Malicet et al. (1995) respectively for wavelengths below 235 nm. Those for water vapour were also taken from Bogumil et al. (2003). For the purposes of calculating the contribution of this absorption on the diffuse flux, these species are assumed to be 100% absorbing and are therefore assigned ω_0 and g values of 0 and 0 respectively.

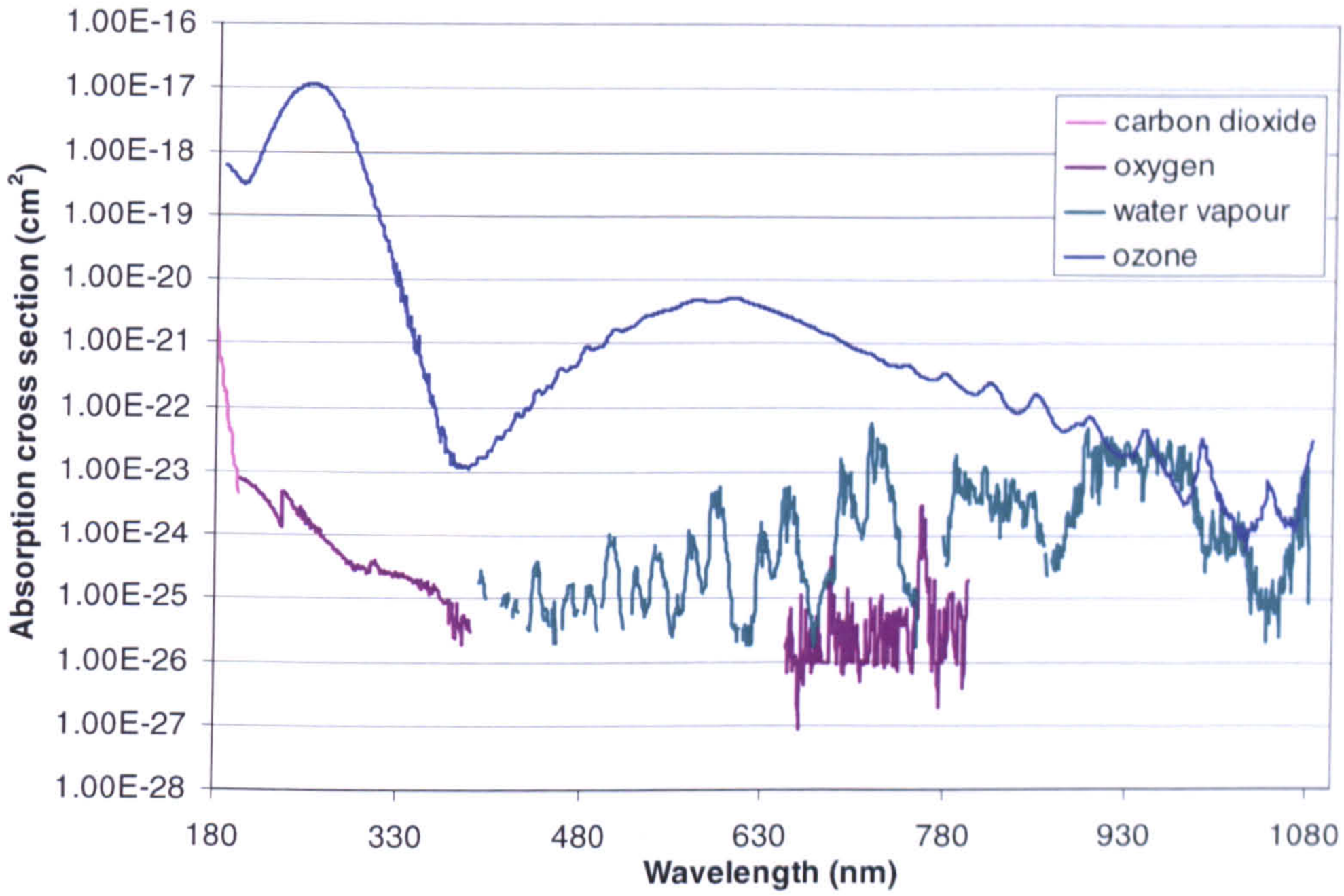

Figure 2.12 – Wavelength dependent absorption cross-sections of relevant species in the martian atmosphere. References for the data on this plot are discussed on the preceding page.

2.1.10 ω_0 and g for the aerosol component

2.1.10.1 Dust aerosol scattering parameters

One of the main areas of uncertainty regarding our knowledge of the martian dust is the optical properties it possesses. Numerous spectra have been gathered of the martian atmosphere, both from orbit and from the planet's surface, but it is extremely difficult to extricate the direct influence of the dust from the other components and processes present. Ideally, this could be achieved through a sample return mission providing extant martian dust that can be studied under controlled laboratory conditions, but this remains for the future. To the present day, a number of attempts have been made to constrain these optical parameters through study of the martian atmosphere at various wavelengths and using different instruments, the most

comprehensive of these, in terms of the wavelength regime covered (and relevance to this work), was done by Ockert-Bell et al. (1997). This work, henceforth referred to as 'Ockert-Bell', is an extension of an analysis carried out by Pollack et al. (1982), where Viking orbiter observations made of the reflected and emitted light from the martian surface were fitted to a model specifying the complex index of refraction and the particle size distribution and shape of the dust. The latter two properties of the dust could be constrained to a certain degree using images taken from the Viking Lander cameras. The original Pollack et al. study covered a wavelength range of 490 to 860 nm; this was extended in Ockert-Bell to a wavelength range of 210 to 4300 nm. Validation of the model was carried out against Viking Orbiter Infrared Thermal Mapper (IRTM) solar channel observations and was found to match the Viking data to within 10%. As part of their analysis Ockert-Bell et al. derived wavelength specific values for the ω_0 and g parameters of the dust and these are the basis for the dust parameters used in this model. A spline interpolation routine was utilised here to increase the Ockert-Bell data to nanometre wavelength resolution.

The Ockert-Bell data also yielded wavelength specific values for another important parameter, the dust extinction coefficient, Q_{ext}; the ratio of the extinction cross-section to the geometric cross-section of the dust particles. The Q_{ext} value at a wavelength of 670 nm ($Q_{ext}{}^{\lambda 670}$) is close to the value of Q_{ext} averaged over the solar spectrum and so can be used to scale the optical depth due to dust extinction with wavelength (Pollack et al., 1979). In the simulation the dust optical depth at a wavelength of 670 nm ($\tau_{\lambda 670}$) is manually input and then the corresponding optical depths at the remaining wavelengths can be determined using the Ockert-Bell values of Q_{ext} for λ = 180-1100 nm through comparison of the ratios given below:

$$\frac{\tau_{\lambda}}{Q_{ext}^{\lambda}} = \frac{\tau_{\lambda 670}}{Q_{ext}^{\lambda 670}} \qquad \textbf{2.17}$$

The right hand side of equation 2.17 is the ratio of the optical depth and the extinction coefficient at $\lambda = 670$ nm ($\tau_{\lambda 670}$ and $Q_{ext}^{\lambda 670}$ respectively) and the left side is the corresponding ratio at the wavelength for which optical depth is being determined.

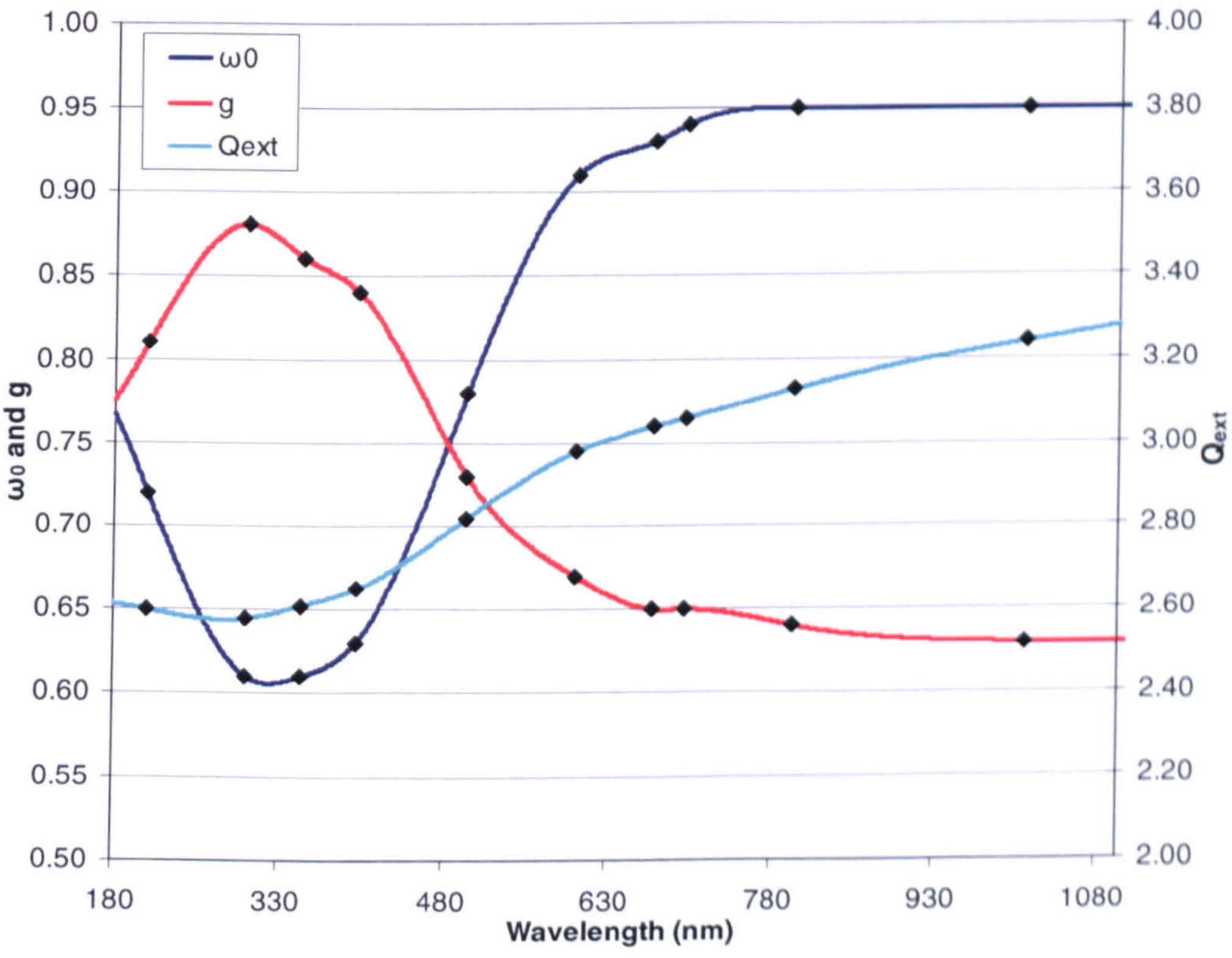

Figure 2.13 – Interpolated Ockert-Bell dust scattering parameter values $\omega 0$, g and Q_{ext} as a function of wavelength. Black diamonds represent original Ockert-Bell data points.

In order to illustrate the uncertainties present in the current knowledge it is useful to compare a number of other studies of the dust scattering parameters with the results

of Ockert-Bell: The first detailed studies of the martian dust were made during the 1970s and were based upon the data returned from Mariner 9, the first artificial satellite of Mars, and the Viking 1 and 2 orbiters and landers. Toon et al. (1977) used data from the Infrared Interferometer Spectrometer (IRIS) on board Mariner 9 to attempt to constrain the mineralogical composition and size distribution of the dust, coming to the conclusion that the dust was likely to be a mixture of materials but dominated by igneous silicates, and that the size distribution of the dust particles was comparable to that observed under certain conditions in terrestrial environments. This work incorporated estimates of the ω_0 parameter ranging from as high as $\omega_0 = 1.0$ to as low as $\omega_0 = 0.36$ and of the g parameter ranging from $g = 0.0$ to 1.0, in an attempt to fit modelled spectra to those returned by IRIS. No wavelength dependence was attributed to the scattering parameters at this stage.

Pollack (1982) used a radiative-convective model in which wavelength dependence was incorporated into the estimation of the ω_0 and g values in order to simulate the atmospheric temperature profiles as obtained by the Viking spacecraft. This study was revisited in Pollack et al. (1995) using an improved analysis technique, including the assumption of non-spherical particles and accounting for some issues with the calibration of the data collected in the NIR waveband. This updated analysis resulted in a general decrease in the estimated values of both ω_0 and g.

Clancy et al. (1995) modified the work of Toon et al. (1977) by proposing a new 'palagonite-like' composition for the dust and a smaller yet broader particle size distribution. Estimates were then determined of the ω_0 and g parameters required to

fit IRIS and Viking spectra at UV and visible wavelengths using the new composition and size distribution data.

Wolff et al. (1997) and (1999) used images taken by the Wide Field Planetary Camera 2 on board the Hubble Space Telescope including those of a 1995 dust storm in Valles Marineris. At longer wavelengths the ω_0 and g parameters used in the analysis are those of the Ockert-Bell study but these are modified at the UV wavelengths to provide a fit to the Hubble data.

The study of Tomasko et al. (1999) is based around images obtained by the Imager for Mars Pathfinder (IMP) camera on board the Mars Pathfinder lander and which was capable of taking images at four wavelengths. The aerosol conditions at each of these wavelengths were modelled in order to determine the scattering parameters required to fit the IMP data. The work of Markiewicz et al. (2002) is a reanalysis of the same IMP data used in Tomasko et al. It incorporates an improved spectral resolution and the correction of some data calibration issues which results in small corrections to the estimated ω_0 values across the wavelength range and an increase to the g values estimated at longer wavelengths.

Examining data returned by the Mars Express instruments OMEGA (a mapping spectrometer for determining the surface composition of the planet and operating in the visible and infrared wavelengths) and PFS (Planetary Fourier Spectrometer for monitoring atmospheric temperatures and pressures), Maattanen et al. (2009) use the statistical method of Independent Component Analysis in conjunction with a radiative transfer model to determine the dust scattering parameters that fit the

observations. The data points resulting from the studies discussed above are compared with the Ockert-Bell values for ω_0 and g in Figure 2.14 and Figure 2.15 respectively.

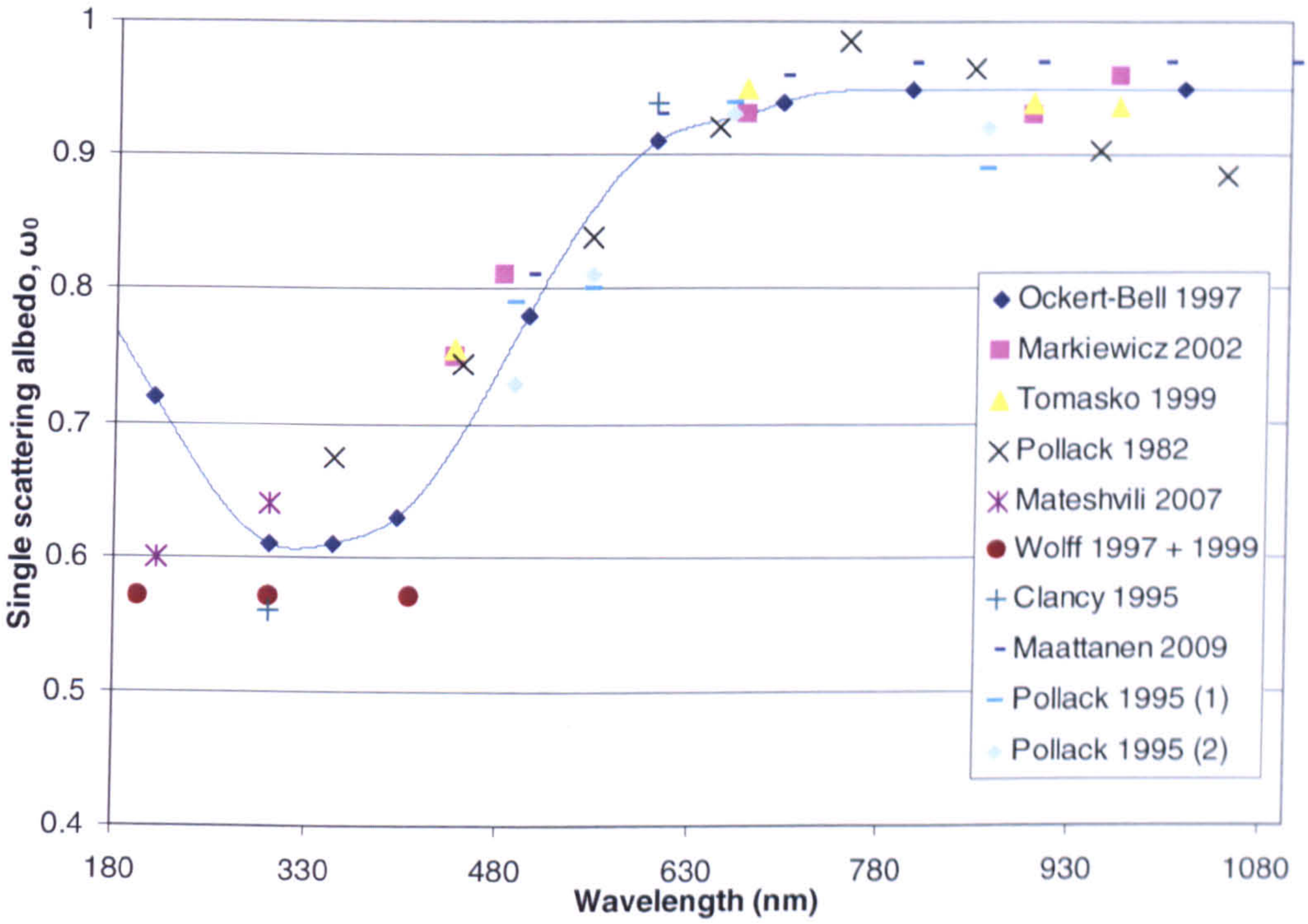

Figure 2.14 – Comparison of Ockert-Bell ω_0 values for the martian dust with a number of different studies.

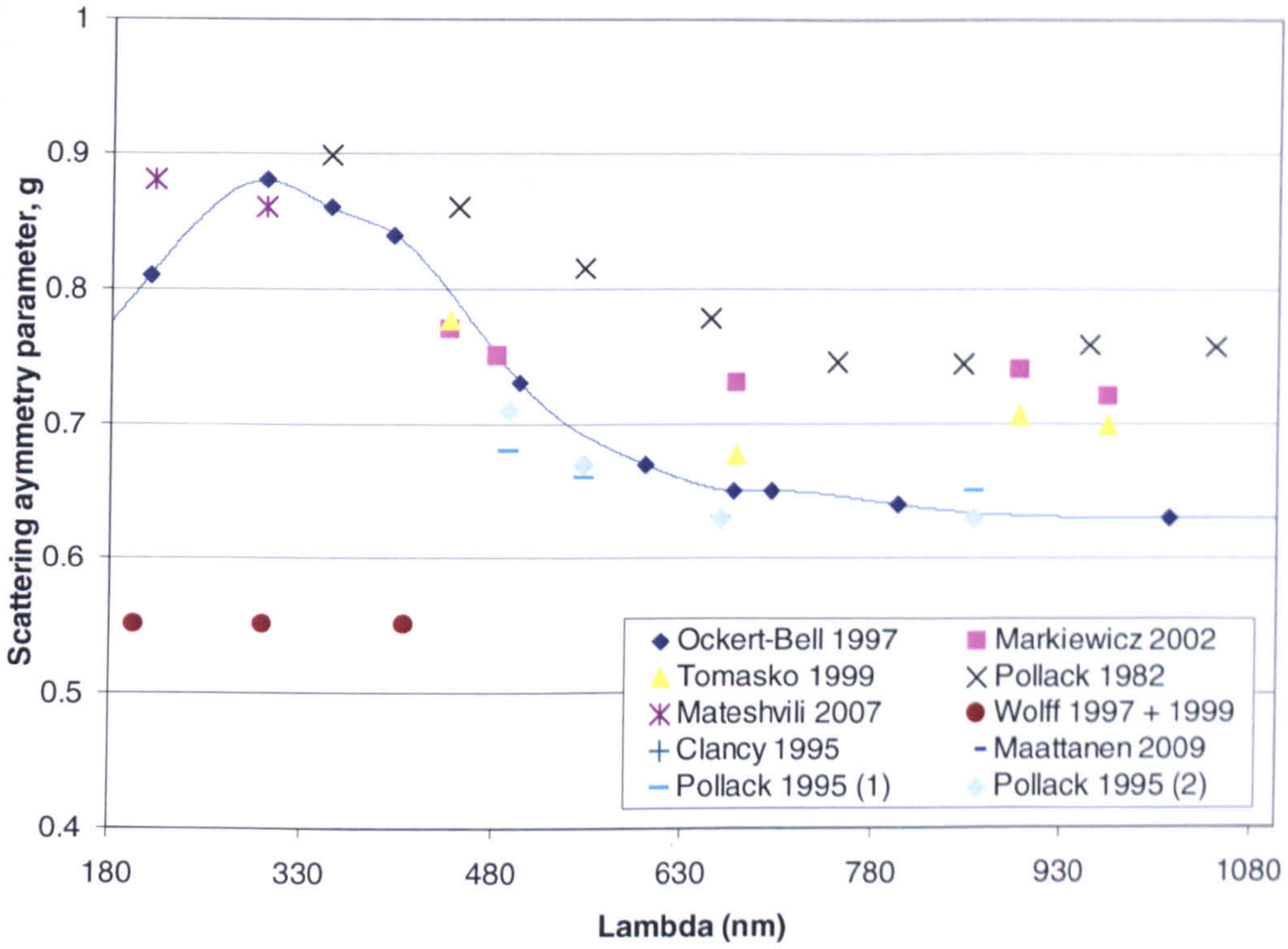

Figure 2.15 – Comparison of Ockert-Bell *g* values for the martian dust with a number of different studies.

Figure 2.14 provides a comparison of the wavelength dependent values derived for the single scattering parameter, ω_0, in the studies discussed above. These are overlaid on the ω_0 curve provided from the Ockert-Bell values used for in the UVIS simulation. The greatest agreement between the different studies occurs in the wavelength range of $\lambda \sim 600$–700 nm, the longer wavelengths of the visible regime, where the derived values from all studies incorporating that wavelength range cover a range of values of $\omega_0 = 0.92$-0.96. At the longer wavelengths, corresponding to the NIR wavelengths of this work, most studies are still within a similar spread of agreed values for ω_0 with the exception of the Pollack studies. The three studies by Pollack, (1982) and (1995) (containing two studies) all derive a decreasing trend in ω_0 as wavelength increases. This leads to a maximum derived value of $\omega_0 = 0.97$ from the Maattanen et al. (2002) study and a minimum derived value of $\omega_0 = 0.86$ from

Pollack (1995). At the UV end of the spectrum the disagreement between different studies becomes even greater with the Ockert-Bell study deriving a sharp increase in ω_0 values shortwards of $\lambda \sim 280$ nm, something that is not echoed by the other studies. The studies by Wolff and by Clancy et al. (1982) show lower values of ω_0 at these wavelengths and no suggestion of an upwards trend to the data points, while Mateshvili (2002) shows a decreasing trend in ω_0 tending towards the values of Wolff. At the short wavelength end of the UV wavelengths the maximum value of ω_0 is provided by Ockert-Bell as $\omega_0 = 0.72$ and the minimum by Wolff as $\omega_0 = 0.57$. With the exception of the upwards trend at short UV wavelengths the interpolated ω_0 values derived from the Ockert-Bell data strikes a fairly consistent average through the values of the rest of the studies.

Figure 2.15 provides a comparison of the scattering asymmetry parameter values, g, derived from the same studies. The disagreement in values for g between the different studies is greater across the whole wavelength range when compared to that for ω_0. Across the visible and NIR wavelengths the maximum and minimum values of g are defined by the different Pollack studies. Pollack (1982) initially derived high values for g and then with the revisiting of the same data in Pollack et al. (1995) revised these down to significantly lower values. The high values of Pollack et al. (1995) at the NIR wavelengths are also approached by those of Markiewicz et al. (2002). Throughout the visible and NIR the Ockert-Bell values tend towards the lower values of the extremes of the range of g. At 1000 nm the maximum derived value of g is $g = 0.76$ while the minimum derived value is $g = 0.63$. At the visible wavelengths the different studies are once again in better agreement over the values of g, with the values of Markiewicz et al. converging on those of Ockert-Bell as

wavelength decreases. The values from Pollack et al. (1995) however still present a large difference in g value compared to those of Ockert-Bell. In the UV waveband the Ockert-Bell data shows a peak in the value of g at approximately 300 nm and then a steep decrease in g values shortwards of this wavelength. The values from Mateshvili et al. (2007) show the opposite trend with the value of g increasing as wavelength decreases, at 300 nm the difference between the Mateshvili et al. and Ockert-Bell value for g is only 0.02 but by 210 nm this difference has increased to 0.07. The only other study which considered the UV waveband is that of Wolff et al. (1997) and (1999) and which derived significantly lower values for g than both Ockert-Bell and Mateshvili et al., for example the value of g derived at 200 nm by Wolff et al. is only $g = 0.55$.

From the comparison carried out here it is clear that despite the numerous studies that have been conducted there is still a significant uncertainty in the current knowledge regarding the martian dust scattering parameters. This uncertainty appears to be at its lowest for the scattering properties of the dust at visible wavelengths, which is not surprising as every mission to the surface of Mars has included a camera operating at visible wavelengths in order to record images of the martian surface. This has resulted in a relative wealth of information available for study at these wavelengths which can be used to reduce the uncertainty in the modelling of the dust scattering parameters. The comparable lack of data for the other wavelength regimes, particularly for the UV wavelengths, leads to a corresponding greater uncertainty in the scattering parameters derived from this data. The provision of a dedicated spectrometer, sensitive across the UV and NIR wavelengths, on board a future mission to the surface of Mars would go a long way

to addressing this data deficit and lead to an improved ability to define accurately the dust scattering parameters across a greater wavelength range.

2.1.10.2 Ice cloud aerosol scattering parameters

The optical properties of the water ice cloud aerosol were taken from Mateshvili et al. (2007) where it was assumed that both the g and ω_0 values remain approximately constant over the considered wavelength regime. Modelling the ice aerosols as spherical particles gives ω_0 and g values of 1.0 and 0.7 respectively and this is in agreement with the studies of the Mie scattering properties of water ice conducted in Key et al. (2002).

2.1.11 Calculation of effective scattering parameters

With the values of optical parameters known for each scattering and absorbing species present it is now required to combine these values to create an effective single scattering albedo, ω_{0eff}, and an effective scattering asymmetry parameter, g_{eff}, for the entire atmosphere:

$$g_{eff} = \frac{(\tau_{dtot} \cdot g_d) + (\tau_{gtot} \cdot g_g) + (\tau_{ctot} \cdot g_c)}{(\tau_{dtot} + \tau_{gtot} + \tau_{ctot})} \qquad \textbf{2.18}$$

$$\omega_{0eff} = \frac{\tau_{dscat} + \tau_{gscat} + \tau_{cscat}}{\tau_{dtot} + \tau_{gtot} + \tau_{ctot}} \qquad \textbf{2.19}$$

The optical depth subscripts in equations 2.18 and 2.19, *dscat, gscat* and *cscat, dtot, gtot,* and *ctot,* refer to the scattering and total (scattering plus absorption) optical depths of the dust, gas and ice cloud components respectively.

2.1.12 Atmospheric structure

For the purposes of computing the diffuse surface flux using the delta-Eddington method the martian atmosphere needs to be divided up into a number of vertically consecutive layers. In the UVIS simulation each layer covers an altitude difference of two kilometres which translates into a total of 71 layers. These layers are numbered from the top down, i.e. the layer at the greatest altitude is layer number 1 and the layer adjacent to the surface of the planet is number 71. The constituent components of the atmosphere and how their altitude distributions are calculated have been outlined previously (see Sections 2.1.5-2.17) and these methods are used to assign the correct abundances of gases and aerosols to each layer. Using this structure the delta-Eddington algorithm effectively passes the incident flux down through to each consecutive layer, assessing the effect that each layer has on the flux at each wavelength. This takes into account the scattering and absorption processes within that layer and also any radiation scattered down from previous layers and upwards from subsequent layers, including the planetary surface (Shettle and Weinman, 1970).

2.1.13 The albedo of the planetary surface

The albedo of the surface of Mars (the ratio of the flux reflected from the surface to the flux incident on the surface) exhibits a wavelength dependence and this needs to be taken into account for a simulation that covers such a wide range of wavelengths. Mallama (2007) has used a comprehensive set of ground based observations dating

from the 1950s up to 2006 to determine the albedo of Mars at wavelengths of λ = 360, 440, 550, 700 and 900 nm. This covers the majority of the wavelength range of the UVIS simulation with the exception of the shortest ultraviolet and the longest near-infrared wavelengths. The ground based observations of Fox et al. (1997) were used to extend the surface albedo to λ = 180 nm and observations made with the Planetary Fourier Spectrometer (PFS) aboard the Mars Express orbiter (Esposito et al., 2007) were used to extend the surface albedo to the long wavelength limit of λ = 1100 nm. Figure 2.16 shows the nanometre resolution wavelength dependent surface albedo generated using a spline interpolation routine with the data points provided from the references given above. It can be seen from the figure how the albedo increases from very low values at UV wavelengths and the blue end of the visible spectrum to comparatively high values at the red end of the visible spectrum and into the NIR. This is of course consistent with Mars' appearance as a red planet.

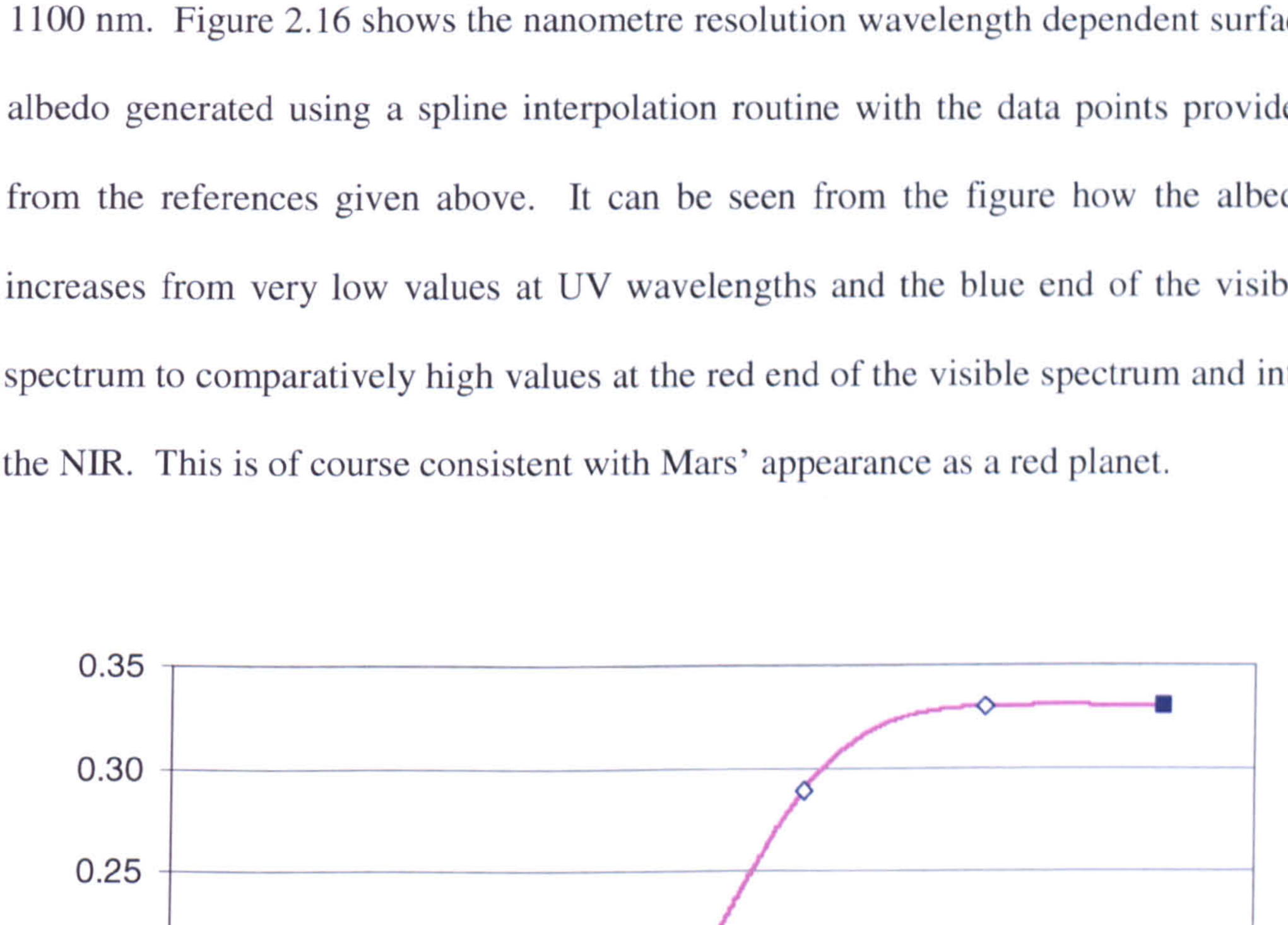

Figure 2.16 – Wavelength dependent surface albedo of Mars.

2.1.14 Details of the delta-Eddington method

The delta-Eddington approximation is a modification of the original Eddington approximation (Shettle and Weinman, 1970). This modification was required because the Eddington approximation deals poorly with the highly asymmetric scattering phase functions characteristic of particulate scattering, i.e. in this case the martian dust (Joseph et al., 1976). It achieves this by modifying the phase function to incorporate a Dirac delta term for the forward scattering peak. Using the condition that the asymmetry factor, g, should be equal to that of the original Eddington phase function creates a series of transformations for the key parameters (equations 2.20, 2.21 and 2.22), which, when substituted into the Eddington method transform it into the delta-Eddington method.

$$g' = \frac{g}{1+g} \qquad \textbf{2.20}$$

$$\omega_0' = \frac{(1-g^2)\omega_0}{(1-\omega_0 g^2)} \qquad \textbf{2.21}$$

$$\tau' = (1-\omega_0 g^2)\tau \qquad \textbf{2.22}$$

For clarity, the prime notation, i.e. g', to represent the delta-Eddington transformed values is not used during the description of the method but it should be remembered that all subsequent references to these three parameters in this chapter are the transformed values of g, ω_0 and τ unless otherwise stated. The delta-Eddington method calculates the total diffuse surface flux from the expression:

$$F = \pi \cdot \left(I_\alpha(\tau) + \frac{2}{3} I_\beta(\tau) \right) \qquad \textbf{2.23}$$

Where the I_α and I_β terms are layer specific quantities found for layer i using the following:

$$I_\alpha^i = C^i \exp[-k_i \cdot \tau_{tot}] + D^i \exp[k_i \cdot \tau_{tot}] - \alpha_i \exp\left[-\tau_{tot}/\mu_0\right] \qquad \textbf{2.24}$$

$$I_\beta^i = p_i \left(C^i \exp[-k_i \cdot \tau_{tot}] - D^i \exp[k_i \cdot \tau_{tot}] \right) - \beta_i \exp\left[-\tau_{tot}/\mu_0\right] \qquad \textbf{2.25}$$

Where:

$$k_i = \sqrt{3\left(1-\omega_{0eff}^i\right) \cdot \left(1-\omega_{0eff}^i g_{eff}^i\right)} \qquad \textbf{2.26}$$

$$p_i = \sqrt{3\left(1-\omega_{0eff}^i\right) / \left(1-\omega_{0eff}^i g_{eff}^i\right)} \qquad \textbf{2.27}$$

$$\alpha_i = \frac{3\omega_{0eff}^i \left(\frac{F_{inc}}{\pi}\right) \mu_0^2 \left(1 + g_{eff}^i \left(1-\omega_{0eff}^i\right)\right)}{4\left(1-k_i^2 \mu_0^2\right)} \qquad \textbf{2.28}$$

$$\beta_i = \frac{3\omega_{0eff}^i \left(\frac{F_{inc}}{\pi}\right) \mu_0 \left(1 + 3g_{eff}^i \left(1-\omega_{0eff}^i\right) \mu_0^2\right)}{4\left(1-k_i^2 \mu_0^2\right)} \qquad \textbf{2.29}$$

The parameter τ_{tot} refers to the cumulative optical depth of the atmosphere down to (and inclusive of) layer i. Parameters ω^i_{0eff} and g^i_{eff} refer to the effective values of ω_0 and g specifically in layer i. The C^i and D^i coefficients are integration constants

which can be derived through the formation of equations using the layer boundary conditions. These conditions are such that at each layer interface the values of I_α and I_β should be constant across this interface, i.e.:

$$I_\alpha^i(\tau_i) = I_\alpha^{i+1}(\tau_i) \qquad i = 1, 2, \ldots, 71 \qquad \textbf{2.30}$$

$$I_\beta^i(\tau_i) = I_\beta^{i+1}(\tau_i) \qquad i = 1, 2, \ldots, 71 \qquad \textbf{2.31}$$

In equations 2.30 and 2.31 τ_i refers to the optical depth owing to the scattering and absorption present only in layer i.

There are also two distinct boundary conditions relating to the top and the bottom of the atmosphere. At the very top of the atmosphere, i.e. the top of layer 1, the downward diffuse flux must be zero, giving equation 2.32:

$$\left(1+\frac{2p_1}{3}\right)C^1 + \left(1-\frac{2p_1}{3}\right)D^1 = \alpha_1 + \frac{2\beta_1}{3} \qquad \textbf{2.32}$$

At the bottom of the atmosphere, i.e. where layer 71 meets the planet's surface, the upward diffuse irradiance must equal the downward directed irradiance multiplied by the albedo of the surface, A, giving:

$$\left(1-A-\frac{2(1+A)p_{71}}{3}\right)\exp[-k_{71}\cdot\tau_{71}]\cdot C^{71} + \left(1-A+\frac{2(1+A)p_{71}}{3}\right)\exp[k_{71}\cdot\tau_{71}]\cdot D^{71}$$
$$= \left((1-A)\alpha_{71} - \frac{2(1+A)\beta_{71}}{3} + A\mu_0\left(\frac{F_{inc}}{\pi}\right)\right)\exp\left[-\frac{\tau_{71}}{\mu_0}\right] \qquad \textbf{2.33}$$

These equations, of which there must be 142 in order to find the 71 C^i and 71 D^i coefficients, can be solved by inverting a 142 × 142 element matrix, in this case using the LU decomposition technique, where the matrix is decomposed into the product of lower and upper triangular matrices (Press et al., 1992). With the determination of these coefficients the values of I_α and I_β can be calculated and from there the surface irradiance. Figure 2.17 shows the interaction of the incident radiation with the atmosphere divided up into layers, as required by the delta-Eddington approximation,

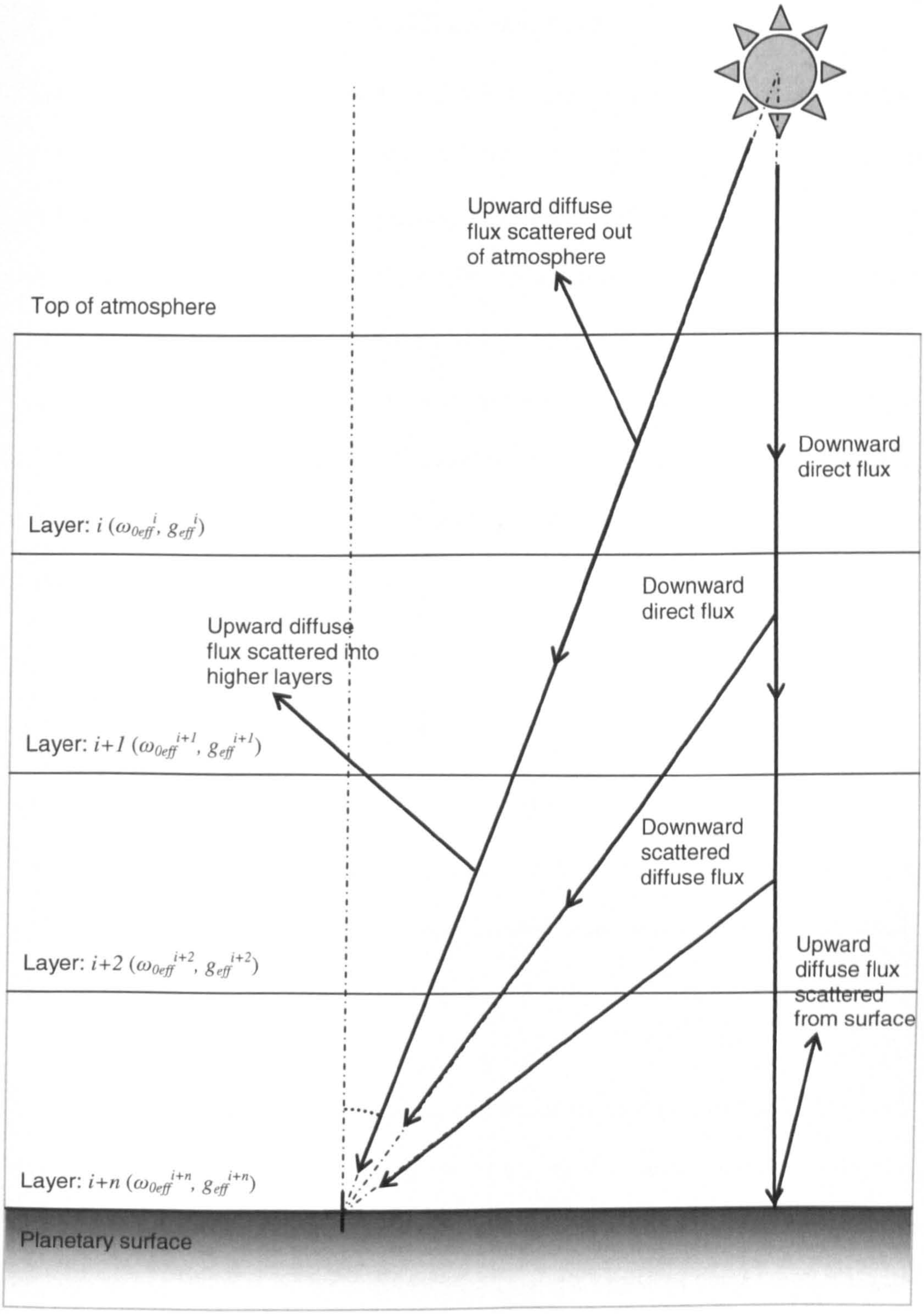

Figure 2.17 – Illustrating how the incident flux interacts with the layered atmosphere of the delta-Eddington approximation.

2.2 Applications of the UVIS simulation

This simulation is a powerful tool for investigating the non-ionising radiation environment at the martian surface. Coupled to environmental data, such as the diurnal or annual cycles of the martian atmosphere and its aerosol component, it allows us to build up a picture of how this radiation environment varies over time and location. These data can be applied to predicting the output of the UVIS spectrometer instrument under different operating scenarios and to assessing the instrument's suitability, in terms of sensitivity and resolution, for certain proposed applications. These applications of both the simulation and the instrument are considered in the subsequent chapters.

2.3 Previous modelling work

Previous work has been conducted in this field with different techniques and methods employed to study aspects of Mars' surface radiation environment. The studies most relevant to the work being presented in this thesis are those of Cockell et al. (2000) and Patel et al. (2002, 2003).

Cockell et al. used a simple single-layer model of the martian atmosphere to look specifically at the UV wavelength regime. It was used to demonstrate the influence of the CO_2 absorption which effectively acts to prevent any significant UV flux reaching the surface at wavelengths shorter than $\lambda \sim 190$ nm. The presence and effects of ozone were also discussed and how the low abundance of ozone allows a greater percentage of the potentially biologically damaging UVB (λ = 280-320 nm) and UVC (λ = 100-280 nm) rays to reach the surface, compared to the equivalent

Earthly scenario. The strong influence of the martian dust on the surface radiation levels is noted with even low levels (optical depths $\tau < 0.1$) seen to produce significant extinction effects, but at the same time the corresponding increase in scattered radiation means shadowed surfaces suffer greater exposure. The matter of the poorly constrained optical parameters of the dust at these wavelengths is also highlighted. The potential effects of cloud cover are ignored for this simulation.

Patel et al. (2002) built upon the work of Cockell at al. by using updated dust scattering parameters and gas absorption cross-section values. This was followed up with the development of an improved delta-Eddington model of the martian atmosphere looking specifically at the UV wavelength regime from 180 to 400 nm in Patel et al. (2003). The Patel model divided the atmosphere up into ten layers, incorporating a vertically distributed dust component and introducing ice cloud aerosols cloud layers, and was used to investigate the variation of the surface UV flux over diurnal and annual scenarios, such as dust storms and dust devil events, and the consequent implications for the habitability of the surface of Mars. This work was done to support the development of the UV sensor mounted on the ill-fated Beagle 2 lander and was the precursor to the studies detailed in this thesis. The UVIS simulation is essentially an upgraded version of the Patel model with higher altitude resolution and extended wavelength coverage to include the visible and near infrared regimes being the major advances between the two.

2.4 The UVIS simulation code

The UVIS simulation code is written in Research Systems Inc's Interactive Data Language (IDL) Version 6.0. Execution of the code, under the current configuration with 71 layers and a wavelength range of λ = 180-1100nm at 1 nm resolution, takes approximately 20 seconds to return data files containing the direct and diffuse components of the surface flux. The code can easily be incorporated into a loop which steps through the variables of choice so that surface flux values can be returned for multiple values of latitude, areocentric longitude (across a martian year) or time at the martian surface (across a martian day). A copy of the code, 'UVIS_sim.pro', can be found in Appendix A.

The initial inputs to the program, specified by the user, are the values of latitude, l, areocentric longitude, L_s, time from noon at the surface, t, and the maximum optical depth values for the atmospheric aerosols (dust and ice), as required for the scenario under investigation. Single value constants, such as the axial obliquity of Mars' rotation and the eccentricity of Mars' orbit, are specified in a designated section of the code and so can be easily edited if required. Input data that exhibit a dependency upon a particular value, either wavelength or altitude, are stored in input files that are automatically read in to the program at the appropriate point during execution of the code. Input data files that contain wavelength dependent values include; the surface albedo, the incident flux at the top of Mars' atmosphere, the gas absorption cross-sections and the aerosol scattering parameters. Input data that exhibit a dependency on altitude include the atmospheric pressure values and the aerosol vertical distribution values. These files can be edited or replaced with alternative files if different atmospheric profiles, aerosol parameters or incident flux scenarios are required. Figure 2.18 is a flow diagram providing an overview of the key operations

of the UVIS simulation. Step 5 of the flow diagram is expanded upon in Figure 2.19, Figure 2.20 and Figure 2.21, which show the steps involved in calculating the contribution to the total atmospheric optical depth by the gas species, the dust aerosols and the ice cloud aerosols, respectively.

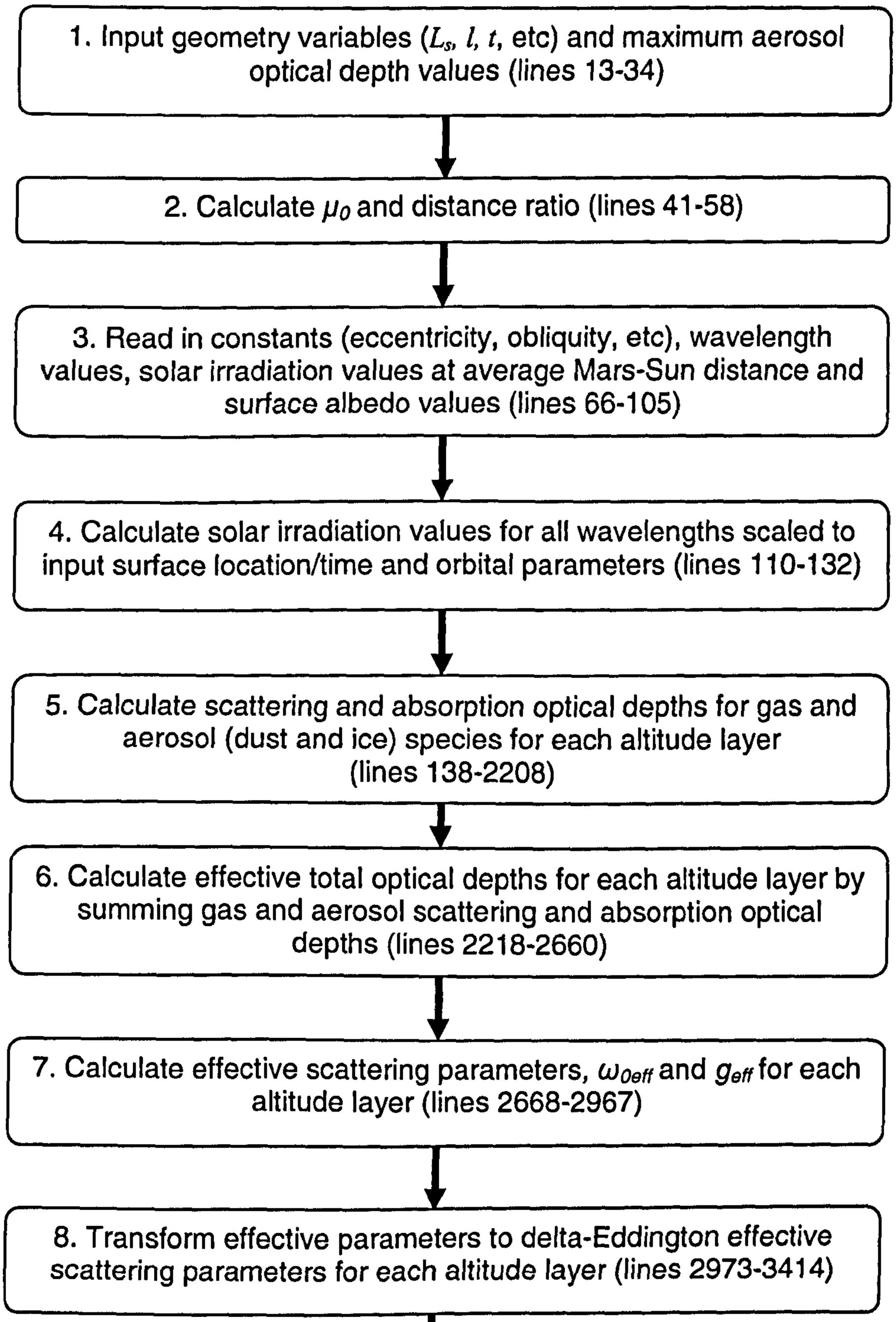
1. Input geometry variables (L_s, l, t, etc) and maximum aerosol optical depth values (lines 13-34)
2. Calculate μ_0 and distance ratio (lines 41-58)
3. Read in constants (eccentricity, obliquity, etc), wavelength values, solar irradiation values at average Mars-Sun distance and surface albedo values (lines 66-105)
4. Calculate solar irradiation values for all wavelengths scaled to input surface location/time and orbital parameters (lines 110-132)
5. Calculate scattering and absorption optical depths for gas and aerosol (dust and ice) species for each altitude layer (lines 138-2208)
6. Calculate effective total optical depths for each altitude layer by summing gas and aerosol scattering and absorption optical depths (lines 2218-2660)
7. Calculate effective scattering parameters, ω_{0eff} and g_{eff} for each altitude layer (lines 2668-2967)
8. Transform effective parameters to delta-Eddington effective scattering parameters for each altitude layer (lines 2973-3414)

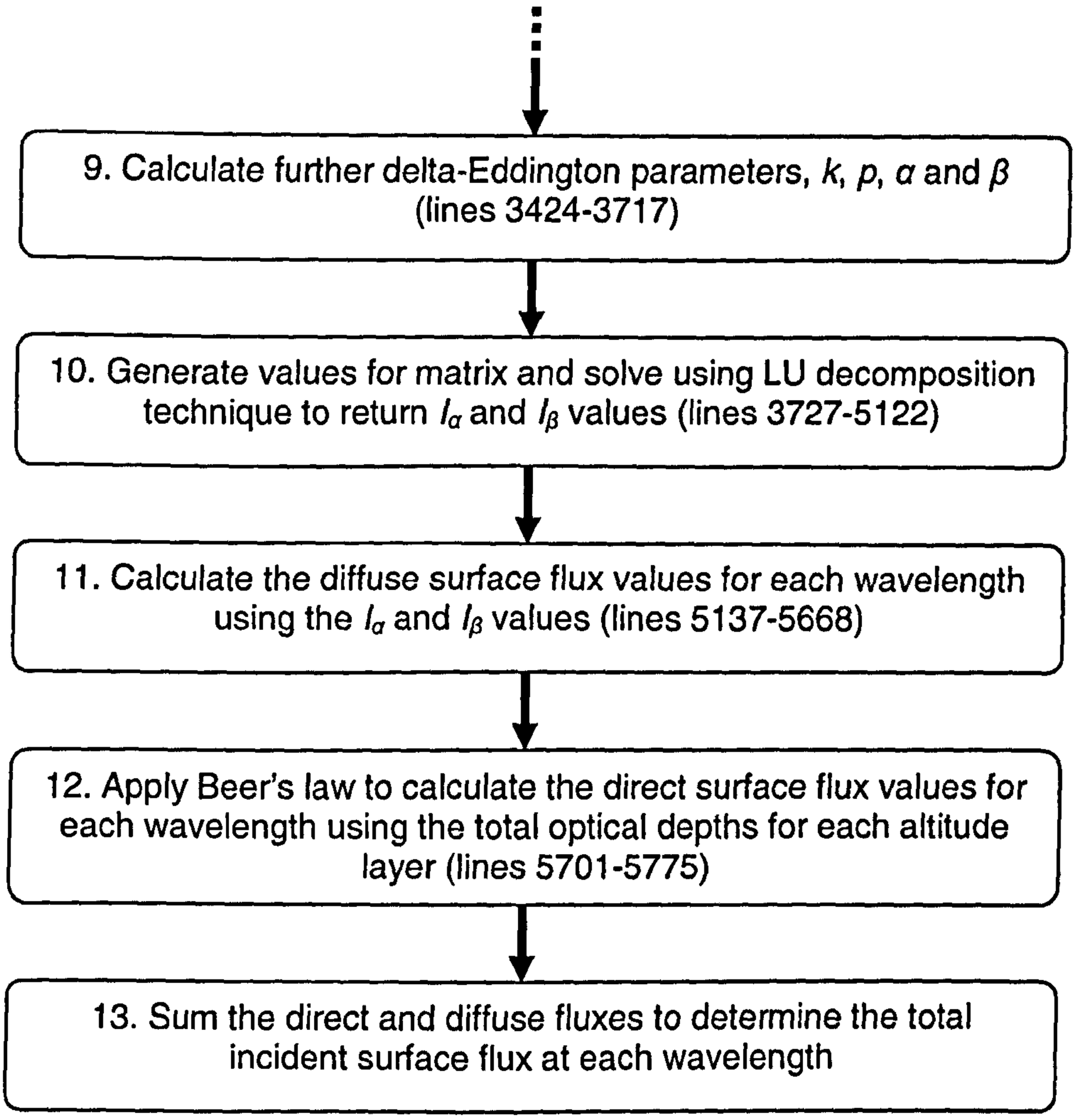

Figure 2.18 – Flow diagram showing the key steps in the execution of the UVIS simulation. The line numbers found in brackets refer to the approximate line numbers of the corresponding sections of the UVIS simulation code (UVIS_sim.pro) found in Appendix A.

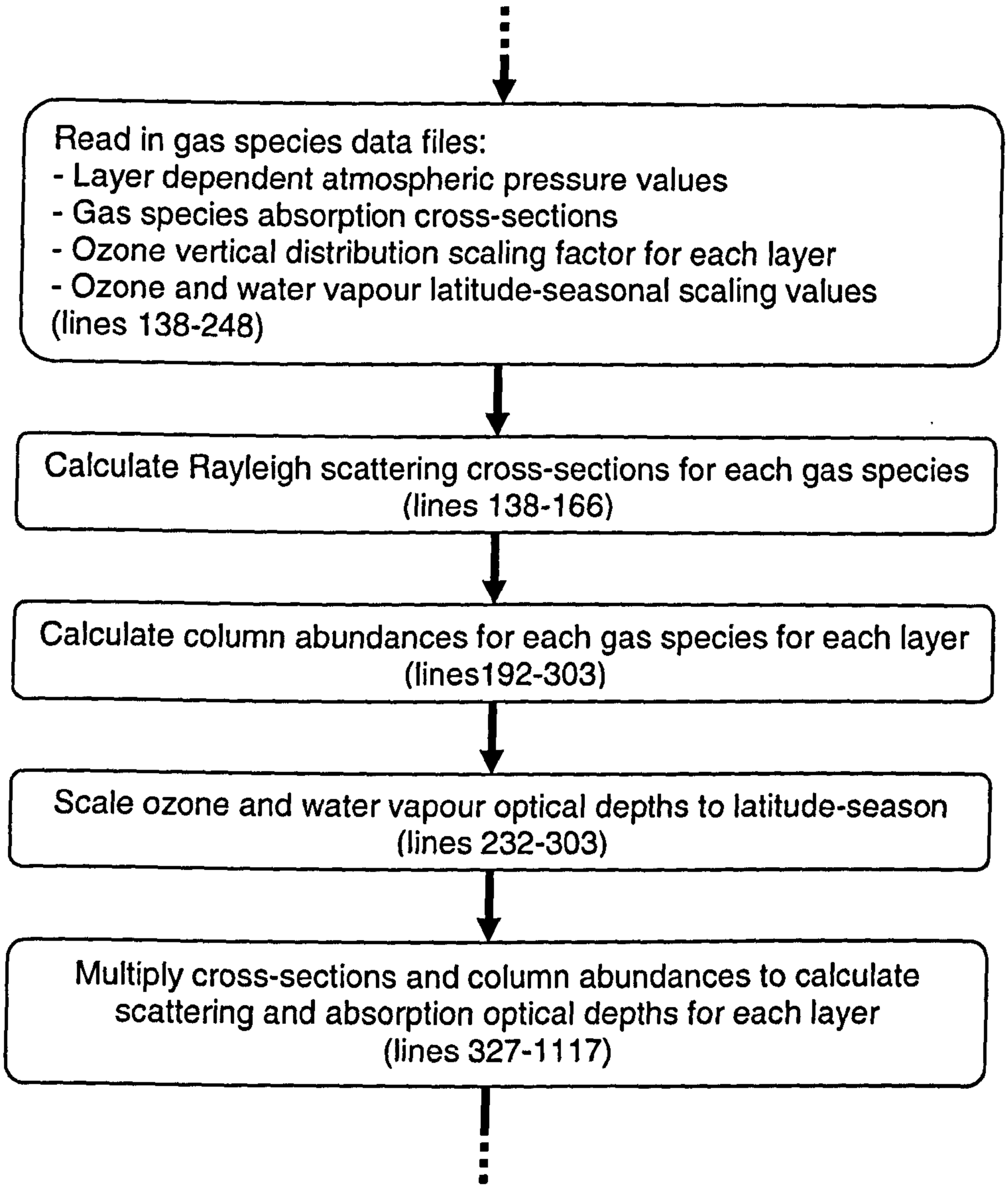

Figure 2.19 – Flow diagram showing the key steps executed by the UVIS simulation for calculating the atmospheric optical depth contribution of the gas species, part of step 5 in Figure 2.18. The line numbers found in brackets refer to the approximate line numbers of the corresponding sections of the UVIS simulation code (UVIS_sim.pro) found in Appendix A.

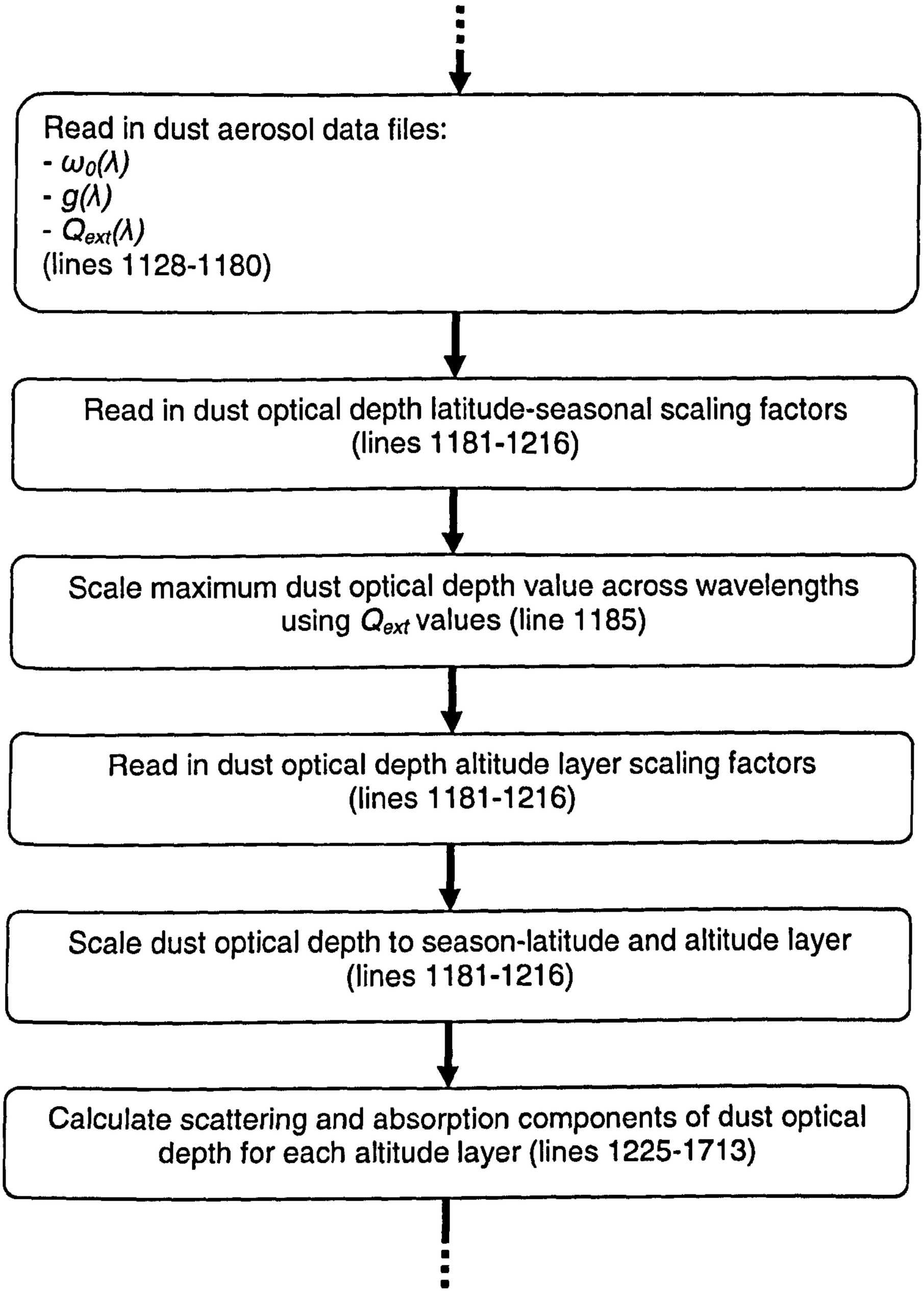

Figure 2.20 – Flow diagram showing the key steps executed by the UVIS simulation for calculating the atmospheric optical depth contribution of the dust aerosols, part of step 5 in Figure 2.18. The line numbers found in brackets refer to the approximate line numbers of the corresponding sections of the UVIS simulation code (UVIS_sim.pro) found in Appendix A.

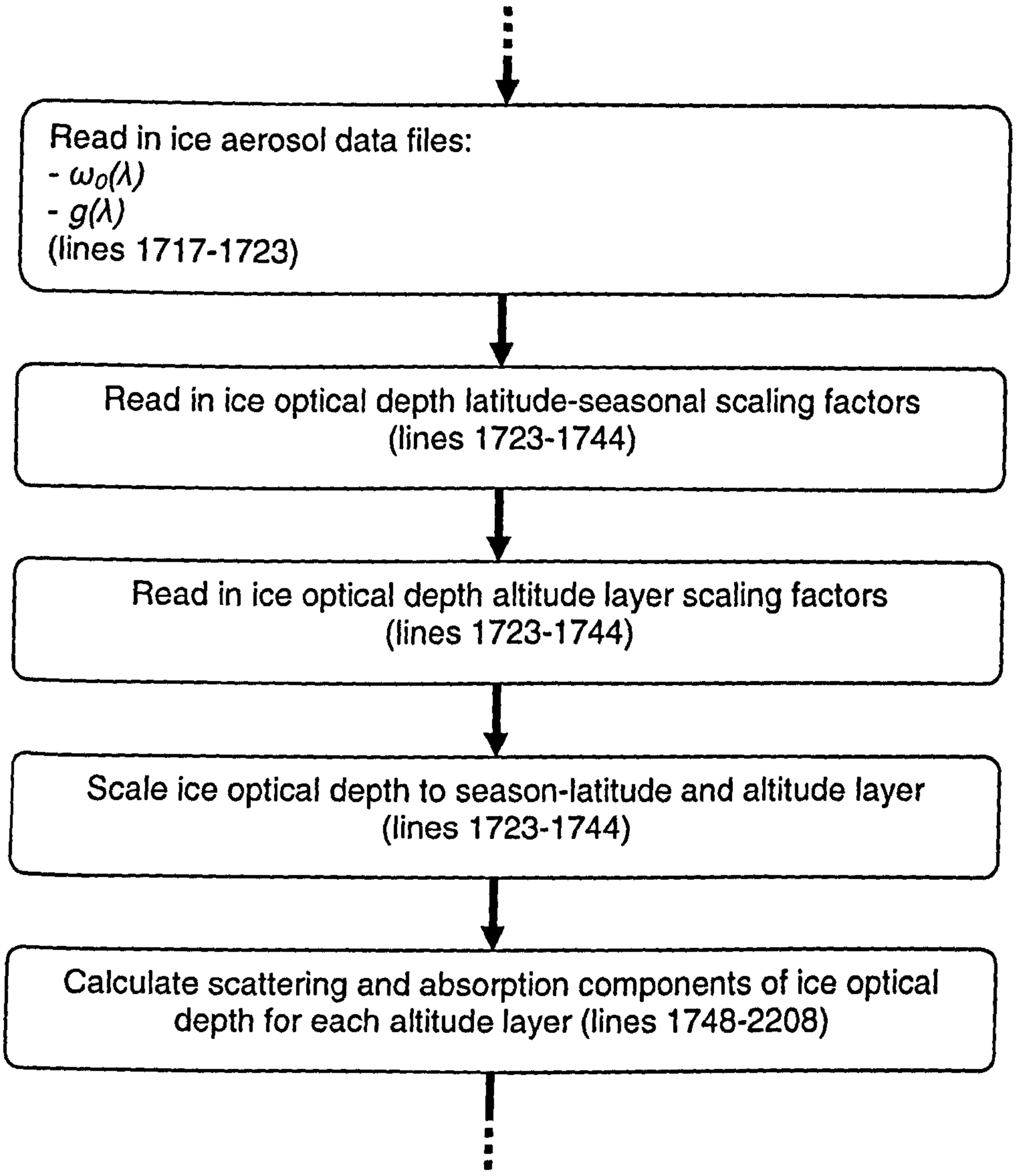

Figure 2.21 – Flow diagram showing the key steps executed by the UVIS simulation for calculating the atmospheric optical depth contribution of the ice aerosols, part of step 5 in Figure 2.18. The line numbers found in brackets refer to the approximate line numbers of the corresponding sections of the UVIS simulation code (UVIS_sim.pro) found in Appendix A.

Chapter 3 – Global and local surface flux studies

In this chapter the UVIS simulation has been applied to study the non-ionising radiative flux at the surface of the planet under a number of different scenarios: Global studies, where the surface flux is predicted across the entire surface of Mars over a full Mars year under varying dust optical depths; local studies, where the radiation environment at some of the past landing sites and other potential landing sites for future missions is considered; and a study focusing on how the direct and diffuse components of the surface flux at different wavelengths are affected by variation in the dust optical depth.

The functional wavelength range of the simulation (180-1100 nm) encompasses the entirety of the visible wavelength regime and extends into the ultraviolet regime at shorter wavelengths and into the near-infrared at longer wavelengths. These regimes are used to define the span of the three wavelength ranges over which some of the studies are carried out. For the purposes of this work the ultraviolet (UV) regime spans λ = 190-400 nm, the visible regime (VIS) covers λ = 401-750 nm and the near-infrared (NIR) the remaining λ = 751-1100 nm. Although the UVIS simulation is set to calculate the surface irradiance starting from a wavelength of 180 nm, the radiation flux below 190 nm at the surface is negligible owing to the high optical depths due to the strong carbon dioxide absorption feature at these wavelengths. This leads to near zero values for the direct irradiance while the values for the delta-

Eddington generated diffuse flux become unreliable as the conditions exceed the range of valid optical depth values (see Table 1 in (Joseph et al., 1976)).

3.1 Surface flux under varying dust optical depth

The following study examines the effects of increasing dust optical depth upon the radiative flux reaching the surface of Mars. This was achieved by running the UVIS simulation multiple times under identical conditions except for the specification of a higher dust optical depth value for each subsequent run. This study was carried out at the equator ($l = 0°$) at $L_s = 220°$; values which were chosen because most potential mission landing sites tend to be within a few degrees either side of the equator and so the equator itself has been chosen as a representative latitude for the tests, while, L_s = 220° was chosen as this represents the point during the martian year of maximum irradiation of the equator and so should result in the highest signal level, i.e. it represents a 'best case' scenario for a strong signal in the spectra recorded by the UVIS instrument. No ice cloud aerosols were included in the atmosphere for this study.

One phenomenon predicted by the following studies is that under certain conditions the *local surface flux* can be greater than the incident flux at the top of the atmosphere. This enhanced surface flux is a locally occurring phenomenon caused by an additional component of 'observed diffuse flux' in the field of view brought about by the scattering effect of the dust aerosols, as illustrated in Figure 3.1. Some of this diffuse flux is scattered towards the point of detection, i.e. the position of the simulated instrument, such that a portion of the incident flux that would not normally

be detected without the presence of a scattering medium (the dust aerosols in this case) is incident at the same surface location as the direct flux component, causing a local enhancement of the total incident surface flux. The *net total downwards flux* however always remains equal to or less than the input flux.

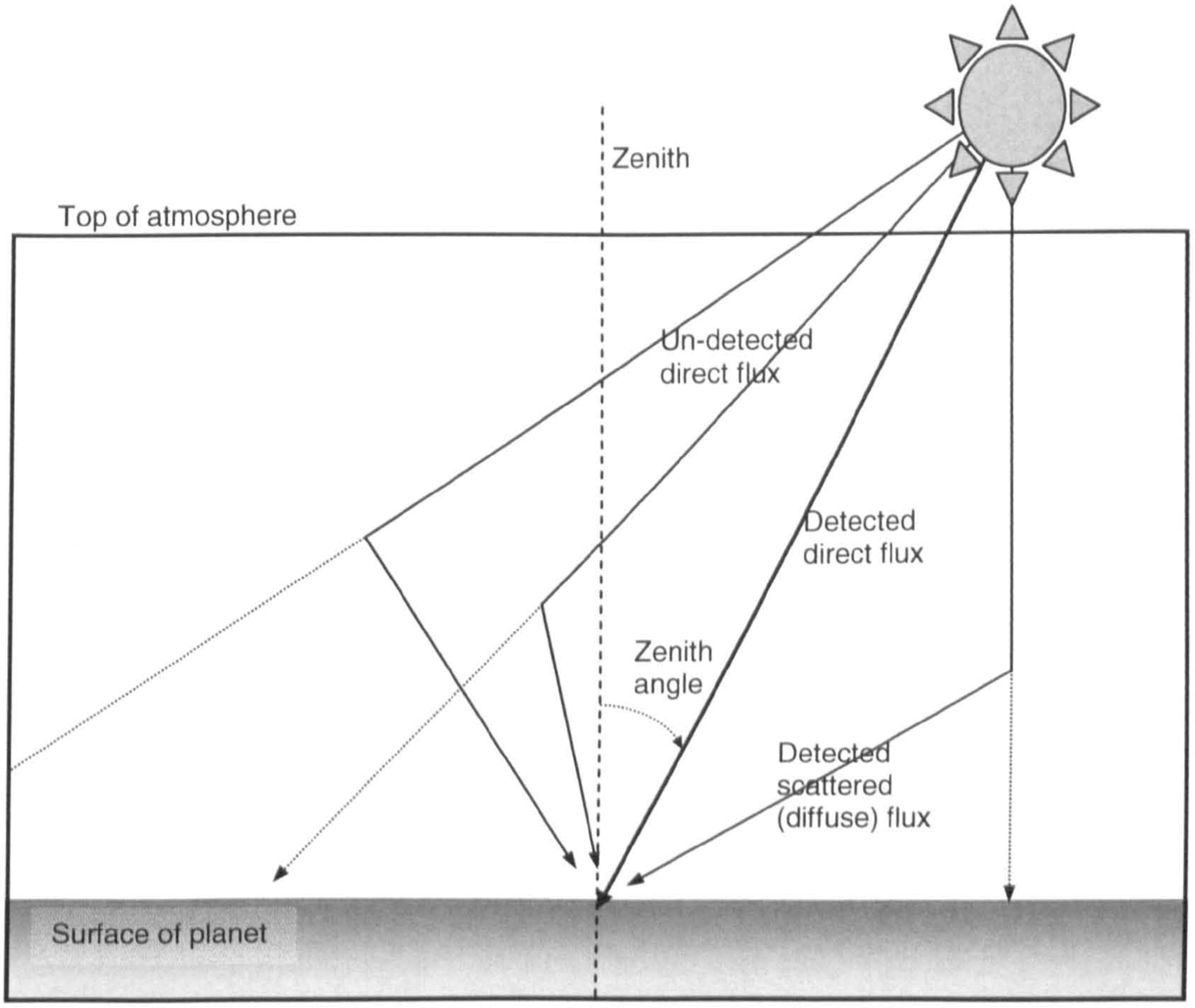

Figure 3.1 – Diagram illustrating how scattering in the atmosphere can create a laterally scattered diffuse flux resulting in enhancement of the locally detected surface flux.

3.1.1 Variation in total surface flux (λ = 180-1100 nm)

Figure 3.2 predicts how the total flux value incident at the martian surface varies under different atmospheric dust loading scenarios. It can be seen that for dust

optical depths of up to approximately $\tau = 3.0$ the combined flux value incident at the surface is greater than that initially incident at the top of the atmosphere, with the combined surface flux peaking at a value ~13% greater than the initial input flux at a dust optical depth of $\tau \sim 1.2$. Figure 3.2 also shows how the direct and diffuse components of flux vary with the optical depth of the atmosphere. At a dust abdundance of close to zero virtually no scattering of the incident flux occurs and the surface incident flux is comprised, as expected, almost completely of the direct component. Increasing the dust abundance leads to a rapid rise in the values of the diffuse component which, at an optical depth of approximately $\tau \sim 0.65$, surpasses the falling values of the direct flux in terms of the contribution made to the combined surface incident flux. At optical depths greater than $\tau \sim 3.0$ the dust abundance is sufficiently great that the combined flux incident at the surface has dropped below the value initially incident at the top of the atmosphere, i.e. the increasing dust column abundance is resulting in an increase in the dust absorption optical depth as well as the dust scattering optical depth and a significant portion of the flux is now being absorbed before it can reach the surface. By a dust optical depth of $\tau \sim 6.0$ the direct component of the surface flux is essentially zero and only 60% of the initially incident flux reaches the surface. A dust optical depth of $\tau = 6.0$ is very high but there is evidence to suggest that optical depths of $\tau > 5.0$ may occur during dust storm scenarios (Lewis et al., 1999).

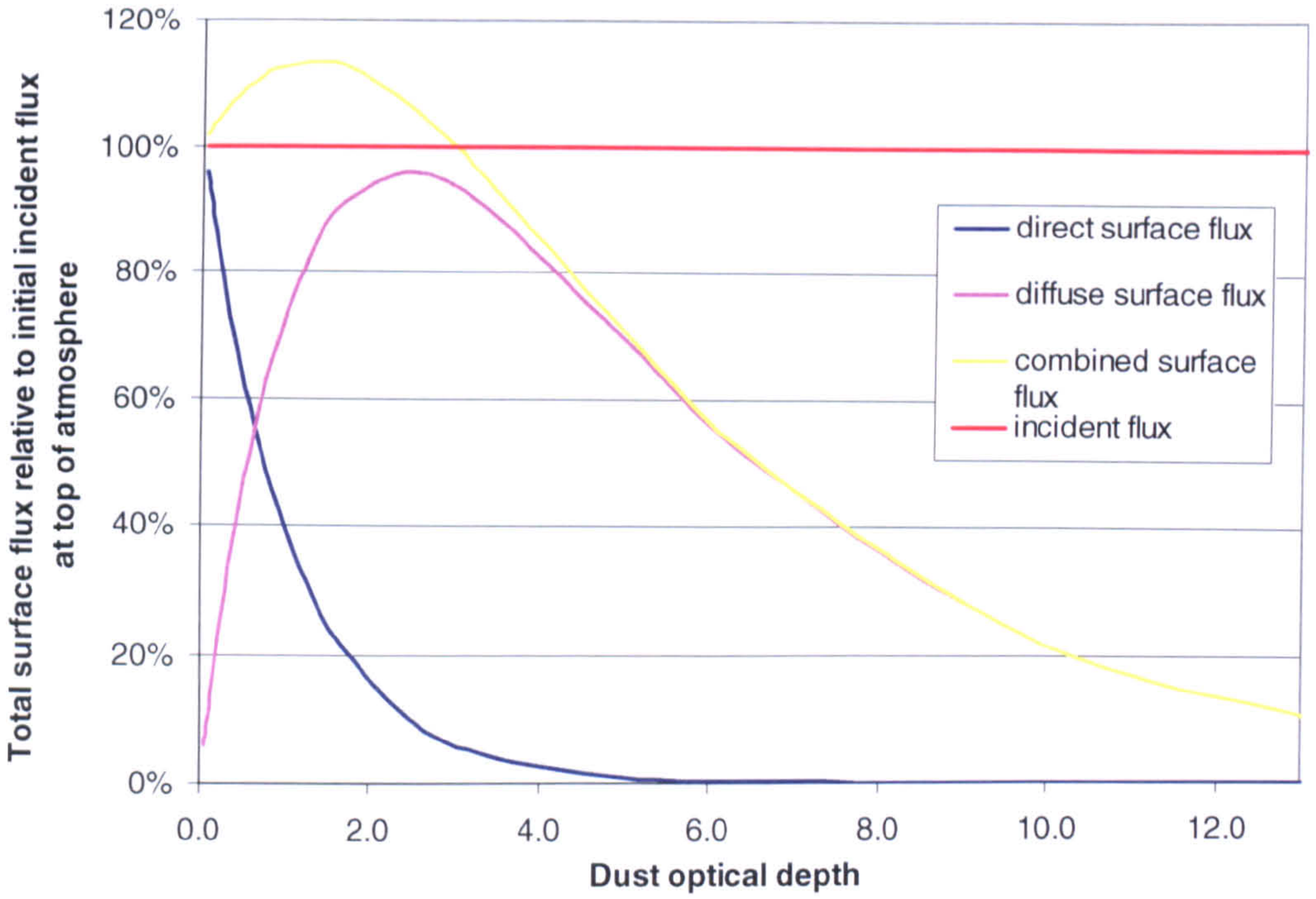

Figure 3.2 - The variation in the components of the total surface flux (180-1100 nm) at $l = 0^\circ$ and $L_s = 220^\circ$ with dust optical depth relative to the initial flux incident at the top of Mars' atmosphere

3.1.2 Variation in UV surface flux

Figure 3.3 describes the total UV regime (λ = 190 - 400 nm) surface flux and its direct and diffuse components. The low value of ω_0 for the dust aerosols at UV wavelengths, compared to the VIS and NIR wavebands also under consideration, means that the dust is much more absorbing at these wavelengths. Figure 3.3 shows how, owing to the lower occurrence of scattering events, the diffuse component of the surface flux remains small when compared to the overall picture presented in Figure 3.2. As the dust abundance increases there is no scattering enhancement of the combined surface flux to values greater than that initially incident at the top of the atmosphere; instead the UV total flux quickly decreases in value and falls to a value roughly half that of the initially incident value for dust optical depths of $\tau \sim$

1.7. Dust optical depths such as this are frequently reached during dust storm events but a more typical dust optical depth range of $\tau = 0.1$ to 0.5 yields reductions in the initially incident flux of up to approximately 20%. Under very heavy atmospheric dust loadings of dust optical depth of $\tau = 5.0$ or greater, such as have been observed to occur in large dust storms, the initial incident flux at UV wavelengths is predicted to attenuate by approximately 85%. This compares with a predicted attenuation of only approximately 30% for the incident flux summed across all wavelengths (λ = 180-1100 nm) at a dust optical depth of $\tau = 5.0$. The low scattering cross-section of the dust at these wavelengths also means that the direct component of the surface flux dominates over the diffuse component until dust optical depths of $\tau \sim 1.7$ are reached.

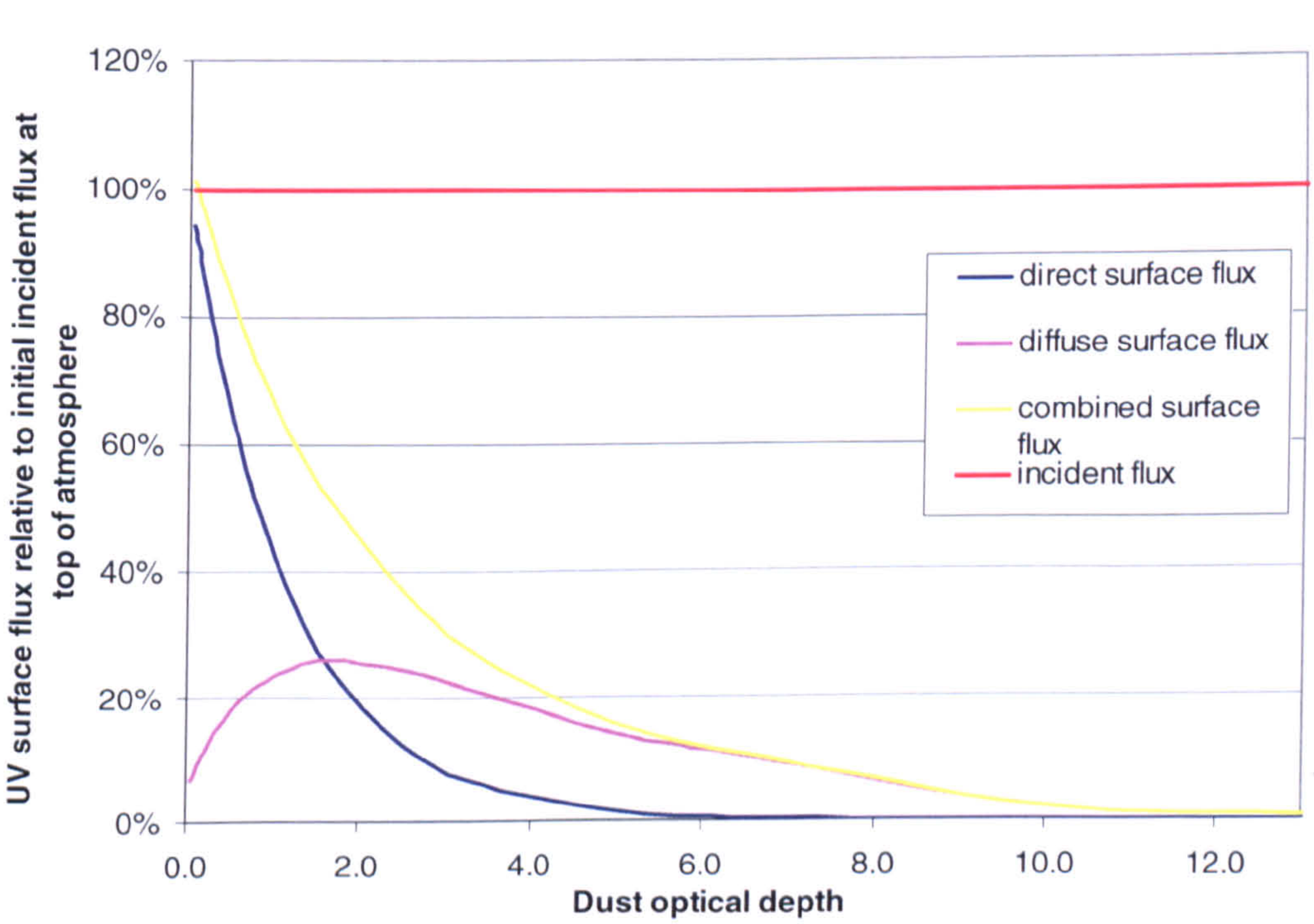

Figure 3.3 - The variation in the components of the UV surface flux (190-400 nm) at $l = 0°$ and $L_s = 220°$ with dust optical depth relative to the initial flux incident at the top of Mars' atmosphere

3.1.3 Variation in VIS surface flux

The value of ω_0 for the dust increases sharply in the VIS waveband (λ = 401–750 nm) leading to an increase in the scattering events occurring at these wavelengths. This can be seen from Figure 3.4 where the levels of the diffuse component of the surface flux are significantly enhanced in value over the levels seen at UV wavelengths (Figure 3.3). At dust optical depths less than approximately $\tau \sim 2.5$ the VIS combined surface flux values are enhanced through scattering to values greater than the initially incident flux, reaching a peak value of approximately 8% greater than the initial incident flux at a dust optical depth of $\tau \sim 1.0$. The diffuse component of the surface flux begins to dominate over the direct component at a dust optical depth of approximately $\tau \sim 0.7$.

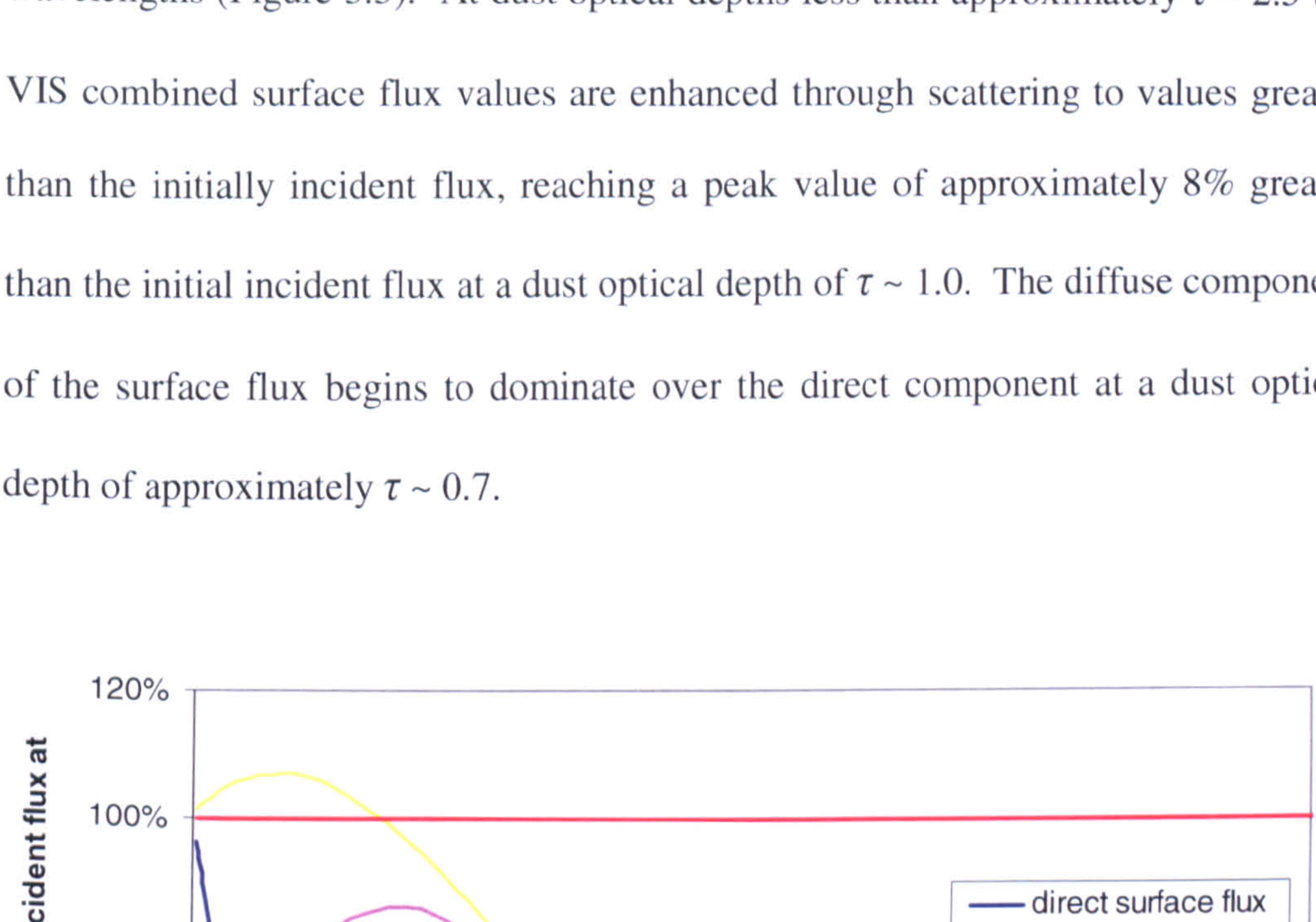

Figure 3.4 - The variation in the components of the VIS surface flux (401-750 nm) at $l = 0°$ and $L_s = 220°$ with dust optical depth relative to the initial flux incident at the top of Mars' atmosphere

3.1.4 Variation in NIR surface flux

At the NIR wavelengths (λ = 751 – 1100 nm) the dust is almost purely scattering presenting only a very small absorption cross-section to the incident flux. The high levels of scattering result in a significantly enhanced NIR surface flux where fluxes representing an approximately 50% increase over the initial incident flux are predicted to occur at a dust optical depth of τ ~ 1.7 (see Figure 3.5). Very little absorption of the incident flux by the dust at these wavelengths leads to the diffuse surface flux persisting at comparitively high values as the dust optical depth increases, i.e. photons tend to be preferentially scattered rather than absorbed and so can persist long enough to be detected at the surface. Dust optical depths of τ ~ 7.0 (very large, even for extreme storm scenarios) are predicted to be required before the combined surface flux is attenuated to 50% of the initially incident value. For comparison, at a dust optical depth of τ = 7.0 the UV surface flux and the VIS surface flux are only ~10% and ~38% respectively of the initial incident flux value. At NIR wavelengths the diffuse flux is predicted to become the dominant component of the total surface flux at a dust optical depth of τ ~ 0.5.

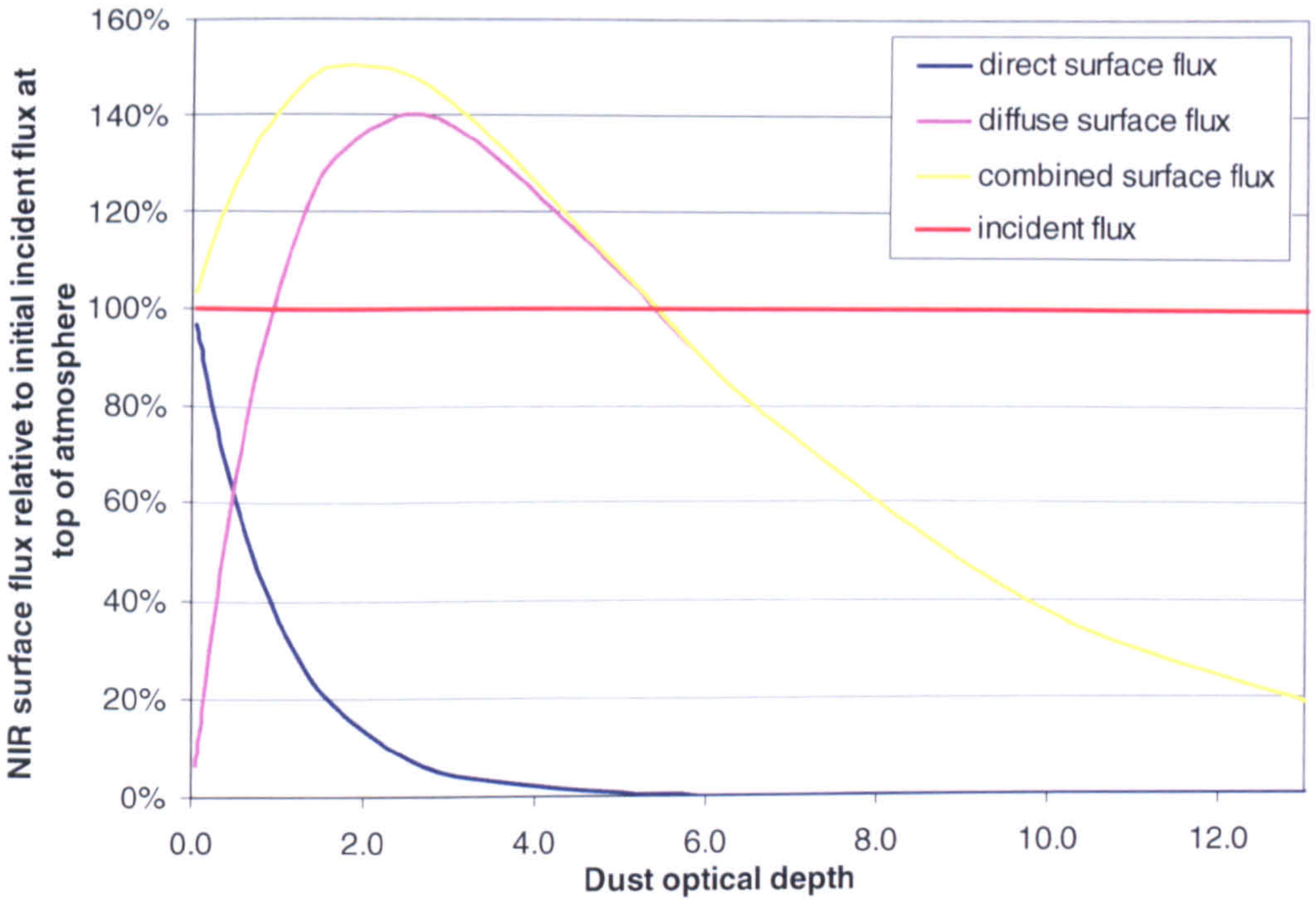

Figure 3.5 - The variation in the components of the NIR surface flux (751-1100 nm) at $l = 0°$ and $L_s = 220°$ with dust optical depth relative to the initial flux incident at the top of Mars' atmosphere

3.2 Global flux studies

By running the simulation multiple times and stepping through the values of surface latitude, l, (at intervals of 10°) and areocentric longitude, L_s, (at intervals of 15°) with each subsequent run, it is possible to use the simulation to characterise the UV-VIS-NIR environment across the surface of the planet and over the course of a Mars year. The simulations are performed under the conditions of a maximum ozone column abundance of 6.40×10^{15} cm^{-2} (based upon column abundance data taken from LeFevre et al. (2004)) and maximum ice cloud optical depth of $\tau_{cloud} = 0.5$, as previously defined (See Chapter 2 sections 2.1.5 and 2.1.7 for discussion of ozone and ice cloud distributions). Each study is repeated so that there are two datasets to compare, the first using the modelled average TES data and the modelled SPICAM

data for the dust aerosol and ice cloud aerosol distributions respectively and the second using the dust and ice cloud aerosol distributions returned by the TES instrument; as discussed in Chapter 2 sections 2.1.6 and 2.1.7. The first of these two scenarios, using the modelled data, will from here on be referred to as the MOD scenario and the second scenario, using the TES data will be referred to as the TES scenario. The purpose of this is to provide a comparison between the modelled data, which by its nature offers a generalised view of the important aerosol distributions, with data that represents the aerosol distributions over an actual and complete Mars year.

The dust optical depth of the study is varied between three scenarios; a 'low' dust scenario where the maximum dust optical depth value is $\tau = 0.1$, a 'typical' dust scenario where the maximum dust optical depth is $\tau = 0.5$, and a 'high' dust scenario where the maximum dust optical depth is $\tau = 1.0$. These values cover the range of optical depths likely to be encountered by a probe at the martian surface outside of the extreme conditions of a large dust storm, where optical depths have been recorded to exceed values of $\tau = 5.0$ (Lewis et al., 1999). The distributions of the dust and ice aerosols and the variable gas component are scaled depending on the latitude and L_s values input, as described in Chapter 2.

3.2.1 Initial incident flux at the top of Mars' atmosphere

Figure 3.6 shows the total irradiance incident at the top of the martian atmosphere, i.e. before any interaction with the atmosphere. The readings span one full martian orbit (L_s = 0-360°), and were generated at midday which corresponds to the peak

diurnal intensity for a full range of surface latitudes (for simplicity no diurnally varying components were incorporated into the model). The contour plot shows an approximately sinusoidal pattern resulting from the obliquity of Mars' rotational axis, meaning the polar regions of the planet only receive direct sunlight for roughly half the year. Another distinctive feature is the greater radiation intensities encountered in the second half of the martian year ($L_s > 180°$) caused by the high eccentricity of Mars' orbit (compared to that of the Earth) bringing the planet closer to the Sun during this period. The large difference between perihelion and aphelion distances leads to an increase in the solar radiation incident at the top of the atmosphere by approximately 46%. For comparison the variation in incident solar flux resulting from the difference between Earth's perihelion and aphelion values is only 7% (Lewis et al., 1993). When combined with Mars' axial tilt this results in the greatest intensities of radiation being focussed upon the southern hemisphere during this period.

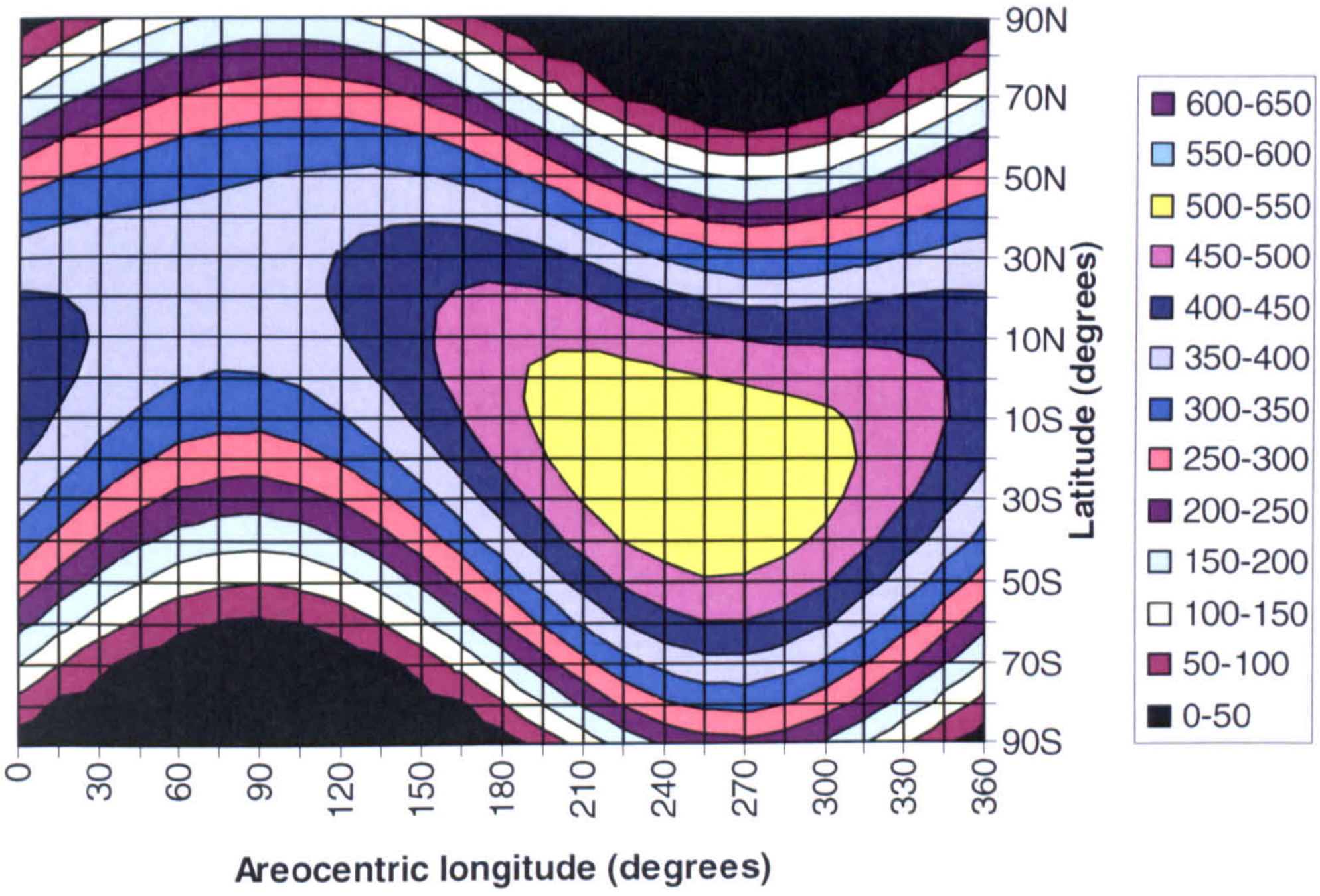

Figure 3.6 - Radiative flux incident at the top of Mars' atmosphere, integrated over 180-1100 nm, at midday over one Mars year as a function of latitude, l and areocentric longitude, L_s. Contours are in units of Wm^{-2}

3.2.2 Comparison of the MOD and TES scenarios

Figure 3.7 and Figure 3.8 show how this incident flux is modified through interaction with the atmosphere of Mars under the 'typical' dust scenario and using the modelled (MOD) and observed (TES) conditions respectively. Probably the most important feature to note is the predicted combined surface flux values incident at the planet's surface are actually higher than the initial incident values at the top of the atmosphere in some cases. This increase is caused by the addition of a scattered component to the flux, as described previously and therefore this increase is most pronounced in the regions where aerosol abundance is enhanced. For both the MOD and TES datasets increases on the order of ~20% are observed to occur around the equator corresponding to the increasing scattering caused by the ice cloud aerosols of the aphelion cloud belt (ACB). A similar effect is observed to occur during the

southern hemisphere summer where the greater volume of dust present in the atmosphere leads to predicted surface irradiation values on the order of ~12% greater than the initial incident flux.

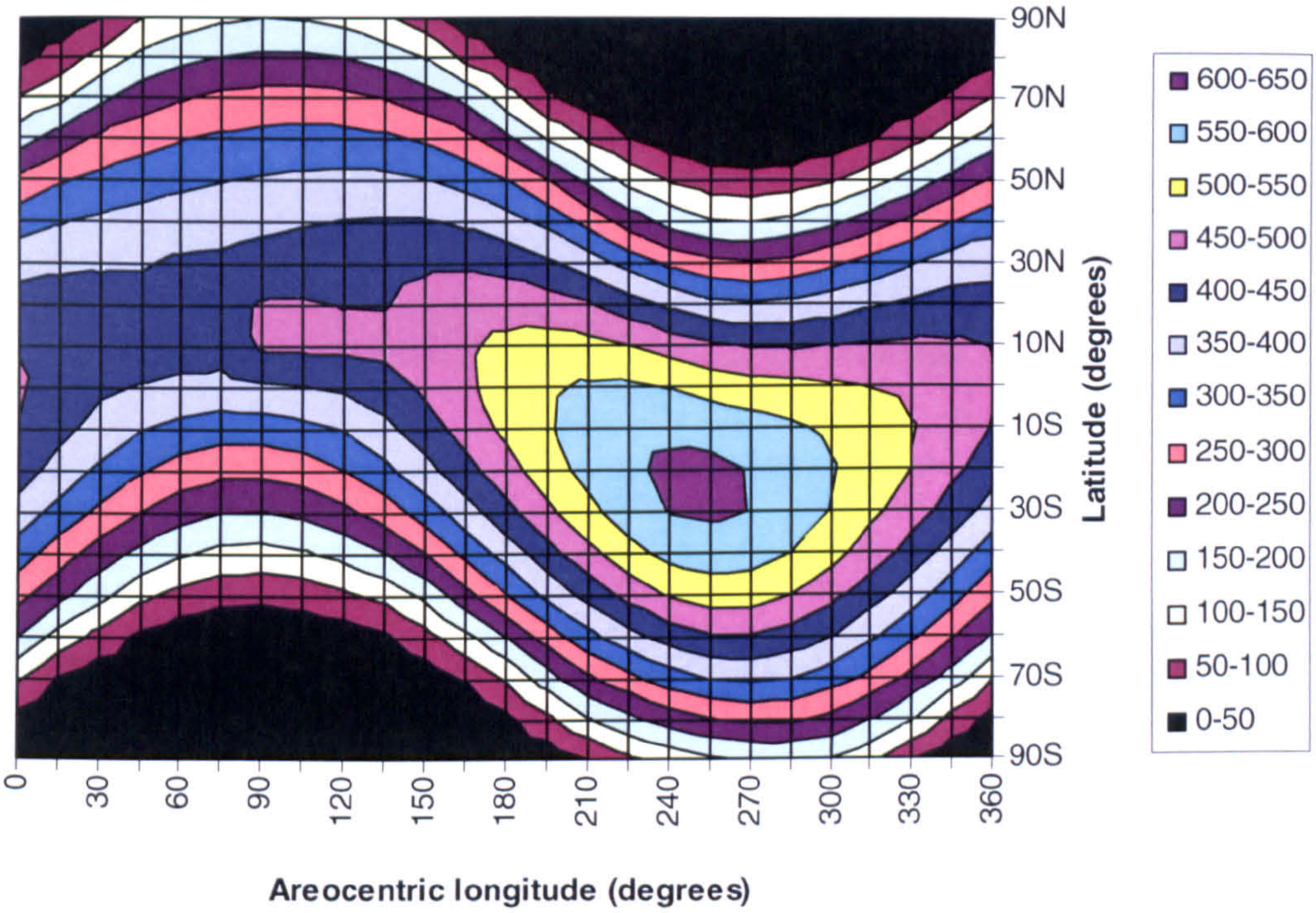

Figure 3.7 – MOD scenario: Combined (direct + diffuse) flux at the surface of Mars, integrated over 180-1100 nm, at midday under 'typical' dust loading over one Mars year as a function of latitude, *l* and areocentric longitude, L_s. Contours are in units of Wm^{-2}

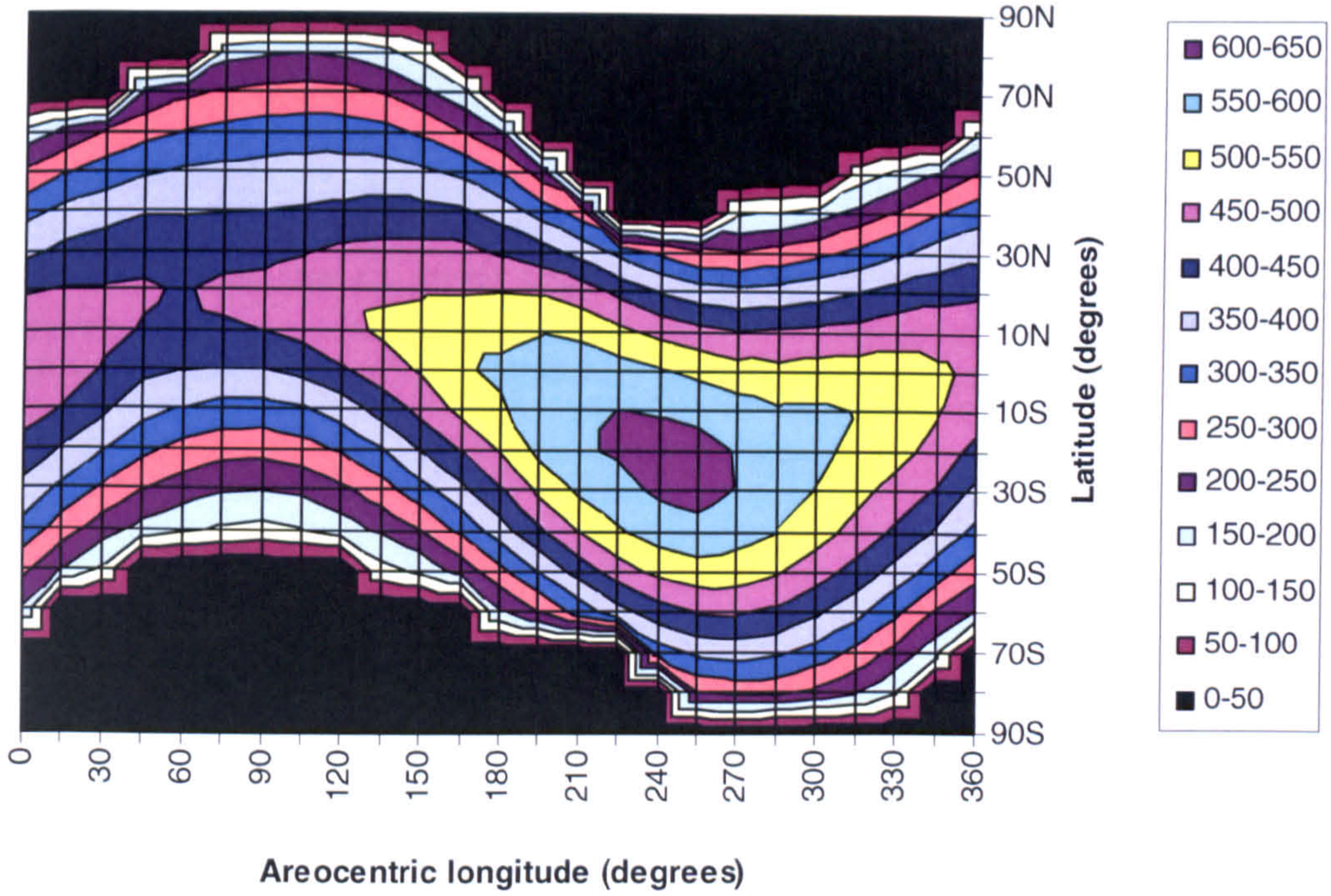

Figure 3.8 – TES scenario: Combined (direct + diffuse) flux at the surface of Mars, integrated over 180-1100 nm, at midday under 'typical' dust loading over one Mars year as a function of latitude, *l* and areocentric longitude, L_s. Contours are in units of Wm^{-2}

At L_s values where the atmospheric aerosol content is low the surface irradiation value tends to be lower than the value incident at the top of the atmosphere owing to the fact that scattering events are less common. The lowest dust abundances tend to occur at higher latitude and, as discussed in Chapter 2, at higher latitudes the increased airmass means the incident radiation encounters a much greater column abundance of atmosphere before reaching the surface of the planet.

It is easier to compare the datasets for the MOD and TES scenario resultant surface flux if the data is presented as values relative to the initial incident flux values. This is shown in Figure 3.9 (MOD scenario) and Figure 3.10 (TES scenario) which at first glance suggest the surface flux under both scenarios to be quite similar. The peak aerosol abundances of the ACB result in the greatest enhancement to the surface flux

under both scenarios although the extent of the aerosol peak, and therefore the enhanced flux, is greater in the TES data. The TES data, taken from Mars Year 25, does however show higher dust abundances either side of the maximum at L_s = 250° in the MOD data. The enhanced scattering here results in consistently higher surface irradiation values within 10-20° either side of the equator, with the percentage increase of the TES surface irradiation values compared to the incident irradiation being typically twice that of the MOD data.

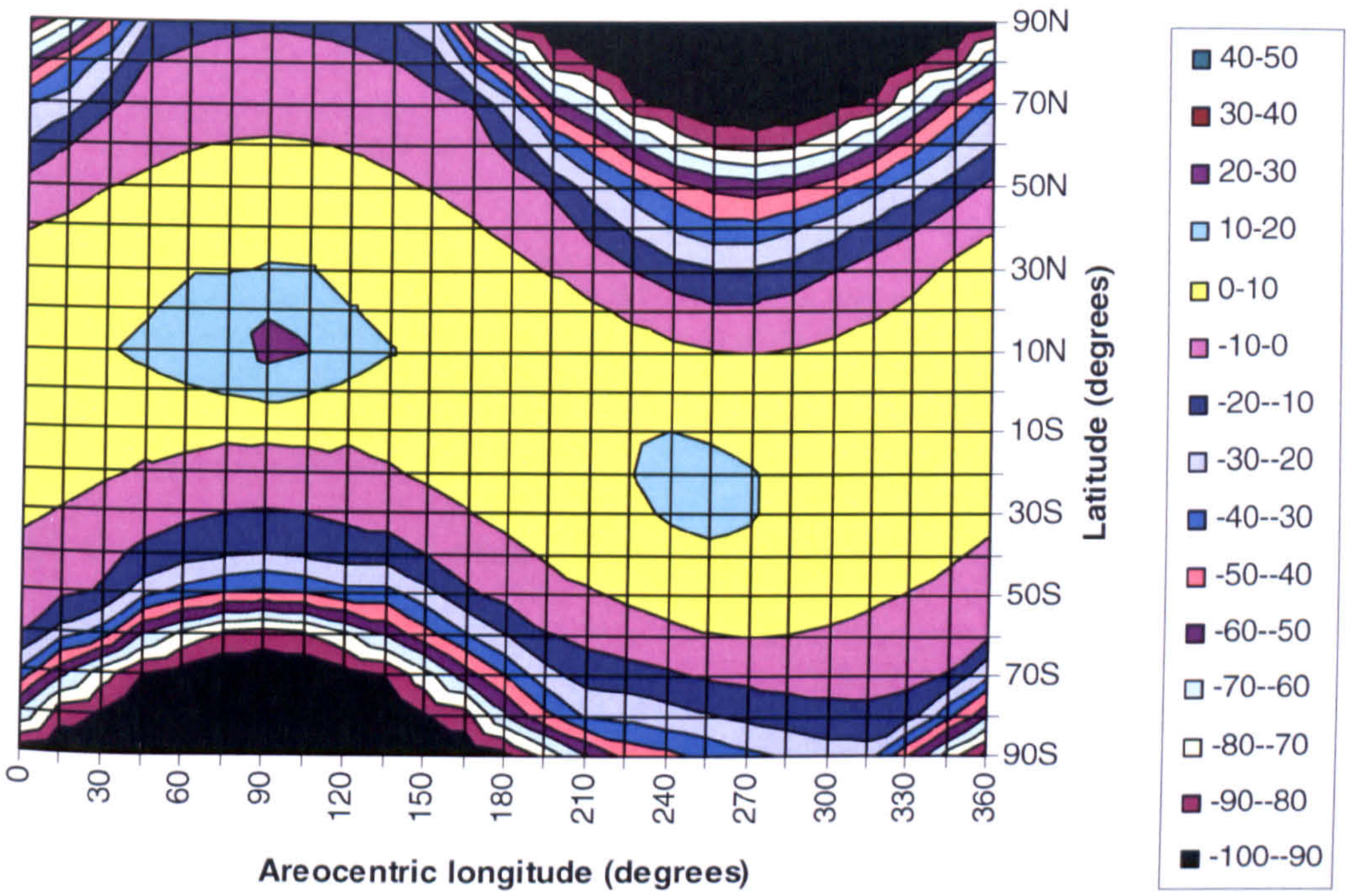

Figure 3.9 – MOD scenario: Percentage difference between initial incident flux at the top of Mars' atmosphere and combined (direct + diffuse) flux at the surface of Mars, both integrated over 180-1100 nm, at midday under 'typical' dust loading and over one Mars year as a function of latitude, *l* and areocentric longitude, L_s. Contours are in units of percent

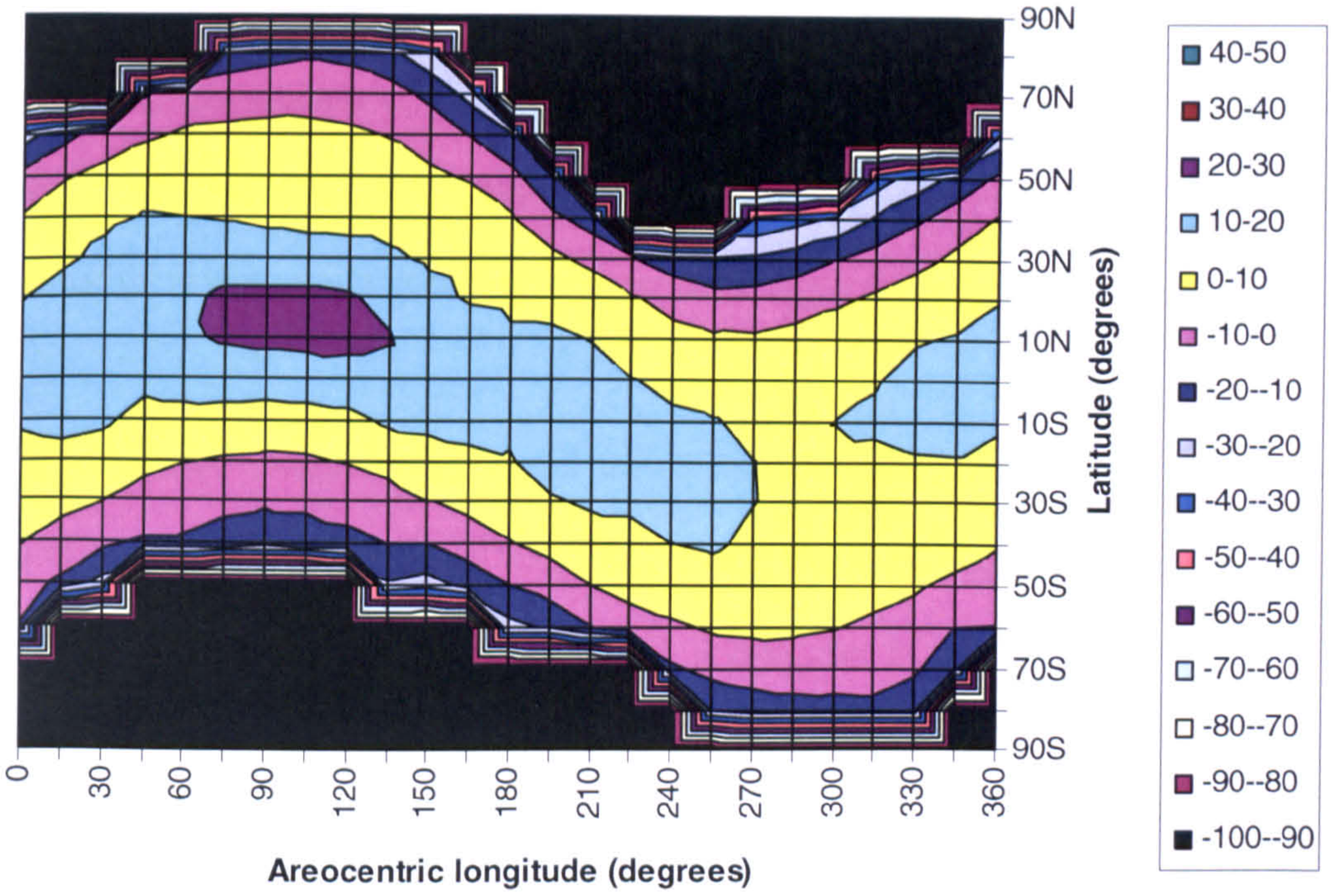

Figure 3.10 – TES scenario: Percentage difference between initial incident flux at the top of Mars' atmosphere and combined (direct + diffuse) flux at the surface of Mars, both integrated over 180-1100 nm, at midday under 'typical' dust loading and over one Mars year as a function of latitude, *l* and areocentric longitude, L_s. Contours are in units of percent

3.2.3 Global flux study at UV wavelengths

The wavelength dependent optical parameters discussed in Chapter 2 suggest that the UV band is where the most significant attenuation of the incident radiation by the dust aerosols will occur. The dust values for ω_0 within the UV wavelength band average $\omega_0 = 0.65$ compared to $\omega_0 = 0.8$ and 0.95 for the VIS and NIR bands respectively and so the dust exhibits a much greater absorption cross-section at these wavelengths than it does at VIS and NIR wavelengths. The results of the simulation support this, showing a decrease in UV flux which is most pronounced under the enhanced dust conditions of L_s values > 180°. Under the MOD conditions, the equatorial regions of Mars experience a maximum decrease in UV irradiation compared to the value incident at the top of the atmosphere, of approximately 20% at

L_s ~250° (near the dust maximum abundance). Travelling north from the equator an even greater attenuation of the UV flux is predicted; at a latitude of l = 30°N the UV flux is only ~40% of the initial incident value. South of the equator the UV attenuation is less pronounced with values ~18% of the initial incident value.

The percentage change in the initial incident flux reaching the surface at the UV wavelengths is given in Figure 3.11. For clarity only the data generated under the TES scenario, i.e. using actual observations, is presented here.

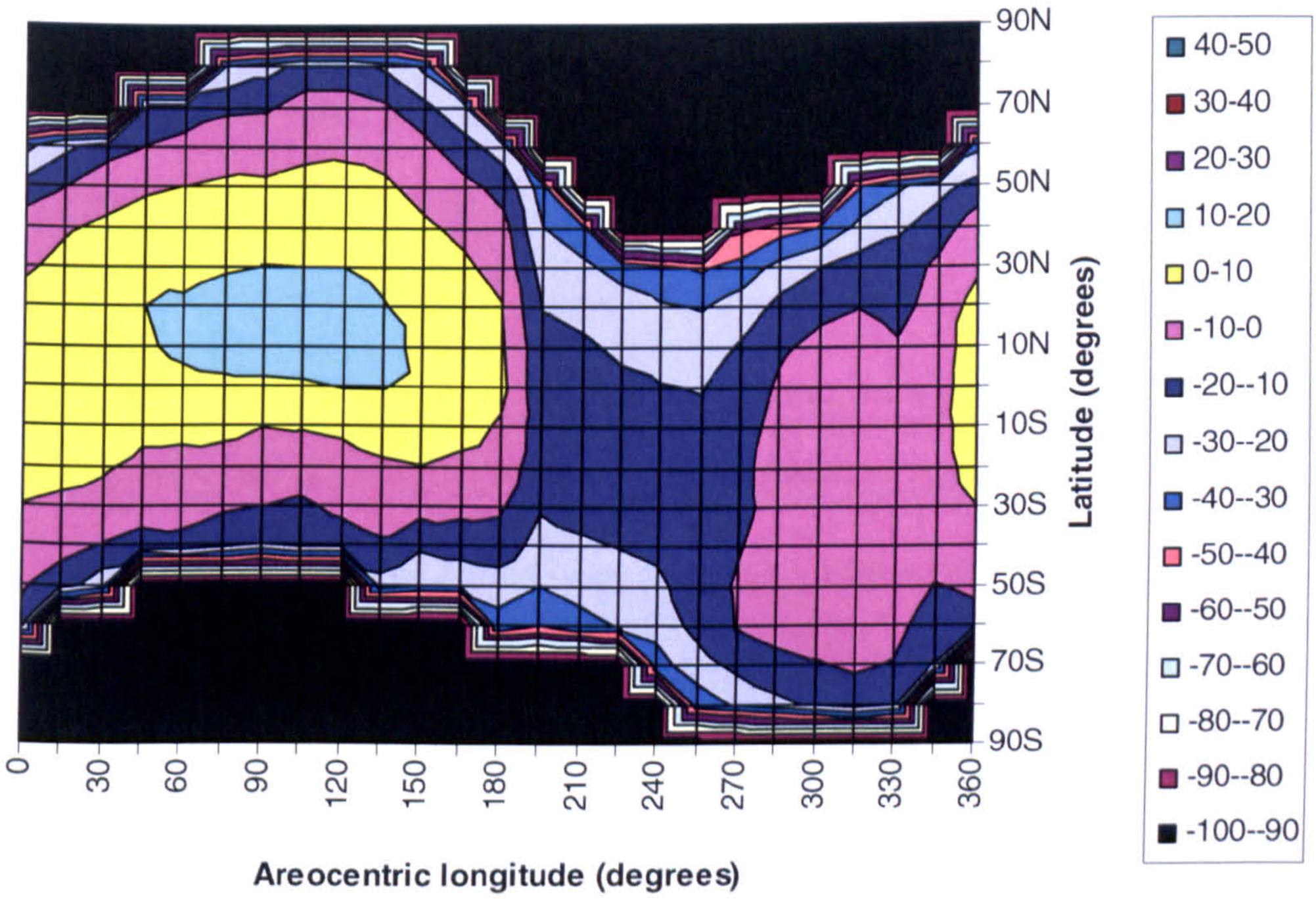

Figure 3.11 – TES scenario at UV wavelengths: Percentage difference between initial incident flux at the top of Mars' atmosphere and combined (direct + diffuse) flux at the surface of Mars at midday under 'typical' dust loading and over one Mars year as a function of latitude, l and areocentric longitude, L_s. Contours are in units of percent

The optical properties of the water ice clouds present in the martian atmosphere are significantly different from the dust aerosols at UV wavelengths. The ice cloud ω_0

value of 1.0 means that the ice cloud particle interaction with incident radiation is purely scattering unlike the significant absorption cross-section presented by the dust. The general anti-correlation between the distribution of dust and ice cloud aerosols creates regions where the dominant aerosol interaction is with ice cloud particles. These regions of intense scattering have the opposite effect of the regions where dust abundance is high, i.e. they enhance the value of the surface flux over the initial incident value.

In the MOD scenario, where the ice cloud aerosol distribution is based on SPICAM observations, the enhancement of the UV flux caused by ice cloud interaction is comparatively low and restricted to a small range of latitude and L_s values (approximately l = 10-20°N and L_s = 60-120° respectively). A maximum increase of ~7% is predicted over the initially incident flux occurring at latitude and L_s values of l ~ 10°N and L_s = 90° respectively. The TES scenario, with an ice cloud distribution taken from TES observations made in MY25, has the ice cloud particles distributed over a much greater range of latitude and L_s values. Under this scenario the relative increase in the UV surface flux is much greater, with the highest regions of UV flux reaching values ~14% greater than the initial incident flux. As with the MOD scenario the largest increases in the UV surface flux coincide with the occurrence of the ACB but the increased spatial and temporal distribution of the ACB under the TES scenario mean that an enhanced UV surface flux is predicted for latitudes of l ~ 20°S to 50°N and across a range of L_s = 0-180°.

3.2.4 Global flux study at VIS wavelengths

At visible wavelengths the scattering cross-section presented by dust is greater than that in the UV wavelength band, with an average ω_0 value of approximately 0.8 while the ω_0 value for the ice cloud aerosols remains at 1.0. Therefore, as discussed above, the enhanced scattering (owing to the dust) leads to an increase in the predicted surface flux, relative to the flux initially incident at the top of the martian atmosphere, under both dusty conditions and where ice cloud aerosols are present.

The percentage change in the initial incident flux reaching the surface at the VIS wavelengths is given in Figure 3.12. For clarity only the data generated under the TES scenario, i.e. using actual observations, is presented here.

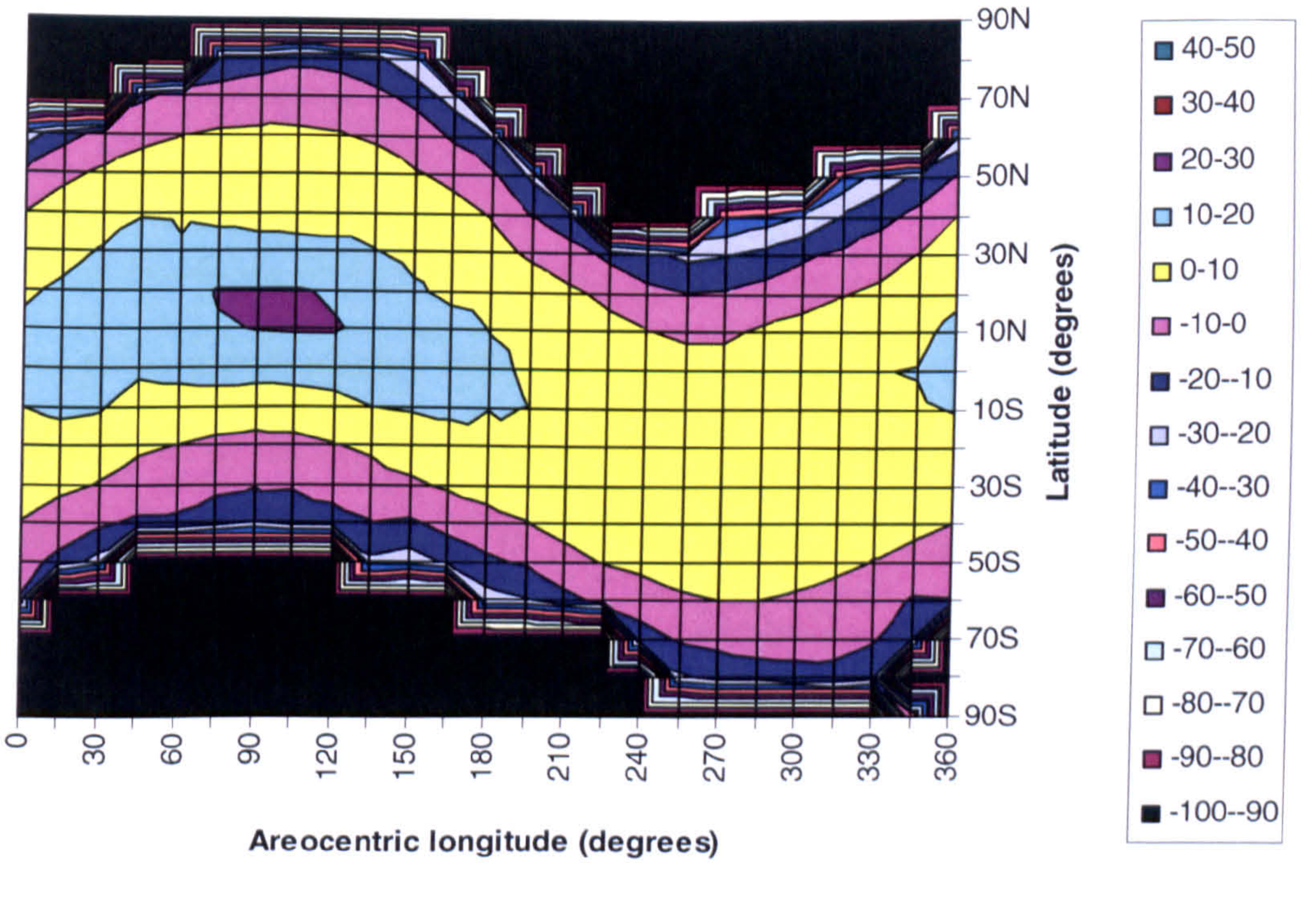

Figure 3.12 – TES scenario at VIS wavelengths: Percentage difference between initial incident flux at the top of Mars' atmosphere and combined (direct + diffuse) flux at the surface of Mars at midday under 'typical' dust loading and over one Mars year as a function of latitude, l and areocentric longitude, L_s. Contours are in units of percent

For the MOD scenario, the maximum increase in the VIS surface flux owing to dust scattering occurs in the southern summer time, around perihelion and at a latitude of *l* ~ 20°S. The maximum VIS surface flux here is predicted to be approximately 7% greater than the initial incident flux. Enhanced surface fluxes are predicted throughout a latitude range beginning at the equator and stretching to around 50°S throughout the southern summer time.

In the northern summer time it is the ice cloud aerosols that dominate the scattering and the surface incident VIS flux is again enhanced over the value initially incident at the top of the atmosphere. Here increases of up to approximately 20% are predicted over the initial values of the incident flux and these occur at a latitude value of $l \sim 10°N$ and an $L_s = 90°$. Lower but still significant enhancements to the initial flux are predicted up to latitudes of $l \sim 40°N$.

Identical trends are observed in the data produced by the TES scenario except that, owing to the maximum dust abundances occurring earlier in the year, the maximum enhancements in the incident VIS flux are present at lower L_s values than for the MOD scenario. The value of VIS flux here is also predicted to be a few percent higher with values of a ~8-9% increase over the initial incident flux predicted.

The TES scenario maximum increase in the flux owing to the ice cloud aerosols is similar to that in the MOD scenario at ~20% above the initial incident flux. However the greater extent of the ice cloud cover in the TES scenario compared to the MOD scenario means values at, or close to, the maximum increase are predicted across a more extensive range of latitude and L_s values ($L_s = 360°$-$180°$ and $l = 30°N$

to 10°S compared to L_s = 35°-120° and l = 30°N to the equator for the TES and MOD scenarios respectively).

The dust and ice cloud aerosol distributions for the TES scenario feature more of an overlap than in the MOD scenario. In the MOD scenario, the situation is simplified to two almost distinct regions; the southern hemisphere in summer where there are dust aerosols and no ice cloud aerosols, and the northern hemisphere summer where there are ice cloud aerosols and fewer dust aerosols. In the TES scenario, these two regions exist but the transition between them is less distinct (as expected in reality), leading to comparatively higher aerosol optical depths around the equatorial regions at the end of the northern summer/start of the southern summer. In turn this leads to enhanced surface flux values being predicted at these L_s values under the TES scenario, up to approximately 10% (compared to the MOD scenario of up to approximately 5%).

3.2.5 Global flux at NIR wavelengths

The general trend in surface flux value predicted at the UVIS simulation's NIR wavelengths is very similar to those seen in the VIS wavelengths. However the scattering cross-section presented by the dust increases again at NIR wavelengths with an average ω_0 value of ~ 0.95; approaching the 100% scattering ω_0 value of the ice cloud aerosols which is exhibited at these wavelengths. This increased scattering adds a significant component to the surface flux as the value of the direct NIR flux is supplemented by radiation scattered into the observed path.

The percentage change in the initial incident flux reaching the surface at the NIR wavelengths is given in Figure 3.13. For clarity only the data generated under the TES scenario, i.e. using actual observations, is presented here.

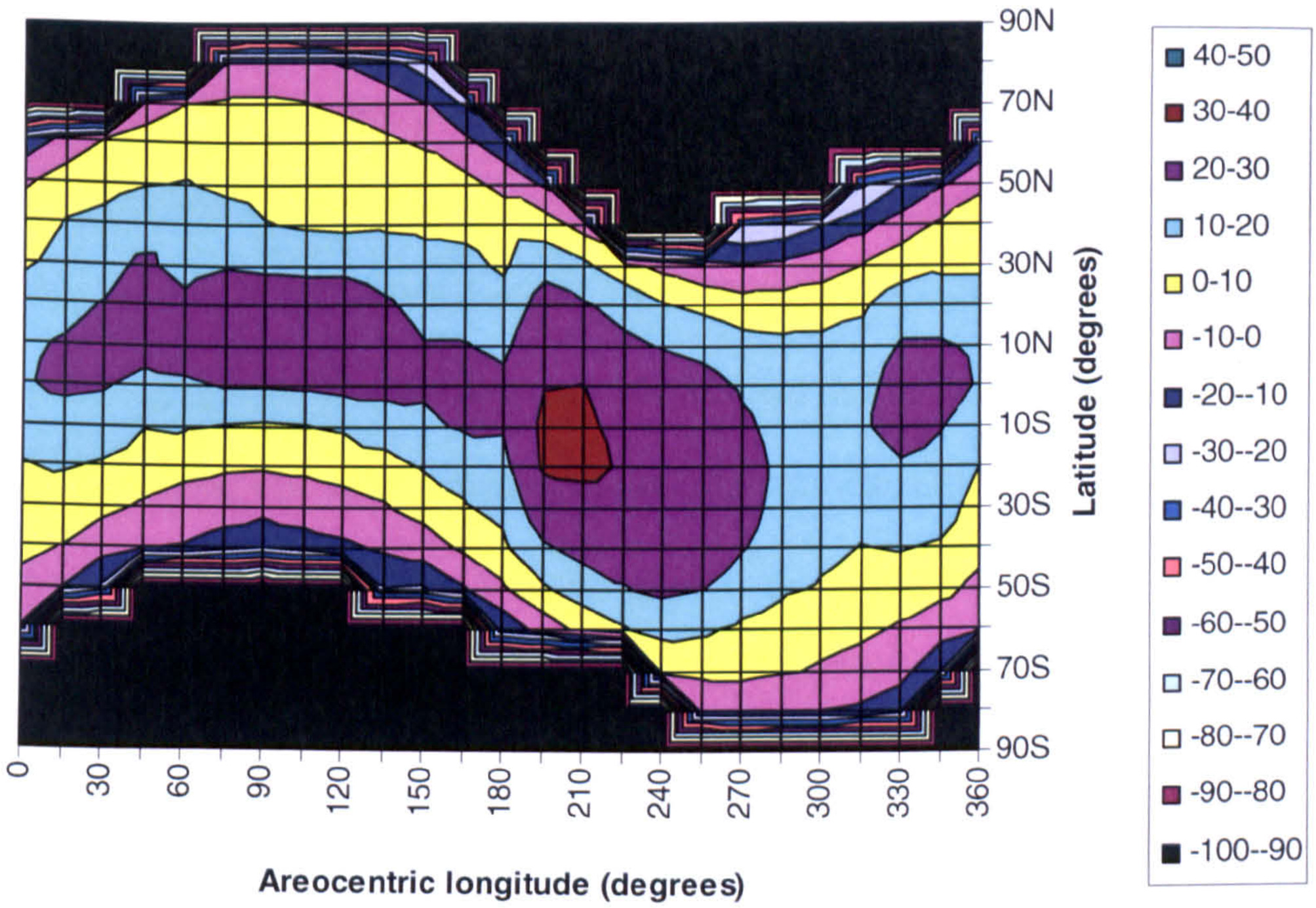

Figure 3.13 – TES scenario at NIR wavelengths: Percentage difference between initial incident flux at the top of Mars' atmosphere and combined (direct + diffuse) flux at the surface of Mars at midday under 'typical' dust loading and over one Mars year as a function of latitude, l and areocentric longitude, L_s. Contours are in units of percent

Under both the MOD and the TES scenarios enhanced surface NIR fluxes are predicted in the latitude range from l = 70°N to 20°S in northern summer and from l = 20°N to 70°S in southern summer time. Under the MOD scenario, during the dusty southern summer time the maximum value of the NIR surface flux represents approximately a maximum of a 28% increase over the flux incident at the top of the atmosphere, while under the TES scenario a maximum increase of approximately 30% is predicted. In the northern summer time under the MOD scenario the

maximum increase in the NIR flux is predicted to be approximately 33%, coinciding with the peak column abundance of the modelled ACB. The corresponding maximum increase in NIR flux predicted under the TES scenario is approximately 28%.

As with the VIS wavelengths the surface flux values predicted to occur at the transition between northern summer and southern summer time are greater under the TES scenario than the MOD scenario. The MOD scenario predicts a surface flux enhanced by up to 16% over the initially incident value, while the TES scenario predicts a surface flux enhancement of up to 30% over the initially incident value.

3.3 Potential landing site studies

One of the most critical aspects of a surface mission to Mars is the selection of the landing site. This usually involves performing a trade-off between selecting a site that will generate the best science return from the mission and a site where the surface probe can safely land and operate. In the following study, the simulation is used to examine the annual and diurnal variation in the surface flux at some of the landing sites that were under consideration for the now delayed ExoMars and some of which are still being considered for NASA's forthcoming MSL mission. Details of the potential landing site latitudes and longitudes are given in Table 2. Figure 3.14 shows a topographic map of the surface of Mars created from data taken by the Mars Orbiter Laser Altimeter (MOLA) on board Mars Global Surveyor. It includes the approximate locations of the landing sites listed in Table 2 and of the landing sites for the Viking, MPF and MER missions.

Site Name	Latitude	Longitude
Nili Fossae	23°N	80°E
Mawrth Vallis	22°N	340°E
Gale Crater	5°N	137°E
Meridiani Planum	0.2°N	360°E
Holden Crater	26°S	330°E

Table 2 – Potential landing sites for future surface missions

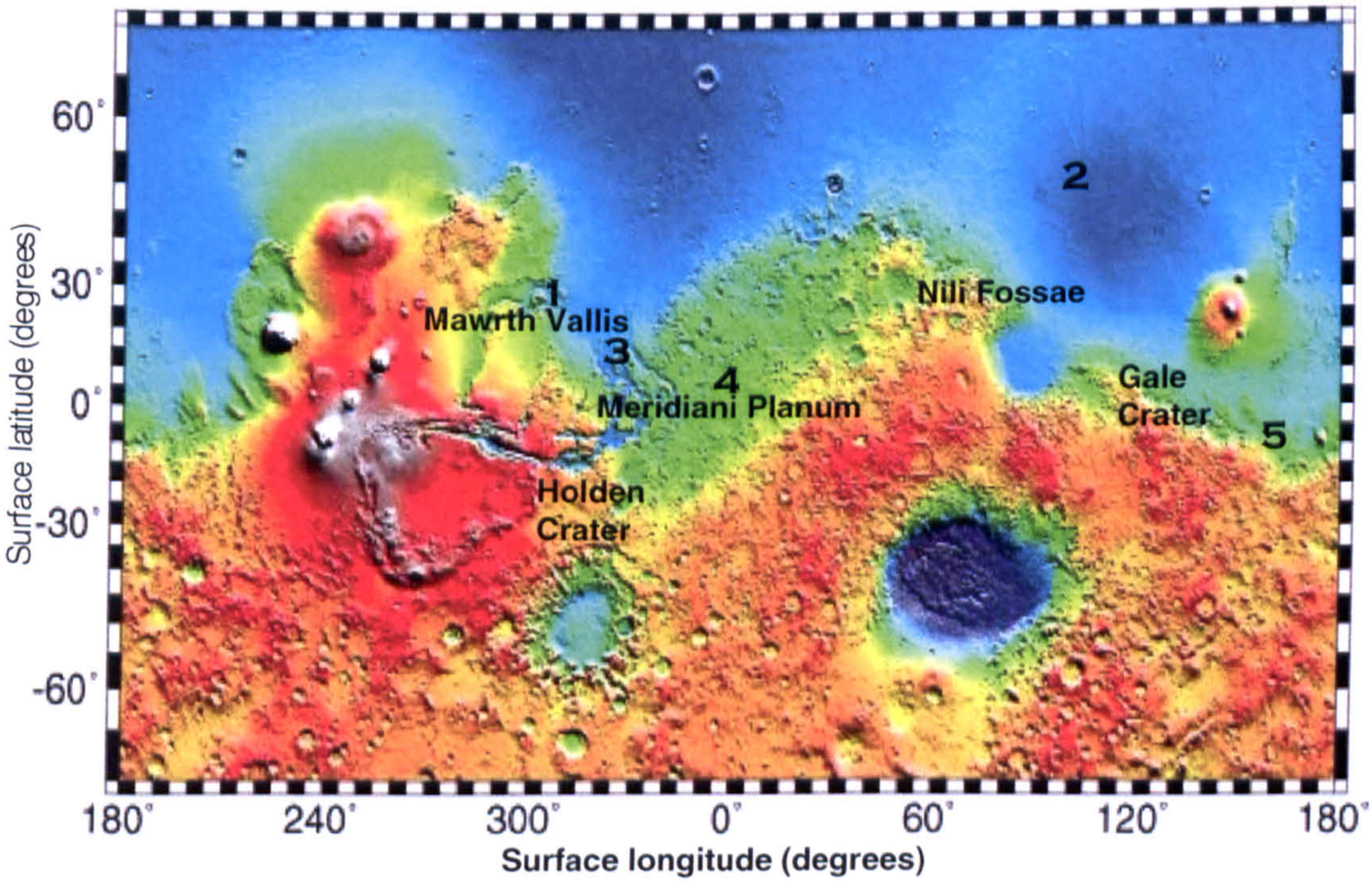

Figure 3.14 – Topographic map of the surface of Mars produced from MOLA data and showing the approximate positions of the proposed landing sites and the landing sites of Viking 1 (1), Viking 2 (2), MPF (3), MER Opportunity (4) and MER Spirit (5). Red regions are high ground and blue regions are low lying.

3.3.1 Annual flux variation at potential landing sites

Figure 3.15 (MOD scenario) and Figure 3.16 (TES scenario) display the total surface irradiation predicted over the course of a Mars year at a range of latitudes covering the possible landing site latitudes given in Table 2. The flux values are those predicted at local noon under the 'typical' dust scenario.

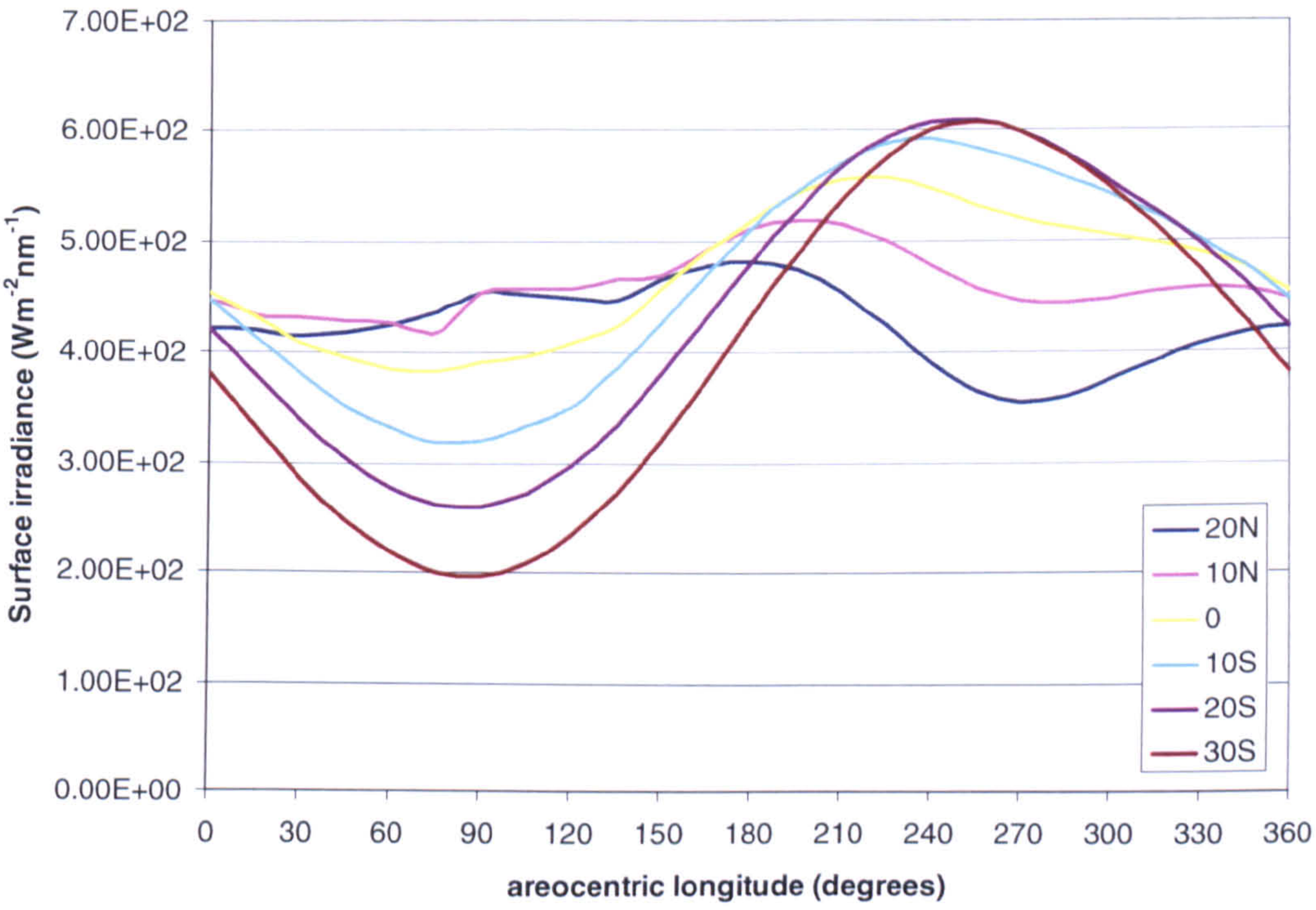

Figure 3.15 – MOD scenario: Comparison of the combined (direct + diffuse) surface flux over one year covering the latitude range of the potential landing sites given in Table 2

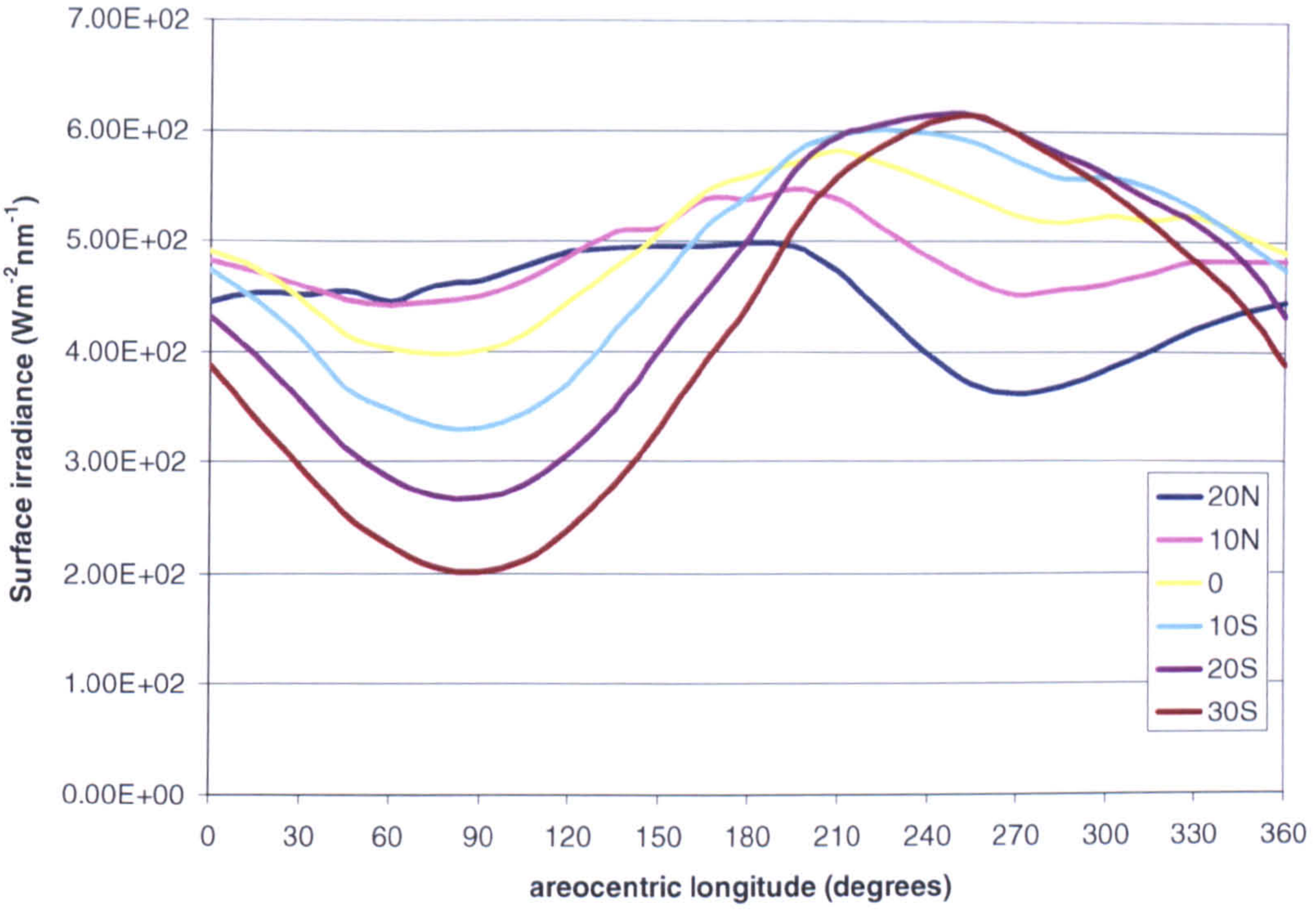

Figure 3.16 – TES scenario: Comparison of the combined (direct + diffuse) surface flux over one year covering the latitude range of the potential landing sites given in Table 2

It is immediately obvious from both figures that the southerly latitude values being considered exhibit a large variation in the surface flux received across the year. Owing to the tilt of Mars' rotational axis and the elliptical nature of the planet's orbit, the southern hemisphere is angled towards the Sun at perihelion and away at aphelion. This results in the southern hemisphere receiving high incident flux values in the southern summer time and correspondingly low flux in the winter. Table 3 contains values for the ratio of the maximum predicted total surface flux value to the minimum predicted surface flux (λ = 190-1100 nm). Both the MOD and TES scenarios predict nearly identical results (within the inherent errors) and the large variation between the maximum and minimum surface flux values encountered at the southerly latitudes can be seen. The most stable latitude in terms of incident flux variation appears to be l = 10°N.

Latitude (degrees)	$Flux_{max}/Flux_{min}$ (MOD scenario)	$Flux_{max}/Flux_{min}$ (TES scenario)
20N	1.35	1.38
10N	1.24	1.24
0	1.45	1.46
10S	1.85	1.82
20S	2.34	2.30
30S	3.08	3.04

Table 3 – Ratio of the annual surface flux maximum with the annual surface flux minimum. Flux values taken at midday under the 'typical' dust scenario for both the MOD and TES scenarios

3.3.2 Diurnal flux variation at potential landing sites

The model developed here can also simulate the irradiance at the planet's surface over the course of a sol. Under the current operating the parameters the UVIS simulation will always return an irradiance variation function which is symmetrical about local noon, as the model does not incorporate any local-time dependent parameters. However, important information can still be gained from studying these spectra as they contain information on the relative variation of the diffuse and direct fluxes.

3.3.2.1 Mawrth Vallis and Nili Fossae

Centred at an approximate latitude of $l = 22°N$, Mawrth Vallis is a large erosion channel cut from the martian surface which shows evidence of having been carved by flowing water. For most of its length of approximately 640 km, the channel

maintains a width of around 15 km suggesting the occurrence of a sizeable and prolonged outflow event. Orbital observations have detected extensive deposits of clay minerals (phyllosilicates) along the course of the Mawrth Vallis (Bishop et al., 2008) and it is thought that these minerals were formed in environments where significant quantities of water were present. As well as acting as a marker for potential past aqueous environments, the presence of phyllosilicates are of interest for the clues that might be found within them relating to the existence (or otherwise) of extant martian life (Ehlmann et al., 2008). The fact that these clay minerals appear to be located between other sedimentary layers potentially suggests cycles of wet and dry periods and adds another interesting twist to the geological history of this region. Further evidence for the flow of liquid water can be found along the base and the sides of the Mawrth Vallis; these features include ridges and terraces compatible with flooding scenarios and also smaller scale channels and gullies eroded from the main channel slopes.

The Nili Fossae features are located at roughly the same latitude as the Mawrth Vallis but are separated by approximately 60° of longitude across the martian surface. They are a series of troughs most likely formed through the sinking of the martian crust between a series of fault features. The troughs are each about 500 m deep and the largest has a diameter of about 26 km. Volcanic activity appears to have covered the floors of the troughs with lava flows but subsequent meteorite impact craters have excavated away the volcanic rock in a number of places exposing the underlying rocks. Orbital observations have shown that these areas and also the ejecta thrown out from them during the impacts appears to contain significant quantities of phyllosilicate clay minerals (Mustard et al., 2007, Mangold et al., 2007).

Figure 3.17 and Figure 3.18 show the diurnal variation in the surface flux for a latitude value of l = 22°N and L_s values of 90° (the northern summer solstice) and 270° (the southern summer solstice) respectively, under the 'typical' dust scenario. The direct and diffuse components that combine to form the total surface flux are also shown. It can be seen in Figure 3.17 that the diffuse component of the flux is dominant over the direct component in this scenario, a situation resulting from the high level of scattering caused by the presence of the aphelion cloud belt.

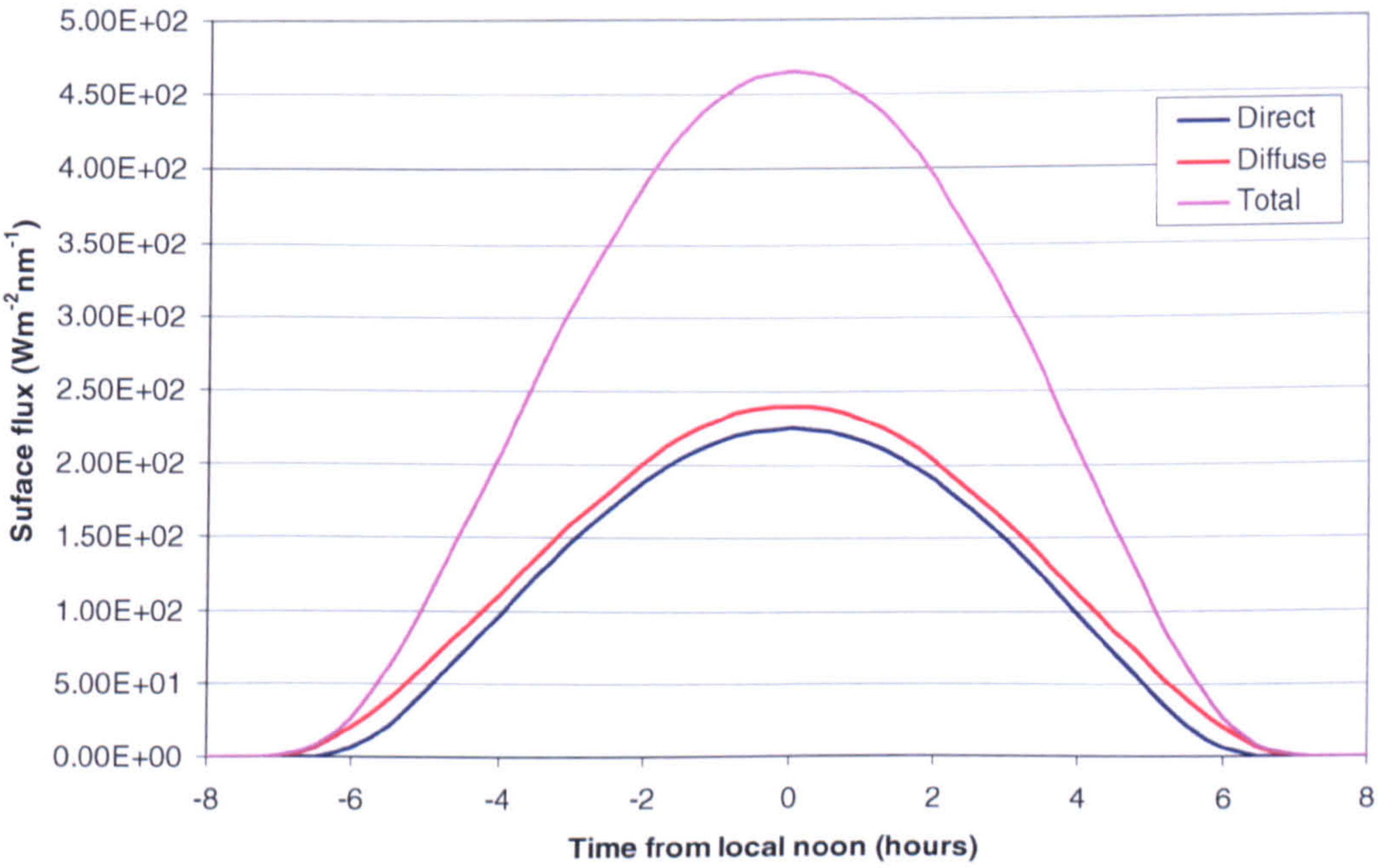

Figure 3.17 – TES scenario: Diurnal variation in surface flux components at l = 22°N and L_s = 90° under 'typical' dust scenario.

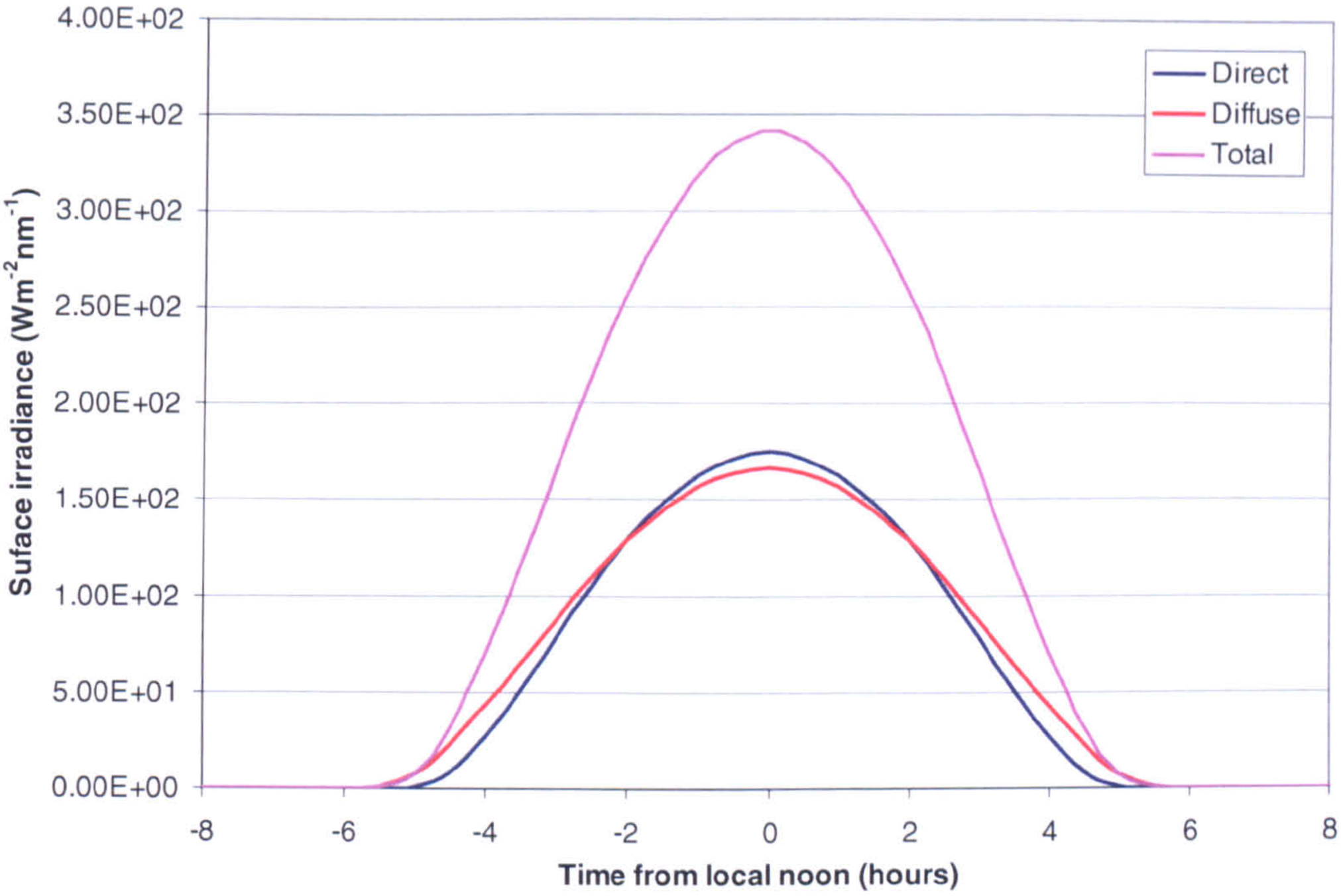

Figure 3.18 – TES scenario: Diurnal variation in surface flux components at l = 22°N and L_s = 270° under 'typical' dust scenario.

In Figure 3.18 corresponding to the dusty southern summer, the elevated levels of dust also create a significant diffuse component which dominates over the direct component at higher solar zenith angles. The direct component is predicted to dominate for a couple of hours either side of midday but once the Sun has dropped sufficiently low in the sky the main source of the surface flux is that reaching the surface via scattering processes. Mawrth Vallis is the most northerly of the proposed landing sites which means a greater column abundance of ice cloud aerosols was observed in the TES data compared to the other proposed landing sites. It is the higher scattering optical depth resulting from the combination of the high dust aerosol abundance and comparatively high ice cloud aerosol abundance that leads to a strong diffuse component predicted at this L_s value. It will be seen that at the more southerly landing sites, where dust abundances are comparable but ice cloud aerosols

are much lower in abundance, that the diffuse component of the surface flux is much weaker.

3.3.2.2 Meridiani Planum

Straddling the martian equator around the Prime Meridian, Meridiani Planum was the landing site for NASA's Opportunity rover which has been successfully studying the surface environment there for more than two martian years. Orbital observations of the region detected significant deposits of the crystalline iron mineral haematite, the presence of which was confirmed by Opportunity. The haematite is located in a sedimentary rock formation and takes the form of small spherical concretions held in the matrix of the surrounding rock. This, amongst other features such as an abundance of sulphate rich minerals, is indicative of Meridiani Planum having undergone an extended period of exposure to aqueous conditions of high salinity and acidity (Squyres et al., 2006b).

Figure 3.19 shows the predicted diurnal variation seen during the maximum ice aerosol abundances of the ACB. The high level of scattering across all wavelengths caused by the ice cloud aerosols results in a strongly dominant diffuse component of the surface flux which is approximately 20% greater than the corresponding direct component of the surface flux.

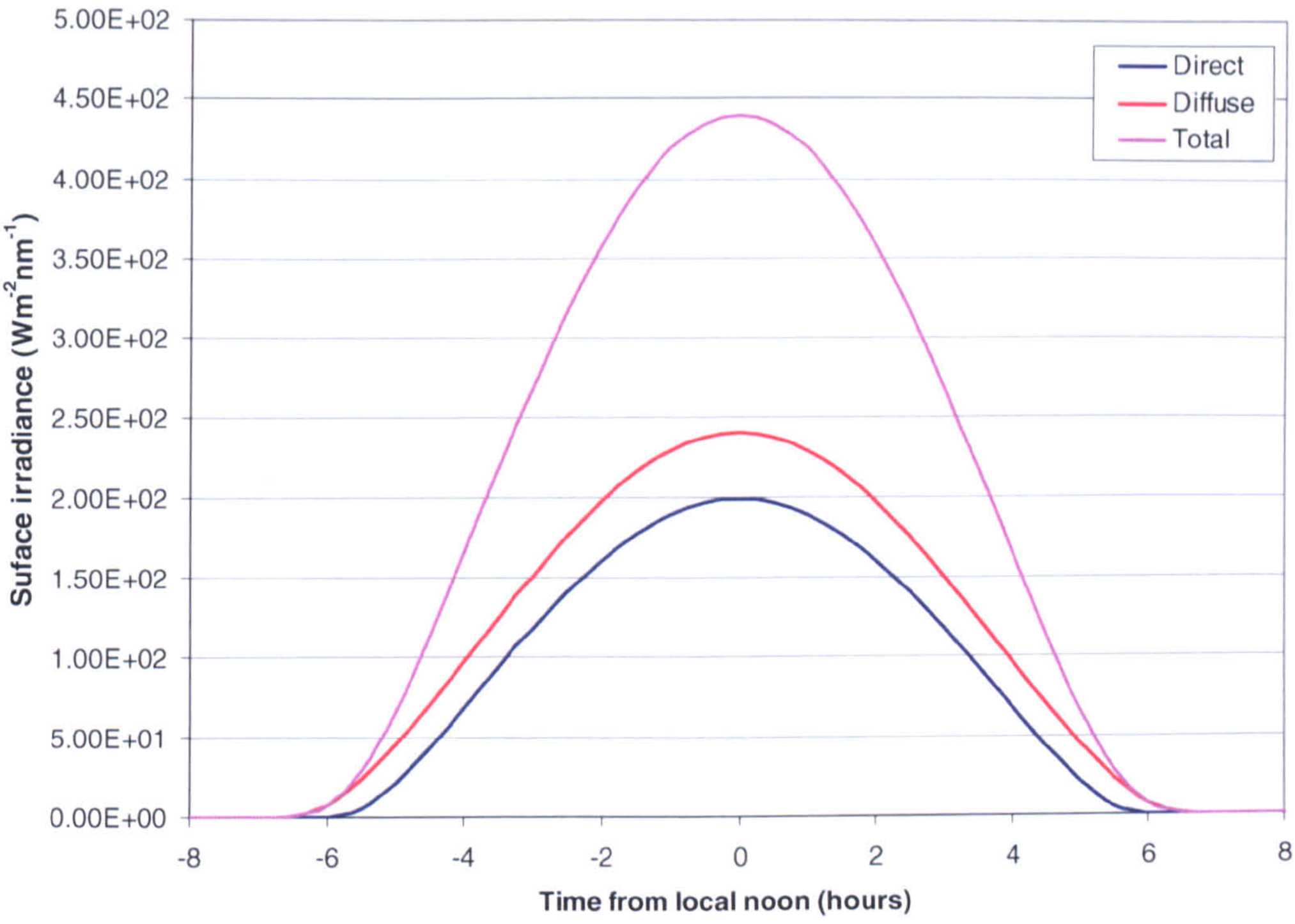

Figure 3.19 – TES scenario: Diurnal variation in surface flux components at $l = 6°$N and $L_s = 90°$ under 'typical' dust scenario.

Figure 3.20 shows the predicted diurnal variation in flux at 6°N and L_s = 270°. Under these circumstances the direct component of the surface is the dominant component for the majority of the day due to the lower relative aerosol abundances, with the diffuse component only matching or surpassing the strength of the direct component at the high zenith angles, and correspondingly high airmass, within an hour or two of sunrise and sunset.

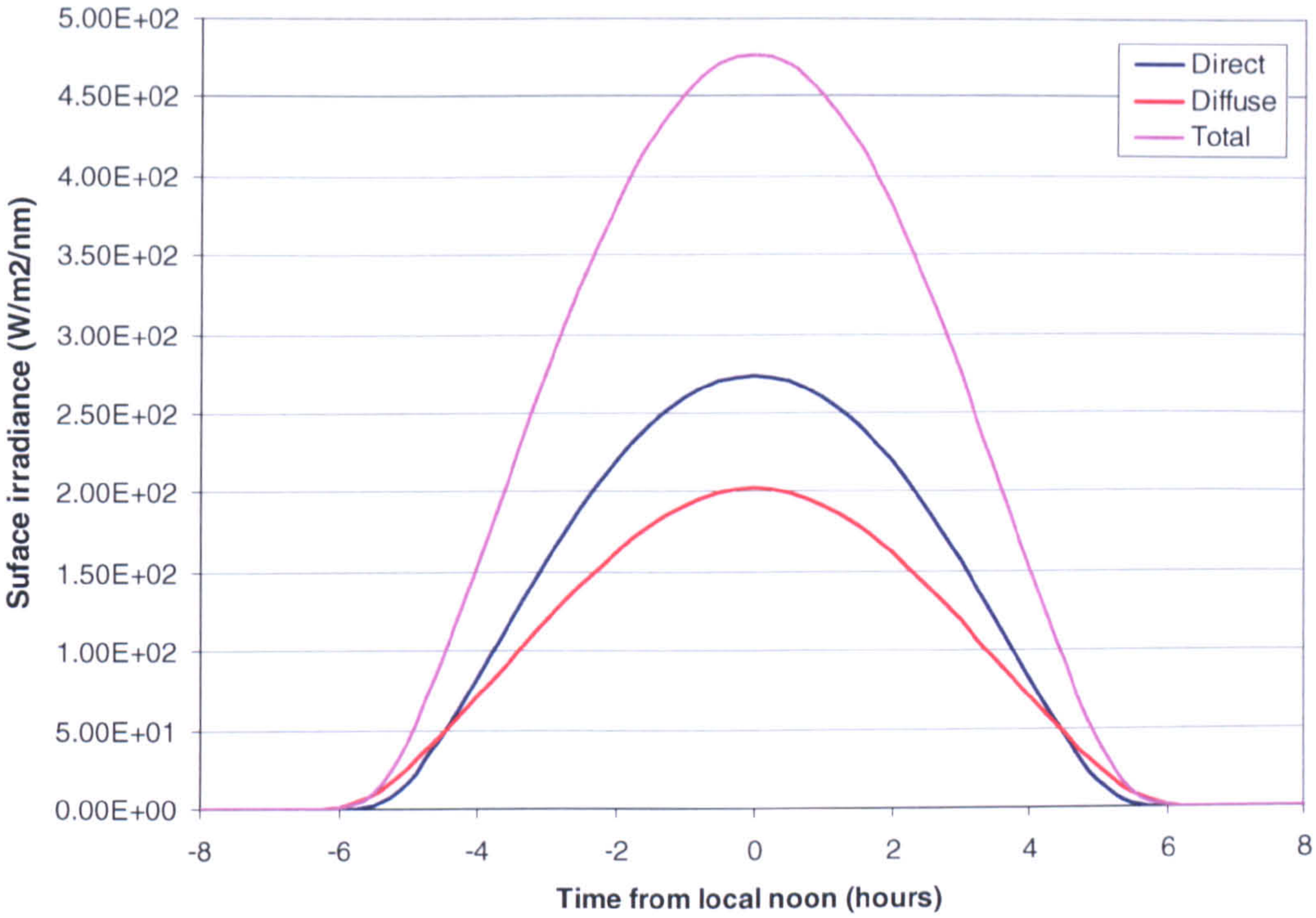

Figure 3.20 – TES scenario: Diurnal variation in surface flux components at l = 6°N and L_s = 270° under 'typical' dust scenario.

3.3.2.3 Gale Crater

Gale crater is located just inside Mars' southern hemisphere at a latitude of around l = 4°S and has a diameter of approximately 150 km. The most notable feature of the crater is an enormous mound of debris located in its centre and rising to heights many kilometres above the crater floor, in places even surpassing the crater walls in height. The origins of this mound are under debate and are one of the main reasons that this location is under consideration as a possible landing site. One theory suggests that the mound was deposited on a lake bed by sedimentation from waters which may have filled the crater at some point in its history (Cabrol et al., 1999), but the mound may also be the result of aeolian processes transporting debris in to the crater from other locations (Stockstill et al., 2007). Whatever its formation history,

orbital imaging of the mound has shown it to exhibit a sedimentary layered structure which has undergone significant erosion.

The greatest column abundances of the ACB are located to the north of Mars' equator meaning that the atmospheric column above the southerly location of Gale crater exhibits a lower scattering optical depth than that of Meridiani Planum. Figure 3.21 shows that while there is still a sufficiently high scattering optical depth for the diffuse component of the surface flux to dominate over the direct component for the entirety of the daylight hours, the two flux components are closer in value than those predicted at Meridiani Planum. The maximum value of the diffuse flux, occurring at midday, is predicted to be approximately 6% greater than the direct component equivalent.

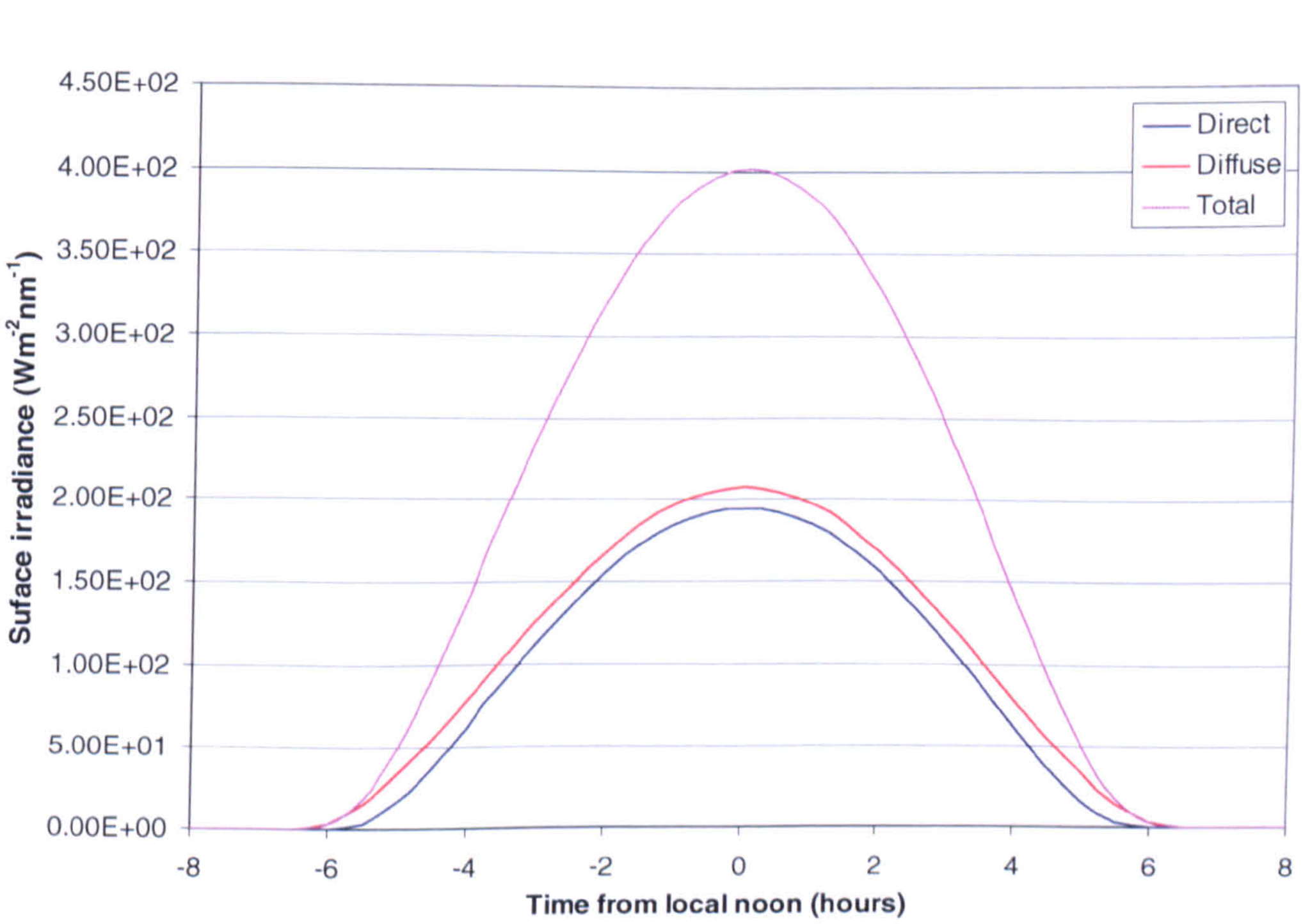

Figure 3.21 – TES scenario: Diurnal variation in surface flux components at $l = 0$ and $L_s = 90°$ under 'typical' dust scenario.

Figure 3.22 shows a similar trend to that predicted for the Meridiani Planum region where, even in the dusty southern summer, the column abundance of dust is not sufficient to elevate the values of the diffuse component of the surface flux above the values of the direct component equivalent until the high zenith angles close to sunrise and sunset.

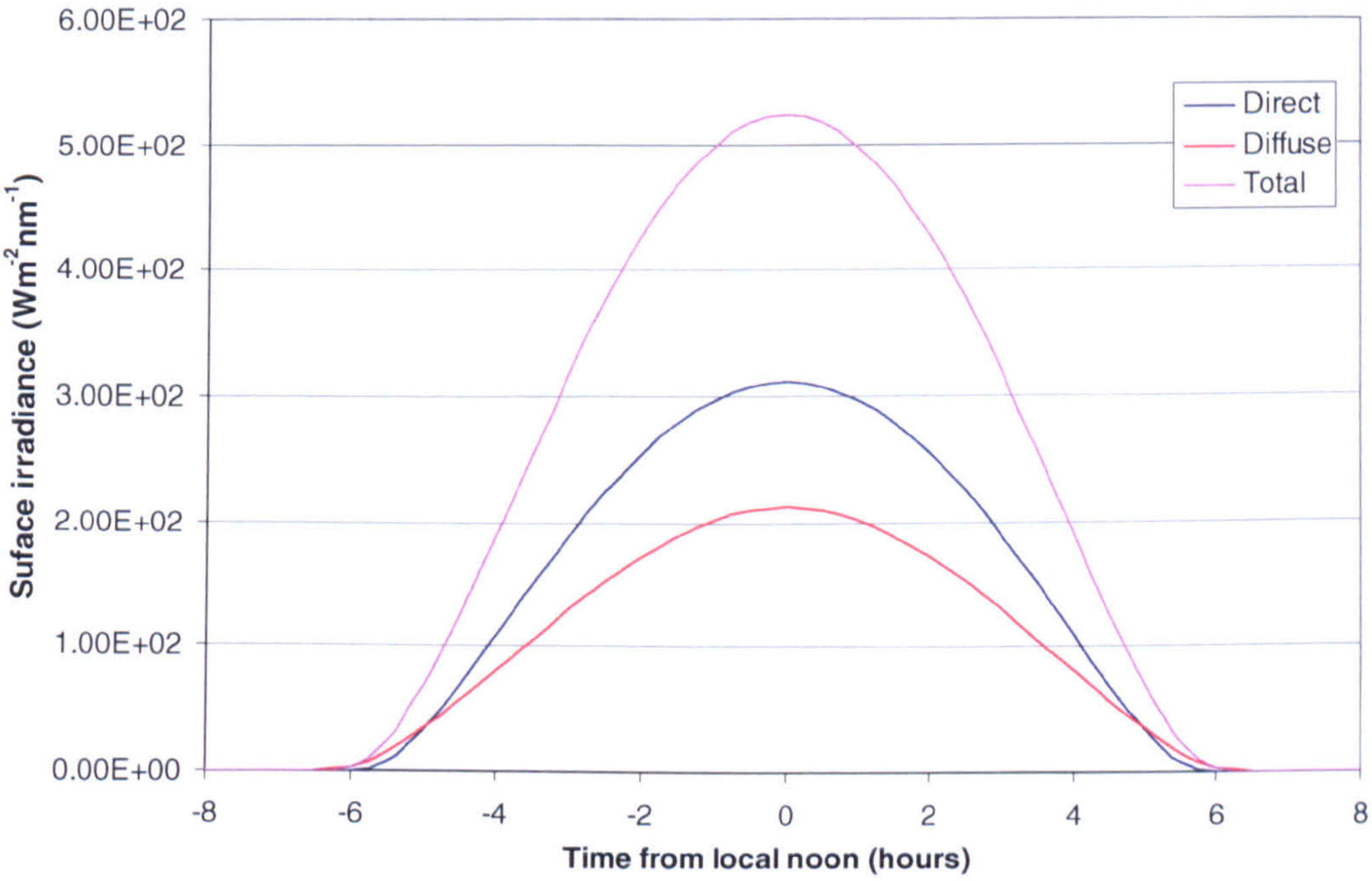

Figure 3.22 – TES scenario: Diurnal variation in surface flux components at $l = 0$ and $L_s = 270°$ under 'typical' dust scenario.

3.3.2.4 Holden Crater

Holden crater is another example of a crater which may have held a lake in the past and exhibits many features which may have been created by flowing water, such as gullies eroded from the crater walls. There is also significant sedimentary deposition present on the crater floor and observations have been made of what appears to be sedimentary formations of alternating bands of light and dark rock. Again these may

be the result of deposition within a crater-lake environment or perhaps of air-fall from volcanic events (Ehlmann et al., 2008). The crater is approximately 140 km wide and is located in the southern highlands at a latitude of around 26°S, making it the most southerly of the potential landing sites.

Figure 3.23 shows the surface flux components in northern summer time at Holden crater (under the TES scenario). Here, under the influence of the ice cloud aerosols, the diffuse component dominates strongly over the direct component of the flux throughout the entire day. The simulation predicts a period of approximately an hour duration at the beginning and end of the day, when solar zenith angles are high, where there is negligible direct component present, only the diffuse.

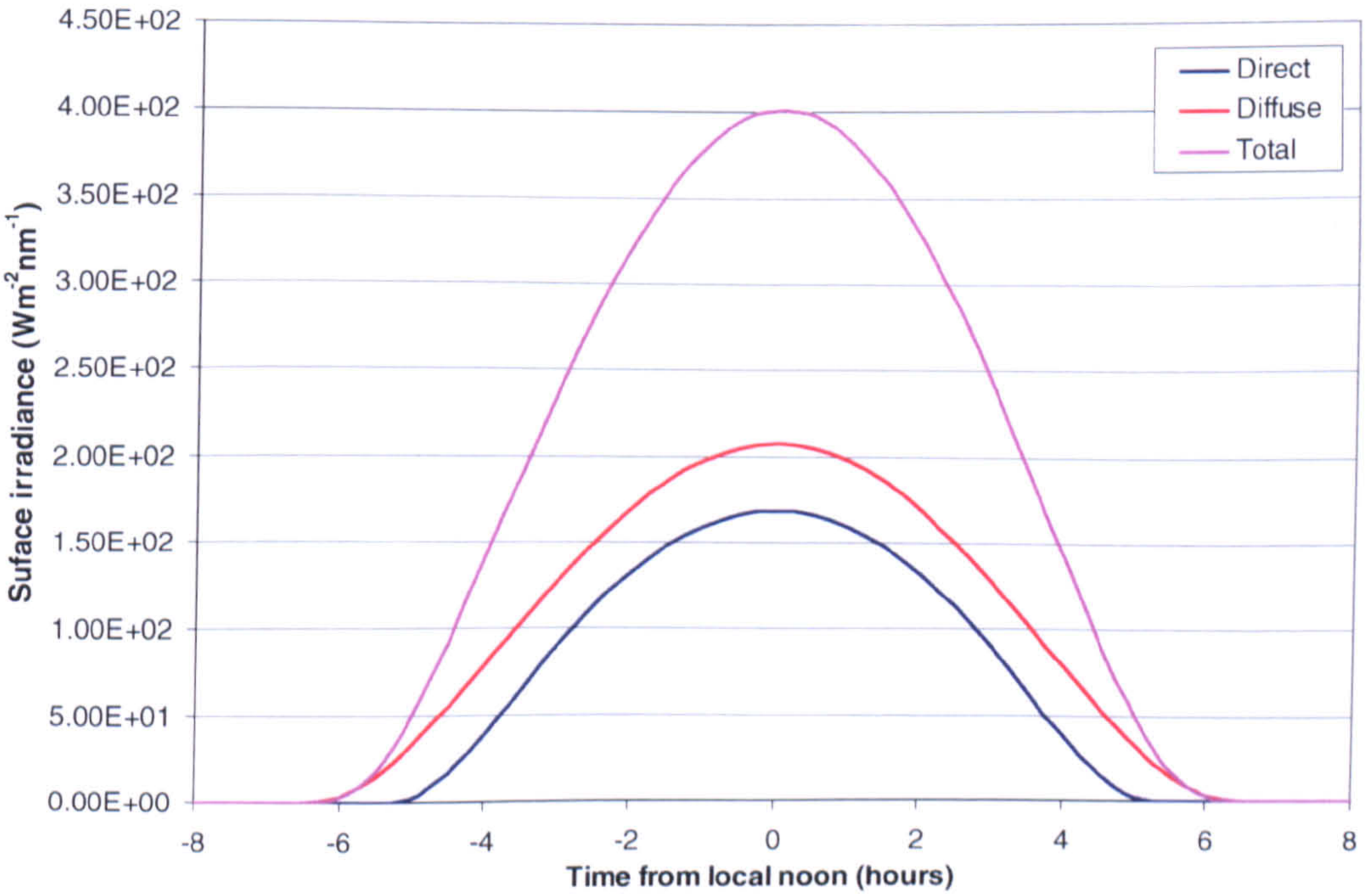

Figure 3.23 – TES scenario: Diurnal variation in surface flux components at l = 26°S and L_s = 90° under 'typical' dust scenario.

Figure 3.24 (surface flux components during the southern summer time at Holden Crater) shows how the simulation predicts that, even at the relatively high dust optical depths ($\tau \sim 0.4$) found at these latitudes at this time of year, it is the direct flux component that dominates for most of the day. At the midday peak the direct component comprises approximately 60% of the combined surface flux value. As seen at the previous latitudes the diffuse flux is predicted to dominate for approximately an hour or so around sunrise and sunset.

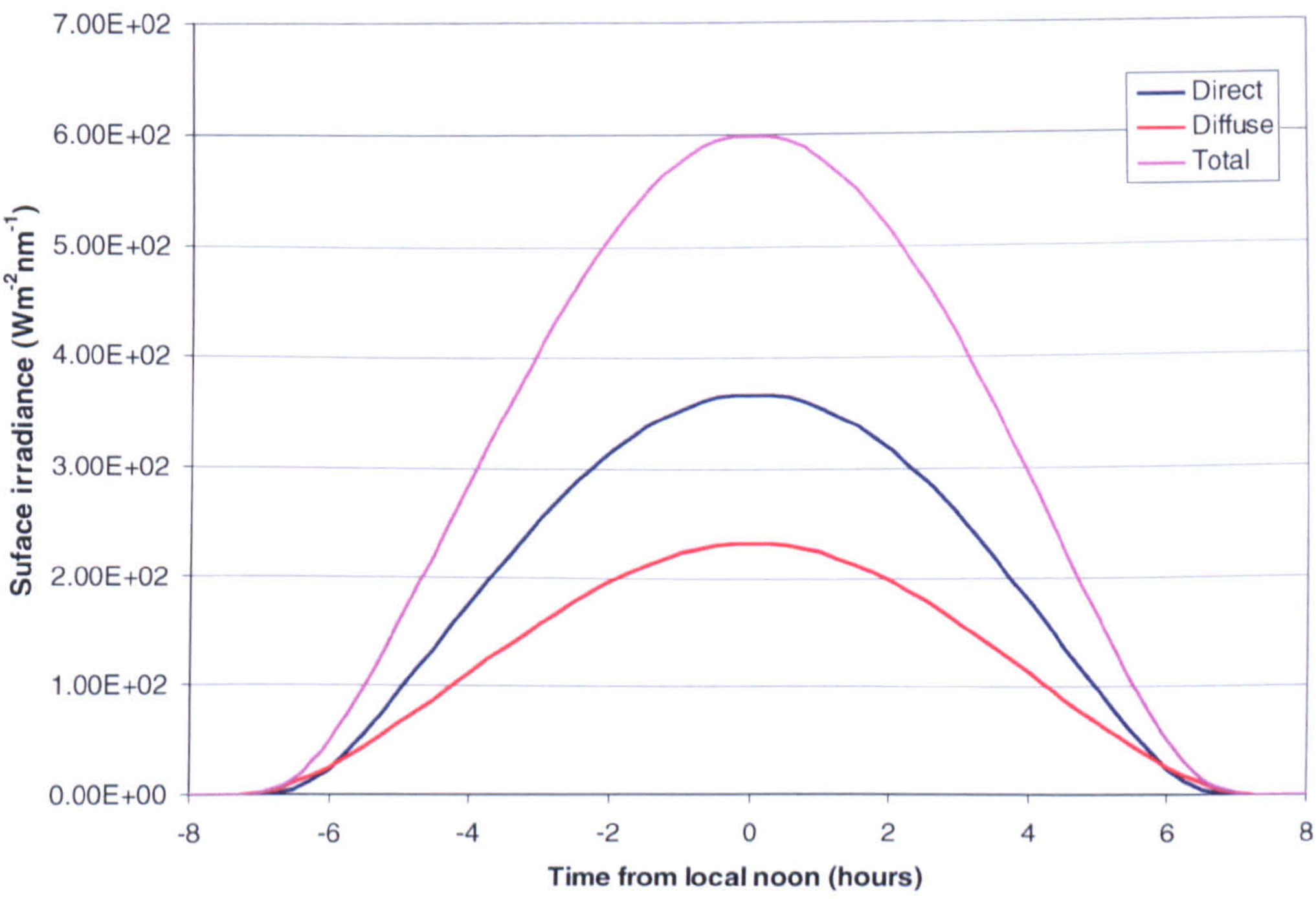

Figure 3.24 – TES scenario: Diurnal variation in surface flux components at $l = 26°S$ and $L_s = 270°$ under 'typical' dust scenario.

3.4 Consequences of flux studies for surface missions

The variation in the surface flux may have ramifications for the application of solar powered exploration of the martian surface. When the flux is high there may be ample energy incident upon the solar cells to provide sufficient power for a complex

lander and extensive suite of instruments; however this may not be the case for the other half of the year where, taking the most southerly of the proposed landing site latitudes at 30°S, the total surface flux is only around a third of the maximum flux value. Therefore, for long duration missions, the design of the mission may have to be a compromise between either the entire capability of the lander being geared towards operating under the minimum power constraints, or alternatively, certain instruments or capabilities only being accessible during periods when there is sufficient power available. For example, the operational activities of the MERs are restricted during seasonal periods of low surface flux, and the rovers have been parked on inclines to optimise solar array sunlight exposure at high zenith angles. A method of avoiding this situation is not to rely upon solar power but to use the only currently viable alternative, radioisotope thermoelectric generators, as is planned for Mars Science Laboratory.

Current photovoltaic cell technology allows for a wide range of wavelengths to be harnessed for the production of electricity (the MERs use triple junction solar cells which primarily respond to the blue end of the visible spectral range and with a long wavelength cut-off of about 650 nm (Landis et al., 2004)) and innovations in solar panel construction results in increased operational efficiency. Under a predominantly direct incident flux, the tilting of solar panels is important to ensure that the maximum surface area is presented to the incident flux. This is not always possible however, for example in the case of a fixed panel static lander, which is confined to the position in which it is initially deployed. For the case of a mobile rover a degree of reorientation can be undertaken by repositioning the entire vehicle but this may be incompatible with the other activities of the rover or with the rover's

current location, for example, should the rover be traversing an incline. The inclusion of repositionable solar panels is generally undesirable due to the potential for the mechanism to fail and leave the panel locked in an unsuitable configuration. One possible way to increase the collecting area of solar panels could be to provide solar cells on the underside of the panels too (Landis et al., 2004). These studies have shown that the VIS and NIR bands of the surface flux both exhibit a significant diffuse component under even moderate dust loadings. Under a surface flux dominated by a diffuse component, the angling of the solar panels towards the zenith becomes less critical as the incident energy is now scattered in from a larger solid angle.

Chapter 4 – Trace gas detection and the CO_2 cut-off

In this chapter a number of studies are conducted in order to assess the suitability of a spectrometer, such as the UVIS instrument, for a number of applications additional to those highlighted in Chapter 3. The studies focus on determining the sensitivity ranges of the instrument required in order to detect the effect of variations in the atmospheric surface pressure and temperature on the surface flux and to detect the presence of trace gases in the atmosphere through the absorption features they create in the surface spectrum. A wavelength resolution of 1 nm is used in the UVIS simulation; this is comparable to the planned wavelength resolution of the UVIS instrument when operating at the surface of Mars.

4.1 The CO_2 cut-off variation with atmospheric pressure

A distinctive feature of the surface spectrum of Mars is the sharp cut-off observed below 200 nm where the intensity of radiation reaching the surface rapidly decreases into insignificance. This cut-off is the result of absorption by CO_2 gas, the absorption cross-section of which exhibits an increase of a few orders of magnitude at these wavelengths (Parkinson et al., 2003). Although the CO_2 absorption cross-sections are approximately four orders of magnitude smaller than the equivalent O_3 absorption cross-sections at these wavelengths, the significantly higher column abundance of CO_2 (the main constituent of the martian atmosphere) results in a strong absorption feature.

The UVIS simulation generates the column abundance of CO_2 using a defined surface pressure value (see Chapter 2 Section 2.1.5). The simulation can therefore be used to study the effect that varying the surface pressure, and the resulting change in the CO_2 column abundance, has upon the surface spectrum. A reduction in the surface pressure value input to the simulation results in a decrease in the CO_2 column abundance and vice versa, and a lower column abundance results in a lower atmospheric optical depth. Therefore the wavelength at which the surface spectrum cuts off should shift to shorter wavelengths as the pressure decreases and less atmospheric absorption of the incident radiation occurs.

All simulations carried out for this chapter were conducted at the equator of Mars and at L_s = 220° degrees. All of the suggested ExoMars landing sites lay within a few degrees either side of the equator and so the equator itself has been chosen as a representative latitude for the tests. L_s = 220° was chosen as this represents the point during the martian year of maximum irradiation of the equator and so should result in the highest signal level for UVIS, i.e. it represents a 'best case' scenario for a strong signal in the UVIS spectra. The 'typical' seasonal scenario of a maximum dust optical depth of $\tau = 0.5$ was used and the maximum ice cloud optical depth was also set to a 'typical' value of $\tau = 0.5$ (see Chapter 3 Section 3.2).

For this study it was the input altitude-pressure curves that were varied. The 'standard' scenario utilising the altitude-pressure curve recorded by the EDLS of the Mars Pathfinder probe and the insensitivity of the surface irradiation values to comparatively small changes in surface pressure have been discussed in Chapter 2.

The pressure changes implemented here represent the extreme ends of the scale likely to be encountered on Mars, from less than 100 Pa at the top of Olympus Mons to greater than 1000 Pa in the depths of Hellas Planitia.

The surface spectra at the wavelengths relevant to the CO_2 cut-off are shown in Figure 4.1 and clearly show that higher values of surface irradiance persist at shorter wavelengths under the lower pressure conditions. Figure 4.1 also highlights how a spectrometer could be employed as a means of crude surface pressure determination. Given a sufficiently sensitive instrument operating continuously or at least at regular intervals, it should be possible to monitor the wavelength value at which the surface spectrum drops below a certain irradiance value. This data could then be cross-correlated with surface pressure data collected by dedicated meteorological instrumentation.

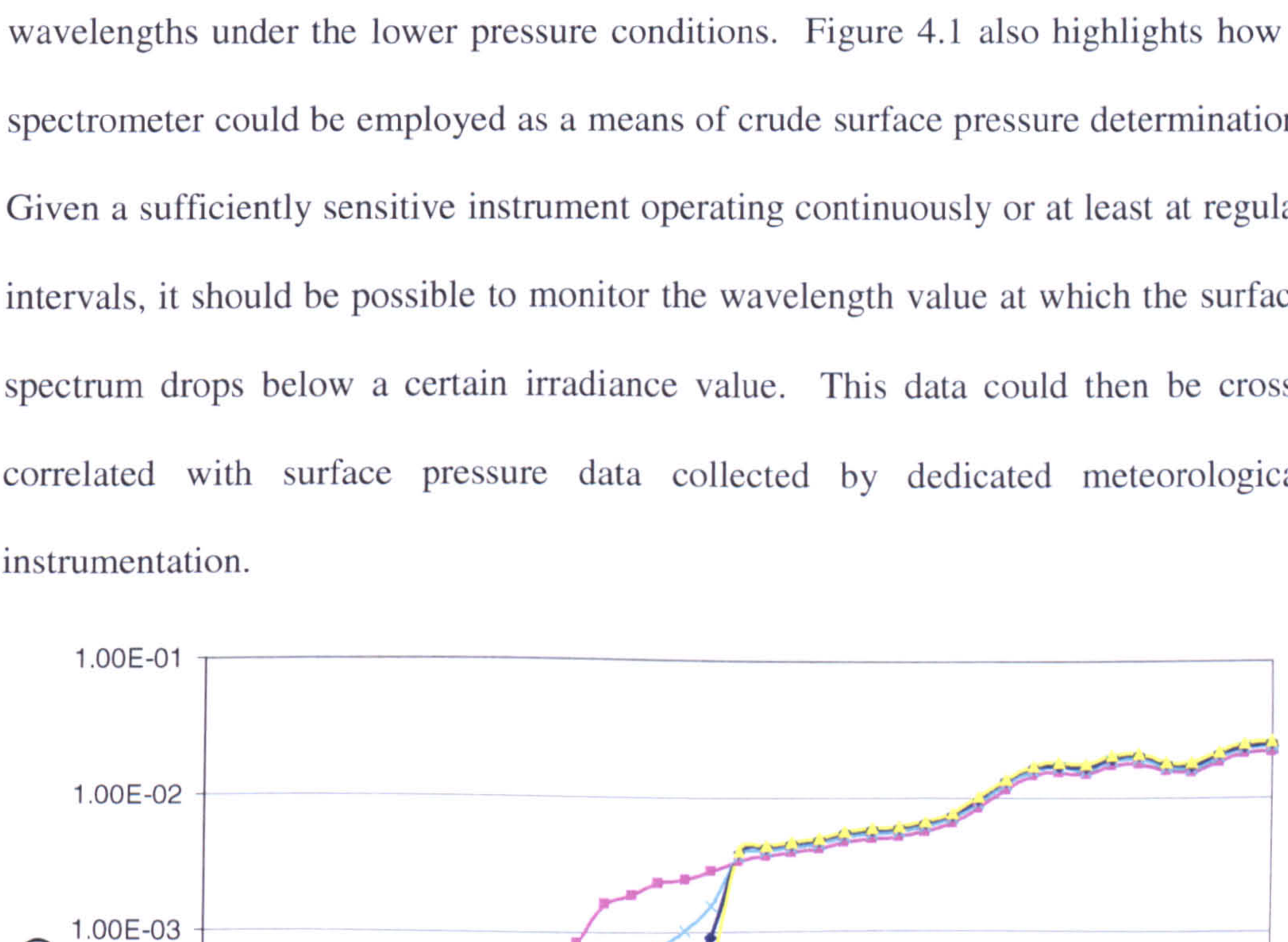

Figure 4.1 - The occurrence of the CO_2 'cut-off' predicted using the UVIS simulation under different surface pressure values.

It can be seen from Figure 4.1 that under the conditions input to the simulation for this study an instrument would require nanometre wavelength resolution or better to monitor the wavelength of the cut-off. The instrument would also require high sensitivity to variation in the surface flux value. Figure 4.1 demonstrates that with a sensitivity on the order of ~ 10^{-2} $Wm^{-2}nm^{-1}$ there is no discernable pressure dependence of the cut-off wavelength, but if the value of the sensitivity is improved by two orders of magnitude to ~ 10^{-4} $Wm^{-2}nm^{-1}$ then a clear distinction can be made for the cut-off wavelength under the different pressure scenarios (for the 100, 400, 680 and 1000 Pa surface pressure values the predicted cut-off wavelengths are 191, 195, 196 and 198 nm respectively). Of course, this is a theoretical study and it is unlikely that an instrument would experience such a wide range of surface pressures during its functional lifetime. The many and complicated issues that must be overcome in safely landing and maintaining a functioning Mars surface probe for any length of time dictate that most missions must be targeted within a few degrees of the equator and land at a sufficiently low altitude for there to be enough atmosphere to slow their descent. The surface pressure encountered by the NASA missions that have successfully reached the martian surface encompass a pressure range of only a few hundred pascals difference at most (Magalhaes et al., 1999, Withers et al., 2002, Withers and Smith, 2006) but using these extreme pressures for the simulation demonstrates how even large differences in pressure are predicted to result in only small changes in the wavelength of the surface spectrum cut-off. For comparison purposes the pressure was scaled up to an earth-like 100,000 Pa at which level the

surface spectrum cut-off, taking a surface flux detection sensitivity of ~ 10^{-4} $Wm^{-2}nm^{-1}$, was found to occur close to 280 nm.

4.2 The CO_2 cut-off variation with atmospheric temperature

As well as being sensitive to changes in atmospheric pressure the wavelength of the CO_2 cut-off should also be affected by the atmospheric temperature, owing to the temperature dependence of the CO_2 absorption cross-section values. The data available for the CO_2 cross-section values at wavelengths relevant to this study (between λ = 180 and 200 nm) only encompasses two different temperature values, 195 and 295 K (Parkinson et al., 2003), but this compares favourably with the temperature range encountered by the Viking surface landers of ~ 170 - 250 K (Kieffer et al., 1976) and those encountered by the MERs at ~ 200 - 260 K (Smith et al., 2006).

Figure 4.2 shows the surface spectrum across the wavelength range incorporating the CO_2 cut-off where the two curves represent the surface flux values using the CO_2 absorption cross-sections for 195 and 295 K. The cross-section values at 195 K are on average ~55% of the value of those at 295 K, i.e. the cross-sections are greater at the higher temperature. This is reflected in Figure 4.2 which shows lower surface flux values at wavelengths less than 200 nm, resulting from greater absorption of the incident flux, for the 295 K curve compared to the 195 K curve. As with the pressure study above, the data gathered can be used to assess the sensitivity required by an instrument in order to differentiate between the two temperature curves. For an

instrument with sensitivity on the order of ~ 10^{-2} $Wm^{-2}nm^{-1}$ there is no discernable difference between the two spectra with the cut-off occurring at λ ~ 209 nm for both curves, but if the sensitivity is improved by an order of magnitude to ~ 10^{-3} $Wm^{-2}nm^{-1}$ then the cut-off now occurs at different wavelengths (λ = 197 and 199 nm for the 195 K curve and 295 K curve respectively). However, in order to achieve this 2 nm difference between the wavelengths at which the cut-off occurs the temperature has been varied by 100 K. Such a temperature range may be encountered over the course of a martian year but over shorter time scales variations are likely to be less than this, for example the Viking 1 lander recorded diurnal variations of ~ 50 K (Kieffer et al., 1976).

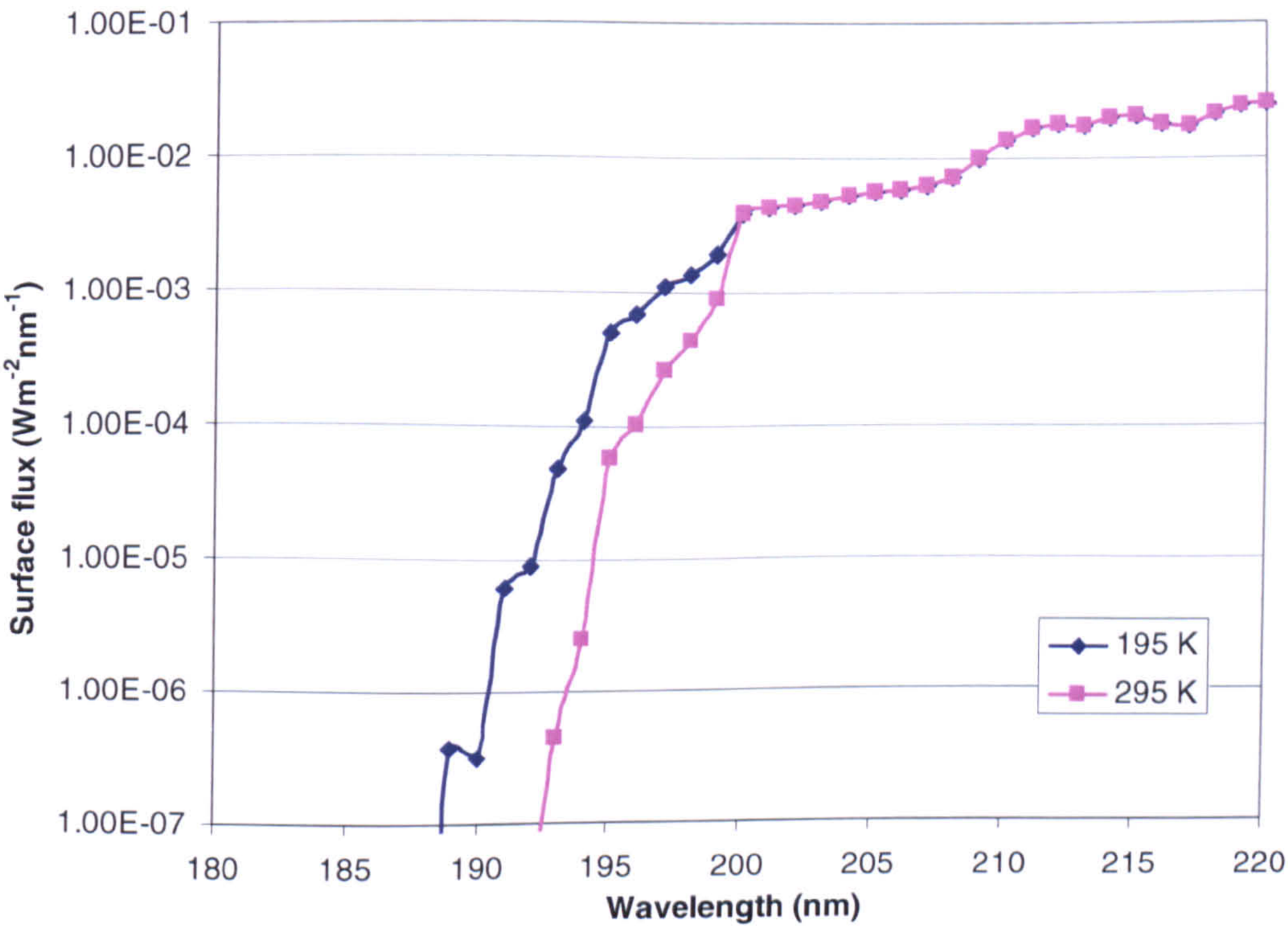

Figure 4.2 - The occurrence of the CO_2 'cut-off' predicted using the UVIS simulation with CO_2 absorption cross-sections determined at two different temperature values.

4.3 The detection of trace gases in the martian atmosphere

One possible application of UVIS is as a means of detecting the presence of trace gases which occur in the martian atmosphere. Certain species are of particular interest owing to either their potential influence upon the martian surface environment, such as ozone and hydrogen peroxide, or, as is the case with methane, because their presence has implications for the geochemical, or even biological, processes occurring on Mars. Ammonia has also been selected for study because although there has been no confirmed detection of indigenous martian ammonia, it can be released as part of the EDLS of surface probes. Each of these gas species has a known wavelength dependent absorption cross-section present within the wavelength regime detectable by the UVIS instrument and so, if present in sufficiently high abundances, will produce an absorption feature in the surface spectrum. The wavelengths at which the absorption features occur and their relative magnitudes can be used to determine the identity of the species likely to be responsible for the feature and also a corresponding abundance for that species in the column above the point of detection. Figure 4.3 shows the absorption cross-sections plotted against wavelength for the trace gas species discussed above. The data for the methane absorption cross-sections are taken from Lucchesini and Gozzini (2005); for the hydrogen peroxide absorption cross-sections from Atkinson et al. (2004); and for the ammonia absorption cross-sections from Chen et al. (1999). Figure 4.4 compares two surface spectrum plots generated under different atmospheric ozone abundances, with the spectral curve corresponding to the higher ozone abundance clearly showing a strong absorption feature, i.e. reduction in surface flux values, at the wavelengths where ozone absorbs strongly.

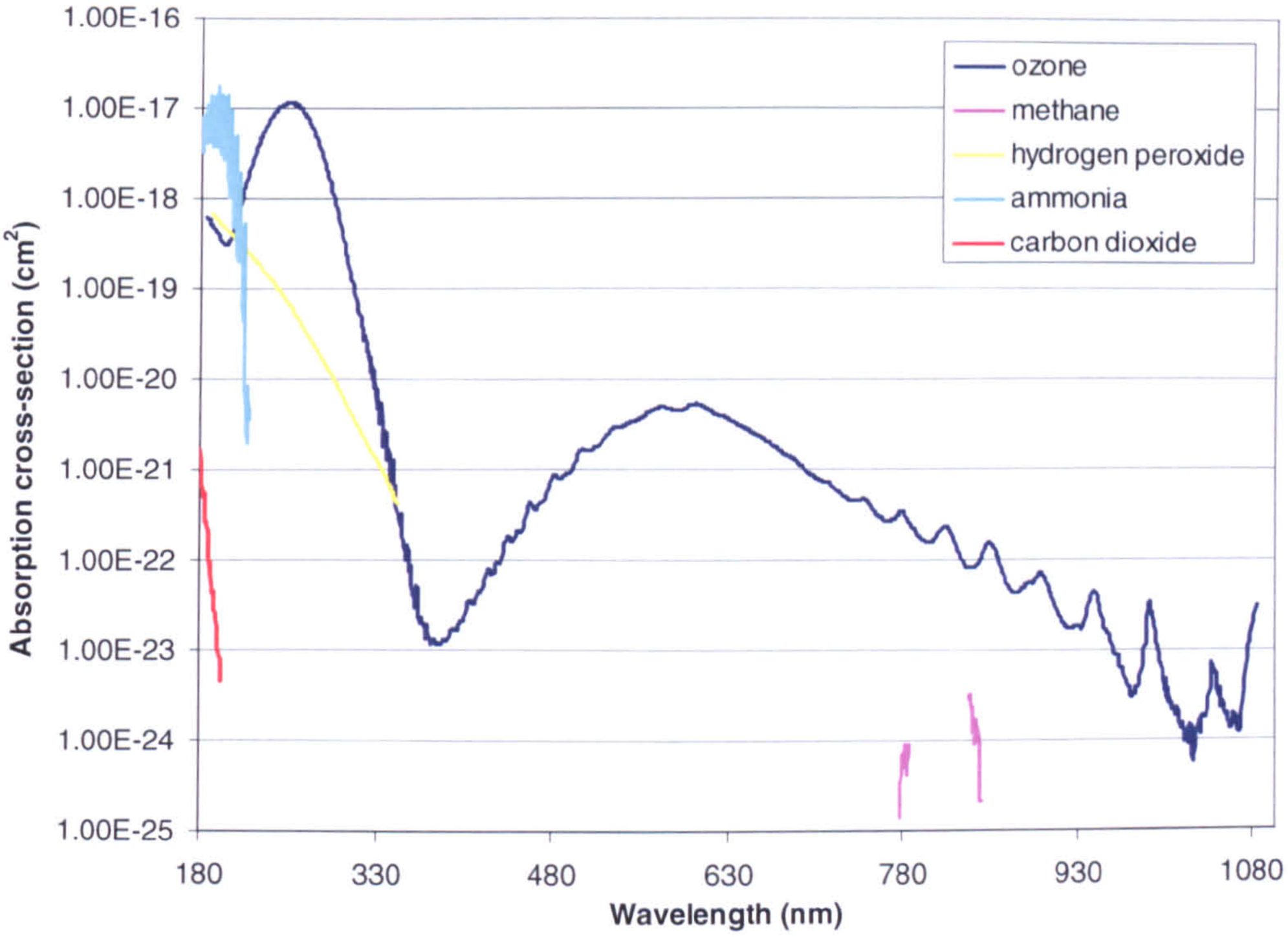

Figure 4.3 - The wavelength dependent absorption cross-sections of the trace gases discussed in this chapter. References for the cross-section data are found in the preceding text.

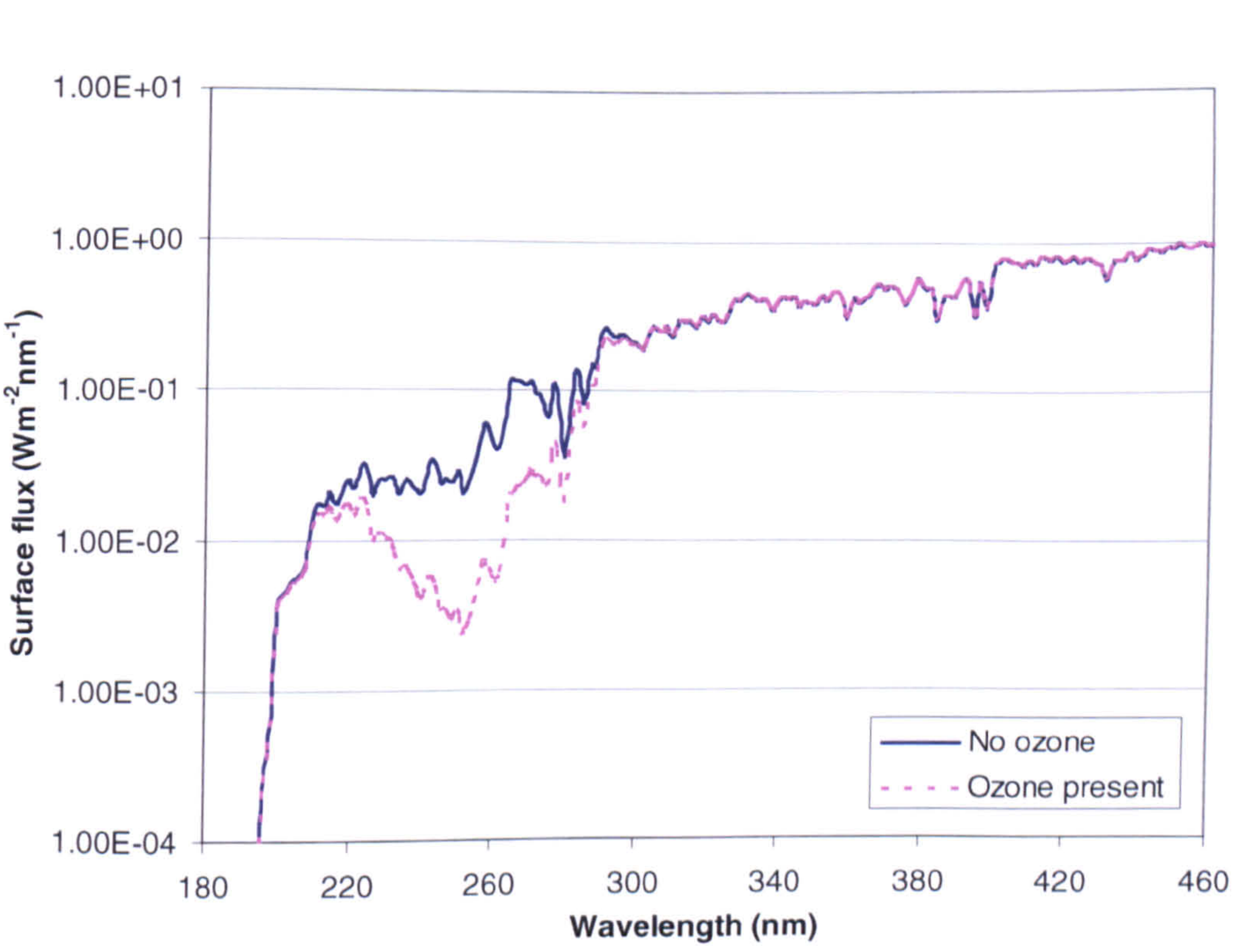

Figure 4.4 – Comparison of surface spectra with and without ozone present (ozone column abundance = $1.0 \times 10^{19} cm^{-2}$).

Comparisons can be made using the UVIS simulation of a total surface spectrum derived in a situation in which there are no trace gases present and a total surface spectrum derived from an identical situation except for the introduction of one of these gases. By steadily increasing the abundance of the trace gas and then dividing one spectrum by the other the percentage change in the spectrum at each wavelength caused by the presence of the gas can be found. In this way the simulation can be used to predict the abundances of these trace gases that are required to produce a signal that should be detectable by the UVIS instrument.

Of course, in the real world application of an instrument it is not possible to take one spectrum with the trace gas present and one without to act as a comparison. This problem can be bypassed by selecting a wavelength within the detectable range at which absorption does not occur, or is at least very low, so that any change in trace gas abundance should have little or no effect upon the surface flux detected at this wavelength. By taking the ratio of the value of this invariant flux with a flux value at a different wavelength that exhibits a dependence upon the gas abundance, it is possible to build up a reference graph of ratio values under different gas abundances. This can then be used as a look-up table for ratio values retrieved from *in situ* measurements and so provide a means of estimating the gas column abundances being observed by the instrument.

As well as determining the ratio discussed above, a detection limit was selected corresponding to a 5% change in UVIS signal recorded between the total surface spectrum with no trace gas present and an identical spectrum with the influence of

the trace gas included. This value was chosen because a percentage change rather than absolute change offers some independence from the uncertainties of the model. This does mean that the change in surface irradiation required to produce a detection is not constant over the wavelength range under investigation. As can be seen from previous chapters (see Chapter 2 Section 2.1.3), the solar output flux rises quite steeply by approximately three orders of magnitude between λ = 180 nm and a maximum around λ = 450 nm, before declining more slowly at longer wavelengths. A 5% change at shorter wavelengths can therefore correspond to a much smaller absolute value than at longer wavelengths. This has been taken into account and will be commented upon where relevant.

All simulations carried out for this chapter were conducted at the equator of Mars and at L_s = 220° degrees. All of the suggested ExoMars landing sites lay within a few degrees either side of the equator and so the equator itself has been chosen as a representative latitude for the tests. L_s = 220° was chosen as this represents the point during the martian year of maximum irradiation of the equator and so should result in the highest signal level for UVIS, i.e. it represents a 'best case' scenario for a strong signal in the UVIS spectra. The 'typical' seasonal scenario of a maximum dust optical depth of τ = 0.5 was used and the maximum ice cloud optical depth was also set to a 'typical' value of τ = 0.5 (see Chapter 3 Section 3.2).

4.3.1 Ozone (O_3)

The ozone content of the martian atmosphere has been studied in great detail by instruments such as TES and SPICAM and through global climate models like the

MCD. It elicits such interest owing to its proposed role in the hydrogen photochemistry of the atmosphere; studying the ozone yields clues to the reactions occurring and the molecular species involved (Lefevre et al., 2004, Perrier et al., 2006). This has meant that seasonal and diurnal variations in distribution and abundance, both latitudinally across the martian surface and also vertically within the atmosphere, have been well characterised. The ozone distributions and profiles used in the UVIS simulation were discussed in Chapter 2 Section 2.1.5.

Ozone exhibits a particularly large absorption cross-section at UV wavelengths which is the reason ozone plays such an important role in the atmosphere of Earth, providing a protective layer that prevents the exposure of the planet's surface to the full effect of the Sun's damaging UV emissions. However ozone levels at Earth, which average around 8.1×10^{18} cm^{-2}, are significantly higher than those at Mars where the highest ozone column abundance so far observed is around 1.6×10^{17} cm^{-2} (Perrier et al., 2006) resulting in comparatively little UV protection for the martian surface. The largest ozone absorption cross-sections occur within the wavelength range of λ = 245 - 260 nm (peaking around 252 nm), conveniently longwards of the CO_2 spectral cut-off, and therefore there is a possibility of UVIS being able to detect an absorption signal resulting from the presence of martian ozone.

Figure 4.5 shows the variation in the ratio between the surface irradiation at λ = 252 nm, where ozone absorption is strong, and λ = 388 nm, where gas absorption processes in the martian atmosphere are negligible. This ratio has been normalised against the value of the 252/388 nm ratio when no ozone is present so that the vertical axis values occupy a range between 0 and 1.0. During operation of the

instrument Figure 4.5 can be used as a reference chart to convert derived wavelength ratios into corresponding gas column abundances, or alternatively, it can be used to determine the required sensitivity of the instrument such that it is able to detect a desired gas column abundance.

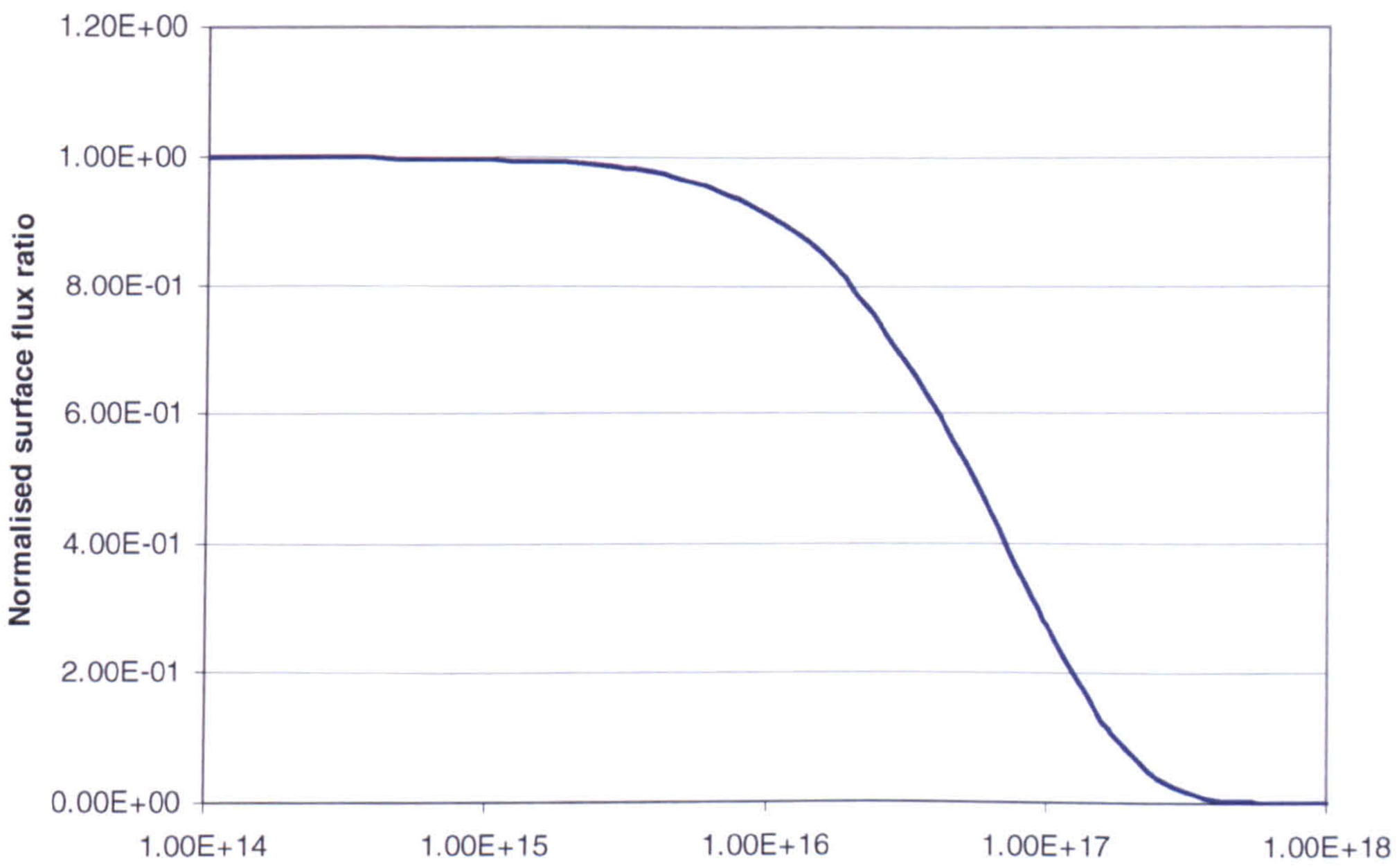

Figure 4.5 – The ratio of the surface flux value at 252 nm, where ozone absorption cross-sections are high, and the surface flux at 388 nm, where ozone absorption is negligible. The values are normalised against the ratio of the surface flux at these two wavelengths with no ozone present.

The UVIS simulation, run under the scenario discussed above, returned a minimum column abundance of 6.7×10^{15} cm^{-2} required to produce a 5% variation in the surface spectrum. This value lies comfortably within the maximum observed ozone value for the martian atmosphere but this value was recorded at latitudes between l = 50°-75°N and both observations and modelling have shown that ozone abundance varies significantly over the martian surface depending upon location and season (Lefevre et al., 2004, Perrier et al., 2006). The highest ozone abundances tend to

occur at higher latitudes approaching the poles ($l > 50°$) where column abundances greater than 1.0×10^{16} cm^{-2} have been repeatedly observed during the wintertime of each hemisphere, but these high column abundances quickly decrease by orders of magnitude as the hemispheres pass into summertime. Therefore although ozone abundances theoretically detectable by a spectrometer instrument do occur on Mars, the fact they occur at higher latitudes which are harder to access with a surface probe, and during wintertime where the surface flux would be very low, suggests this is a scenario unlikely to be encountered during the course of a viable mission. Equatorial latitudes present comparatively easier to access landing sites and more stable annual surface flux values, however equatorial ozone abundances are lower than those encountered at higher latitudes, tending to peak on the order of $1 \times 10^{15}cm^{-2}$ but can often be much less. Therefore these latitudes, where missions such as MSL and ExoMars are likely to be targeted, may exhibit ozone column abundances close to the derived 5% detection value but observations suggest that for much of the year this will not be the case.

4.3.2 Methane (CH_4)

Detection of methane in the martian atmosphere has come only in the last few years (2003 and after) but this discovery has been of immense importance (Krasnopolsky et al., 2004, Formisano et al., 2004). Calculations of the predicted lifetime of methane under martian conditions suggest that it is unlikely to persist in the atmosphere for longer than a few hundred years before being broken down through UV photolysis or oxidation processes (Atreya et al., 2007). This means that for there to be a detectable methane presence on Mars there must be some process which is

actively replenishing the atmospheric methane content. The methane present in the Earth's atmosphere is estimated to be approximately 60% biogenic in origin (Simpson et al., 1999, Ehhalt et al., 2001) and it has been postulated that the martian methane too could be indicative of biological processes occurring, possibly below the planet's surface (Krasnopolsky et al., 2004). However there are also alternative explanations as to the origin of the martian methane, such as possible periodic releases from deep within Mars through volcanic activity, geochemical processes occurring closer to the martian surface such as serpentinization, or exogenous delivery through comets, meteorites and other space debris. The latest observations to be published relating to the martian methane suggest that it occurs in extended plumes indicating a discrete source of methane release rather than, for example, uniform production in the atmosphere (Mumma et al., 2009).

Methane exhibits a known absorption cross-section, peaking in the NIR at 839 nm, but it is smaller by a number of orders of magnitude compared to that exhibited by ozone (Figure 4.3). Figure 4.6 shows the variation in the ratio of the surface flux at λ = 839 nm with that at λ = 388 nm and has been normalised as discussed above for ozone. The estimate of the minimum column abundance required to produce a 5% difference between a 'clean' surface spectrum and one calculated with methane present gives a value of 1.0×10^{22} cm^{-2}, which is approximately seven orders of magnitude greater than the methane levels observed during the plume events of Mars' northern summer in 2003 where column abundances of ~ 1.0×10^{15} cm^{-2} were detected. A column abundance of 1.0×10^{22} cm^{-2} is only one order of magnitude smaller than the CO_2 column abundance derived by the UVIS simulation. The form of these plumes may suggest they are being emitted from a localized source and then

detected as they undergo dispersion in the atmosphere and therefore the observed column abundances are probably lower than those at the source (Mumma et al., 2009). However seven orders of magnitude would require a very large release of methane which, based upon current observational evidence, seems unlikely, so that even positioned close to a methane source an instrument with the functional wavelength of UVIS is unsuitable as a means of methane detection.

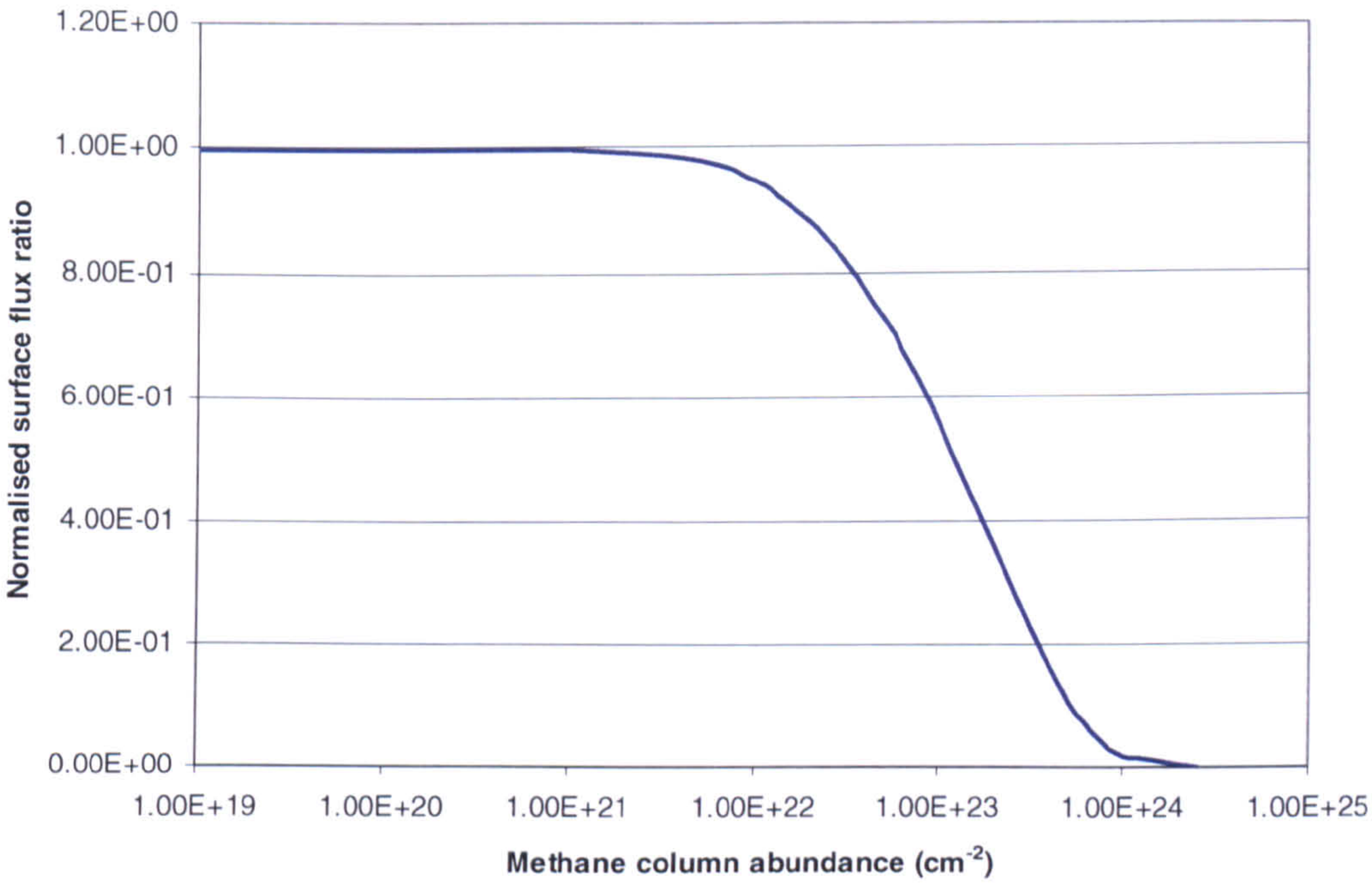

Figure 4.6 - The ratio of the surface flux value at 839 nm, where methane absorption cross-sections are high, and the surface flux at 388 nm, where methane absorption is negligible. The values are normalised against the ratio of the surface flux at these two wavelengths with no methane present.

4.3.3 Hydrogen peroxide (H_2O_2)

H_2O_2 is of great interest owing to the role it is thought to play in creating the surface conditions present on the red planet. It is a strongly oxidizing species and it has been proposed that H_2O_2 may be present at sufficient levels to have effectively sterilized

the surface down to a depth of a number of metres (Bullock et al., 1994). If this is the case it would create an environment that would be incredibly hostile to any life forms attempting to inhabit the planet's upper surface layers. These conditions also mean that is highly likely that any organic evidence that life may have left traces in the martian regolith of its past existence would have been destroyed by the oxidising conditions.

Photochemical models of the martian atmosphere show H_2O_2 formation as the end result of a process beginning with the photolysis of water vapour in the martian atmosphere and ending with the photodissociation of H_2O_2 into two OH radicals (Encrenaz et al., 2004). Another mechanism for the formation of H_2O_2 may result from the static electricity generated by the swirling of dust particles in the dust devils and storms observed at the martian surface. The electric fields generated are predicted to be strong enough to dissociate H_2O and CO_2 molecules and so provide the building blocks for H_2O_2 formation (Atreya et al., 2006b). These two formation mechanisms would seem to suggest that an anti-correlation should be observed between H_2O_2 and water vapour abundances and a correlation between H_2O_2 abundances and dust activity respectively. However, high resolution seasonally distributed observations of H_2O_2 abundances have not been made in sufficient detail yet to conclusively confirm these correlations; the first successful observations of H_2O_2 were only published comparatively recently in 2003 (Clancy et al., 2004).

H_2O_2 exhibits a large absorption cross-section at the short end of the wavelength regime covered by the simulation, the peak of which coincides with the wavelengths at which the CO_2 absorption feature dominates the surface spectrum ($\lambda < 200$ nm).

At 200 nm and above absorption by CO_2 decreases significantly while the H_2O_2 absorption cross-sections remain comparatively large (similar to the ozone cross-section values at equivalent wavelengths) allowing the effects of absorption due to H_2O_2 to be more clearly observed. Figure 4.7 shows the variation of the ratio of the surface flux at λ = 200 nm with that at λ = 388 nm under increasing H_2O_2 column abundance and has been normalised as discussed previously.

The UVIS simulation predicts a minimum column abundance of 7.6×10^{16} cm^{-2} is required to create a 5% change in the detected surface spectrum which is approximately an order of magnitude greater than the column abundance observed by Encrenaz where the inferred value was ~ 7.5×10^{15} cm^{-2} (Brown and Kasting, 1991, Encrenaz et al., 2004). Although there have been few dedicated observations of H_2O_2, Encrenaz et al. suggests that this observed column abundance is in good agreement with the H_2O_2 abundances predicted from Mars GCMs and photochemical simulations. This order of magnitude difference probably makes the detection of H_2O_2 unlikely with a UVIS like instrument. The wavelengths at which H_2O_2 is strongly absorbing may also make it difficult to isolate the absorption effects resulting from H_2O_2 as the surface spectrum is dominated by CO_2 absorption at these wavelengths.

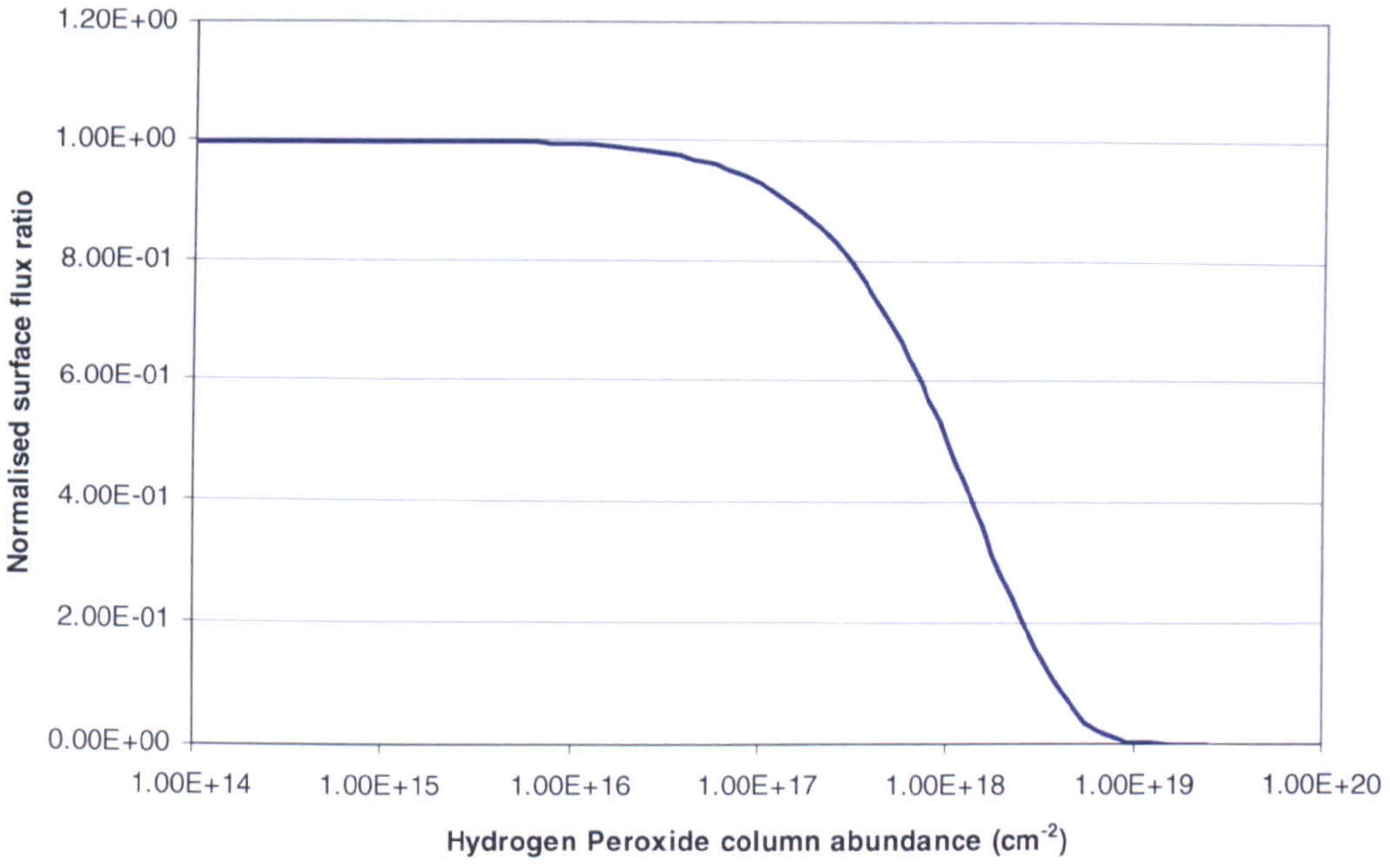

Figure 4.7 – The ratio of the surface flux value at 200 nm, where hydrogen peroxide absorption cross-sections are high, and the surface flux at 388 nm, where hydrogen peroxide absorption is negligible. The values are normalised against the ratio of the surface flux at these two wavelengths with no hydrogen peroxide present.

4.3.4 Ammonia (NH_3)

Ammonia, like methane, is considered to be an important biomarker (Kaltenegger et al., 2002) as naturally occurring ammonia on earth comes predominantly from the breakdown of nitrogenous organic matter (Simpson et al., 1999). Ammonia can also be released from inorganic processes such as volcanism or as part of the rain of space debris that is constantly entering earth's atmosphere but these represent small volumes compared to the decay of organic matter (Allen et al., 1987, Bird et al., 1997).

Up to the time of writing there has been no conclusive evidence for the existence of ammonia on Mars and photochemical simulations have shown that ammonia would

be broken down by UV photolysis reactions (Brown and Kasting, 1991). As with methane this means that should ammonia be observed to be present then there must be some mechanism of replenishment releasing ammonia into the martian atmosphere within this timescale.

One novel method by which ammonia can be released into the martian atmosphere is from the airbag landing systems of Mars surface probes, as a by-product of the gas generation reactions used to inflate the airbags (Ianotta, 2004, Allouis et al., 2005). Although there appears to be no, or at least very little, ammonia naturally occurring in the atmosphere of Mars, if sufficient quantities are released from the landing system used to deploy the instrument on the surface then a trace of this imported ammonia may be visible in the surface spectra.

Ammonia exhibits a large absorption cross-section in the UV around λ = 180 to 200 nm but this quickly becomes weaker longwards of 200 nm (Figure 4.3). This means the chances of detecting an absorption signature from ammonia suffers the same complication as that of H_2O_2; separating any absorption caused by the presence of ammonia from the strongly dominant absorption effects of the CO_2 at these wavelengths. Again this implies the requirement of an instrument with a high flux detection sensitivity. The UVIS simulation returns a minimum column abundance of 2.6×10^{15} cm^{-2} to produce the required 5 % change in the surface spectra.

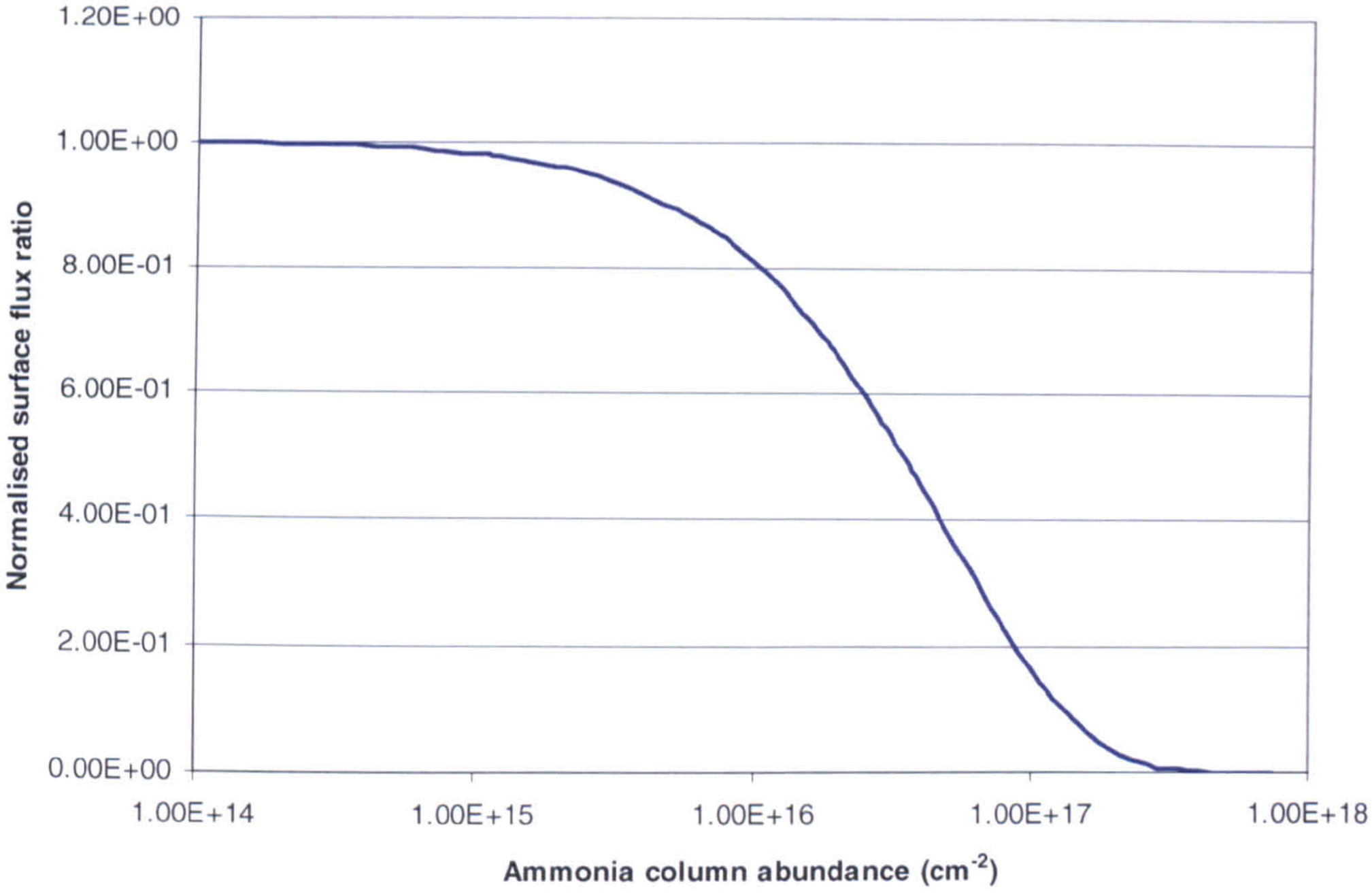

Figure 4.8 – The ratio of the surface flux value at 201 nm, where ammonia absorption cross-sections are high, and the surface flux at 388 nm, where ammonia absorption is negligible. The values are normalised against the ratio of the surface flux at these two wavelengths with no ammonia present.

Chapter 5 – Varying aerosol scattering parameters

A number of studies have been carried out in an attempt to characterise the scattering parameters of the martian dust across a range of wavelengths (see Chapter 2 Section 2.1.10.1). While there is fairly good agreement between these studies on the scattering parameters at VIS and NIR wavelengths, owing to the comparable lack of data at UV wavelengths, larger uncertainties remain over the scattering parameters at shorter wavelengths. This chapter is concerned with assessing the potential of a spectrometer instrument as a means of monitoring the scattering parameters, ω_0 and g, of the martian dust across the wavelength regime of λ = 180-1100 nm. The UVIS simulation is used to constrain the sensitivity that such an instrument would require in order to track variations in the scattering parameters during the course of a mission.

5.1 Dust aerosol scattering parameters

In order to demonstrate how the uncertainty in the dust scattering parameters can effect the estimation of the surface flux value the dust scattering parameters of Ockert-Bell used thus far in the simulation were replaced by the dust scattering parameters of Pollack et al. (1995) and the outputs were compared. The Pollack et al. study only covers the VIS and NIR wavebands and so the dust scattering parameter values of Mateshvili et al. (2007) were used to extend these data into the UV waveband. The combined Pollack and Mateshvili (hence forth P+M) data were

then interpolated to a nanometre resolution across the working wavelength range using a spline interpolation routine.

Figure 5.1 shows a graphical comparison of the Ockert-Bell and P+M dust scattering parameters where the ω_0 and g curves represent the Ockert-Bell ω_0 and g parameter values minus the corresponding P+M ω_0 and g values respectively. The greatest differences between the two parameter sets occur at the UV and NIR wavelengths for both the ω_0 and g parameters. At the shorter wavelength end of the UV regime the P+M ω_0 values are on the order of 15% lower than the corresponding Ockert-Bell values but by the transition from the UV to the VIS regime the P+M ω_0 values are approximately 10% greater than those of Ockert-Bell, i.e. the P+M dust exhibits a greater absorption cross-section at shorter wavelengths compared to the Ockert-Bell dust but a greater scattering cross-section at the longer wavelengths of the UV regime. The corresponding P+M UV wavelength values of g show a reverse trend to that of the ω_0 values, with greater values of g at shorter wavelengths and lower values at longer wavelengths in comparison to the Ockert-Bell equivalents, i.e. the P+M dust exhibits greater forward scattering at shorter wavelengths than the Ockert-Bell dust and vice versa at longer wavelengths.

Within the VIS regime there is closer agreement between the two data sets, with the P+M ω_0 values staying within 7% of the Ockert-Bell values, although the P+M dust does vary from exhibiting a larger scattering cross-section at the short end of the VIS regime, to a larger absorption cross-section at the mid wavelengths, and then a larger scattering cross-section (by only a few percent) again at the longer wavelengths. The g values of the P+M dust at the VIS wavelengths are consistently lower than the

Ockert-Bell equivalents by on the order of 3%. At the transition between the VIS and NIR wavelengths the P+M g value increases relative to the Ockert-Bell value so that the P+M dust becomes slightly more forward scattering than the Ockert-Bell dust at the longest wavelengths of the study. The NIR ω_0 values for the P+M dust are consistently lower then their Ockert-Bell equivalents, meaning the P+M dust is more absorbing at these wavelengths, with the maximum difference between the two datasets comparable to that in the UV at about 14 %.

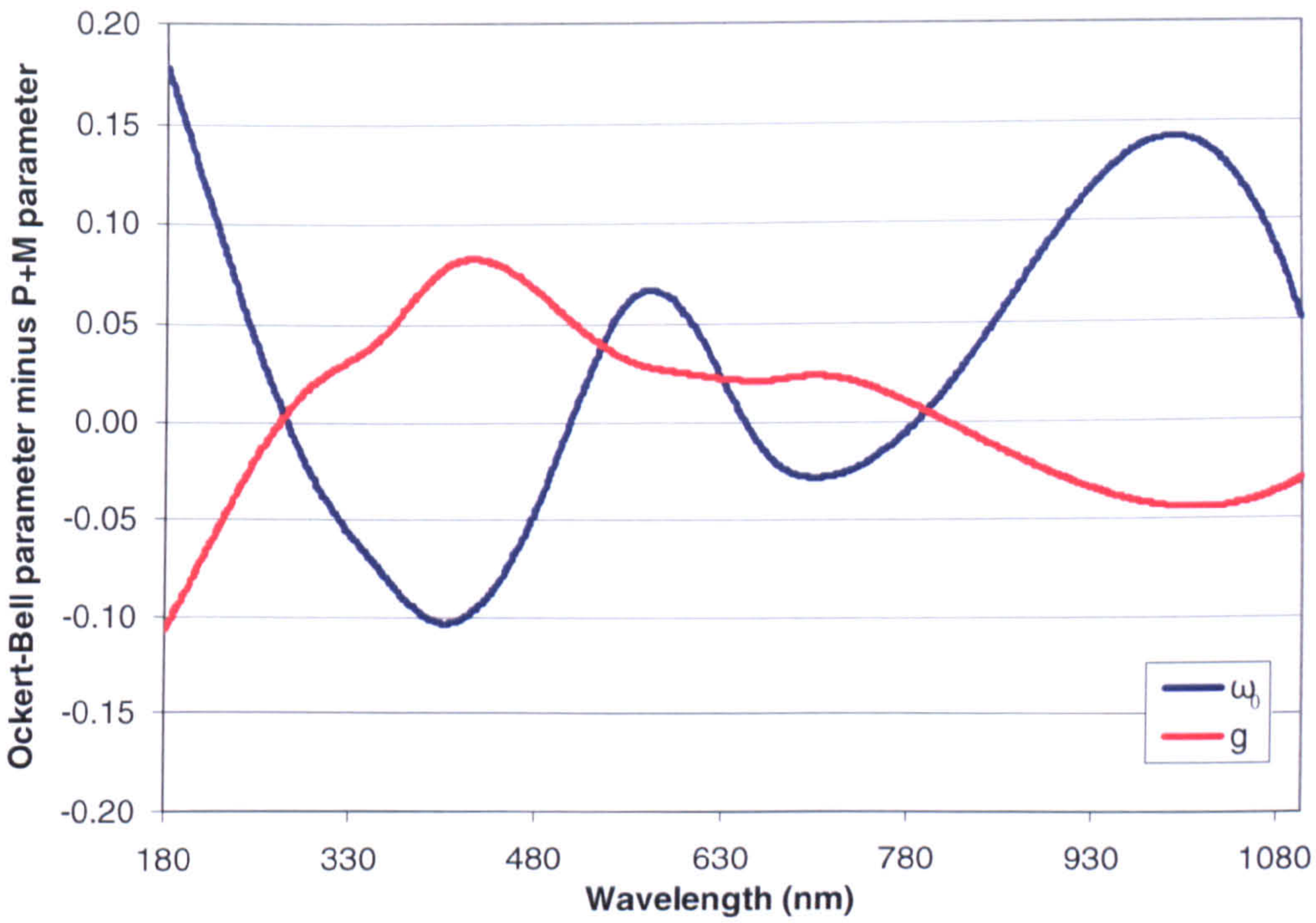

Figure 5.1 – P+M dust scattering parameters subtracted from corresponding Ockert-Bell dust scattering parameters.

Figure 5.2 shows how the difference in scattering parameters discussed above translates into variation in the surface flux by providing a comparison between the surface flux values generated using the Ockert-Bell dust parameters under a 'typical' dust scenario and the surface flux values generated under exactly the same conditions except for the replacement of the Ockert-Bell dust parameters with those of P+M.

The curve shown in Figure 5.2 is the ratio of the P+M surface flux with that of the Ockert-Bell surface flux at each wavelength.

It can be seen from Figure 5.2 that the enhanced scattering cross-section of the P+M dust over the Ockert-Bell dust leads to a predicted increase of approximately 10% in the surface flux occurring at the transition wavelengths between the UV and VIS wavebands, with a second smaller peak of a less than 5% increase occurring near the transition between the VIS and NIR wavelength regimes. The wavelength ranges where the P+M dust exhibits a reduced scattering cross-section relative to the Ockert-Bell dust show a corresponding reduction in surface flux values: At the shorter wavelength end of the UV the curve shows a drop in surface flux value on the order of 8%, a small dip in surface flux of a few percent is predicted centred at λ ~ 580 nm and the NIR sees a significant decrease in the predicted surface flux values across the whole wavelength range, with a maximum relative decrease of the order of 13% occurring at ~ 1000 nm. At wavelengths below λ ~ 200 nm the surface spectrum is dominated by the strong CO_2 absorption feature and not by the incident flux interactions with the dust.

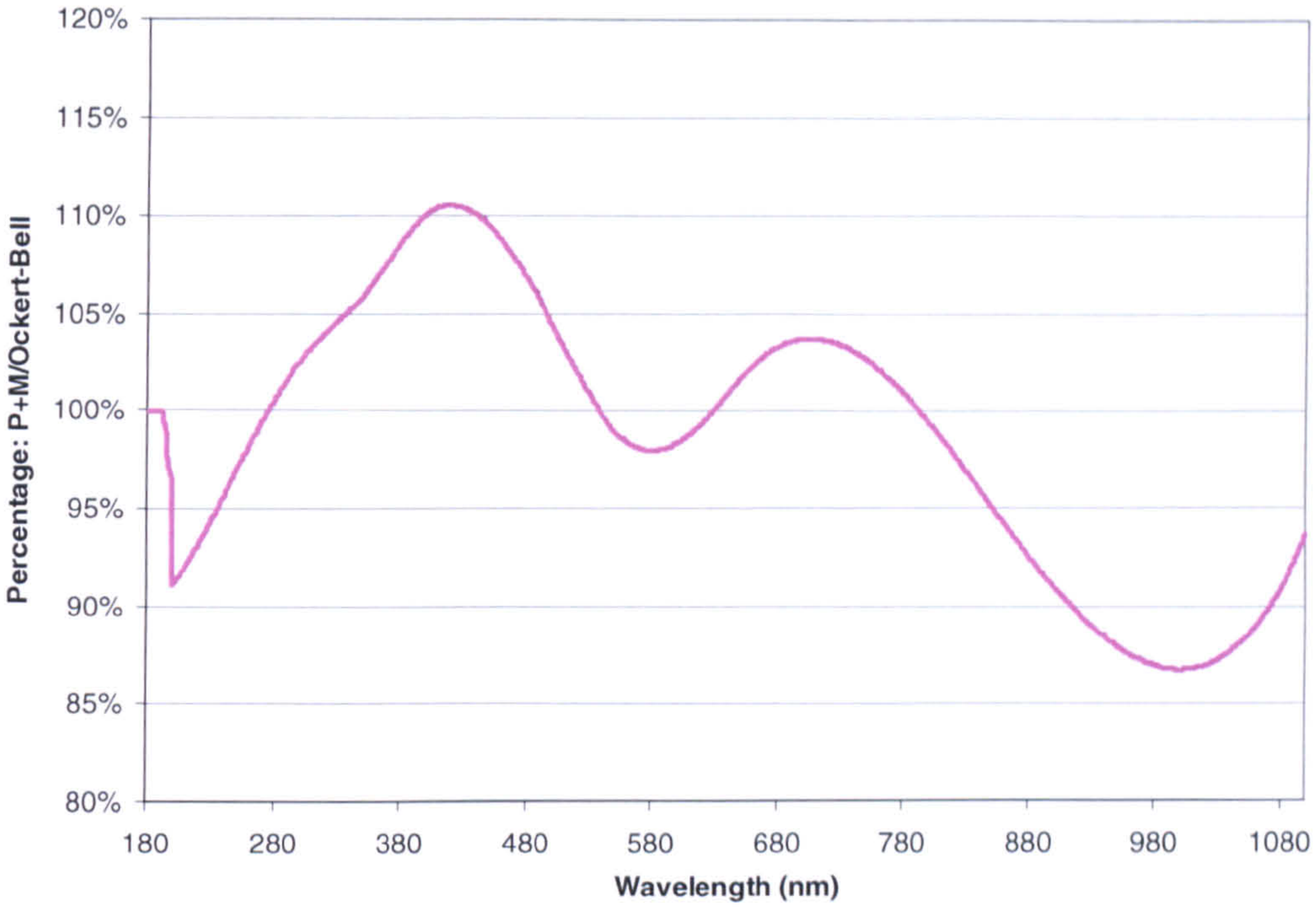

Figure 5.2 – Surface flux generated using the P+M scattering parameters shown relative to the surface flux generated using the Ockert-Bell parameters.

This comparison was conducted to indicate how the uncertainty in the dust scattering parameters translates into an uncertainty in the predicted surface flux values generated by the simulation. For the majority of the VIS wavelengths, where the scattering parameters are relatively well constrained, this uncertainty is on the order of only a few percent. At the UV and NIR wavelengths, where there is less observational data to base the theoretical work upon, the greater uncertainties in the scattering parameters translate into uncertainties of up to 10% and 13% in the surface flux for each wavelength range respectively.

5.1.1 Isolating the effects of ω_0 and g

In order to examine the effect on the surface flux caused by ω_0 and by g individually the simulation was run using the Ockert-Bell parameters under a 'typical' dust scenario to establish a baseline total surface flux. The UVIS simulation was then run repeatedly under the same conditions except that the ω_0 and g parameters were systematically varied so that a surface flux value could be generated for a number of combinations of ω_0 and g values. This was carried out across a range of values spanning 0.1 either side of the initial Ockert-Bell ω_0 and g values and with ω_0 and g varying in steps of 0.01. As with the studies carried out in Chapter 4 a wavelength value of λ = 388 nm was chosen at which to study the effects of the scattering parameters. At this wavelength the lack of any significant gas absorption features means any change in the surface flux should only be the result of the atmosphere's scattering media. The results of this study are shown in Figure 5.3.

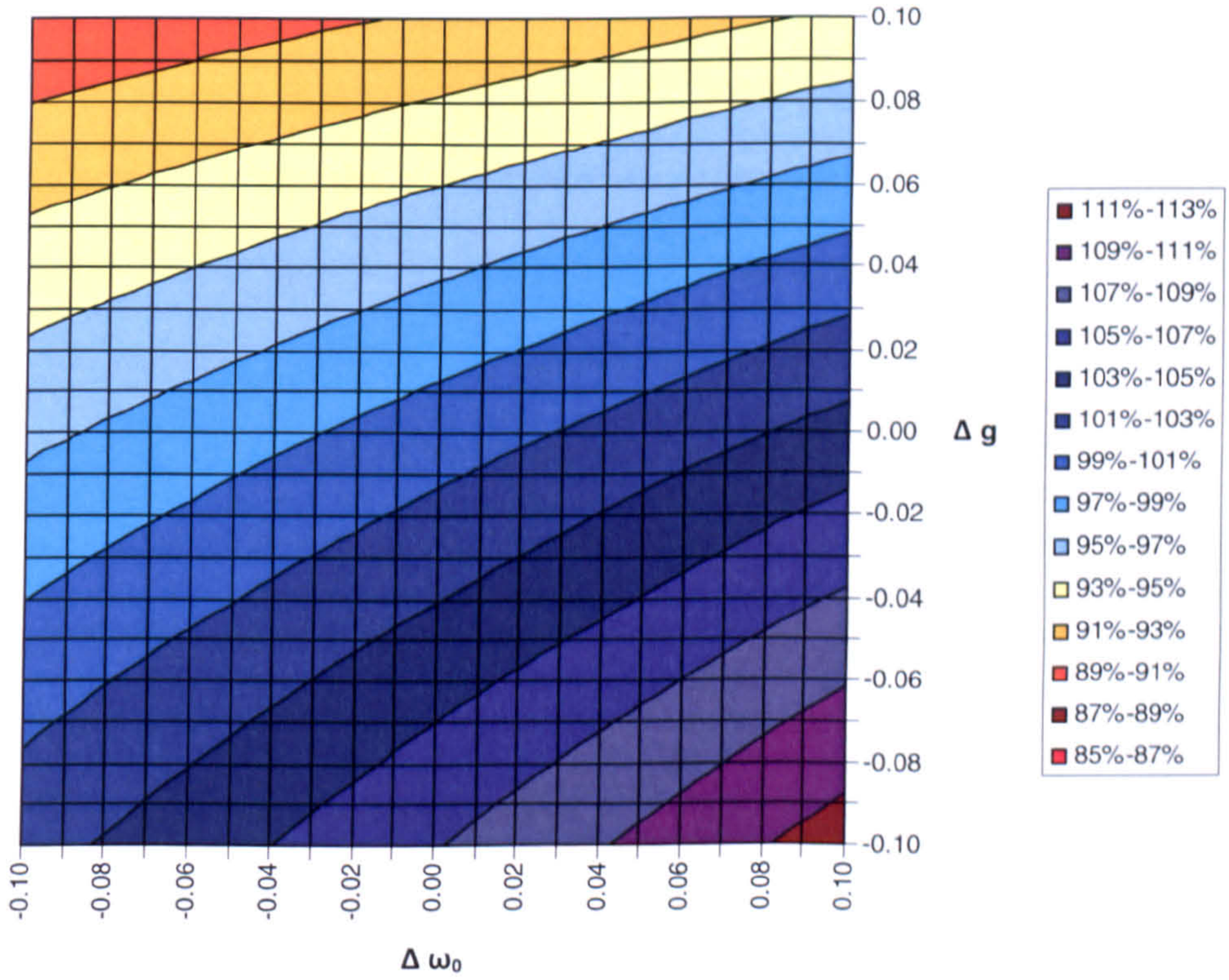

Figure 5.3 – Surface flux value at 388 nm generated by varying the ω_0 and g parameters about the Ockert-Bell default values. Flux is given as a percentage of the flux using the Ockert-Bell default values.

From Figure 5.3 it can be seen that the greatest enhancement of the surface flux occurs when ω_0 is maximized and g is minimized and vice versa. Increasing ω_0 means the dust presents a larger scattering cross-section to the incident flux leading to enhanced scattering away from the zenith angle path of incidence into the diffuse component of the flux. Increasing g constrains the direction of scatter of the dust particles such that radiation is preferentially scattered forwards along the angle of incidence rather than out of the path of incidence to contribute to the diffuse component of the flux. Therefore an increasing ω_0 and a decreasing g both lead to an increase in the diffuse surface flux and a corresponding greater value for the total surface flux. As can be seen from the multiple studies considered in Figure 2.14 and Figure 2.15 of Chapter 2 the scattering parameters appear to follow a generally inverse trend with respect to each other; wavelengths where ω_0 is relatively high tend to exhibit a relatively low value of g and vice versa. Considering Figure 5.3; an increase (decrease) in ω_0 coupled with a decrease (increase) in g produces the largest change in the surface flux value while an increase (decrease) in ω_0 coupled with an increase (decrease) in g more closely follows the contours of the plot. Therefore, it may be possible for changes in the dust scattering parameters to occur but, even if the individual change in ω_0 or g was theoretically sufficient to produce a surface flux change detectable by the instrument, the change in one parameter could be effectively countered by a change in the other parameter. The result of this being to produce little or no corresponding change in the surface flux as the change in one parameter compensates for the other.

5.1.2 Instrument sensitivity to changes in dust ω_0 and g

The dust scattering parameters cannot be directly derived from a measurement of surface flux but need to be modelled based upon a number of different input criteria. Therefore an accurate determination of the surface flux value is invaluable in reducing the uncertainty inherent in the modelling of these parameters. Although it is not possible to measure directly the values of the dust scattering parameters it is possible to use a surface based spectrometer to determine variations in the parameters over the course of a mission lifetime.

It is likely that dust scattering parameters are not constant over the surface of the planet, for the simple reason that the dust itself is unlikely to be of a single uniform variety across the planet. Different erosion rates and mechanisms can lead to different shapes and different size distributions of dust grain. The composition of the surface outcrops from which the dust is derived also plays a part as the chemical composition of the rock can add wavelength dependent absorption features to the dust contribution to the surface spectrum. During the dust storms that form a regular part of the martian climate the size distribution of the dust grain aerosols is likely to vary from that found to occur during more clement weather as the higher wind speeds allow for the lofting of bigger dust grains. Therefore a change in dust scattering parameters may be detectable in the surface spectra recorded through the onset, duration and aftermath of a dust storm event. A further predicted mechanism for causing variation in the dust scattering parameters is the condensation of ice onto the dust grains, a scenario most likely to be observed at the start of the day (Petrova et al., 1996, Ockert-Bell et al., 1997) where the dust grains may act as nucleation centres for atmospheric water vapour. Under these conditions the ω_0 value of the

dust grains will appear to increase owing to the reflective coating of ice enhanced the grain's scattering properties.

An instrument with a good enough sensitivity may be able to detect the changes in the surface flux caused by varying scattering parameters. The UVIS simulation has been used to estimate the sensitivity of an instrument required to be able to detect a certain change in the values of the scattering parameters. In order to do this the simulation was run multiple times with each individual run featuring a small change in the ω_0 value and then the process was repeated this time with the g value varying. By changing ω_0 and g in small increments and noting the corresponding variation in the surface flux value the sensitivity of the surface flux owing purely to the scattering parameters can be shown.

Figure 5.4 plots the effect on the total surface flux at a wavelength of λ = 388 nm caused by the variation in ω_0 and g. As considered previously, the change in the ω_0 and g values is given as an increment (or decrement) to the Ockert-Bell value used in the UVIS simulation. The initial value of g for the Ockert-Bell data at λ = 388 nm is 0.85 while the Ockert-Bell value of ω_0 at λ = 388 nm is 0.62.

The results of this study suggest that an instrument with a maximum sensitivity of ~ 1.0×10^{-2} $Wm^{-2}nm^{-1}$ at λ = 388 nm would only be sensitive to changes in ω_0 greater than ~ +/- 0.06, or conversely, the surface flux value detected by an instrument with this maximum sensitivity would be insensitive to changes in ω_0 of less than ~ +/- 0.06. It can be seen from Figure 2.14 that most of the wavelength dependent values of ω_0 determined in the numerous studies fall within, or very close to, a +/- 0.05

envelope either side of the Ockert-Bell values. The exceptions to this occurring at the short wavelength end of the UV waveband and the longer wavelength end of the NIR waveband. This suggests that, unless the dust ω_0 parameter varies strongly away from the range of values on which the various studies appear to agree, an instrument of maximum sensitivity ~1.0 × 10^{-2} $Wm^{-2}nm^{-1}$ will be insensitive to variations in the ω_0 parameter within this range.

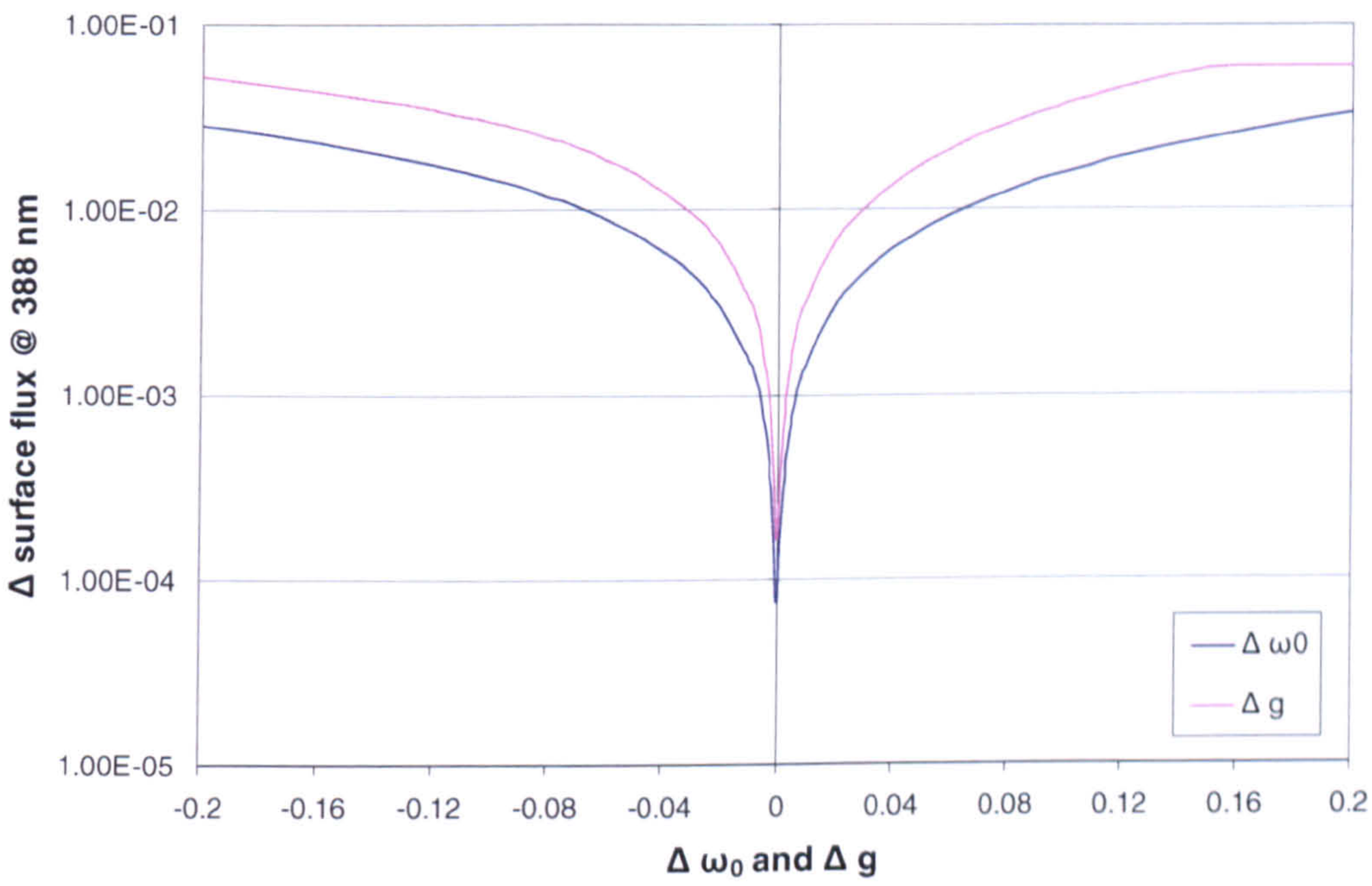

Figure 5.4 – Change in surface flux value as a result of a change in the dust scattering parameter values ω_0 and g.

The effect upon the surface flux of varying g is slightly more pronounced than that of ω_0 which leads to easier detection of changes in g. For an instrument of maximum sensitivity of ~1.0 × 10^{-2} $Wm^{-2}nm^{-1}$ changes in g of greater than ~ +/- 0.03 are estimated to produce a detectable effect. Figure 2.15 shows how there is less agreement between the studies which have determined the wavelength dependent

values for *g*. Differences of greater than 0.1 are observed between the highest and lowest estimates of *g* at some wavelengths and the Ockert-Bell values generally tend towards to the lower boundary of the value of *g* within the VIS and NIR wavebands. An instrument of maximum sensitivity ~ 1.0×10^{-2} $Wm^{-2}nm^{-1}$ should therefore have the potential to detect the changes in the surface flux resulting from the current uncertainty range of *g*.

If the maximum instrument sensitivity is improved by an order of magnitude to ~ 1.0×10^{-3} $Wm^{-2}nm^{-1}$ then changes in the value of ω_0 as small as +/- 0.008 may produce a detectable change in the surface spectrum. For the *g* value changes as small +/- 0.004 are estimated to produce a detectable change in the surface flux. These variations in both ω_0 and *g* fall well within the uncertainty ranges for the two parameters as defined by the existing studies and therefore an instrument capable of achieving this level of sensitivity could be used as a means of tracking the variation of the scattering parameters of the martian dust.

This study was carried out at a single wavelength and this has some bearing upon the results. As the dust scattering parameters are both dimensionless factors that serve to scale the input flux into its diffuse component then the absolute changes in surface flux are greater when the input flux is greater and vice versa. This means that a change of, for example, +/- 0.05 in the value of ω_0 will be more detectable at wavelengths with a higher incident flux. To illustrate this Figure 5.5 shows the absolute change in surface flux at each wavelength caused by increasing the Ockert-Bell value of ω_0 for that wavelength by 0.05. The peak in this absolute difference, of the order of ~ 10^{-2} $Wm^{-2}nm^{-1}$ corresponds to the wavelengths with the highest initial

incident flux while at the short end of the spectrum, where the incident flux is much lower, the absolute changes are of the order of ~ 10^{-4} $Wm^{-2}nm^{-1}$.

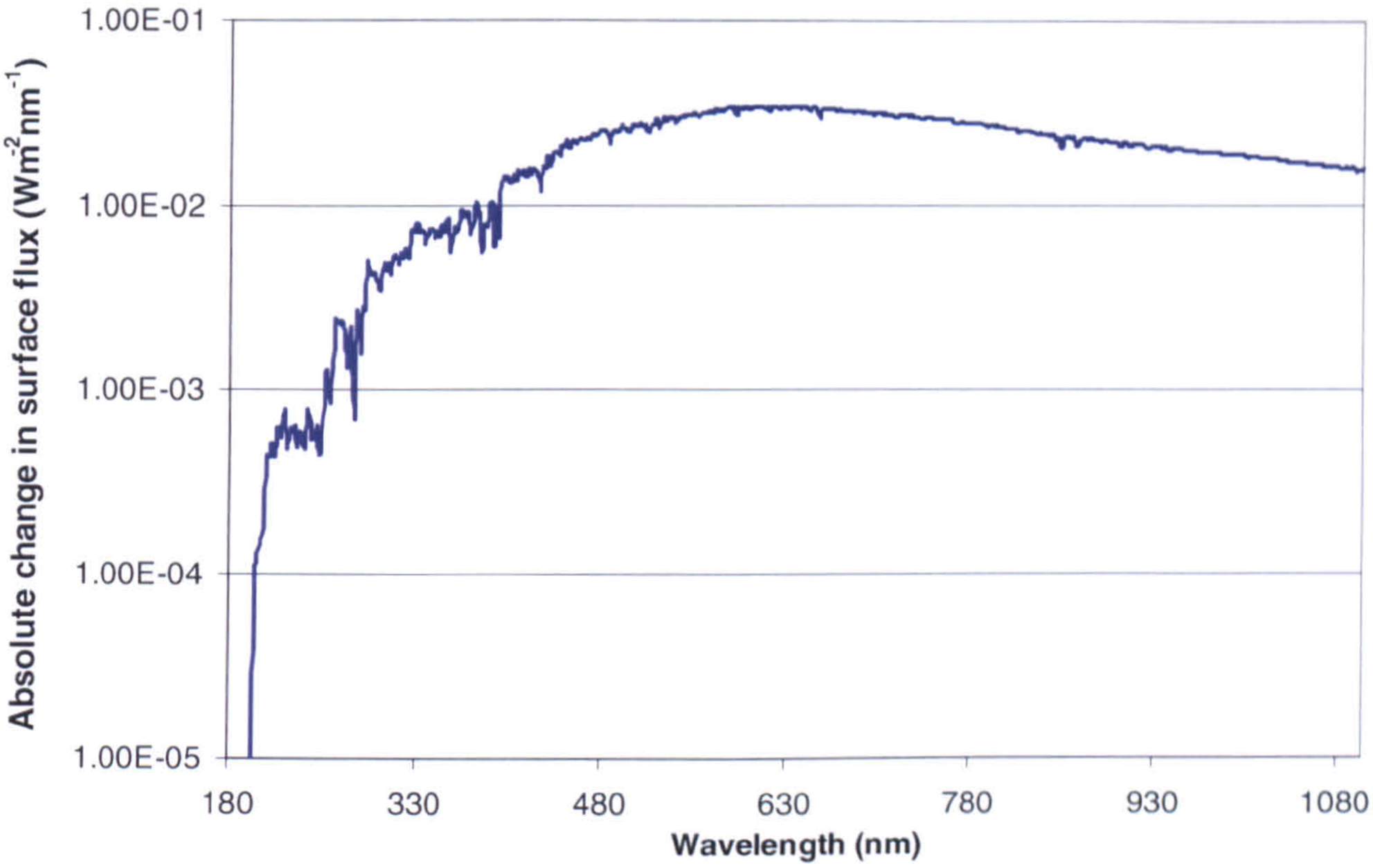

Figure 5.5 – Absolute change in the surface flux value at each wavelength resulting from increasing the Ockert-Bell ω_0 parameter by 0.05.

Of course, monitoring the dust scattering parameters is not as simple as just detecting the resulting change in the surface spectrum as this change can be caused by a number of different factors. Monitoring a wavelength at which these factors are minimised is one way to mitigate this problem, for example as is used here where the wavelength of λ = 388 nm has been utilised owing to the lack of gas absorption features at this wavelength. A comprehensive suite of instruments offers the possibility of eliminating other factors, such as changes in dust optical depth, by combining the observations from a number of different techniques. Independent determination of these factors allows their effects on the surface spectrum to be

modelled and therefore eliminated to a certain degree when considering the changes owing to variation in the scattering parameters.

5.2 Ice aerosol scattering parameters

The ice cloud scattering parameters used in the UVIS simulation are set at values of $\omega_0 = 1.0$ and $g = 0.7$ for all wavelengths, i.e. unlike the dust the ice cloud aerosols are considered to scatter all wavelengths uniformly. A good number of observations of such clouds in the martian atmosphere have been made using ground based, orbital and, to a lesser extent, surface based instruments, which has allowed the scattering parameters to be fairly well constrained. The fine detail in these parameters though, as studies of ice clouds here on Earth have shown, exhibits a dependence upon the size and crystalline shape of the ice cloud particles. As with the dust it is unlikely that the ice cloud scattering parameters remain constant during the martian year and at different locations above the martian surface. Different formation conditions, dependent upon factors such as temperature, pressure and nucleation particles present, will result in a range of values for the scattering parameters. A study by Key et al. (2002) suggests that for different size distributions and different ice crystal shapes, at the wavelengths of interest here, the consideration of a purely scattering ice aerosol ($\omega_0 = 1.0$) is a good approximation. The g parameter tends to display greater dependence upon these factors with variation between limits of approximately $g \sim 0.70$ to 0.85.

The effect on the surface flux caused by varying the ice cloud scattering parameters has also been investigated by running the UVIS simulatin at the equator and at L_s =

90°. These coordinates correspond to the peak abundance of the aphelion cloud belt under the MOD scenario of the simulation and so ice cloud optical depth is high and dust aerosol optical depth relatively low. The ice cloud ω_0 value is already set at a maximum of 1.0 and so can only be reduced from this value. Lowering the ice cloud ω_0 value to 0.9 results in an approximately ~6% reduction in the surface flux predicted across all wavelengths. The value of g is set at 0.7 and so was varied by +/- 0.1 about this value. Increasing g is predicted to decrease the flux received at the surface by approximately ~7% while the decrease in the value of g is predicted to increase the total surface flux by approximately ~6%. The variation in surface flux caused by varying the ice cloud aerosol scattering parameters can be seen in Figure 5.6.

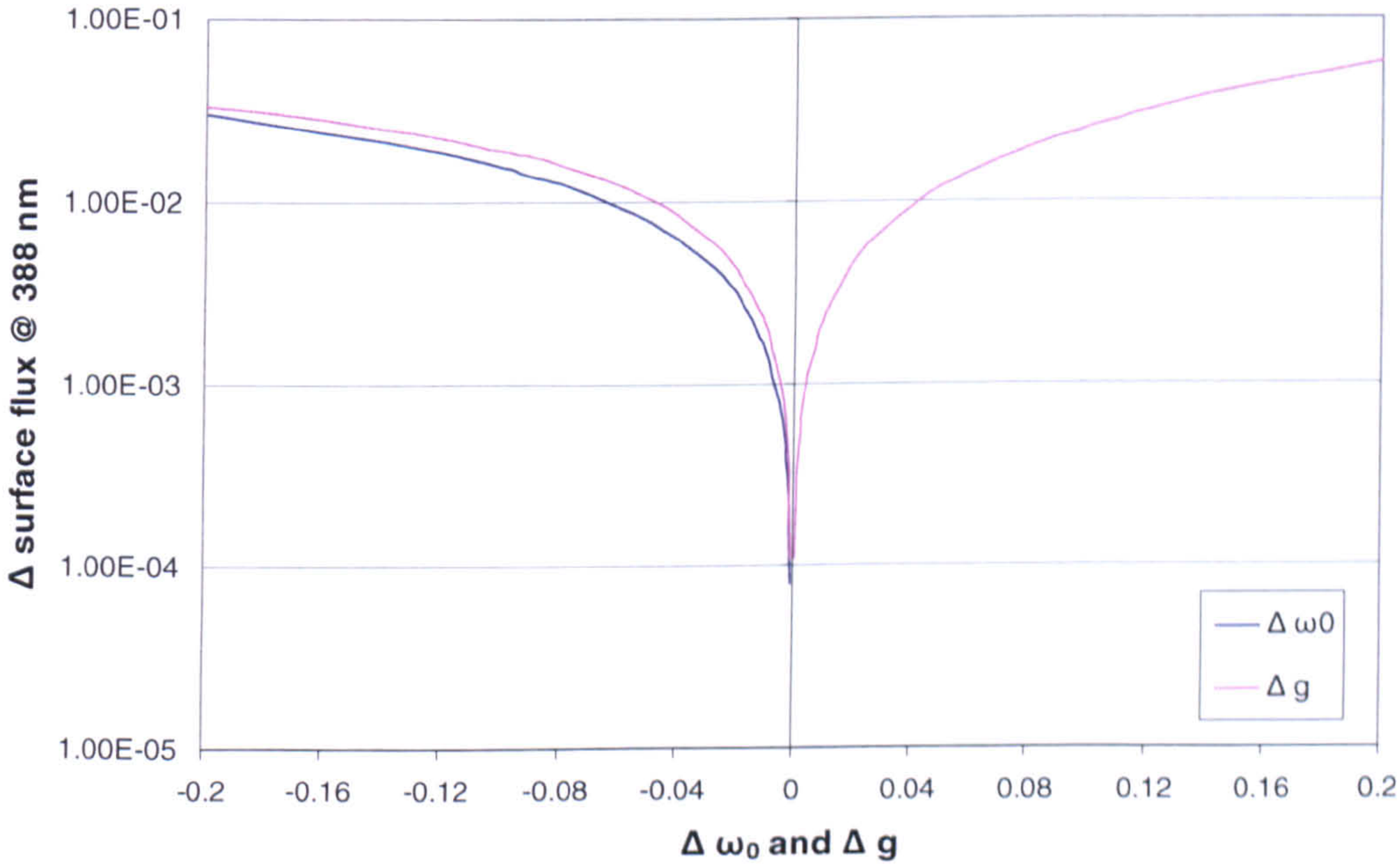

Figure 5.6 – Change in surface flux value as a result of a change in the ice scattering parameter values ω_0 and g.

5.3 Differentiating between dust and cloud influence

It is important to be able distinguish whether the variation in surface flux being detected is the result of variation in the dust aerosol or the ice cloud aerosol parameters. For the purposes of the simulation the variations introduced into the scattering parameter values were done so uniformly across the full wavelength range, i.e. each wavelength specific value of ω_0 or g was varied by the same amount. This is unlikely to be the case for the actual dust where, for example, dust particles of different mineralogical composition are likely to exhibit different scattering parameters. This means that in a similar way to that discussed in Chapter 4 regarding trace gas detection, wavelengths from across the spectral range can be compared to one another to determine relative changes in the different spectral regimes. Mie theory studies of ice cloud aerosol scattering parameters suggest that both ω_0 and i take fairly uniform value across the wavelength range of this study, with variations in crystal structure and particle size causing a uniform variation in the scattering parameters at all wavelengths. Therefore it should be possible to differentiate changes in the dust scattering parameters over changes in ice cloud scattering parameters by comparing the relative change in surface flux at different wavelengths.

Chapter 6 – Discussion and further work

The work contained within this thesis was originally intended to support the development of the UVIS spectrometer instrument for the static lander component of the European ExoMars mission. However, during the course of this work it was announced that the ExoMars mission was to be both delayed and de-scoped, a process which included the removal of the static lander component, and therefore the UVIS instrument, from the mission. Although no longer part of ExoMars, the development of the UVIS instrument continues with the aim of inclusion in future planetary mission payloads.

This thesis is concerned with the development and application of a model of the martian atmosphere, the UVIS simulation, in order to simulate the surface spectra which UVIS may return when operational on the surface of Mars. Over the previous chapters the UVIS simulation has been applied to a number of scenarios in order to assess potential applications of the UVIS instrument. Studies were conducted to characterise how variations in the martian environment and climate affect the surface flux across the wavelength range of the model, and into how the operational limits of the instrument, for example sensitivity or resolution, affect the instrument's suitability for different tasks.

6.1 Discussion of Chapter 3

6.1.1 Dust optical depth and the surface flux

The main objective of the UVIS instrument is to provide a means of monitoring the surface flux, across the operational wavelengths, at a mission landing site. Over a long duration mission the data from the instrument can be used to build up a picture of how the surface flux varies owing to the season and the environmental conditions, ideally over a number of Mars years. As well as simply detecting and recording the surface flux it is of course of interest to infer what is responsible for causing any variations detected. The prime candidate, owing to its well documented seasonal variation and strong interaction with the incident flux, is the ubiquitous Mars dust.

Varying the atmospheric dust loading of the UVIS simulation allowed for the investigation of how the surface flux observed by the instrument may change under different dust optical depths. The surface flux as a percentage of the initial incident flux was plotted against dust optical depth for both the total flux over the operational wavelength of the simulation and the individual UV, VIS and NIR wavelength regimes. At the latitude and L_s value at which the study was conducted the simulation predicts that increasing the dust optical from initially low values to values comparable to 'typical' dust optical depths ($\tau \sim 0.5$), or even to high optical depths ($\tau \sim 1.0$), actually results in local surface flux values which are greater than the local initial incident flux values; a phenomenon caused by the scattering effect of the dust producing a diffuse flux component some of which is scattered into the path of incidence (see Chapter 3 Section 3.1). If the dust optical depth is further increased then the absorption effect of the dust begins to become important and the local surface flux begins to steadily decrease in value with increasing optical depth.

Studies such as this demonstrate the ability of the spectrometer to act as a means of monitoring the dust loading, and therefore weather conditions, at the martian surface. For example, the approach of a dust storm across a mission landing site could be tracked by a tell-tale increase and then decrease in the local surface flux detected over time as the dust optical depth in the atmosphere above the landing site increases to dust storm levels. An instrument with a resolution on the order of +/- 10% with respect to the surface flux value should be capable of confirming the occurrence of such an event. However, if the instrument is to be utilised to monitor small changes in the dust optical depth, for example on the order of $\tau = 0.5$ or below, then the behaviour of the surface flux under increasing dust optical depth poses a problem. The shallow gradient predicted either side of the peak surface flux means that between the dust optical depth values of approximately $\tau \sim 0.5$ and $\tau \sim 2.5$ the maximum change in the predicted surface flux is only on the order of a few percent. Away from the peak surface flux, steeper gradients mean greater changes in surface flux are predicted for equivalent changes in dust optical depth but it is this zone of dust optical depth values from $\tau \sim 0.5$-2.5, encompassing the 'typical' and 'high' dust scenarios of the UVIS simulation, which is most likely to be encountered during instrument operation. Therefore comparatively high instrument sensitivity is required in order to accurately characterise the surface flux response to increasing dust optical depth under the anticipated operating conditions.

A significant difference is observed in the behaviour of the surface flux within the three wavelength regimes specified in this work. At UV wavelengths the larger absorption cross-section presented by the dust (compared to the other VIS and NIR

regimes) means there is no enhancement of the flux above the initial incident value and the direct flux is the dominant component until significant dust optical depths are reached. Overall the UV flux shows strong attenuation under the dust (see Chapter 3 Section 3.1.2). A different trend is observed at VIS and NIR wavelengths where the strongly scattering dust leads to large diffuse flux components, particularly in the NIR (see Chapter 3 Sections 3.1.3 and 3.1.4). This in turn leads to enhancement of the local surface flux with the diffuse component corresponds to radiation being scattered into the path of incidence. This enhancement is predicted to persist for optical depth up to $\tau \sim 2.5$ for the VIS wavelengths and optical depth approaching $\tau \sim 6.0$ for the NIR. At higher optical depths dust abundances are sufficiently high that the absorption cross-section of the dust aerosols also becomes important and predicted surface flux value declines.

6.1.2 Global flux studies

In the future it may be possible to realise a network of surface science stations distributed across the planet's latitudes and regions of interests, such as the proposed NetLander (Harri et al., 1999, Marsal et al., 2002) and MetNet (Harri et al., 2003) missions. These stations will monitor the local surface environment in terms of, for example, the temperatures, pressures, wind speeds, seismic activity and the radiation levels. The spectrometer would make an ideal addition to a mission of this kind; able to record the variations in the non-ionising surface flux as a basic function but, depending upon the final operating wavelength range and sensitivity, with potential applications in aerosol scattering parameter characterisation and trace gas detection.

In Chapter 3 the UVIS simulation was used to examine the effect that changing aerosol optical depth has on the surface flux over a global scale. In effect this is simulating the deployment of a network of instruments across the martian surface albeit in greater numbers than is likely to occur in the missions of the foreseeable future. This was achieved by running the simulation at intervals of 10° and 15° across the planet's latitudes and orbital L_s values respectively and recording the surface flux predicted at local midday at each interval. It can be clearly seen from the resulting plots (see Chapter 3 Sections 3.2.3-3.2.5) that the major factors influencing the surface flux are first and foremost the orbital L_s value and the planet's axial tilt. Overlain on these is the effect due to the martian atmosphere itself, i.e. the absorption and scattering of the incident flux by the atmospheric gases and aerosols.

One of the important things demonstrated in this section of the study is how at different times of the year and at different latitudes different atmospheric aerosols dominate the incident flux interactions. During the northern hemisphere summertime dust activity tends to be low and it is the ice cloud aerosols of the aphelion cloud belt that have the greatest influence on the flux reaching the planet's surface. Where ice cloud optical depths are sufficiently large the highly scattering properties of the ice cloud aerosols are predicted to result in local values of the surface flux which are greater than the initial incident values. A situation that arises as interactions with the ice cloud aerosols scatters radiation into the incident path. The maximum optical depths of the aphelion cloud belt tend occur near the equator and centred around a value of L_s = 90°, under these conditions significant enhancements of the total surface flux, on the order of ~20-30% relative to the initial incident flux, are predicted to occur.

During the southern hemisphere summertime it is the turn of the dust to dominate the incident photon interactions. The period of maximum atmospheric dust optical depth varies from year to year but generally occurs within +/- 30° of L_s = 270° and across most latitudes. Within this period dust optical depths can reach values greater than τ ~ 1.0 (the limit of the 'high' dust activity scenario used in the simulation).

Considering the total surface flux, i.e. across the whole wavelength range under study, under 'typical' dust opacities the presence of the dust has an enhancing effect with local total surface flux values being greater than the initial incident flux. The level of enhancement is seen to increase under 'high' dust conditions. As the dust is not as purely scattering as the ice cloud aerosols equivalent optical depths of dust produce a lower enhancement of the local surface flux compared to the ice cloud aerosols. Unlike the uniform scattering parameters of the ice cloud aerosols the values of the dust scattering parameters exhibit a strong wavelength dependence, particularly at shorter wavelengths and this means there are notably different results for how the UV, VIS and NIR regimes of the incident flux are affected by interaction with the dust aerosols. As can be seen from the results of the study involving increasing dust optical depth, in the NIR regime (see Chapter 3 Section 3.2.5) dust exhibits a high average scattering average cross-section and so the local surface flux exhibits the greatest relative enhancement at these wavelengths. In the VIS regime the dust exhibits lower scattering cross-sections (and correspondingly higher absorption cross-sections) and so relative enhancements of the surface flux are lower. In the UV regime the average scattering cross-section is lower still and at these

wavelengths the local surface flux values are lower than the initial incident values, rather than the enhanced flux seen for the VIS and NIR regimes.

This study highlights the usefulness of an instrument capable of operating over a large wavelength range. This allows the wavelength dependent variations in the dust interaction with the incident flux to be characterised and also affords the ability to compare wavelength regimes against one another. For example, the surface visible flux has been studied in much greater detail than the surface UV flux thanks to instruments sensitive to these wavelengths being present on all previous surface landing missions and therefore these previous studies can be used to validate the results obtained by the spectrometer. If the spectrometer is capable of monitoring across both UV and VIS wavelength regimes then the validation of the VIS results would suggest the ability to apply the same instrument and techniques to the poorly characterised UV regime with a reasonable degree of confidence.

6.1.3 Landing site studies

Also contained within Chapter 3 is a study of the potential landing sites proposed for future Mars surface missions such as MSL or ExoMars (see Chapter 3 Section 3.3). This study takes the form of a characterisation of the predicted surface flux at the latitudes corresponding to the landing sites over a full Mars year. This is used to assess the suitability of each landing site for the deployment of a spectrometer in terms of the flux values received and possible science returns.

The landing sites within a latitude band stretching from approximately the equator to l = 20°N, which encompasses Meridiani Planum and Gale Crater and parts of Mawrth Vallis and Nili Fossae, appear to be the most suitable for the deployment of a spectrometer. This is owing to the relatively high and relatively constant surface flux which is received at these latitudes throughout the entire year. For the potential southern hemisphere landing sites the variation in flux level across the year is significant, at l = 30°S the maximum surface flux is around three times greater than the minimum surface flux, and, for comparison, this minimum surface flux is only about half the value of the minimum surface flux predicted at the equator. In general a high flux signal is preferred as this presents a better signal to noise ratio for the instrument, although whether the low value of the southern hemisphere minimum flux proves a limiting factor in the operation of the instrument depends of course on what the final operating sensitivity of the instrument is.

The equatorial and low northern latitudes are also of scientific interest in that they are exposed to two significant components of the martian climate. The high dust optical depths present in the southern hemisphere summer tend to extend up to and above the equator, while during the northern hemisphere summer the maximum optical depth of the ice cloud aerosols tends to be located over approximately equatorial latitudes. During a year of operation at equatorial latitudes the instrument would therefore be able to characterise the effects on the surface flux resulting from both the dust and the ice cloud aerosol components of the atmosphere across a wide range of wavelengths.

6.1.4 Diurnal flux studies

As well as the ability to characterise seasonal and long term effects on the surface flux a spectrometer could also be used over smaller timescales to characterise the local flux over the course of a sol. These studies were carried out at the landing site latitudes and were used to predict the diurnal local flux variation at L_s values of 0°, 90°, 180° and 270°. The main point of interest highlighted by this study is the comparison of the direct and diffuse components of the surface flux over the course of the day and how the ratio of the two components is affected by the atmospheric conditions. Although a spectrometer would only be able to detect the total surface flux and not the two distinct components, it is useful to use this capability of the simulation to investigate the composition of the detected flux.

The studies showed that under low atmospheric optical depths the diurnal flux is dominated by the direct component for the majority of the day with the diffuse component only approaching the levels of the direct component at the high zenith angles (and corresponding high airmass) encountered shortly before and after sunrise (see Chapter 3 Sections 3.3.2.1-3.3.2.4). Under 'typical' dust optical depths the direct component still dominates around the solar zenith but the diffuse component is predicted to come to prominence at lower zenith angles. As the atmospheric optical depth increases the zenith angle value at which the diffuse flux component begins to dominate over the direct flux component continues to decrease, i.e. the period of dominance of the diffuse component becomes closer to midday, until at sufficiently high optical depths even the flux at the zenith is primarily diffuse. Owing to the higher scattering cross-sections of the ice cloud aerosols the dominance of the local surface flux by the diffuse component occurs at lower atmospheric optical depths of

this aerosol compared to dust aerosols. Taking as an example the simulated diurnal profiles under the 'typical' dust scenario occurring at the equator and at $L_s = 90°$ and $L_s = 270°$ (see Figure 3.21 and Figure 3.22); it can be seen that at $L_s = 90°$ the local diurnal flux is dominated by the diffuse component throughout the day while the diurnal profile at $L_s = 270°$ is dominated by the direct component of the local flux for all except the first and final hour or so of daylight. The $L_s = 90°$ diurnal profile represents the local surface flux under the influence of the peak optical depths of the aphelion cloud belt while the diurnal profile at $L_s = 270°$ corresponds to the local surface flux under the influence of a comparable dust optical depth near the peak value of the dusty season.

6.2 Discussion of Chapter 4

There are a number of gas species of scientific interest that occur in trace amounts in the martian atmosphere and some of these have well characterised absorption cross-section values within the wavelength range under study. Therefore, if present in sufficiently high abundance, these gases should produce absorption features in the surface spectrum which could be detected by a surface based spectrometer. In Chapter 4 a study was conducted to determine the sensitivity of a spectrometer required to detect the presence of these trace gases at varying levels of abundance. This was done by running the simulation multiple times with all parameters kept constant with the exception of the column abundance of the gas species under study. The value of the surface irradiance at a wavelength corresponding to high absorption cross-sections of the gas was ratioed with the surface irradiance value at a

wavelength where gas absorption is negligible and the value of this ratio was then plotted as a function of increasing gas abundance.

Of the trace gases under consideration ozone has been detected in the greatest abundance and is thought to be created through photolysis reactions in the planet's atmosphere. The UVIS simulation was applied to calculate the ratio of the surface flux at λ = 252 nm (where ozone absorption cross-sections are large) against the surface flux at λ = 388 nm (where ozone absorption cross-sections are negligible) under conditions of increasing ozone abundance. This ratio showed little variation until ozone column abundances of approximately 1.0×10^{16} cm^{-2} were reached and then the variation remained less than an order of magnitude until column abundances in excess of 1×10^{17} cm^{-2} were encountered.

Although ozone column abundances on the order of these magnitudes have been observed in the martian atmosphere, they occur at higher latitudes away from the equator. Nearer the equator, where the geographical and environmental conditions tend to be more suitable for surface mission landing sites, the observed ozone column abundances are much lower and even maximum ozone column abundances are likely to be too low to for an instrument such as UVIS to detect.

The confirmed detection of methane in the atmosphere of Mars has only come in the last few years and speculation remains as to the source of the gas, in particular whether the gas may be of biological origin. For this reason the characterisation of the methane gas distribution and abundance is of great interest and may well be considered as an important objective for future Mars missions.

Unfortunately methane presents only a comparatively small absorption cross-section (approximately six orders of magnitude smaller than the peak ozone absorption cross-section) at the wavelengths relevant to this study, with the peak absorption occurring at $\lambda = 839$ nm. This means that a large abundance of methane, on the order of 1.0×10^{22} cm^{-2} (only an order of magnitude smaller than the corresponding CO_2 column abundance), is predicted to be required to produce an absorption signature within the surface spectrum. The highest methane column abundance that has so far been observed is approximately seven orders of magnitude less than this and therefore it is unlikely that these wavelengths are suitable for conducting studies of the methane content of the martian atmosphere.

Hydrogen peroxide is predicted to be created in the martian atmosphere through the photolysis of water vapour and is a highly reactive species which has been proposed as one of the main species responsible for the strongly oxidising environment at the surface of Mars. Hydrogen peroxide exhibits a large absorption cross-section between λ = 190 and 215 nm which steadily decreases in magnitude at longer wavelengths. This range of peak absorption coincides with strong absorption from both ozone and carbon dioxide and so could make it difficult to distinguish the effect of absorption owing to the presence of hydrogen peroxide rather than the other two species. The study in Chapter 4 (Section 4.3.3) takes into account only the effects of variation in the hydrogen peroxide abundance.

The ratio of the surface flux at λ = 200 nm with that at λ = 388 nm showed no variation until hydrogen peroxide abundances close to 1×10^{17} cm^{-2} were reached.

The highest hydrogen peroxide column abundances so far inferred from observations of Mars are slightly less than 1×10^{16} cm^{-2} suggesting that there is approximately one order of magnitude difference between the current maximum observed hydrogen peroxide column abundances and the column abundance required to produce detectable changes in the surface spectrum.

There has been so far no conclusive proof of the detection of ammonia in the martian atmosphere but it was included in this study because although it may not naturally occur on Mars in any significant quantity it may be transported to Mars within the EDLS of surface mission probes.

Like ozone and hydrogen peroxide, ammonia exhibits a large absorption cross-section at the shorter wavelengths of this study ($\lambda < 205$ nm) and so any ammonia absorption effects in the surface spectrum may be difficult to separate from the effects of the other species which absorb at these wavelengths. Owing to the large absorption cross-section a column abundance on the order of only 1×10^{15} cm^{-2} and above of ammonia results in variation in the ratio between the surface spectrum at λ = 201 nm and at λ = 388 nm.

Also assessed in Chapter 4 was the potential of a spectrometer instrument to study the variation in the atmospheric pressure at the martian surface. This could be achieved through the pressure dependence of the surface spectrum 'cut-off' point observed at the short wavelength end of the spectral range of this study. The studies carried out here using the UVIS simulation predict that increasing the surface pressure causes the spectral cut-off to occur at longer wavelengths. Over a surface

pressure test range of 100 to 1000 Pa it was shown that an instrument with nm wavelength resolution requires a surface flux sensitivity on the order of 1×10^3 $Wm^{-2}nm^{-1}$ or better to detect pressure related variations in the surface spectrum cut-off point.

6.3 Discussion of Chapter 5

The studies in Chapter 5 were concerned with the aerosol scattering parameters and how variations in these parameters influence the radiative flux reaching the planet's surface. The potential of a surface based spectrometer to detect the changes in the surface flux resulting from these scattering parameter variations was also considered.

6.3.1 Dust aerosol scattering parameters

The large uncertainties in the determined values of the dust scatting parameters was demonstrated by comparing the surface flux results using the Ockert-Bell et al. (1997) parameters (Ockert-Bell dust), the 'default' parameters for the UVIS simulation, with an alternative set of parameters composed of the values determined in the studies of Pollack et al. (1995) and Mateshvili et al. (2007) (P+M dust). The largest discrepancy between these two datasets occurs at UV and NIR wavelengths with P+M dust presenting a significantly greater absorption cross-section and exhibiting a more forward scattering phase function than the Ockert-Bell dust at the two extremes of the wavelength range. The datasets also differ at the transition wavelengths between the UV and VIS regimes where the P+M dust exhibits dust exhibits a greater scattering cross-section than the Ockert-Bell dust. Better

agreement between the two datasets occurs across most of the VIS wavelengths (see Chapter 5 Section 5.1).

Comparing the surface fluxes resulting from running the UVIS simulation using the two datasets echoed the large uncertainties of the UV and NIR wavelengths with correspondingly large differences in the surface flux values generated. The difference between the two surface fluxes remained less than 5% across most of the VIS wavelengths but at UV and NIR wavelengths differences on the order of 10% are predicted. This highlights the fact that the results of the investigations carried out in for thesis must be considered in light of the dust scattering parameters chosen for the simulation and the large uncertainties present in their values.

The UVIS simulation was also used in this chapter to study the effects of varying the dust scattering parameters about the default Ockert-Bell values (see Section 5.1.1). Each parameter, ω_0 and g, was varied in incremental steps and the surface flux generated for each combination of ω_0 and g. This study highlighted how changes in one parameter can theoretically be compensated for by changes in the other parameter such that, although the scattering parameters of the dust have changed, there is little or no resultant change in the predicted surface spectrum. Correspondingly though changes in the dust parameters can also combined to result in greater surface flux variation. Generally increases (decreases) in ω_0 combined with decreases (increases) in g result in the greatest change to the surface flux value while if both ω_0 and g decrease or increase the changes in the surface flux value are less.

Also covered in Chapter 5 (see Section 5.1.2) was an assessment of the sensitivity required from a surface based spectrometer instrument in order to monitor changes in the dust scattering parameters. The study suggests that changes in the dust parameters on the order of +/- 0.01 about the Ockert-Bell values at each wavelength would produce a change in the surface flux theoretically detectable by an instrument with sensitivity on the order of 1×10^{-3} $Wm^{-2}nm^{-1}$ or better. At the wavelength used for the study ($\lambda = 388$ nm) a change in g of +/- 0.04 is theoretically detectable by an instrument with sensitivity on the order of 1×10^{-2} $Wm^{-2}nm^{-1}$ or better but at this sensitivity it requires changes on the order of +/- 0.07 in the ω_0 value before detection is theoretically possible.

6.3.2 Ice cloud aerosol scattering parameters

The results of varying the ice cloud aerosol scattering parameters were also considered in Chapter 5 (see Section 5.2), using the same methodology as was applied to the dust particles. This study was carried out at the equator and at $L_s = 90°$ corresponding to the seasonal occurrence of the aphelion cloud belt when ice aerosol optical depths are high and dust aerosol abundance is low. The ice cloud aerosols were assumed to be purely scattering at the wavelengths under study and correspondingly assigned a value of $\omega_0 = 1$. The scattering asymmetry parameters were assigned a value of $g = 0.7$ and again this was constant across the entire wavelength range.

The ω_0 value for the ice cloud aerosols is already at the maximum permitted value and so could only be reduced from this value. Lowering the ω_0 value by 0.1 results

in a ~6% reduction in the surface flux value as the reduction in scattering by the ice cloud aerosols reduces the diffuse component of the flux being scattered into the path of incidence of the local surface flux. The g value was varied by +/- 0.1 either side of the initial value of $g = 0.7$ and it was predicted that the increase in g, i.e. scattering becomes more concentrated along the path of incidence, would result in a decrease in surface flux of ~7%. Decreasing the value of g, i.e. scattering becomes more isotropic, is predicted to result in a ~6% increase in the surface flux.

6.4 Further work

The UVIS simulation is a powerful tool for analysing the non-ionising radiation environment at the surface of Mars and is suitable for application to a large and varied range of studies. It was planned to include some of the applications discussed below within the scope of this thesis however time constraints prevented this.

The simulation does not currently feature any parameters that exhibit local-time dependence. It is known that various components of the atmosphere do vary in abundance over the course of a Mars day and included amongst these is the optical depth of the dust (Smith and Lemmon, 1999; Formisano et al., 2001). It would be useful to incorporate this time dependence into the dust optical depth used during the diurnal studies in order to present a more accurate prediction for the surface variation across a Mars day. Observations and modelling of early morning fogs and hazes at the martian surface could also be incorporated in the simulation by varying the optical depths and scattering parameters appropriately with a local-time dependence. It would be interesting to characterise the effect of the increased scattering likely to

be caused by these fogs and hazes upon the relative magnitudes of the diffuse and direct components of the local surface flux.

In Chapter 3 of this thesis the variation in the direct, diffuse and corresponding total surface flux caused by increasing the dust optical depth was investigated (see Section 3.1), however the study presented here was performed only at a single wavelength. An interesting follow up of that study would be to compare how the direct and diffuse components of the surface flux vary across the full wavelength range of the study, especially at different L_s values where the predominant scattering aerosol in the atmosphere may vary between dust and ice clouds. Although the ice clouds are modelled with wavelength invariant scattering parameters this is not the case for the dust. At the longer wavelengths the dust is significantly more scattering than at the shorter wavelength and therefore at certain optical depths it is predicted that at shorter wavelengths the direct component of the flux will dominate while the diffuse component is dominant at the long wavelengths. This implies there is a cross-over point in the spectrum where the dominant flux component swaps from direct to diffuse. An interesting study would be to characterise this cross-over point as a function of dust optical depth, in order to see if changes in optical depth shift the cross-over to different wavelengths. If this is the case then determination of the cross-over point wavelength during operation of the instrument could be used as a means of inferring the present atmospheric dust optical depth.

The UVIS simulation could also be utilised to conduct long duration studies of the non-ionising radiation flux at the planet's surface. By either developing the existing simulation or by running the simulation in conjunction with a GCM, for example, it

would be possible to provide continuously varying input to the simulation in order to represent a constantly evolving atmosphere. Interesting scenarios could include monitoring the change in surface flux before, during and after a large scale dust storm or perhaps during the onset of the major cloud formations. Now that the stage has been reached where the atmosphere of Mars has been monitored continuously in detail for consecutive years it would be possible to recreate a period of recent Mars history for the UVIS simulation. The values predicted by the simulation over this period could then be compared with numerous points of reference provided by the wealth of orbital and surface based observations that are being accrued.

Further applications could include studying exposure to the surface flux in relation to shielding by certain surface features of Mars, for example crater walls, the sides of hills or dunes and surface cracks and crevices. A study of this kind has been carried out by Moores at al. (2007) to look specifically at the shielding afforded at UV wavelengths. A similar study could involve extending this across the range of the UVIS simulation to see how shielding potential varies with wavelength. As was discussed in Chapter 3, the UV flux under significant dust loading tends to be lower than the initial flux incident at the top of the atmosphere but the opposite is true of the VIS and NIR wavelengths where local enhancement of the flux over the initial incident value is predicted. These enhancements take the form of a large diffuse flux component which is harder to shield against. While the UV flux is generally considered harmful to living organisms this is not the case for the longer wavelengths, in particular, the VIS wavelengths can be utilised as a an energy source to drive photosynthetic reactions. Therefore, in addition in the UV 'safe havens' considered in Moores et al. , it may also be possible to find safe havens where

photosynthetic life forms could exist, shielded from the direct flux and its UV wavelengths yet still receiving sufficient diffuse longer wavelengths for energy production.

Such surface flux studies could also be used to consider the conditions at potential landing sites during a mission's development phase. The consequences of the flux studies conducted in Chapter 3 for the use of solar power as a surface probe power source were discussed at the end of that chapter. A more detailed study, characterising the direct and diffuse components across the diurnal and seasonal cycles would offer an insight into how to optimise the power generating potential of the probe's solar array. For example, direct flux dominated scenarios may require positioning of the panels to meet the incident flux, while a diffuse dominated scenario may indicate that a fixed panel solution is suitable. The simulation is also capable of determining the upwelling diffuse flux reflected from the surface of the planet and again, characterisation of this may be relevant to solar array design. A great enough upwards flux could warrant the deployment of a bi-facial solar array, i.e. an array with photovoltaic cells on both the upper and lower sides of the panel, potentially allowing for a smaller solar array footprint. This idea has been considered by NASA for future missions (Landis et al., 2004) and may benefit from a more detailed approach in which the wavelength dependence of the individual flux components can be predicted.

Although designed to predict the incident flux at the surface of Mars, the UVIS simulation is not necessarily restricted to this application. By changing the relevant input parameters, such as the atmospheric pressure profile, the gas and aerosol

species present and their associated scattering and absorption values, the UVIS simulation could be applied to study the radiative transfer processes in other atmospheres within our solar system. For example, of the inner terrestrial planets, Venus, Earth and Mars all have appreciable atmospheres, while the outer planets, the 'gas giants' Jupiter, Saturn, Uranus and Neptune, could be considered to be composed mostly of atmosphere. Then there is also Saturn's moon Titan which exhibits an atmosphere denser than that found around the Earth.

The atmosphere of Earth has of course been studied in great detail over many years using a number of complex models supported by detailed observations. Away from Earth though, information on the atmospheres of the different solar system bodies must be gathered from Earth based observations or by sending difficult and expensive robotic probe missions. Correspondingly there is still much work to do in characterising these atmospheres and understanding the processes that drive the observed phenomena.

The main limiting factor determining the scenarios in which the UVIS simulation can be applied is the optical depth of the atmosphere under study, with the simulation breaking down at higher optical depths (Joseph et al., 1976). This is fine when considering the atmospheres of Earth and Mars within the wavelength range given in this study but may limit application in the more optically dense atmospheres of Venus and the gas giant planets. Here, the UVIS simulation could still be applied to the upper levels of the atmosphere, where optical depths are lower, in order to predict the penetration of the incident solar flux at different wavelengths and its interaction with the constituent species found there.

Similarly the optically dense atmosphere of Saturn's moon Titan may mean that the UVIS simulation could not be used to generate surface flux predictions but could be used to simulate the radiative transfer in the upper atmosphere. This could be a particularly interesting application of the simulation as observations returned by the Huygens probe, which reached the surface of Titan in 2005 (Niemann et al., 2005), and the continuing Cassini mission (Matson et al., 2002, Mitchell, 2008), in orbit around the Saturnian system since 2004, have provided a wealth of useful data on Titan's atmosphere. In particular Titan's atmosphere exhibits some unusual organic chemistry and processes, which it is thought are driven by the solar flux incident on the atmosphere and includes a methane cycle which appears to operate along the same lines as the water cycle on Earth (Atreya et al., 2006a, Tomasko et al., 2008, Lebreton et al., 2009, Hirtzig et al., 2009). The UVIS simulation could potentially be used to predict the penetration of the solar flux into the atmosphere and the wavelengths available for interaction with the organic species present there.

Looking further afield than the Solar System, the presence of planets around stars other than our Sun (exoplanets) is beginning to be confirmed with increasing regularity. The quality of these observations has even reached the stage where it has been possible to infer data on the chemical constituents of the atmospheres of some of these planets through the detected spectra (Tinetti et al., 2007, Swain et al., 2008). As the observational technology continues to improve with proposed missions such as NASA's Space Interferometry Mission (Unwin et al., 2008) and Terrestrial Planet Finder (Beichman, 1998) and ESA's Darwin (Léger et al., 1996) it is hoped to be able to directly image Earth-sized planets in orbit around other stars and to gain

detailed spectra of their atmospheres. As a clearer picture of these planets is obtained by characterising such things as their distance from their parent star, the parent star's output flux and the atmospheric densities and constituent species, the UVIS simulation could be applied to infer the radiative transfer conditions present in their atmospheres and, for Earth or Mars-like atmospheres, the non-ionising radiation flux at the planet's surface.

6.5 Final summary

This thesis has detailed the development of the UVIS simulation; a radiative transfer model of the atmosphere of Mars designed to simulate the radiative flux occurring at the surface of Mars across the ultraviolet, visible and near infrared wavelengths. It has been demonstrated how the UVIS simulation can be applied to support the development of instrumentation for future Mars missions, such as the UVIS spectrometer originally intended for the now delayed and de-scoped ExoMars mission. Specifically it has been shown how simulating the changes in the predicted surface flux, caused by the presence of trace gases and aerosols, can be applied to constrain the operational requirements of instruments intended to study these phenomena. The UVIS simulation has also been applied to more generalised studies of the martian surface environment by characterising variations in the local surface flux across diurnal and annual timescales and across surface latitudes. It is intended that these initial studies will be continued and extended and that the UVIS simulation might also be applied in a wider field of study beyond the atmosphere of Mars.

References

Allen, M., Delitsky, M., Huntress, W., Yung, Y., Ip, W. H., Schwenn, R., Rosenbauer, H., Shelley, E., Balsiger, H. and Geiss, J. (1987) 'Evidence for methane and ammonia in the coma of comet P/Halley', *Astronomy and Astrophysics,* **187,** 502-512.

Allouis, E., Ellery, A. and Welch, C. S. (2005) 'Entry descent and landing systems for small planetary missions: Parametric comparison of parachutes and inflatable systems for the proposed Vanguard Mars mission', *Acta Astronautica,* **59,** 911-922.

Amoruso, A., Crescentini, L., Silvia Cola, M. and Fiocco, G. (1996) 'Oxygen absorption cross-section in the Herzberg continuum', *Journal of Quantitative Spectroscopy and Radiative Transfer,* **56,** 145-152.

Anderson, F. S., Haldeman, A. F. C., Bridges, N. T., Golombek, M. P., Parker, T. J. and Neumann, G. A. (2003) 'Analysis of MOLA data for the Mars Exploration Rover landing sites', *Journal of Geophysical Research E: Planets,* **108**, 8084.

Arvidson, R. E., Poulet, F., Morris, R. V., Bibring, J.-P., Bell III, J. F., Squyres, S. W., Christensen, P. R., Bellucci, G., Gondet, B., Ehlmann, B. L., Farrand, W. H., Fergason, R. L., Golombeck, M., Griffes, J. L., Grotzinger, J., Guinness, E. A., Herkenhoff, K. E., Johnson, J. R., Klingelhöfer, G., Langevin, Y., Ming, D., Seelos, K., Sullivan, R. J., Ward, J. G., Wiseman, S. M. and Wolff, M. J. (2006a) 'Nature and origin of the hematite-bearing plains of Terra

Meridiani based on analyses of orbital and Mars Exploration rover data sets', *Journal of Geophysical Research E: Planets,* **111**, E12S08.

Arvidson, R. E., Squyres, S. W., Anderson, R. C., Bell III, J. F., Blaney, D., Brückner, J., Cabrol, N. A., Calvin, W. M., Carr, M. H., Christensen, P. R., Clark, B. C., Crumpler, L., Des Marais, D. J., de Souza, P. A., d'Uston, C., Economou, T., Farmer, J., Farrand, W. H., Folkner, W., Golombek, M. P., Gorevan, S., Grant, J. A., Greeley, R., Grotzinger, J., Guinness, E., Hahn, B. C., Haskin, L., Herkenhoff, K. E., Hurowitz, J. A., Hviid, S., Johnson, J. R., Klingelhöfer, G., Knoll, A. H., Landis, G., Leff, C., Lemmon, M., Li, R., M.B., Malin, M. C., McLennan, S. M., McSween, H. Y., Ming, D. W., Moersch, J., Morris, R. V., Parker, T., Rice, J. W., Richter, L., Rieder, R., Rodionov, D. S., Schröder, C., Sims, M., Smith, M., Smith, P., Soderblom, L. A., Sullivan, R., Thompson, S. D., Tosca, N. J., Wang, A., Wänke, H., Ward, J., Wdowiak, T., Wolff, M. and Yen, A. S. (2006b) 'Overview of the Spirit Mars Exploration Rover Mission to Gusev Crater: Landing site to Backstay Rock in the Columbia Hills', *Journal of Geophysical Research E: Planets,* **111**, E02S01.

ASTM-E490 (2006) 'Standard Solar Constant and Zero Air Mass Solar Spectral Irradiance Tables', ASTM International, West Conshohocken, PA.

Atkinson, R., Baulch, D. L., Cox, R. A., Crowley, J. N., Hampson, R. F., Hynes, R. G., Jenkin, M. E., Rossi, M. J. and Troe, J. (2004) 'Evaluated kinetic and photochemical data for atmospheric chemistry: Volume I - gas phase reactions of Ox, HOx, NOx and SOx species', *Atmospheric Chemistry and Physics,* **4**, 1461-1738.

Atreya, S. K., Adams, E. Y., Niemann, H. B., Demick-Montelara, J. E., Owen, T. C., Fulchignoni, M., Ferri, F. and Wilson, E. H. (2006a) 'Titan's methane cycle', *Planetary and Space Science,* **54,** 1177-1187.

Atreya, S. K., Mahaffy, P. R. and Wong, A.-S. (2007) 'Methane and related trace species on Mars: Origin, loss, implications for life, and habitability', *Planetary and Space Science,* **55,** 358-369.

Atreya, S. K., Wong, A. S., Renno, N. O., Farrell, W. M., Delory, G. T., Sentman, D. D., Cummer, S. A., Marshall, J. R., Rafkin, S. C. R. and Catling, D. C. (2006b) 'Oxidant enhancement in martian dust devils and storms: Implications for life and habitability', *Astrobiology,* **6,** 439-450.

Baker, V. R. (2001) 'Water and the martian landscape', *Nature,* **412,** 228-236.

Barnes, D., Battistelli, E., Bertrand, R., Butera, F., Chatila, R., Del Biancio, A., Draper, C., Ellery, A., Gelmi, R., Ingrand, F., Koeck, C., Lacroix, S., Lamon, P., Lee, C., Magnani, P., Patel, N., Pompei, C., Re, E., Richter, L., Rowe, M., Siegwart, R., Slade, R., Smith, M. F., Terrien, G., Wall, R., Ward, R., Waugh, L. and Woods, M. (2006) 'The ExoMars rover and Pasteur payload Phase A study: An approach to experimental astrobiology', *International Journal of Astrobiology,* **5,** 221-241.

Beichman, C. A. (1998) 'The Terrestrial Planet Finder: The search for life-bearing planets around other stars' In *Proceedings of SPIE - The International Society for Optical Engineering*, Vol. 3350, pp. 719-723.

Biemann, K., Oro, J., Toulmin III, P., Orgel, L. E., Nier, A. O., Anderson, D. M., Simmonds, P. G., Flory, D., Diaz, A. V., Rushneck, D. R. and Biller, J. A. (1976) 'Search for organic and volatile inorganic compounds in two surface samples from the chryse planitia region of Mars', *Science,* **194,** 72-76.

Bird, M. K., Huchtmeier, W. K., Gensheimer, P., Wilson, T. L., Janardhan, P. and Lemme, C. (1997) 'Radio detection of ammonia in comet Hale-Bopp', *Astronomy and Astrophysics,* **325**, L5-L8.

Bishop, J. L., Dobrea, E. Z. N., McKeown, N. K., Parente, M., Ehlmann, B. L., Michalski, J. R., Milliken, R. E., Poulet, F., Swayze, G. A., Mustard, J. F., Murchie, S. L. and Bibring, J.-P. (2008) 'Phyllosilicate diversity and past aqueous activity revealed at Mawrth Vallis, Mars', *Science,* **321,** 830-833.

Bogumil, K., Orphal, J., Homann, T., Voigt, S., Spietz, P., Fleischmann, O. C., Vogel, A., Hartmann, M., Kromminga, H., Bovensmann, H., Frerick, J. and Burrows, J. P. (2003) 'Measurements of molecular absorption spectra with the SCIAMACHY pre-flight model: instrument characterization and reference data for atmospheric remote-sensing in the 230-2380 nm region', *Atmospheric Photochemistry,* **157,** 167-184.

Boynton, W. V., Feldman, W. C., Squyres, S. W., Prettyman, T. H., Brückner, J., Evans, L. G., Reedy, R. C., Starr, R., Arnold, J. R., Drake, D. M., Englert, P. A. J., Metzger, A. E., Mitrofanov, I., Trombka, J. I., D'Uston, C., Wänke, H., Gasnault, O., Hamara, D. K., Janes, D. M., Marcialis, R. L., Maurice, S., Mikheeva, I., Taylor, G. J., Tokar, R. and Shinohara, C. (2002) 'Distribution of hydrogen in the near surface of Mars: Evidence for subsurface ice deposits', *Science,* **297,** 81-85.

Brown, L. L. and Kasting, J. F. (1991) 'Photochemical model for NH3 in an early Martian atmosphere', *Workshop on the Evolution of the Martian Atmosphere,* Kona, HI, Jun 29 – Jul 1.

Bullock, M. A., Stoker, C. R., McKay, C. P. and Zent, A. P. (1994) 'A Coupled Soil-Atmosphere Model of H2O2 on Mars', *Icarus,* **107,** 142-154.

Cabrol, N. A., Grin, E. A., Newsom, H. E., Landheim, R. and McKay, C. P. (1999) 'Hydrogeologic Evolution of Gale Crater and Its Relevance to the Exobiological Exploration of Mars', *Icarus,* **139,** 235-245.

Cameron, A. G. W. (1983) 'Origin of the atmospheres of the terrestrial planets', *Icarus,* **56,** 195-201.

Carr, M. H. (1987) 'Water on Mars', *Nature,* **326,** 30-35.

Cassi, C. and Giorgio, V. (2008) 'ExoMars mission and spacecraft design' In *International Astronautical Federation - 59th International Astronautical Congress 2008, IAC 2008*, Vol. 2, pp. 1300-1307.

Catling, D. C., Cockell, C. S. and McKay, C. P. (1999) 'Ultraviolet Radiation on the Surface of Mars', *The Fifth International Conference on Mars*, Pasadena, California, July 18-23

Chassefière, E. and Leblanc, F. (2004) 'Mars atmospheric escape and evolution; interaction with the solar wind', *Planetary and Space Science,* **52,** 1039-1058.

Chen, F. Z., Judge, D. L., Wu, C. Y. R. and Caldwell, J. (1999) 'Low and room temperature photoabsorption cross sections of NH3 in the UV region', *Planetary and Space Science,* **47,** 261-266.

Chicarro, A., Martin, P. and Trautner, R. (2003) 'The Mars Express mission: An overview', *European Space Agency, (Special Publication) ESA SP*, 3-13.

Clancy, R. T., Lee, S. W., Gladstone, G. R., McMillan, W. W. and Rousch, T. (1995) 'A New Model for Mars Atmospheric Dust Based Upon Analysis of Ultraviolet through Infrared Observations from Mariner-9, Viking, and Phobos', *Journal of Geophysical Research-Planets,* **100,** 5251-5263.

Clancy, R. T. and Nair, H. (1996) 'Annual (perihelion - aphelion) cycles in the photochemical behaviour of the global Mars atmosphere', *journal of Geophysical Research-Planets,* **101,** 12785-12790.

Clancy, R. T., Sandor, B. J. and Moriarty-Schieven, G. H. (2004) 'A measurement of the 362 GHz absorption line of Mars atmospheric H2O2', *Icarus,* **168,** 116-121.

Clancy, R. T., Sandor, B. J., Wolff, M. J., Christensen, P. R., Smith, M. D., Pearl, J. C., Conrath, B. J. and Wilson, R. J. (2000) 'An intercomparison of ground-based millimeter, MGS TES, and Viking atmospheric temperature measurements: Seasonal and interannual variability of temperatures and dust loading in the global Mars atmosphere', *Journal of Geophysical Research E: Planets,* **105,** 9553-9571.

Cockell, C. S., Catling, D. C., Davis, W. L., Snook, K., Kepner, R. L., Lee, P. and McKay, C. P. (2000) 'The Ultraviolet Environment of Mars: Biological Implications Past, Present, and Future', *Icarus,* **146,** 343-359.

Connerney, J. E. P., Acuña, M. H., Wasilewski, P. J., Kletetschka, G., Ness, N. F., Rème, H., Lin, R. P. and Mitchell, D. L. (2001) 'The global magnetic field of Mars and implications for crustal evolution', *Geophysical Research Letters,* **28,** 4015-4018.

Conrath, B. J. (1975) 'Thermal structure of the Martian atmosphere during the dissipation of the dust storm of 1971', *Icarus,* **24,** 36-46.

Crisp, J. A., Adler, M., Matijevic, J. R., Squyres, S. W., Arvidson, R. E. and Kass, D. M. (2003) 'Mars Exploration Rover mission', *Journal of Geophysical Research E: Planets,* **108**, 8061.

Crumpler, L. S., Squyres, S. W., Arvidson, R. E., Bell, J. F., Blaney, D., Cabrol, N. A., Christensen, P. R., DesMarais, D. J., Farmer, J. D., Fergason, R., Golombek, M. P., Grant, F. D., Grant, J. A., Greeley, R., Hahn, B., Herkenhoff, K. E., Hurowitz, J. A., Knudson, A. T., Landis, G. A., Li, R., Maki, J., McSween, H. Y., Ming, D. W., Moersch, J. E., Payne, M. C., Rice, J. W., Richter, L., Ruff, S. W., Sims, M., Thompson, S. D., Tosca, N., Wang, A., Whelley, P., Wright, S. P. and Wyatt, M. B. (2005) 'Mars exploration rover geologic traverse by the spirit rover in the plains of Gusev crater, Mars', *Geology,* **33,** 809-812.

Curtis, S. A. and Ness, N. F. (1988) 'Remanent magnetism at Mars', *Geophysical Research Letters,* **15,** 737-739.

Drake, S. (1957) 'Discoveries and opinions of Galileo' Anchor Books, New York, pp. 101-143.

Ehhalt, D., Prather, M., Dentener, F., Derwent, R., Dlugokencky, E., Holland, E., Isaksen, I., Katima, J., Kirchhoff, V., Matson, P., Midgley, P. and Wang, M. (2001) 'Chapter 4 - Atmospheric Chemistry and Greenhouse Gases' In *IPCC Third Assessment Report - Climate Change 2001: The Scientific Basis*, pp. 248-251.

Ehlmann, B. L., Mustard, J. F., Fassett, C. I., Schon, S. C., Head Iii, J. W., Des Marais, D. J., Grant, J. A. and Murchie, S. L. (2008) 'Clay minerals in delta deposits and organic preservation potential on Mars', *Nature Geoscience,* **1,** 355-358.

Encrenaz, T., Bézard, B., Greathouse, T. K., Lacy, J. H., Richter, M. J., Atreya, S. K., Wong, A. S., Lebonnois, S., Forget, F. and Lefèvre, F. (2004) 'Hydrogen

peroxide on Mars: Evidence for spatial and seasonal variations', *Icarus,* **170,** 424-429.

Esposito, F., Giuranna, M., Maturilli, A., Palomba, E., Colangeli, L. and Formisano, V. (2007) 'Albedo and photometric study of Mars with the Planetary Fourier Spectrometer on-board the Mars Express mission', *Icarus,* **186,** 527-546.

Fairén, A. G., Schulze-Makuch, D., Rodríguez, A. P., Fink, W., Davila, A. F., Uceda, E. R., Furfaro, R., Amils, R. and McKay, C. P. (2009) 'Evidence for Amazonian acidic liquid water on Mars-A reinterpretation of MER mission results', *Planetary and Space Science,* **57,** 276-287.

Farrand, W. H., Bell III, J. F., Johnson, J. R., Jolliff, B. L., Knoll, A. H., McLennan, S. M., Squyres, S. W., Calvin, W. M., Grotzinger, J. P., Morris, R. V., Soderblom, J., Thompson, S. D., Watters, W. A. and Yen, A. S. (2007) 'Visible and near-infrared multispectral analysis of rocks at Meridiani Planum, Mars, by the Mars Exploration Rover Opportunity', *Journal of Geophysical Research E: Planets,* **112,** E06S02.

Forget, F., Hourdin, F., Fournier, R., Hourdin, C., Talagrand, O., Collins, M., Lewis, S. R., Read, P. L. and Huot, J.-P. (1999) 'Improved general circulation models of the Martian atmosphere from the surface to above 80 km', *Journal of Geophysical Research-Planets,* **104,** 24,155.

Formisano, V., Grassi, D., Ignatiev, N. and Zasova, L. V. (2001) 'IRIS Mariner 9 data revisited: water and dust daily cycles', *Planetary and Space Science,* **49,** 1331-1346.

Formisano, V., Atreya, S., Encrenaz, T., Ignatiev, N. and Giuranna, M. (2004) 'Detection of methane in the atmosphere of Mars', *Science,* **306,** 1758-1761.

Fox, G. K., Code, A. D., Anderson, C. M., Babler, B. L., Bjorkman, K. S., Johnson, J. J., Meade, M. R., Nordsieck, K. H., Sanders, W. T., Weitenbeck, A. J., Zellner, N. E., Edgar, R. J. and Lupie, O. L. (1997) 'Solar System observations by the Wisconsin Ultraviolet Photopolarimeter experiment. 1. The first ultraviolet linear spectropolarimetry of Mars', *Astronomical Journal,* **113,** 1152-1157.

Golombek, M. P., Anderson, R. C., Barnes, J. R., Bell III, J. F., Bridges, N. T., Britt, D. T., Brückner, J., Cook, R. A., Crisp, D., Crisp, J. A., Economou, T., Folkner, W. M., Greeley, R., Haberle, R. M. H., R.B., Harris, J. A., Haldemann, A. F. C., Herkenhoff, K. E., Hviid, S. F., Jaumann, R., Johnson, J. R., Kallemeyn, P. H., Keller, H. U., Kirk, R. L., Knudsen, J. M., Larsen, S., Lemmon, M. T., Madsen, M. B., Magalhães, J. A., Maki, J. N., Malin, M. C., Manning, R. M., Matijevic, J., McSween Jr., H. Y., Moore, H. J., Murchie, S. L., Murphy, J. R., Parker, T. J., Rieder, R., Rivellini, T. P., Schofield, J. T., Seiff, A., Singer, R. B., Smith, P. H., Soderblom, L. A., Spencer, D. A., Stoker, C. R., Sullivan, R., Thomas, N., Thurman, S. W., Tomasko, M. G., Vaughan, R. M., Wänke, H., Ward, A. W. and Wilson, G. R. (1999) 'Overview of the Mars Pathfinder Mission: Launch through landing, surface operations, data sets, and science results', *Journal of Geophysical Research E: Planets,* **104,** 8523-8553.

Golombek, M. P., Grant, J. A., Crumpler, L. S., Greeley, R., Arvidson, R. E., Bell III, J. F., Weitz, C. M., Sullivan, R. J., Christensen, P. R., Soderblom, L. A. and Squyres, S. W. (2006) 'Erosion rates at the Mars Exploration Rover landing sites and long-term climate change on Mars', *Journal of Geophysical Research E: Planets,* **111,** E12S10.

Greeley, R., Whelley, P. L., Arvidson, R. E., Cabrol, N. A., Foley, D. J., Franklin, B. J., Geissler, P. G., Golombek, M. P., Kuzmin, R. O., Landis, G. A., Lemmon, M. T., Neakrase, L. D. V., Squyres, S. W. and Thompson, S. D. (2006) 'Active dust devils in Gusev crater, Mars: Observations from the Mars Exploration Rover Spirit', *Journal of Geophysical Research E: Planets,* **111,** E12S09.

Grotzinger, J., Bell, J., Herkenhoff, K., Johnson, J., Knoll, A., McCartney, E., McLennan, S., Metz, J., Moore, J., Squyres, S., Sullivan, R., Ahronson, O., Arvidson, R., Joliff, B., Golombek, M., Lewis, K., Parker, T. and Soderblom, J. (2006) 'Sedimentary textures formed by aqueous processes, Erebus crater Meridiani Planum, Mars', *Geology,* **34,** 1085-1088.

Gulick, V. C. (2001) 'Origin of the valley networks on Mars: a hydrological perspective', *Geomorphology,* **37,** 241-268.

Harri, A.-M., Makkonen, P., Polkko, J., Lappalainen, H., Pellinen, R., Vorontsov, V., Polyakov, A., Ivankov, A., Linkin, V., Gotlib, V. and Lipatov, A. (2003) 'Metnet - The next generation lander for martian atmospheric science' In *54th International Astronautical Congress of the International Astronautical Federation (IAF), the International Academy of Astronautics and the International Institute of Space Law*, Vol. 2, pp. 3603-3609.

Harri, A.-M., Marsal, O., Lognonne, P., Leppelmeier, G. W., Spohn, T., Glassmeier, K.-H., Angrilli, F., Banerdt, W. B., Barriot, J. P., Bertaux, J.-L., Berthelier, J. J., Calcutt, S., Cerisier, J. C., Crisp, D., Dehant, V., Giardini, D., Jaumann, R., Langevin, Y., Menvielle, M., Musmann, G., Pommereau, J. P., Di Pippo, S., Guerrier, D., Kumpulainen, K., Larsen, S., Mocquet, A., Polkko, J., Runavot, J., Schumacher, W., Siili, T., Simola, J. and Tillman, J. E. (1999)

'Network science landers for Mars', *Advances in Space Research,* **23,** 1915-1924.

Heddle, D. W. O. (1962) 'Photon scattering processes', *Journal of Quantitative Spectroscopy and Radiative Transfer,* **2,** 349-357.

Hirtzig, M., Tokano, T., Rodriguez, S., Le Mouélic, S. and Sotin, C. (2009) 'A review of Titan's atmospheric phenomena', *Astronomy and Astrophysics Review,* **17,** 105-107.

Horowitz, N. H., Hobby, G. L. and Hubbard, J. S. (1976) 'The Viking Carbon Assimilation Experiments: Interim Report', *Science,* **194,** 1321-1322

Huygens, C. (1698) 'Book 1 - Planets Have Water' In *Cosmotheoros* (Ed, Utrecht, U.) Timothy Childe, London, pp. 24-27.

Hynek, B. M. (2004) 'Implications for hydrologic processes on Mars from extensive bedrock outcrops throughout Terra Meridiani', *Nature,* **431,** 156-159.

Ianotta, B. (2004) 'Happy landings on Mars', *Aerospace America,* **42,** 30-35.

Jacobson, M. Z. (2006) 'Global Stratospheric Ozone Reduction' In *Atmospheric pollution: history, science and regulation* Cambridge University Press, Cambridge, pp. 273-307.

Jakosky, B. M. and Phillips, R. J. (2001) 'Mars' volatile and climate history', *Nature,* **412** 237-244.

Joseph, J. H., Wiscombe, J. and Weinman, J. A. (1976) 'The Delta-Eddington Approximation for Radiative Flux Transfer', *Journal of the Atmospheric Sciences,* **33,** 2452 - 2459.

Kaltenegger, L., Fridlund, M. and Kasting, J. (2002) 'Review on habitability and biomarkers', *European Space Agency (Special Publication)* **ESA SP 514,** 277-282.

Kanavarioti, A. and Mancinelli, R. L. (1990) 'Could organic matter have been preserved on Mars for 3.5 billion years?' *Icarus,* **84,** 196-202.

Kasten, F. and Young, A. (1989) 'Revised optical air mass tables and approximation formula', *Applied Optics,* **28,** 4735-4738.

Key, J. R., Yang, P., Baum, B. A. and Nasiri, S. L. (2002) 'Parameterization of shortwave ice cloud optical properties for various particle habits', *Journal of Geophysical Research - Atmospheres,* **107,** 4181.

Kieffer, H. H., Christensen, P. R. and Martin, T. Z. (1976) 'Temperatures of the martian surface and atmosphere: Viking observation of diurnal and geometric variations', *Science,* **194,** 1346-1351.

Klein, H. P. (1978) 'The Viking biological experiments on Mars', *Icarus,* **34,** 666-674.

Klein, H. P., Horowitz, N. H., Levin, G. V., Oyama, V. I., Lederberg, J., Rich, A., Hubbard, J. S., Hobby, G. L., Straat, P. A., Berdahl, B. J., Carle, G. C., Brown, F. S. and Johnson, R. D. (1976) 'The viking biological investigation: Preliminary results', *Science,* **194,** 99-105.

Knauth, L. P., Burt, D. M. and Wohletz, K. H. (2005) 'Impact origin of sediments at the Opportunity landing site on Mars', *Nature,* **438,** 1123-1128.

Krasnopolsky, V. A., Maillard, J. P. and Owen, T. C. (2004) 'Detection of methane in the martian atmosphere: Evidence for life?' *Icarus,* **172,** 537-547.

Lammer, H., Kasting, J. F., Chassefière, E., Johnson, R. E., Kulikov, Y. N. and Tian, F. (2008) 'Atmospheric escape and evolution of terrestrial planets and satellites', *Space Science Reviews,* **139,** 399-436.

Landis, G. A., Kerslake, T. W., Jenkins, P. P. and Scheiman, D. A. (2004) 'Mars Solar Power', *NASA Technical Memorandum 2004-213367.*

Lange, M. A. and Ahrens, T. J. (1982) 'The evolution of an impact-generated atmosphere', *Icarus,* **51,** 96-120.

Lebonnois, S., Quémerais, E., Montmessin, F., Lefèvre, F., Perrier, S., Bertaux, J.-L. and Forget, F. (2006) 'Vertical distribution of ozone on Mars as measured by SPICAM/Mars Express using stellar occultations', *Journal of Geophysical Research E: Planets,* **111**, E09S05.

Lebreton, J.-P., Coustenis, A., Lunine, J., Raulin, F., Owen, T. and Strobel, D. (2009) 'Results from the Huygens probe on Titan', *Astronomy and Astrophysics Review,* **17,** 149-179.

Lefevre, F., Lebonnois, S., Montmessin, F. and Forget, F. (2004) 'Three-dimensional modeling of ozone on Mars', *Journal of Geophysical Research-Planets,* **109**, E07004.

Léger, A., Mariotti, J. M., Mennesson, B., Ollivier, M., Puget, J. L., Rouan, D. and Schneider, J. d. (1996) 'Could we search for primitive life on extrasolar planets in the near future? The DARWIN project', *Icarus,* **123,** 249-255.

Leighton, R. B., Murray, B. C., Sharp, R. P., Allen, J. D. and Sloan, R. K. (1965) 'Mariner IV Photography of Mars: Initial Results', *Science,* **149,** 627-630.

Leighton, R. B., Horowitz, N. H., Murray, B. C., Sharp, R. P., Herriman, A. H., Young, A. T., Smith, B. A., Davies, M. E. and Leovy, C. B. (1969) 'Mariner 6 and 7 television pictures: Preliminary analysis', *Science,* **166,** 49-67.

Lemmon, M. T., Wolff, M. J., Smith, M. D., Clancy, R. T., Banfield, D., Landis, G. A., Ghosh, A., Smith, P. H., Spanovich, N., Whitney, B., Whelley, P., Greeley, R., Thompson, S., Bell, J. F. and Squyres, S. W. (2004) 'Atmospheric imaging results from the Mars exploration rovers: Spirit and Opportunity', *Science,* **306,** 1753-1756.

Levin, G. V. and Straat, P. A. (1976) 'Viking Labeled Release Biology Experiment: Interim Results', *Science,* **194,** 1322-1329.

Lewis, K. W., Aharonson, O., Grotzinger, J. P., Squyres, S. W., Bell III, J. F., Crumpler, L. S. and Schmidt, M. E. (2008) 'Structure and stratigraphy of Home Plate from the Spirit Mars Exploration Rover', *Journal of Geophysical Research E: Planets,* **113**, E12S36.

Lewis, S. R., Matthews, M. S. and Guerrieri, M. L. (1993) 'Atmospheric Effects On The Utility Of Solar Power On Mars' In *Resources Of Near-Earth Space* The University of Arizona Press, Tucson, pp. 845-887.

Lewis, S. R., Collins, M., Read, P. L., Forget, F., Hourdin, F., Fournier, R., Hourdin, C., Talagrand, O. and Huot, J.-P. (1999) 'A climate database for Mars', *Journal of Geophysical Research,* **104,** 24,177.

Lockwood, M. K. (2006) 'Introduction: Mars Science Laboratory: The next generation of Mars Landers', *Journal of Spacecraft and Rockets,* **43, 257.**

Lowell, P. (1906) 'Part IV - The Canals and Life' In *Mars and its Canals* The Macmillian Company, New York, pp. 337-385.

Lowell, P. (1910) 'Schiaparelli', *Popular Astronomy,* **18,** 456-467.

Lucchesini, A. and Gozzini, S. (2005) 'Methane diode laser overtone spectroscopy at 840 nm', *Journal of Quantitative Spectroscopy & Radiative Transfer,* **103,** 209-216.

Lundin, R., Lammer, H. and Ribas, I. (2007) 'Planetary magnetic fields and solar forcing: Implications for atmospheric evolution', *Space Science Reviews,* **129,** 245-278.

Määttänen, A., Fouchet, T., Forni, O., Forget, F., Savijärvi, H., Gondet, B., Melchiorri, R., Langevin, Y., Formisano, V., Giuranna, M. and Bibring, J. P.

(2009) 'A study of the properties of a local dust storm with Mars Express OMEGA and PFS data', *Icarus,* **201,** 504-516.

Magalhaes, J. A., Schofield, J. T. and Seiff, A. (1999) 'Results of the Mars Pathfinder atmospheric structure investigation', *Journal of Geophysical Research,* **104,** 8943-8955.

Malicet, J., Daumont, D., Charbonnier, J., Parisse, C., Chakir, A. and Brion, J. (1995) 'Ozone UV spectroscopy II: Absorption cross sections and temperature dependence', *Journal of Atmospheric Chemistry,* **21,** 263-273.

Malin, M. C. and Edgett, K. S. (2000) 'Evidence for Recent Groundwater Seepage and Surface Runoff on Mars', *Science,* **288,** 2330-2335.

Mallama, A. (2007) 'The magnitude and albedo of Mars', *Icarus,* **192,** 404-416.

Mangold, N., Poulet, F., Mustard, J. F., Bibring, J.-P., Gondet, B., Langevin, Y., Ansan, V., Masson, P., Fassett, C., Head III, J. W., Hoffmann, H. and Neukum, G. (2007) 'Mineralogy of the Nili Fossae region with OMEGA/Mars Express data: 2. Aqueous alteration of the crust', *Journal of Geophysical Research E: Planets,* **112**, E08S04.

Markiewicz, W. J., Keller, H. U., Thomas, N., Titov, D. and Forget, F. (2002) 'Optical properties of the Martian aerosols in the visible spectral range', *Advances in Space Research,* **29,** 175-181.

Marsal, O., Venet, M., Counil, J.-L., Ferri, F., Harri, A.-M., Spohn, T. and Block, J. (2002) 'The netlander geophysical network on the surface of Mars: General mission description and technical design status', *Acta Astronautica,* **51,** 379-386.

Masursky, H., Batson, R. M., Mccauley, J. F., Soderblom, L. A., Wildey, R. L., Carr, M. H., Milton, D. J., Wilhelms, D. E., Smith, B. A., Kirby, T. B., Robinson,

J. C., Leovy, C. B., Briggs, G. A., Duxbury, T. C., Acton Jr., C. H., Murray, B. C., Cutts, J. A., Sharp, R. P., Smith, S., Leighton, R. B., Sagan, C., Veverka, J., Noland, M., Lederberg, J., Levinthal, E., Pollack, J. B., Moore Jr., J. T., Hartmann, W. K., Shipley, E. N., De Vaucouleurs, G. and Davies, M. E. (1972) 'Mariner 9 television reconnaissance of Mars and its satellites: Preliminary results', *Science,* **175,** 294-305.

Mateshvili, N., Fussen, D., Vanhellemont, F., Bingen, C., Dodion, J., Montmessin, F., Perrier, S., Dimarellis, E. and Bertaux, J.-L. (2006) 'Martian ice cloud distribution obtained from SPICAM nadir UV measurements', *Journal of Geophysical Research E: Planets,* **112**, E07004.

Mateshvili, N., Fussen, D., Vanhellemont, F., Bingen, C., Dodion, J., Montmessin, F., Perrier, S. and Bertaux, J. L. (2007) 'Detection of Martian dust clouds by SPICAM UV nadir measurements during the October 2005 regional dust storm', *Advances in Space Research,* **40,** 869-880.

Matson, D. L., Spilker, L. J. and Lebreton, J.-P. b. (2002) 'The Cassini/Huygens mission to the saturnian system', *Space Science Reviews,* **104,** 1-58.

McCleese, D. J. (2003) 'MSL Project Science Integration Group Final Report', *NASA Mars Exploration Program Analysis Group*, May 2003.

McCleese, D. J. (2006) 'Robotic Mars Exploration Strategy 2007-2016', *NASA Mars Advanced Planning Group*, March 2006.

Melosh, H. J. and Vickery, A. M. (1989) 'Impact erosion of the primordial atmosphere of Mars', *Nature,* **338,** 487-489.

Miller, T. M. (1991) 'Atomic and Molecular Polarizabilities', In *CRC Handbook of Chemistry and Physics*, *CRC* Press, Boston, pp 10/194-10/210.

Misra, A. K. (2006) 'Overview of NASA Program on Development of Radioisotope Power Systems with High Specific Power', *4th International Energy Conversion Engineering Conference and Exhibit*, San Diego, California, 26-29 June 2006

Mitchell, R. T. (2008) 'The Cassini Mission exploring Saturn', *Acta Astronautica*, **63**, 61-67.

Montmessin, F., Forget, F., Rannou, P., Cabane, M. and Haberle, R. M. (2004) 'Origin and role of water ice clouds in the Martian water cycle as inferred from a general circulation model', *Journal of Geophysical Research-Planets*, **109**, E10004.

Moores, J. E., Smith, P. H., Tanner, R., Schuerger, A. C. and Venkateswaran, K. i. (2007) 'The shielding effect of small-scale martian surface geometry on ultraviolet flux', *Icarus*, **192**, 417-433.

Moroz, V. I. and Ksanfomaliti, L. V. (1972) 'Preliminary results of astrophysical observations of Mars from Mars-3', *Icarus*, **17**, 408-422.

Mumma, M. J., Villanueva, G. L., Novak, R. E., Hewagama, T., Bonev, B. P., DiSanti, M. A., Mandell, A. M. and Smith, M. D. (2009) 'Strong Release of Methane on Mars in Northern Summer 2003', *Science*, **323**, 1041-1043.

Mustard, J. F., Poulet, F., Head III, J. W., Mangold, N., Bibring, J.-P., Pelkey, S. M., Fassett, C. I., Langevin, Y. and Neukum, G. (2007) 'Mineralogy of the Nili Fossae region with OMEGA/Mars Express data: 1. Ancient impact melt in the Isidis Basin and implications for the transition from the Noachian to Hesperian', *Journal of Geophysical Research E: Planets*, **112**, E08S03.

Mutch, T. A., Binder, A. B., Huck, F. O., Levinthal, E. C., Liebcs Jr., S., Morris, E. C., Patterson, W. R., Pollack, J. B., Sagan, C. and Taylor, G. R. (1976) 'Thc surface of Mars: The view from the Viking 1 lander', *Science,* **193,** 791-801.

Niemann, H. B., Atreya, S. K., Bauer, S. J., Carignan, G. R., Demick, J. E., Frost, R. L., Gautier, D., Haberman, J. A., Harpold, D. N., Hunten, D. M., Israel, G., Lunine, J. I., Kasprzak, W. T., Owen, T. C., Paulkovich, M., Raulin, F., Raaen, E. and Way, S. H. (2005) 'The abundances of constituents of Titan's atmosphere from the GCMS instrument on the Huygens probc', *Nature,* **438,** 779-784.

Novak, R. E., Mumma, M. J. and DiSanti, M. A. (2003) 'Seasonal/Diurnal Mapping of Ozone and Water in the Martian Atmosphere', *Sixth International Conference on Mars*, Pasadena, California, July 20-25.

Ockert-Bell, M. E., Bell, J. F., Pollack, J. B., McKay, C. P. and Forget, F. (1997) 'Absorption and scattering properties of the Martian dust in the solar wavelengths', *Journal of Geophysical Research E: Planets,* **102,** 9039-9050.

Owen, T. (1992) 'The Composition and Early History of the Atmosphere of Mars' In *Mars* (Ed, H.H. Kieffer, B. M. J., C.W. Snyder and M.S. Matthews) University of Arizona Press, Tucson, pp. 818-834.

Oyama, V. I., Berdahl, B. J. and Carle, G. C. (1977) 'Preliminary findings of the Viking gas exchange experiment and a model for Martian surface chemistry', *Nature,* **265,** 110-114.

Parkinson, W. H., Rufus, J. and Yoshino, K. (2003) 'Absolute absorption cross section measurements of CO2 in the wavelength region 163-200 nm and the temperature dependence', *Chemical Physics,* **290,** 251-256.

Patel, M. R., Zarnecki, J. C. and Catling, D. C. (2002) 'Ultraviolet radiation on the surface of Mars and the Beagle 2 UV sensor', *Planetary and Space Science*, **50**, 915-927.

Patel, M. R., Berces, A., Kolb, C., Lammer, H., Rettberg, P., Zarnecki, J. C. and Selsis, F. (2003) 'Seasonal and diurnal variations in Martian surface ultraviolet irradiation: biological and chemical implications for the Martian regolith', *International Journal of Astrobiology*, **2**, 21-34.

Patel, M. R., Berces, A., Kerekgyarto, T., Ronto, G., Lammer, H. and Zarnecki, J. C. (2004a) 'Annual solar UV exposure and biological effective dose rates on the Martian surface' In *Space Life Sciences: Search for Signatures of Life, and Space Flight Environmental Effects on the Nervous System*, Vol. 33, pp. 1247-1252.

Patel, M. R., Towner, M. C., Zarnecki, J. C., Leese, M. R., Davies, A. and Husbands, A. (2004b). A miniature UV-VIS spectrometer for the surface of Mars. In: *35th Lunar and Planetary Science Conference*, 15-19 March 2004, Houston, Texas.

Pepin, R. O. (1991) 'On the origin and early evolution of terrestrial planet atmospheres and meteoritic volatiles', *Icarus*, **92**, 2-79.

Perrier, S., Bertaux, J. L., Lefèvre, F., Lebonnois, S., Korablev, O., Fedorova, A. and Montmessin, F. (2006) 'Global distribution of total ozone on Mars from SPICAM/MEX UV measurements', *Journal of Geophysical Research-Planets*, **111**, E09S06.

Petrova, E., Keller, H. U., Markiewicz, W. J., Thomas, N. and Wuttke, M. W. (1996) 'Ice hazes and clouds in the Martian atmosphere as derived from the Phobos/KRFM data', *Planetary and Space Science*, **44**, 1163-1176.

Pieria, D. (1976) 'Distribution of small channels on the Martian surface', *Icarus,* **27,** 25-50.

Pollack, J. B. (1982) 'Properties of dust in the martian atmosphere and its effect on temperature structure', *Advances in Space Research,* **2,** 45-56.

Pollack, J. B., Colburn, D. S., Flasar, F. M., Kahn, R. A., Carlston, C. E. and Pidek, D. (1979) 'Properties and Effects of Dust Particles Suspended in the Martian Atmosphere', *Journal of Geophysical Research,* **84,** 2929–2945.

Pollack, J. B., OckertBell, M. E. and Shepard, M. K. (1995) 'Viking Lander image analysis of Martian atmospheric dust', *Journal of Geophysical Research,* **100,** 5235 - 5250.

Press, W. H., Flannery, B. P., Teukolsky, S. A. and Vetterling, W. T. (1992) 'LU Decomposition and Its Applications' In *Numerical Recipes in FORTRAN: The Art of Scientific Computing* Cambridge University Press, Cambridge, England, pp. 34-42.

Reeves, R. (1994) 'Introduction' In *The Superpower Space Race: An Explosive Rivalry Through The Solar System* Plenum Press, New York, pp. 1-21.

Rothschild, L. J. (1990) 'Earth analogs for Martian life. Microbes in evaporites, a new model system for life on Mars', *Icarus,* **88,** 246-260.

Rothschild, L. J. and Mancinelli, R. L. (2001) 'Life in extreme environments', *Nature,* **409,** 1092-1101.

Rukes, B. and Dooley, R. B. (2001) 'Guideline on the Use of Fundamental Physical Constants and Basic Constants of Water' The International Association for the Properties of Water and Steam, Gaithersburg, Maryland, USA.

Schofield, J. T., Barnes, J. R., Crisp, D., Haberle, R. M., Larsen, S., Magalhaes, J. A., Murphy, J. R., Seiff, A. and Wilson, G. (1997) 'The Mars Pathfinder

Atmospheric Structure Investigation/Meteorology (ASI/MET) Experiment', *Science,* **278,** 1752-1758.

Schubert, G., Russell, C. T. and Moore, W. B. (2000) 'Geophysics: Timing of the Martian dynamo', *Nature Geoscience*, 666-667.

Shettle, E. P. and Weinman, J. A. (1970) 'The Transfer of Solar Irradiance Through Inhomogeneous Turbid Atmospheres Evaluated by Eddington's Approximation', *Journal of Atmospheric Sciences,* **27,** 1048 - 1055.

Simpson, D., Winiwarter, W., Börjesson, G., Cinderby, S., Ferreiro, A., Guenther, A., Hewitt, C. N., Janson, R., Khalil, M. A. K., Owen, S., Pierce, T. E., Puxbaum, H., Shearer, M., Skiba, U., Steinbrecher, R., Tarrasón, L. and Öquist, M. G. (1999) 'Inventorying emissions from nature in Europe', *Journal of Geophysical Research D: Atmospheres,* **104,** 8113-8152.

Smith, M. D. (2002) 'The annual cycle of water vapor on Mars as observed by the Thermal Emission Spectrometer', *Journal of Geophysical Research E: Planets,* **107,** 25-1.

Smith, M. D. (2004) 'Interannual variability in TES atmospheric observations of Mars during 1999-2003', *Icarus,* **167,** 148-165.

Smith, M. D., Wolff, M. J., Spanovich, N., Ghosh, A., Banfield, D., Christensen, P. R., Landis, G. A. and Squyres, S. W. (2006) 'One Martian year of atmospheric observations using MER Mini-TES', *Journal of Geophysical Research-Planets,* **111**, E12S13.

Smith, P. H. and Lemmon, M. (1999) 'Opacity of the Martian atmosphere measured by the Imager for Mars Pathfinder', *Journal of Geophysical Research E: Planets,* **104,** 8975-8985.

Soffen, G. A. (1976) 'Scientific results of the Viking missions', *Nature,* **194,** 1274-1276.

Solomon, S. C., Aharonson, O., Aurnou, J. M., Banerdt, W. B., Carr, M. H., Dombard, A. J., Frey, H. V., Golombek, M. P., Hauck, S. A., Head, J. W., Jakosky, B. M., Johnson, C. L., McGovern, P. J., Neumann, G. A., Phillips, R. J., Smith, D. E. and Zuber, M. T. (2005) 'New Perspectives on Ancient Mars', *Science,* **307** 1214-1220.

Spanovich, N., Smith, M. D., Smith, P. H., Wolff, M. J., Christensen, P. R. and Squyres, S. W. (2006) 'Surface and near-surface atmospheric temperatures for the Mars Exploration Rover landing sites', *Icarus,* **180,** 314-320.

Squyres, S. W. and Kasting, J. F. (1994) 'Early Mars: How warm and how wet?' *Science,* **265,** 744-749.

Squyres, S. W., Arvidson, R. E., Bollen, D., Bell III, J. F., Brückner, J., Cabrol, N. A., Calvin, W. M., Carr, M. H., Christensen, P. R., Clark, B. C., rumpler, L., Des Marais, D. J., d'Uston, C., Economou, T., Farmer, J., Farrand, W. H., Folkner, W., Gellert, R., Glotch, T. D., Golombek, M. P., Gorevan, S., Grant, J. A., Greeley, R., Grotzinger, J., Herkenhoff, K. E., Hviid, S., Johnson, J. R., Klingelhöfer, G., Knoll, A. H., Landis, G., Lemmon, M. T., Li, R., Madsen, M. B., Malin, M. C., McLennan, S. M., McSween, H. Y., Ming, D. W., Moersch, J., Morris, R. V., Parker, T., Rice, J. W., Richter, L., Rieder, R., Schröder, C., Sims, M., Smith, M., Smith, P., Soderblom, L. A., Sullivan, R. J., Tosca, N. J., Wänke, H., Wdowiak, T., Wolff, M. J. and Yen, A. S. (2006a) 'Overview of the Opportunity Mars Exploration Rover Mission to Meridiani Planum: Eagle Crater to Purgatory Ripple', *Journal of Geophysical Research E: Planets,* **111,** E12S12.

Squyres, S. W., Knoll, A. H., Arvidson, R. E., Clark, B. C., Grotzinger, J. P., Jolliff, B. L., McLennan, S. M., Tosca, N., Bell III, J. F., Calvin, W. M., Farrand, W. H., Glotch, T. D., Golombek, M. P., Herkenhoff, K. E., Johnson, J. R., Klingelhöfer, G., McSween, H. Y. and Yen, A. S. (2006b) 'Two years at Meridiani Planum: Results from the opportunity rover', *Science,* **313,** 1403-1407.

Stockstill, K. R., Moersch, J. E., McSween Jr., H. Y., Piatek, J. and Christensen, P. R. (2007) 'TES and THEMIS study of proposed paleolake basins within the Aeolis quadrangle of Mars', *Journal of Geophysical Research E: Planets,* **112.**, E01001

Sullivan, R., Banfield, D., Bell III, J. F., Calvin, W., Fike, D., Golombek, M., Greeley, R., Grotzinger, J., Herkenhoff, K., Jerolmack, D., Malin, M., Ming, D., Soderblom, L. A., Squyres, S. W., Thompson, S., Watters, W. A., Weitz, C. M. and Yen, A. (2006) 'Aeolian processes at the Mars Exploration Rover Meridiani Planum landing site', *Nature,* **436,** 58-61.

Swain, M. R., Vasisht, G. and Tinetti, G. (2008) 'The presence of methane in the atmosphere of an extrasolar planet', *Nature,* **452,** 329-331.

Tinetti, G., Vidal-Madjar, A., Liang, M.-C., Beaulieu, J.-P., Yung, Y., Carey, S., Barber, R. J., Tennyson, J., Ribas, I., Allard, N., Ballester, G. E., Sing, D. K. and Selsis, F. (2007) 'Water vapour in the atmosphere of a transiting extrasolar planet', *Nature,* **448,** 169-171.

Tomasko, M. G., Doose, L., Engel, S., Dafoe, L. E., West, R., Lemmon, M., Karkoschka, E. and See, C. (2008) 'A model of Titan's aerosols based on measurements made inside the atmosphere', *Planetary and Space Science,* **56,** 669-707.

Tomasko, M. G., Doose, L. R., Lemmon, M., Smith, P. H. and Wegryn, E. (1999) 'Properties of dust in the Martian atmosphere from the Imager on Mars Pathfinder', *Journal of Geophysical Research-Planets,* **104,** 8987-9007.

Toon, O. B., Pollack, J. B. and Sagan, C. (1977) 'Physical-Properties of Particles Composing Martian Dust Storm of 1971-1972', *Icarus,* **30,** 663-696.

Tourna, J. and Wisdom, J. (1993) 'The chaotic obliquity of mars', *Science,* **259,** 1294-1297.

Unwin, S. C., Shao, M., Tanner, A. M., Allen, R. J., Beichman, C. A., Boboltz, D., Catanzarite, J. H., Chaboyer, B. C., Ciardi, D. R., Edberg, S. J., Fey, A. L., ischer, D. A., Gelino, C. R., Gould, A. P., Grillmair, C., Henry, T. J., Johnston, K. V., Johnston, K. J., Jones, D. L., Kulkarni, S. R., Law, N. M., Majewski, S. R., Makarov, V. V., Marcy, G. W., Meier, D. L., Olling, R. P., Pan, X., Patterson, R. J., Pitesky, J. E., Quirrenbach, A., Shaklan, S. B., Shaya, E. J., Strigari, L. E., Tomsick, J. A., Wehrle, A. E. and Worthey, G. (2008) 'Taking the measure of the universe: Precision astrometry with SIM PlanetQuest', *Publications of the Astronomical Society of the Pacific,* **120,** 38-88.

Ward, W. R. (1982) 'Comments on the long-term stability of the Earth's obliquity', *Icarus,* **50,** 444-448.

Ward, W. R. and Rudy, D. J. (1991) 'Resonant obliquity of Mars?' *Icarus,* **94,** 160-164.

Westall, F., Brack, A., Hofmann, B., Horneck, G., Kurat, G., Maxwell, J., Gabriele Ori, G., Pillinger, C., Raulin, F., Thomas, N., Fitton, B., Clancy, P., Pricur, D. and Vassaux, D. (2000) 'An ESA study for the search for life on Mars', *Planetary and Space Science,* **48,** 181-202.

Williamson, M. (2009) 'EXOMARS: Europe rises to the challenge', *Aerospace America,* **47,** 38-45.

Withers, P., Lorenz, R. D. and Neumann, G. A. (2002) 'Comparison of viking lander descent data and MOLA topography reveals kilometer-scale offset in Mars atmosphere profiles', *Icarus,* **159,** 259-261.

Withers, P. and Smith, M. D. (2006) 'Atmospheric entry profiles from the Mars Exploration Rovers Spirit and Opportunity', *Icarus,* **185,** 133-142.

Wolff, M. J., Lee, S. W., Clancy, R., Martin, L. J., Bell III, J. F. and James, P. B. (1997) '1995 observations of Martian dust storms using the Hubble Space Telescope', *Journal of Geophysical Research,* **102,** 1679-1692.

Wolff, M. J., Bell III, J. F., James, P. B., Clancy, R. and Lee, S. W. (1999) 'Hubble Space Telescope observations of the Martian aphelion cloud belt prior to the Pathfinder mission: Seasonal and interannual variations', *Journal of Geophysical Research,* **104,** 9027-9041.

Wolff, M. J., Smith, M. D., Clancy, R. T., Spanovich, N., Whitney, B. A., Lemmon, M. T., Bandfield, J. L., Banfield, D., Ghosh, A., Landis, G., Christensen, P. R., Bell, J. F. and Squyres, S. W. (2006) 'Constraints on dust aerosols from the Mars Exploration Rovers using MGS overflights and Mini-TES', *Journal of Geophysical Research-Planets,* **111,** E12S17.

Zurek, R. W. and Martin, L. J. (1993) 'Interannual variability of planet-encircling dust storms on Mars', *Journal of Geophysical Research,* **98,** 3247-3259.